EFFICIENT AND ACCURATE ALGORITHMS FOR ULTRA-WIDEBAND WIRELESS SYSTEM PROPAGATION MODELLING AND CLIENT LOCATION.

by

John B Diskin, B.Eng.

A dissertation submitted to Dublin City University
for the degree of
Doctor of Philosophy
January 2011

Research Supervisor:

Dr. Conor Brennan

Declaration

I hereby certify that this material, which I now submit for assessment on the programme of study leading to the award of Doctor of Philosophy is entirely my own work, that I have exercised reasonable care to ensure that the work is original, and does not to the best of my knowledge breach any law of copyright, and has not been taken from the work of others save and to the extent that such work has been cited and acknowledged within the text of my work.

Signed : . . . . . ID No. : 50033529 Date : 19/01/2011

Abstract

The aims of this work include the refinement of ray-tracing based radio propagation simulation and the development of a novel wide-band indoor geo-location technique.

The proliferation in the use of indoor radio based data communication systems in recent years has lead to a growing demand for accurate but efficient propagation prediction techniques for the purposes of optimizing performance and planning infrastructure in varied environments. This work further improves the efficiency of ray-tracing and adapts it for use in wide-band technologies such as Ultra-wideband (UWB).

Initially, a visibility algorithm is developed which improves the computational efficiency of ray-tracing. This technique yields faster simulations of large scale environments by identifying and removing redundant scattering surfaces from ray trajectory computations at a pre-processing stage.

An efficient approach to UWB ray-tracing simulations is also developed. This acceleration technique allows for frequency domain UWB channels to be computed from a reduced set of sample frequencies, while rigorously accounting for frequency dependent propagation effects over UWB bandwidths. Applying this technique to a conventional frequency domain simulator results in reduced simulation times while maintaining the capability to including frequency dependent scattering effects.

The large bandwidths associated with UWB channels offer the possibility of obtaining very precise time based location measurements. In recognition of this, the aforementioned UWB ray-tracing acceleration technique is employed in order to aid the development of a novel reflection-based geo-location algorithm. This technique allows for reduced infrastructure when obtaining time difference of arrival (TDOA) positioning measurements in indoor environments. In addition, an accelerated computation technique is demonstrated, which offers an efficient alternative to existing autocorrelation based techniques when obtaining TDOA measurement between consecutively received UWB pulses.

To my Family and Friends

Contents

List of Figures

List of Tables

Chapter 1

Introduction

This thesis is concerned with the development of efficient ray tracing tools for the purposes of designing novel location algorithms. Accordingly this work has two distinct but complementary objectives:

- The refinement of classical radio ray tracing based propagation modelling in terms of efficiency and accuracy. Specifically, this entails developing novel algorithms for the purposes of improving the computational efficiency of a ray tracing based propagation simulator.
- The development of novel indoor radio geo-location algorithms aided by the use of accelerated ray-tracing simulations.

Recent years have seen a proliferation in the use of indoor radio based data communication systems such as wireless LAN (Local Area Networks), UWB (Ultra-wideband) and bluetooth connectivity technologies. With the arrival of these schemes, propagation modelling was required for the purposes of optimizing performance and planning infrastructure in varied environments. To date, a variety of propagation models exist which can provide this information to varying levels of accuracy. These include statistical or empirical based techniques such as those of [1, 2, 3]. However, in more recent times planners have increasingly turned to deterministic models, which attempt to solve the relevant Maxwell's equations for particular combinations of wireless schemes and environments. Ray tracing is one such modelling method that has come to prominence in recent times [4]. While ray-tracing is an asymptotic method and may not be as computationally accurate as full wave methods [5, 6], it offers a deterministic but more efficient means of propagation modelling in large-scale environments at high frequencies. This work builds on a narrow-band ray tracing simulator developed at Trinity College Dublin during the Ph.D

candidature of Dr. Eamon Kenny [7].

Ultra-wideband signal propagation is a recurring topic through-out this work. The sanctioning of Ultra-Wideband (UWB) as a wireless communications medium by the Federal Communication Commission (FCC) in 2002, constituted a significant potential for development of novel capabilities in wireless applications [8, 9]. In particular the large bandwidth implied by UWB offered the possibility of unprecedented large data-rates and enhancements to other periphery applications such as wireless geo-location [10]. Owing to the restrictive power limits imposed by regulators on wide-band transmissions and the narrow time domain pulses used, UWB represents an ideal platform for indoor geo-location [10]. Recognizing this and given the focus of this project on geo-location applications, it was deemed necessary to incorporate UWB channel propagation into ray tracing simulations. However, due to the large numbers of frequencies present in an UWB channel, such an extension to ray tracing has a detrimental effect on the efficiency of simulations resulting in increased computational requirements. Accordingly, the efforts of this work have been concerned with reducing this and other computational burdens associated with ray based propagation modelling.

Since the emergence of modern wireless communication networks, there has been a growing interest in geo-location. The prospect of position location capabilities has lead to speculation of various possible future applications such as logistical tracking in warehouses, co-ordination of rescue services and medical patient tracking amongst others [11]. Early applications were concerned with providing outdoor geo-location over large areas. These include the Global Position System (GPS) [12] and the E-911 [13] emergency mobile phone location system. However, in contrast, this work focuses on short range indoor schemes with a particular emphasis on UWB based systems [10, 14]. Prior to the advent of UWB, indoor positioning relied on legacy narrow band platforms such as the IEEE 802.11b/g wireless LAN standard. An example of such a geo-location scheme was presented in [15] where received signal strengths from multiple base-stations are associated with a unique discrete physical location. Using this information, a physical location can be calculated from a particular combination of received signal strengths. However, since the arrival of UWB, recent research has shifted to employing time based algorithms for precision location [16, 17, 18, 19]. The focus of the latter part of this thesis is on refinements to such UWB based geo-location schemes. Specifically, novel approaches are presented in Chapter 5, which aim to reduce the infrastructure

and computational requirements of deploying an indoor geo-location system.

The initial stages of this research project were concerned with improving the computational efficiency of ray tracing propagation modelling. This yielded the algorithm presented in Chapter 3, which removes redundant reflecting surfaces at a pre-processing stage of simulations. Subsequent efforts were focussed on the computational burden associated with modelling UWB channels. Accordingly, the novel frequency sweep acceleration technique of Chapter 4 was developed in order to address this problem. Following such improvements to ray tracing modelling, work began on the reflection based geo-location algorithm of Chapter 5. This UWB time-based technique was developed and tested using channels generated by the accelerated ray tracing simulator.

The overall structure of this thesis is as follows:

Chapter 2 contains background discussions of the central topics pertaining to this project. This includes an introduction to ray tracing propagation modelling, the Ultra Wideband channel and geo-location technologies. In addition, the frequency dependent phenomena associated with wide-band channel modelling are also introduced.

In Chapter 3 a novel visibility algorithm for ray tracing engines is presented. This technique involves removing redundant reflecting surfaces at a pre-processing stage thus reducing the computational burden of point to point ray tracing in environments containing a large amount of reflecting surfaces. This algorithm was specifically designed for use with simulations that account for rays propagating through several consecutive walls. In addition, it should be noted that the proposed technique is applicable to both wide-band and narrow-band simulators. This work was previously presented at the 2006 European Conference on Antennas and Propagation in Nice, France [20].

A key advantage of employing frequency domain based simulations is that frequency dependent channel variations can be rigorously calculated over wide bandwidths such as those used in Ultra-Wideband (UWB). However, the enormous UWB channel bandwidth of several Giga-Hertz can result in an increased computational overhead. In Chapter 4 an acceleration technique is introduced that aims to reduce this burden. This algorithm allows full sweep UWB channels to be approximated from a ray tracing simulation using a reduced set of sample frequencies. This technique has been presented at the 65^{th} IEEE Vehicular Technology Conference in 2007 [21] and at the 25^{th} Progress In Electromagnetics Research Symposium (PIERS) of 2008 in Beijing China [22].

Initially in Chapter 5 a reflection based geo-location scheme is outlined that allows for a receiver's position to be obtained using less infrastructure than existing schemes [10, 19, 18]. This technique has been developed with the aid of the accelerated UWB ray tracing modelling algorithm introduced in Chapter 4. In addition, this chapter is also concerned with alleviating the computational cost associated with the timing acquisition of received UWB pulses. The operation of time based geo-location techniques [16,17,18,19] depends on such timing acquisitions. In particular, the reflection based geo-location techniques developed in this work require the ability to compute the time difference of arrival (TDOA) between two consecutively received pulses. To date the most efficient means of carrying out such an operation has been to use auto-correlation based on Fast Fourier Transforms (FFT) [23]. However, in this chapter an alternative approach is developed, which reduces the overall computational requirements when such obtaining time difference of arrival measurements.
Finally a general conclusion and possible future developments are presented in Chapter 6.

Chapter 2

Background

2.1 Ray Tracing

In the context of this work the term "ray tracing" entails the use of Geometric Optics (GO) in combination with the Uniform Theory of Diffraction (UTD) [24] for the purposes of modelling electromagnetic scattering effects. This method is a computationally efficient means of predicting electromagnetic propagation within large scale environments at high frequencies. Ray tracing offers a deterministic alternative to statistical or empirical based models such as those of [1, 2, 3]. However, it should be noted that this modelling technique is an approximate technique that assumes propagation at high frequencies occurs along straight line trajectories or 'rays' between scattering events. Alternative numerically exact electromagnetic computational techniques have also been developed. These include integral equation, finite element and finite difference time domain methods [5]. The integral equation method's computations are based on the integral form of Maxwell's equations. The technique requires each scattering object to be discretised in order to compute the currents induced by an electric field incident on the object. For a homogenous object the scattered field can be obtained if the surface currents are known. In the case of an in-homogenous object, the currents within each element over the entire volume of the scattering object must be specified. Alternatively, the Finite Difference Time Domain (FDTD) and Finite Element Methods (FEM) rely on the solution of the partial differential equations associated with the differential form of Maxwell equations. FDTD requires the propagation environment to be divided into a uniform mesh of cells, upon which the electric and magnetic fields are solved. By employing a "leapfrog" strategy, FDTD allows for the direct computation of electric and magnetic fields at a range of discrete instances

in time [6]. While FEM also uses the differential form of Maxwell's equations, only the entire space surrounding a scattering object is subdivided into a large number of regions known as elements. The size of each element can vary throughout the space allowing a denser element concentration at areas of interest. This also enables FEM to cope effectively with complex geometries. However, a common characteristic of these numerically exact methods is that they require intensive discretisation of either the scattering object or the entire scattering environment. In addition, the level of discretisation per unit volume or area grows with frequency making these methods impractical for high frequency scattering problems over large scale areas. Consequently, ray tracing techniques have gained popularity for the purpose of computing propagation channels in such large environments [25,4]. Accordingly, this method is central to the remaining discussions of this work.

In a free-space medium the time-harmonic electric and magnetic fields satisfy Maxwell's equations,

$$\nabla \times \mathbf{E}(\mathbf{r}, \omega) + j\omega\mu_0 \mathbf{H}(\mathbf{r},\omega) = 0, \tag{2.1}$$

$$\nabla \times \mathbf{H}(\mathbf{r}, \omega) - j\omega\epsilon_0 \mathbf{E}(\mathbf{r},\omega) = 0, \tag{2.2}$$

$$\nabla \cdot \mathbf{E}(\mathbf{r}, \omega) = 0, \tag{2.3}$$

$$\nabla \cdot \mathbf{H}(\mathbf{r}, \omega) = 0, \tag{2.4}$$

where the position vector is given by $\mathbf{r}$, and ω denotes the angular frequency. μ_0 and ϵ_0 represent the free space permeability and permittivity respectively. By combining Equations (2.1-2.4) the magnetic field vector $\mathbf{H}$ can be eliminated yielding the Helmholtz Equation,

$$\nabla^2 \mathbf{E}(\mathbf{r}, \omega) + \beta^2 \mathbf{E}(\mathbf{r}, \omega) = 0 \tag{2.5}$$

where

$$\beta^2 = \omega^2 \mu_o \epsilon_0. \tag{2.6}$$

The Luneberg-Kline high frequency expansion allows the electric field to be approximated as [26, 27],

$$\mathbf{E}(\mathbf{r},\omega) \sim e^{-j\beta_0\psi(\mathbf{r})} \sum_{m=0}^{\infty} \frac{\mathbf{E}_m(\mathbf{r})}{(j\omega)^m}, \tag{2.7}$$

where $\psi(\mathbf{r})$ is the eikonal surface (Equation 2.10) at a position $\mathbf{r}$. As the angular frequency ω tends to infinity the Luneberg-Kline expansion becomes,

$$\mathbf{E}(\mathbf{r})_{\omega\to\infty} \sim e^{-j\beta_0\psi(\mathbf{r})}\mathbf{E}_0(\mathbf{r}). \tag{2.8}$$

The flow of energy along a path length s is governed by transport equations. Combining Equation 2.8 with the previous Maxwell Equations (Equations 2.1-2.4) and the Helmholtz Equation (Equation 2.5) results in a zeroth order transport equation,

$$\frac{\partial \mathbf{E}_0}{\partial s} + \frac{1}{2}\{\frac{\nabla\psi}{n}\}\mathbf{E}_0 = 0. \tag{2.9}$$

Additionally, the eikonal equation is expressed as

$$\mid \nabla\psi \mid^2 = n^2, \tag{2.10}$$

where n is the refractive index of the propagation medium and for a free-space medium is equal to 1. Propagation occurs at a direction normal to the eikonal surface such that,

$$\nabla\psi = \hat{s}. \tag{2.11}$$

Integrating the transport equation of Equation 2.9 over the path of the ray s gives the following expression for the electric field of Equation 2.8 as,

$$\mathbf{E}(s) = \mathbf{E}_0^{'} e^{j\phi(0)} \sqrt{\frac{\rho_1\rho_2}{(\rho_1+s)(\rho_2+s)}} e^{-j\beta_0 s}. \tag{2.12}$$

This equation describes the effects on a ray as it travels a length s in the direction of the unit vector $\hat{s}$, where $\mathbf{E}_0^{'} e^{j\phi(0)}$ represents the value of the complex electric field at $s = 0$. The phase variation of this electric field along a length s is determined by $e^{-j\beta_0 s}$. Spatial attenuation due to the spreading of the wavefront from an astigmatic source, as shown in Figure 2.1, is accounted for by the term,

$$\sqrt{\frac{\rho_1\rho_2}{(\rho_1+s)(\rho_2+s)}}, \tag{2.13}$$

where ρ_1 and ρ_2 are radii of curvature of the eikonal surface at $s = 0$. In the case of a spherical wavefront emanating from an point source, ρ_1 and ρ_2 are of equal length. However, other types wavefront can also be accommodated by employing different configurations of ρ_1 and ρ_2. In the case of a cylindrical wavefront, $\rho_1 = \infty$ and for planar wavefronts, $\rho_2 = \rho_1 = \infty$. A detailed derivation of Equation 2.12 is available in Chapter 2 of [28]. The author shows the steps involved in combining Maxwell's equations with the Luneberg-Kline expansion in order to obtain an expression for propagation in the form of a ray. However, for the purposes of this work, the expression in Equation 2.12 is sufficient for computing the values of electric field from a source in a free space propagation medium.

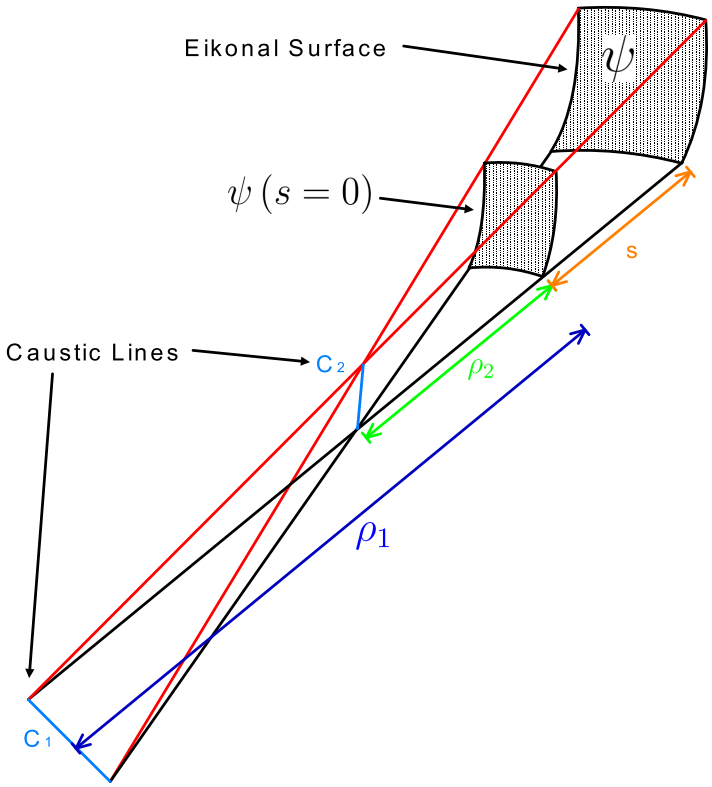

Figure 2.1: Astigmatic Source

In addition to propagation in free space, scattering effects from objects in the ray path must also be considered. When rays interact with obstacles in the propagation environment there is either a resultant reflection, transmission or diffraction. Reflection and transmission coefficients are used to account for the proportion of energy that is reflected from and transmitted through an object's surface. Diffraction coefficients are employed in order to allow additional effects due to edges, formed when two object surfaces intersect, to be computed.

2.1.1 Reflected Rays

Figure 2.2 shows the reflection of a ray from a flat surface. In this scenario a free space incident ray encounters a surface at the point **Q** and subsequently undergoes a reflection. The reflected ray follows a trajectory forming an angle matching the angle θ_i made by the incident ray with respect to the surface normal $\hat{n}$.

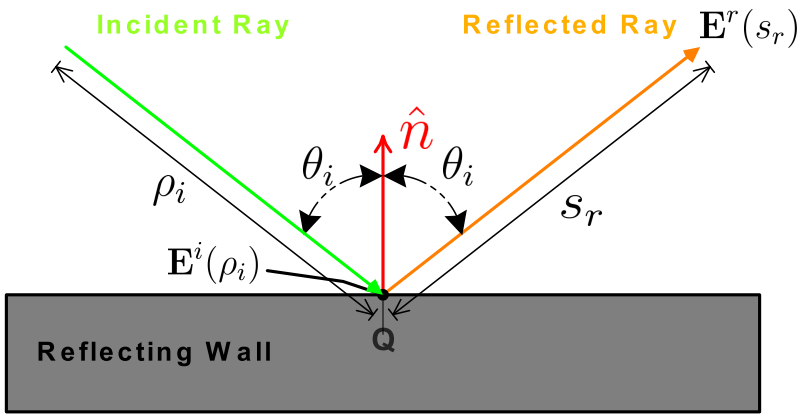

Figure 2.2: Reflected Ray

The electric field associated with the reflected ray of Figure 2.2 is expressed as,

$$\mathbf{E}^r(s_r) = \mathbf{E}^i(\rho_i) \cdot \overline{\mathbf{R}} \frac{\rho_i}{\rho_i + s_r} e^{-j\beta_0 s_r}, \tag{2.14}$$

where $\mathbf{E}^i(\rho_i)$ is the incident field at the point of reflection **Q** at a distance ρ_i from an isotropic point source. The $\frac{\rho_i}{\rho_i + s_r}$ term accounts for the spatial attenuation of the reflected signal. The dyadic reflection coefficient $\overline{\mathbf{R}}$ determines the proportion of a ray's energy that is reflected from the surface. In order to compute this coefficient the incident electric field $\mathbf{E}^i(\rho_i)$ must be decomposed into two separate components where,

$$\mathbf{E}^i(\rho_i) = E^i_\perp(\rho_i)\hat{e}_\perp + E^i_\parallel(\rho_i)\hat{e}_\parallel, \tag{2.15}$$

and

$$E^i_\perp(\rho_i) = \mathbf{E}^i(\rho_i) \cdot \hat{e}_\perp, \tag{2.16}$$

$$E^i_\parallel(\rho_i) = \mathbf{E}^i(\rho_i) \cdot \hat{e}_\parallel. \tag{2.17}$$

$E^i_\perp(\rho_i)$ and $E^i_\parallel(\rho_i)$ represent the perpendicular and parallel components of $\mathbf{E}^i(\rho_i)$ with respect to the incidence plane of Figure 2.3.

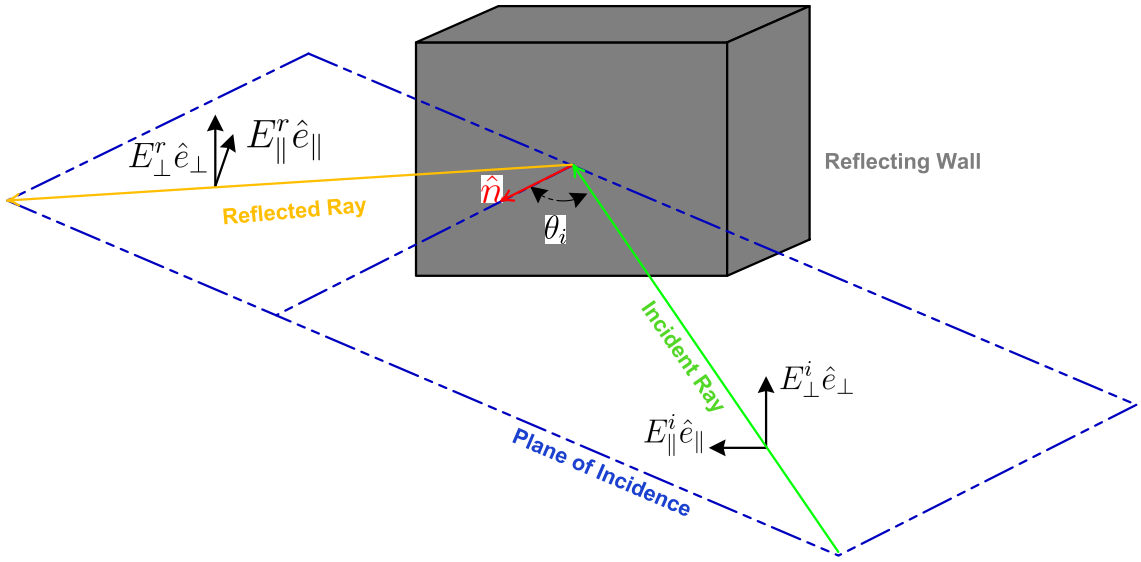

Figure 2.3: Polarisation with respect to Incidence Plane

Correspondingly the reflection coefficient $\overline{\mathbf{R}}$ is also divided into separate components and applied individually to both $E^i_\perp(\rho_i)$ and $E^i_\parallel(\rho_i)$ such that,

$$\overline{\mathbf{R}} = \begin{pmatrix} R_\perp(\omega) & 0 \\ 0 & R_\parallel(\omega) \end{pmatrix}, \tag{2.18}$$

where

$$R_\perp(\omega) = \frac{\cos\theta_i - \sqrt{\frac{\varepsilon(\omega)}{\varepsilon_0} - \sin^2\theta_i}}{\cos\theta_i + \sqrt{\frac{\varepsilon(\omega)}{\varepsilon_0} - \sin^2\theta_i}}, \tag{2.19}$$

and

$$R_\parallel(\omega) = \frac{-\frac{\varepsilon(\omega)}{\varepsilon_0}\cos\theta_i + \sqrt{\frac{\varepsilon(\omega)}{\varepsilon_0} - \sin^2\theta_i}}{\frac{\varepsilon(\omega)}{\varepsilon_0}\cos\theta_i + \sqrt{\frac{\varepsilon(\omega)}{\varepsilon_0} - \sin^2\theta_i}}. \tag{2.20}$$

In the above expressions the free space permittivity is given by ε_0 while ω represents angular frequency. $\varepsilon(\omega)$ is the effective complex permittivity of the reflecting medium where [29],

$$\varepsilon(\omega) = \varepsilon'(\omega) - \jmath\varepsilon''(\omega)\, p_e(\omega). \tag{2.21}$$

and

$$\varepsilon^{'}(\omega) = \varepsilon_r(\omega)\,\varepsilon_0, \tag{2.22}$$

while $\varepsilon_r(\omega)$ is the relative permittivity of the material and p_e represents the effective loss tangent, defined as

$$p_e(\omega) = \frac{\omega\varepsilon^{''}(\omega) + \sigma(\omega)}{\omega\varepsilon^{'}(\omega)}. \tag{2.23}$$

$\varepsilon^{''}(\omega)$ is attributable to dielectric loss and $\sigma(\omega)$ corresponds to the macroscopic loss. Since it is difficult to separate these two effects they are combined in $p_e(\omega)$ as an effective loss tangent in Equation 2.23 [30]. It should be noted that the variation of the material permittivity $\varepsilon(\omega)$ of Equation 2.21 with ω introduces a corresponding frequency dependency in the reflection coefficients $R_{\parallel}(\omega)$ and $R_{\perp}(\omega)$. Further discussion of the frequency dependent variation of material permittivity is deferred until Section 2.1.5

2.1.2 Transmission of Ray through a Facet

In addition to reflection, incident rays generally undergo a transmissions when their trajectories intersects an object. Figure 2.4 depicts such a scenario where a ray propagates through a regular slab. In a typical indoor environment this slab could be considered representative of a typical wall or other structural facet. However, it should be noted that for the scenario depicted in Figure 2.4, it is assumed that both the transmitter and receiver are located in far field regions with respect to the thickness of the slab.
The ray emerging from the slab in Figure 2.4 is expressed as

$$\mathbf{E}^t(s_t) = \mathbf{E}^i(\rho_i) \cdot \overline{\mathbf{T}}^{12} \cdot \overline{\mathbf{T}}^{21} \frac{\rho_i}{\rho_i + s_t} e^{-k_2 s_t} \tag{2.24}$$

where $\mathbf{E}^i(\rho_i)$ is the incident field at the surface of the slab. s_t is the propagation length inside the slab and is computed as,

$$s_t = \frac{d}{\cos\theta_t}, \tag{2.25}$$

where d is the width of the slab and θ_t is the transmission angle. θ_t is computed using Snell's law of refraction where,

$$\sin\theta_t = \frac{1}{\sqrt{\varepsilon_r}} \sin\theta_i \tag{2.26}$$

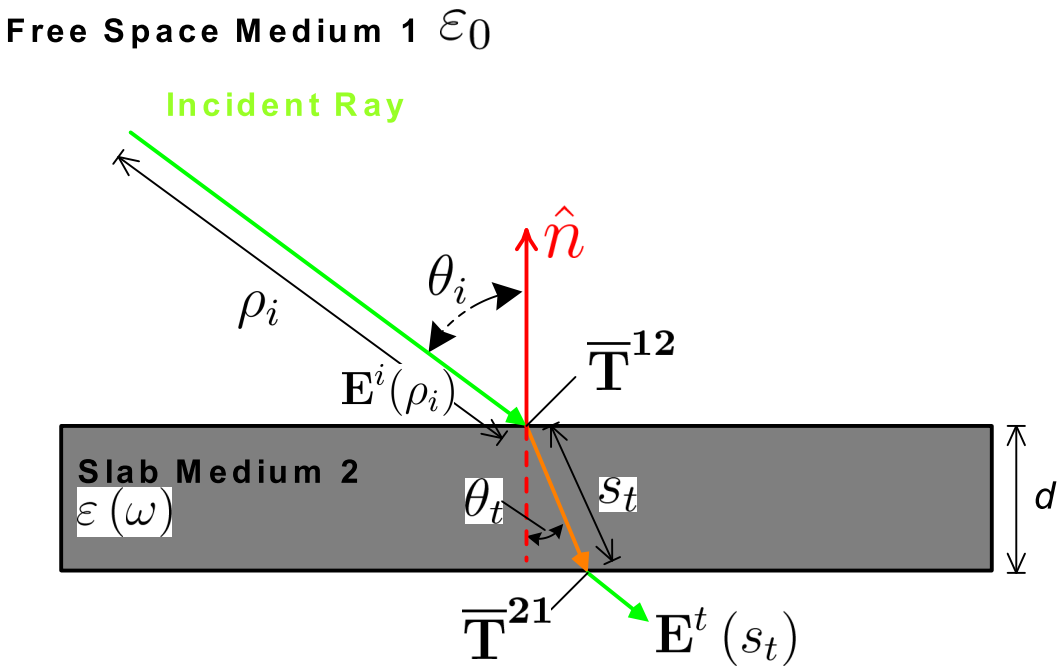

Figure 2.4: Transmission through a Slab

Combining Snell's law with Equation 2.25 allows the propagation length inside the slab to be calculated as,

$$s_t = \frac{d\sqrt{\varepsilon_r}}{\sqrt{\varepsilon_r - \sin^2\theta_i}} \tag{2.27}$$

Propagation within the slab produces the phase term,

$$e^{-k_2 s_t} \tag{2.28}$$

The propagation constant, which appears as k_2 in the above expression, is given by

$$k_2 = \alpha + \jmath\beta, \tag{2.29}$$

where

$$\alpha = \omega\sqrt{\mu_1\varepsilon'(\omega)}\{\frac{1}{2}[\sqrt{1+p_e^2}-1]\}^{\frac{1}{2}}, \tag{2.30}$$

$$\beta = \omega\sqrt{\mu_1\varepsilon'(\omega)}\{\frac{1}{2}[\sqrt{1+p_e^2}+1]\}^{\frac{1}{2}}. \tag{2.31}$$

μ_1 is the permeability of the slab and for non-ferromagnetic materials is assumed to be equivalent to free space permeability μ_0. Balanis Chapter 4 [31]

characterises good dielectrics as having a loss tangent $p_e^2 \ll 1$. For such materials α and β of Equations 2.30-2.31 can be approximated as,

$$\alpha = \frac{\omega p_e(\omega)}{2}\sqrt{\mu_1 \varepsilon'(\omega)} \tag{2.32}$$

$$\beta = \omega\sqrt{\mu_1 \varepsilon'(\omega)} \tag{2.33}$$

The proportion of the incident ray that enters the slab at the point **Q** is given by the transmission coefficient $\overline{\mathbf{T}}^{12}$.

$$\overline{\mathbf{T}}^{12} = \begin{pmatrix} T_{\perp}^{12}(\omega) & 0 \\ 0 & T_{\parallel}^{12}(\omega) \end{pmatrix} \tag{2.34}$$

$$T_{\perp}^{12} = \frac{2\cos\theta_i}{\cos\theta_i + \sqrt{\frac{\varepsilon(\omega)}{\varepsilon_0} - \sin^2\theta_i}} \tag{2.35}$$

$$T_{\parallel}^{12} = \frac{2\sqrt{\frac{\varepsilon(\omega)}{\varepsilon_0}}\cos\theta_i}{\frac{\varepsilon(\omega)}{\varepsilon_0}\cos\theta_i + \sqrt{\frac{\varepsilon(\omega)}{\varepsilon_0} - \sin^2\theta_i}} \tag{2.36}$$

As in the case of reflections this dyadic coefficient is applied to both horizontal and parallel components of the incident field in Figure 2.3 respectively. An additional transmission coefficient $\overline{\mathbf{T}}^{21}$ is required to account for the effect of the rays re-emerging from the slab material where

$$\overline{\mathbf{T}}^{21} = \begin{pmatrix} T_{\perp}^{21}(\omega) & 0 \\ 0 & T_{\parallel}^{21}(\omega) \end{pmatrix} \tag{2.37}$$

$$T_{\perp}^{21} = \frac{2\frac{\varepsilon(\omega)}{\varepsilon_0}\cos\theta_t}{\frac{\varepsilon(\omega)}{\varepsilon_0}\cos\theta_t + \sqrt{1 - \frac{\varepsilon(\omega)}{\varepsilon_0}\sin^2\theta_t}} \tag{2.38}$$

$$T_{\parallel}^{21} = \frac{2\cos\theta_t}{\sqrt{\frac{\varepsilon_0}{\varepsilon(\omega)}}\cos\theta_t + \sqrt{1 + \frac{\varepsilon(\omega)}{\varepsilon_0}\sin^2\theta_t}} \tag{2.39}$$

Combining both transmission coefficients, $T_{\perp}^{21}$ and $T_{\parallel}^{21}$ with the internal propagation effects (accounted for by the term $e^{-k_2 s_t}$), allows the ray $\mathbf{E}^t$, that re-emerges from the slab, to be computed using Equation 2.24.

When computing the transmission angle θ_t, the slab material is assumed to have the characteristics of a "good dielectric" characterised in Balanis [31]

Chapter 4 as having a loss tangent such that $p_e^2 \ll 1$. As a result snell's law of refraction of Equation 2.26 is applicable for such materials. In the case of a "good conductor" material, defined in [31] as when $p_e^2 \gg 1$, an alternative approach for finding the transmission angle must be used. In such cases Equation 2.26 does not yield a valid real valued angle for θ_t. Consequently, an angle of transmission Ψ_2 is defined which corresponds to the inclination of the constant phase planes of the electric fields inside the slab. Chapter 5 of [31] defines this angle for an electric field passing from a free space medium to a conductor material. However for such materials classified as "good conductors", fields inside the slab are severely attenuated due to their narrow skin depths. The skin depth of a material is defined as the distance a electric field will propagated inside the a medium until it is attenuated to 36.8% of its original amplitude [32]. Considering this prohibitive attenuation, transmission through such conducting materials is not considered for the purposes of the ray tracing simulation.

2.1.3 Diffractions

Classical Geometric Optics (GO) computes ray propagation paths by accounting for local transmission and reflection effects from surfaces as described in Sections 2.1.1and 2.1.2. However, GO fails to account for diffracted fields from wedges formed at the intersection of two such surfaces as in Figure 2.5. A Geometrical Theory of Diffraction (GTD) was originally developed by Keller [33] in order to overcome this shortcoming in GO and allowed diffracted fields to be computed at different observation angles ϕ by means of diffraction coefficients applied to an incident ray. However, GTD results in singularities at the vicinity of certain observation angles that correspond to the shadow boundaries of the regions, depicted as ϕ_{ISB} and ϕ_{RSB} in Figure 2.5. In [24] Kouyoumjian and Pathak introduced the Uniform Theory of Diffraction for perfectly conducting edges which overcame this drawback by offering a continuous diffraction coefficient free from problematic singularities. Further extensions to UTD involved modifying diffraction coefficient formulations in order to model diffractions from edges of dielectric materials [34].

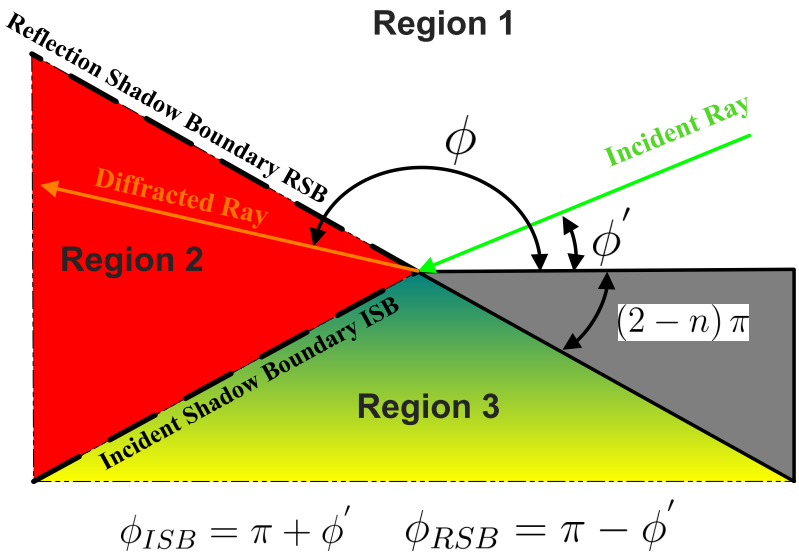

Figure 2.5: 2D Planar view of Diffraction Edge

Considering the scenario of Figure 2.6, where a ray trajectory intersects with a dielectric wedge, the diffracted ray is expressed as,

$$\mathbf{E}^d = \mathbf{E}^i(\mathbf{P}) \cdot \overline{\mathbf{D}} \frac{s'}{s'+s} e^{-j\beta_0 s} \tag{2.40}$$

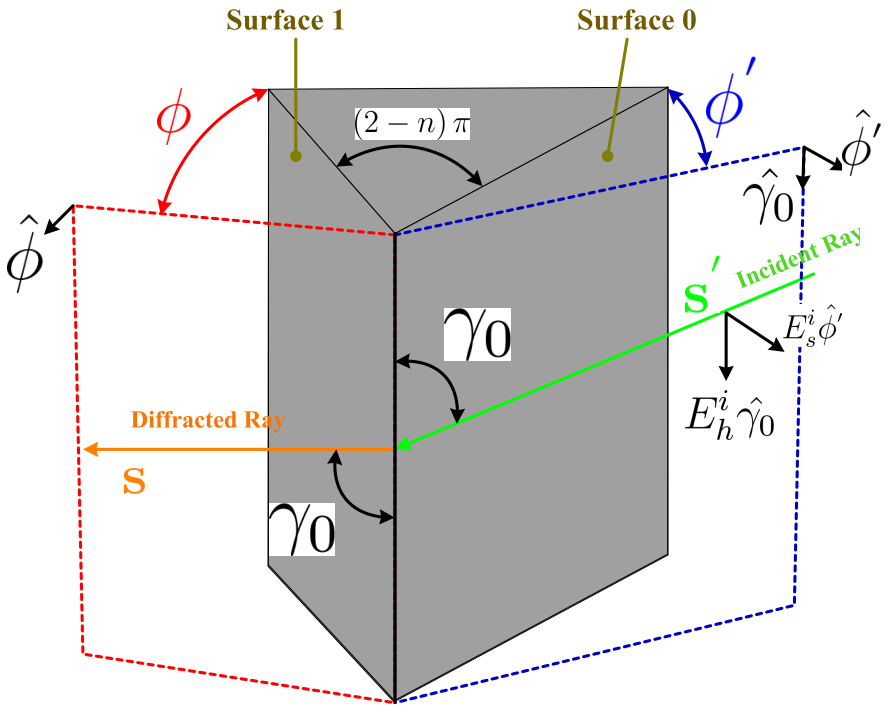

Figure 2.6: 3D Diffraction Edge

where $\mathbf{E}^i(\mathbf{P})$ is the incident field at the point of diffraction $\mathbf{P}$ and $\frac{s'}{s'+s}$ is the attenuation due to the spreading of the wavefront. s' is equivalent to the distance travelled by the ray from its source to the diffraction point, while s is the length of the ray path from the diffraction to the observation point. The dyadic diffraction coefficient $\overline{\mathbf{D}}$ is given by,

$$\overline{\mathbf{D}} = \begin{pmatrix} -D_s & 0 \\ 0 & -D_h \end{pmatrix}, \tag{2.41}$$

The diffraction coefficient is composed of two components; the hard coefficient D_h and soft coefficient D_s which are applied individually to the incident electric field. Consequently, prior to computing diffracted rays, the incident field $\mathbf{E}^i$ is separated into components perpendicular ($\hat{\phi}'$) and parallel ($\hat{\gamma_0}$) to the incident diffraction plane of Figure 2.6 such that,

$$\mathbf{E}^i = E_s^i \hat{\phi}' + E_h^i \hat{\gamma_0}. \tag{2.42}$$

The soft and hard diffraction coefficients are computed as (Chapter 13 of [31]),

$$D_s = C[D_e^+(\zeta^-) + D_e^-(\zeta^-) + R_0^\perp(\omega) D_e^-(\zeta^+) + R_1^\perp(\omega) D_e^+(\zeta^+)] \tag{2.43}$$

and

$$D_h = C[D_e^+(\zeta^-) + D_e^-(\zeta^-) + R_0^\parallel(\omega) D_e^-(\zeta^+) + R_1^\parallel(\omega) D_e^+(\zeta^+)], \tag{2.44}$$

where

$$\zeta^+ = \phi + \phi', \tag{2.45}$$

$$\zeta^- = \phi - \phi', \tag{2.46}$$

$$C = \frac{e^{j\beta_0 s'}}{\sqrt{s'}}, \tag{2.47}$$

$$D_e^+(\zeta^-) = \cot\left(\frac{\pi + \zeta^-}{2n}\right) F\left[2\beta_0 V \cos^2\left(\frac{2n\pi N^+ - \zeta^-}{2}\right)\right], \tag{2.48}$$

$$D_e^+(\zeta^+) = \cot\left(\frac{\pi+\zeta^+}{2n}\right) F\left[2\beta_0 V\cos^2\left(\frac{2n\pi N^+ - \zeta^+}{2}\right)\right], \tag{2.49}$$

$$D_e^-(\zeta^-) = \cot\left(\frac{\pi-\zeta^-}{2n}\right) F\left[2\beta_0 V\cos^2\left(\frac{2n\pi N^- - \zeta^-}{2}\right)\right]. \tag{2.50}$$

$$D_e^-(\zeta^+) = \cot\left(\frac{\pi-\zeta^+}{2n}\right) F\left[2\beta_0 V\cos^2\left(\frac{2n\pi N^- - \zeta^+}{2}\right)\right]. \tag{2.51}$$

$$F(x) = 2j\sqrt{x}e^{jx}\int_{\sqrt{x}}^{\infty} e^{-j\tau^2}d\tau, \tag{2.52}$$

$$V = \frac{ss'\sin^2\gamma_0}{s+s'}. \tag{2.53}$$

The value of n in the previous equation is determined by the angle of the diffracting wedge such that $(2-n)\,\pi$ is equal to the angle at which the surfaces meet. N^+ is computed as the nearest integer satisfying $2n\pi N^+ - \zeta^\pm = \pi$. Correspondingly, N^- is the nearest integer where $2n\pi N^- - \zeta^\pm = -\pi$. The function $F(x)$ represents a Fresnel transition function and a subroutine for approximating this function over the range $0 \leq X \leq 10$ is available from Chapter 13 of Balanis [31]. For dielectric materials the diffraction computations include the reflection coefficients,

$$R_0^\perp(\omega) = \frac{\cos\theta_0 - \sqrt{\frac{\varepsilon(\omega)}{\varepsilon_0} - \sin^2\theta_0}}{\cos\theta_0 + \sqrt{\frac{\varepsilon(\omega)}{\varepsilon_0} - \sin^2\theta_0}}, \tag{2.54}$$

$$R_0^\parallel(\omega) = \frac{-\frac{\varepsilon(\omega)}{\varepsilon_0}\cos\theta_0 + \sqrt{\frac{\varepsilon(\omega)}{\varepsilon_0} - \sin^2\theta_0}}{\frac{\varepsilon(\omega)}{\varepsilon_0}\cos\theta_0 + \sqrt{\frac{\varepsilon(\omega)}{\varepsilon_0} - \sin^2\theta_0}}, \tag{2.55}$$

$$R_1^\perp(\omega) = \frac{\cos\theta_1 - \sqrt{\frac{\varepsilon(\omega)}{\varepsilon_0} - \sin^2\theta_1}}{\cos\theta_1 + \sqrt{\frac{\varepsilon(\omega)}{\varepsilon_0} - \sin^2\theta_1}}, \tag{2.56}$$

$$R_1^\parallel(\omega) = \frac{-\frac{\varepsilon(\omega)}{\varepsilon_0}\cos\theta_1 + \sqrt{\frac{\varepsilon(\omega)}{\varepsilon_0} - \sin^2\theta_1}}{\frac{\varepsilon(\omega)}{\varepsilon_0}\cos\theta_1 + \sqrt{\frac{\varepsilon(\omega)}{\varepsilon_0} - \sin^2\theta_1}}, \tag{2.57}$$

where $\varepsilon(\omega)$ is the permittivity of the diffracting wedge and

$$\theta_0 = \frac{\pi}{2} - \phi', \tag{2.58}$$

$$\theta_1 = \frac{\pi}{2} - (n\pi - \phi). \tag{2.59}$$

Observing the two surfaces that form the diffracting wedge of Figure 2.6, θ_0 corresponds to the angle the incident ray forms with respect to the normal of surface 0. Correspondingly θ_1 is the angle between the diffracted ray and the normal of surface 1 of the wedge.

By combining Geometrical Optics (GO) with the Uniform theory of Diffraction (UTD), ray tracing is capable of modelling scattering effects in the presence of edges. Other authors have extended UTD further in order to account for corner diffractions [7, 28]. However, diffraction computations in this work are limited to edge diffraction.

2.1.4 Ray Trajectories

The Geometrical Optics (GO) and Uniform Theory of Diffraction (UTD) coefficients introduced in the previous sections account for the scattering effects that occur when a ray interacts with an object. However, a typical ray travels in linear piecewise paths in free space between such scattering events. Prior to computing these scattering effects the propagation path of the ray from transmitter to receiver must be known. There are two main approaches used to compute ray paths in ray based simulators, Shoot and Bounce (SBR) and Point to Point ray tracing.

Previous authors [25, 35, 36, 37] have employed Shoot and Bounce ray tracing (SBR). This approach models propagation as a series of rays simultaneously leaving a source each at a different solid angle θ_l as in Figure 2.7. The path of each of these rays is computed until it leaves the propagation environment. Some of these rays contribute to the received field at the receiver location (RX), while others will simply propagate without intersecting with any receiver position. Ray paths that breach a prior specified environment boundary are discounted from further computations.

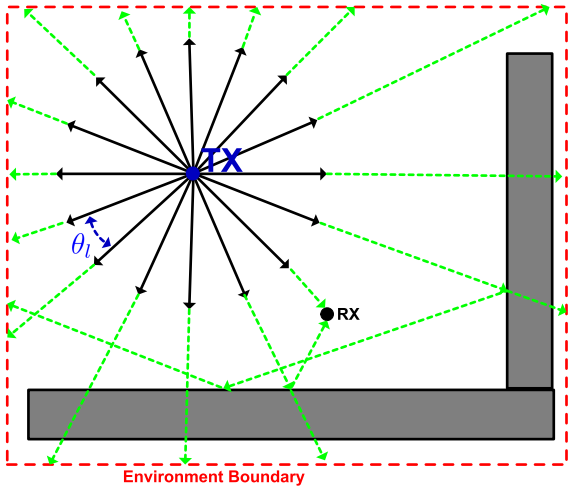

Figure 2.7: Shoot and Bounce Ray Tracing

Point to point ray tracing, as used in this work, offers an alternative to SBR by utilizing image theory. This method considers only ray trajectories that will propagate to a specified receiver's location. Figure 2.8 shows the image created when calculating a ray trajectory subject to a reflection from a single wall. It can be observed that the image and transmitter are equidistant from the reflecting surface. Both transmitter and image positions lie on a straight line that

is perpendicular to the reflecting surface. By tracing a virtual path from the receiver to the image, the point of reflection **Q**, the ray path and angle of incidence θ_i are obtained. An advantage of using images is realised when finding additional ray paths terminating at different receiver locations. If such paths involve a reflection from the same surface, the original image point can be reused thus producing a computationally efficient means of simulating channels at multiple receiver points.

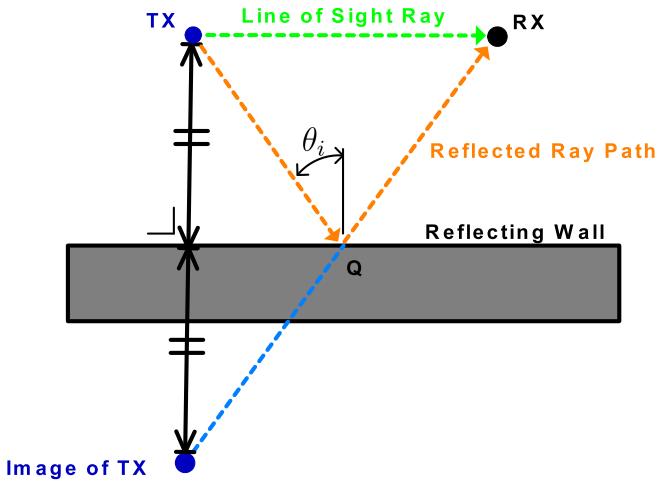

Figure 2.8: Point to Point Ray Tracing using 1^{st} order reflectors

Images are also employed in order to create rays that undergo more than one reflection. The number of reflections in a ray path is referred to as the order of reflection. For example, 2 reflections in a ray path results in a ray with 2^{nd} order reflections hereafter referred to as a 2^{nd} order ray. When computing the path of such a 2^{nd} order ray, depicted in Figure 2.9, both a 1^{st} and 2^{nd} order image are required. As in the case of a single reflection, the 1^{st} image is derived from the source location (TX). Similarly, the 2^{nd} order image of Figure 2.9 is computed as an image of this $1st$ order image.

The method of computing ray paths using images can be extended to an arbitrary order of reflections. In considering this, an O^{th} order image is simply computed as an image of a previous order $(O-1)^{th}$ image. In extending image theory to the several multi-path rays that propagate between a transmitter and receiver, a hierarchial tree of images similar to that of Figure 2.10 emerges. From this tree it is observed that two rays, shown in red, share a common first order image. This corresponds to two separate paths that are initially reflected from the same surface but subsequently undergo further scattering from

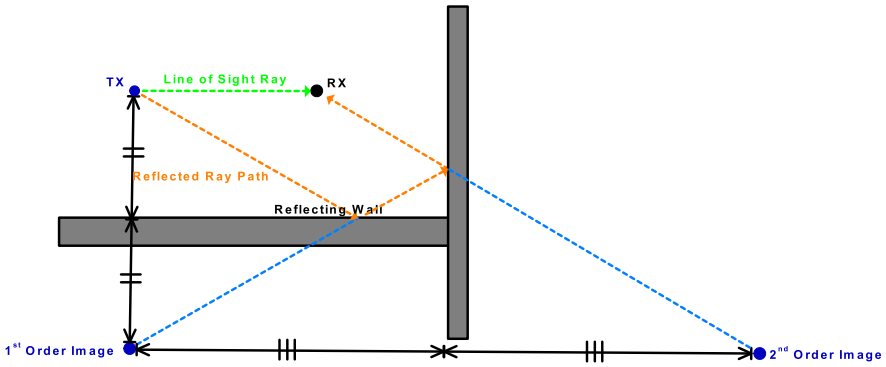

Figure 2.9: Point to point ray tracing using 2^{nd} order reflectors

different surfaces. This reveals an inherent advantage of using image theory; different ray paths can reuse the the same 1^{st} order image point if they are initially reflected from the same surface after leaving the transmitter. Also it is possible for two separate ray paths to have a collection of images from more than one order in common.

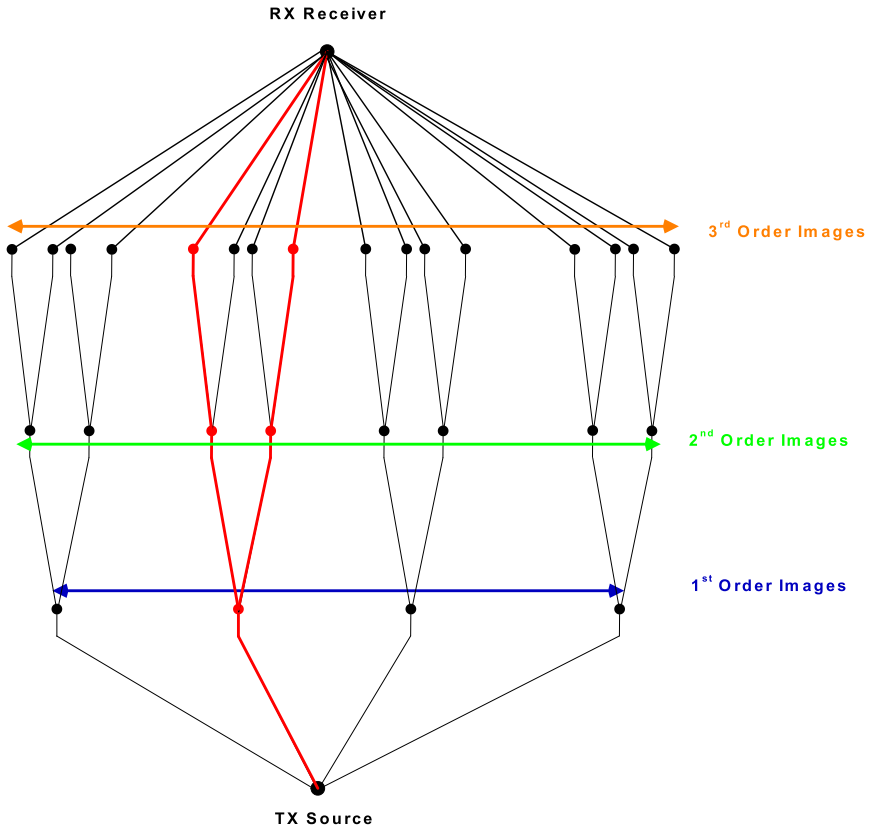

Figure 2.10: 3^{rd} Order Image Tree

Image theory based ray tracing simulators impose a limit on the maximum order of reflections O. While Shoot and Bounce (SBR) schemes compute rays until they breach a particular prior defined propagation boundary, for point to point ray tracing there is, in theory, an infinite number of reflected ray path solutions that can be computed for an environment containing more than one reflecting surface. Limiting the maximum order of a ray sets an artificial limit on the computation required for ray tracing in such scenarios.

In computing a ray path in an indoor environment, diffraction effects, such as those in Section 2.1.3, must also be considered. While single point images can be used when accounting for rays comprised solely of reflections or transmission, the presence of a diffraction necessitates a slight modification of this technique. In such a case, as shown in Figure 2.11, an image of the entire diffraction edge must be created. This edge image of Figure 2.12 is created for the purposes of computing reflections paths subsequent to the diffraction. While for each ray the diffraction occurs only at the single point **P**, this may vary for other ray paths where diffraction may occur at a different height on the edge. An image of the entire edge lends itself to be reused for other rays that diffract from the same edge in Figure 2.11 but thereafter have differing paths.

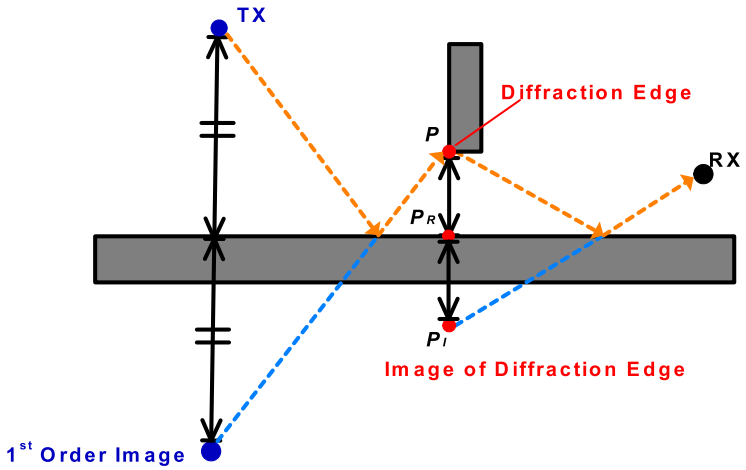

Figure 2.11: Diffractions and reflection in Ray Trajectory

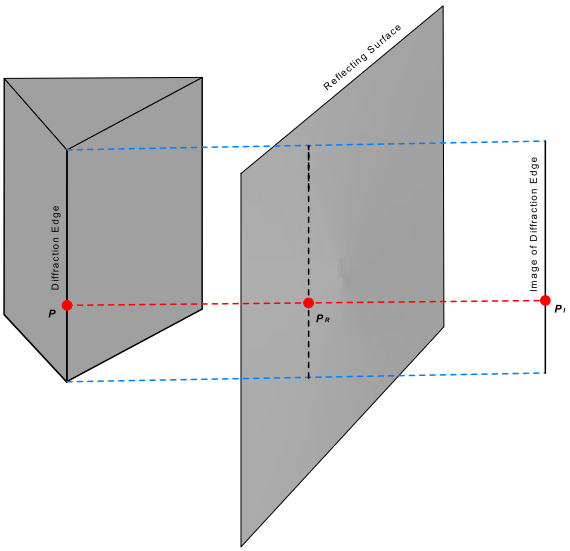

Figure 2.12: Image of Diffraction Edge

2.1.4.1 Ray Nodes

After obtaining ray paths using image theory the effects of the scattering events such as Diffraction, Reflection and Transmission introduced in Sections 2.1.1-2.1.3 can be computed. A ray can be conceived of as a series of such scattering events separated by propagation through free space. Consequently, the ray information is stored as a series of sequential scattering events or nodes that occur between leaving the transmitter antenna and arriving at the receiver. Figure 2.13 shows such nodes for an example ray in a multi-path propagation environment.

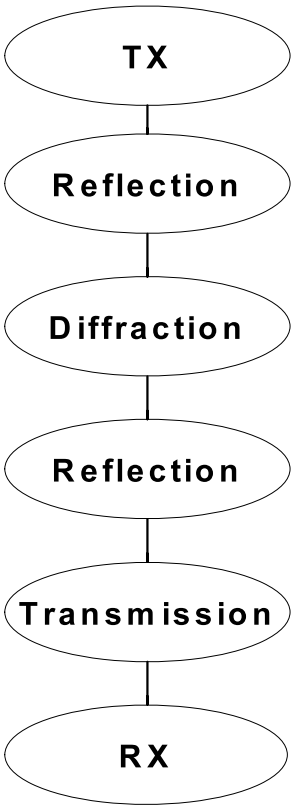

Figure 2.13: Ray Nodes

The response[1] of an individual ray $\mathbf{R}_i(\mathbf{r})$ terminating at a receiver point $\mathbf{r}$ is composed of a product of the individual scattering events and the phase shift incurred due to free space propagation such that for the example ray of Figure 2.13,

$$\mathbf{R}_i(\mathbf{r}) = \overline{\mathbf{R}}_1 \cdot \overline{\mathbf{D}}_1 \cdot \overline{\mathbf{R}}_2 \cdot \overline{\mathbf{T}}^{12} \cdot \overline{\mathbf{T}}^{21} \cdot e^{k_2 s_t} A_s e^{-\jmath\phi_d} \tag{2.60}$$

where $\overline{\mathbf{R}}$, $\overline{\mathbf{T}}$ and $\overline{\mathbf{D}}$ are the scattering coefficients corresponding to the reflection, transmission and diffraction events of Figure 2.13. The term $e^{-k_2 s_t}$ accounts for the phase effects from a ray propagating through a slab with material propagation constant k_2 (See Section 2.1.2). Knowing the free-space propagation length of the ray d, the phase shift due to free space propagation ϕ_d is easily computed as

$$\phi_d = \frac{d\omega}{c}, \tag{2.61}$$

where ω and c are the angular frequency and speed of light. Spatial attenuation is accounted for by the A_s term in Equation 2.60. An individual ray's response is usually expressed as a component of an antenna polarisation $\hat{e}_{pol}$ at the receiver location such that

$$R_i(\mathbf{r}) = \mathbf{R}_i(\mathbf{r}) \cdot \hat{e}_{pol}, \tag{2.62}$$

where $\hat{e}_{pol}$ represents the receiver antenna polarisation. Finally a complete channel response $H(\mathbf{r})$ at a point $\mathbf{r}$ is given by,

$$H(\mathbf{r}) = \sum_{i=1}^{N} R_i(\mathbf{r}). \tag{2.63}$$

This expression is a sum of all the individual multi-path ray responses for a particular transmitter-receiver combination such as that of Figure 2.14.

[1] The response being the total effect of propagation on the electric field or $\frac{E^R}{E^T}$ where E^R and E^T are the respective electric fields at the receiver and transmitter

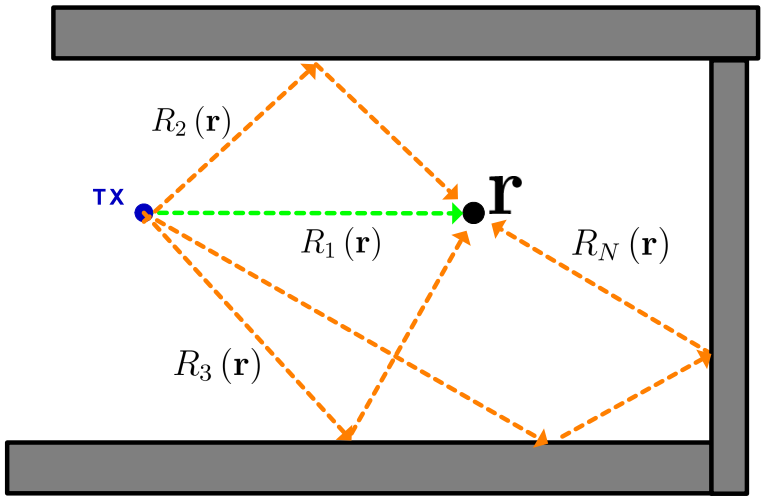

Figure 2.14: Multi-Path Ray Channel

2.1.5 Propagation Modelling for wide-band Systems

When employing ray-tracing to model wide bandwidth channels, such as those of Ultra-Wideband(UWB), frequency dependent variations in scattering effects must be considered. The source of such variation can be attributed to frequency domain fluctuation of the effective material permittivity given by,

$$\varepsilon(\omega) = \varepsilon^{'}(\omega) - \jmath\varepsilon^{'}(\omega)\, p_e(\omega), \tag{2.64}$$

The effective loss tangent $p_e(\omega)$ of the above equation can be written as

$$p_e(\omega) = \frac{\omega\varepsilon^{''}(\omega) + \sigma(\omega)}{\omega\varepsilon^{'}(\omega)}, \tag{2.65}$$

where $\varepsilon^{''}(\omega)$ and $\sigma(\omega)$ are attributable to the respective dielectric and macroscopic conductive losses. Due to difficulty of separating these effects they are combined to form an effective loss tangent $p_e(\omega)$ [30]. Combining this loss tangent with the real valued dielectric permittivity $\varepsilon^{'}(\omega)$ yields the complex valued effective permittivity $\varepsilon(\omega)$ of Equation 2.64.
The frequency variations of $\varepsilon^{'}(\omega)$ and $p_e(\omega)$ have been the subject of research by Muqaibel et al in [29, 38]. Empirical measurements for the values of these properties were recorded over an UWB bandwidth spanning from 3 GHz to 10 GHz. While this section is concerned with the effective material permit-

tivity variations over such a bandwidth, it will be noted in Section 2.2 that actual UWB channels (as permitted by communication regulators) occupy a slightly different bandwidth from 3.1 to 10.6 GHz. However the effects over both bandwidths would be of a similar nature owing to the small difference between them. A range of common indoor materials including concrete and drywall were subject to this experiment. Shown below in Figure 2.15 is the measured results of the material permittivity and loss tangent for concrete. It should be noted that additional frequency dependant effects can occur due to variations in a scattering surface's texture [39]. Such variations may lead to extra unaccounted diffusion reflection effects. However in what follows, all surfaces are considered to be smooth with respect to the wavelength of the incident fields and as a result, texture dependant effects will not be considered.

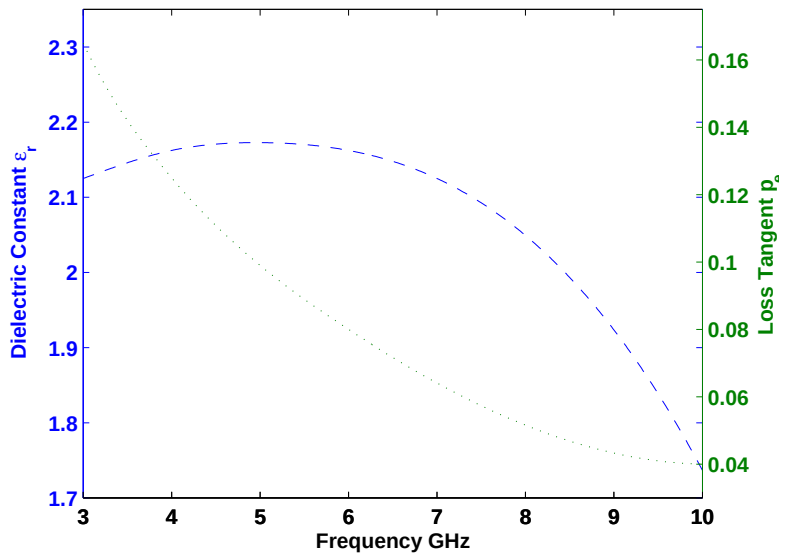

Figure 2.15: Frequency Dependency of Permittivity for Concrete Dashed Line: Dielectric Constant Dotted Line Loss Tangent

In this work these measurements for concrete were incorporated into the computations of the ray tracing scattering effects. Such effects were previously introduced as Reflection, Transmission and Diffraction coefficients in Sections 2.1.1-2.1.3. The knock on frequency variation in these coefficients will be examined in the subsequent sections below.

2.1.5.1 Frequency Dependent Reflections

Recalling the discussion of ray scattering of Section 2.1.1, the effects of reflection from an object surface are computed using the reflection coefficient $\overline{\mathbf{R}}$ be-

low,

$$\overline{\mathbf{R}} = \begin{pmatrix} R_{\perp}(\omega) & 0 \\ 0 & R_{\parallel}(\omega) \end{pmatrix}, \tag{2.66}$$

where the parallel $R_{\parallel}$ and perpendicular $R_{\perp}$ components of the coefficients are given by

$$R_{\perp}(\omega) = \frac{\cos\theta_i - \sqrt{\frac{\varepsilon(\omega)}{\varepsilon_0} - \sin^2\theta_i}}{\cos\theta_i + \sqrt{\frac{\varepsilon(\omega)}{\varepsilon_0} - \sin^2\theta_i}}, \tag{2.67}$$

and

$$R_{\parallel}(\omega) = \frac{-\frac{\varepsilon(\omega)}{\varepsilon_0}\cos\theta_i + \sqrt{\frac{\varepsilon(\omega)}{\varepsilon_0} - \sin^2\theta_i}}{\frac{\varepsilon(\omega)}{\varepsilon_0}\cos\theta_i + \sqrt{\frac{\varepsilon(\omega)}{\varepsilon_0} - \sin^2\theta_i}}. \tag{2.68}$$

These components were first introduced in Equations 2.19-2.20 and their values are dependent on the incident angle θ_i and effective material permittivity $\varepsilon(\omega)$. The simulated variations of the reflection coefficients for a concrete block surface over the UWB bandwidth are shown in Figures 2.16-2.23. The material properties of Figure 2.15 were assumed for concrete. In Figures 2.16-2.17 the incident angle was varied over a range from 0^o to 90^o and the magnitudes of the resultant parallel and perpendicular coefficient were recorded at 1 GHz separated spot frequencies from 3 GHz to 10 GHz. This resulted in the coefficients at each spot frequency yielding slightly different coefficient values. However, a clearer overview of this effect is observed in Figure 2.18-2.23, where the coefficients' magnitudes are plotted in the frequency domain over the 3 GHz to 10 GHz bandwidth. While a gradual increase in the reflection coefficients with frequency is observed at 30^o and 80^o, the parallel reflection coefficient $|R_{\parallel}|$ at 63^o exhibits the greatest fluctuation. This is attributable to 63^o corresponding to an inflection point for the value of $|R_{\parallel}|$ in Figure 2.17.

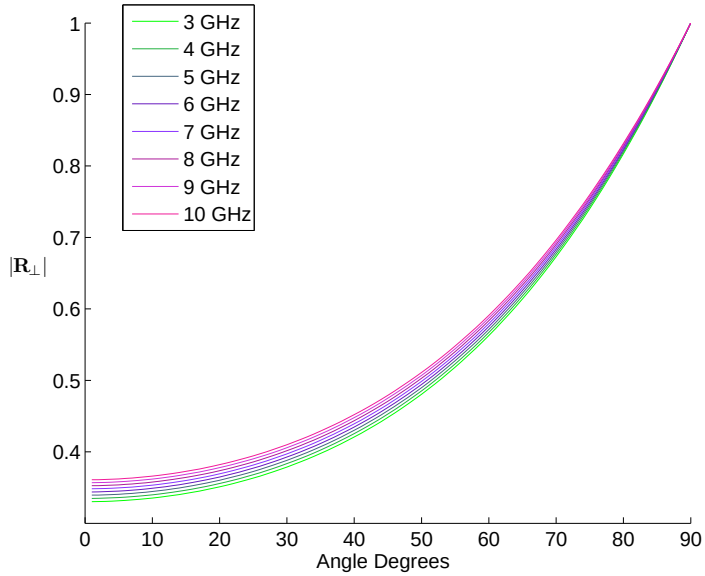

Figure 2.16: Variation of Perpendicular Reflection Coefficient $R_\perp$ with incident angle from 3-10 GHz

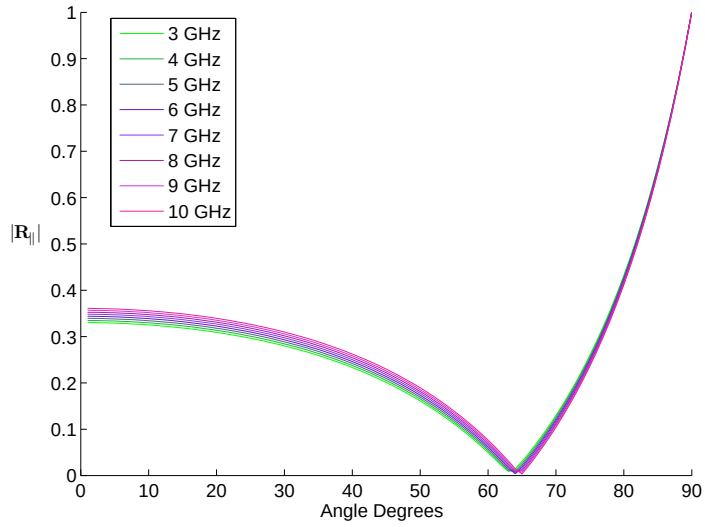

Figure 2.17: Variation of Parallel Reflection Coefficient $R_\parallel$ with incident angle from 3-10 GHz

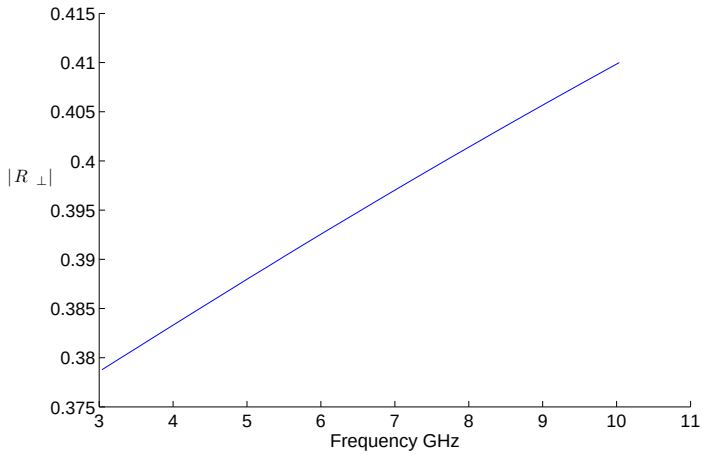

Figure 2.18: Variation of Perpendicular Reflection Coefficient $R_{\perp}$ with Frequency at incident angle of 30^o

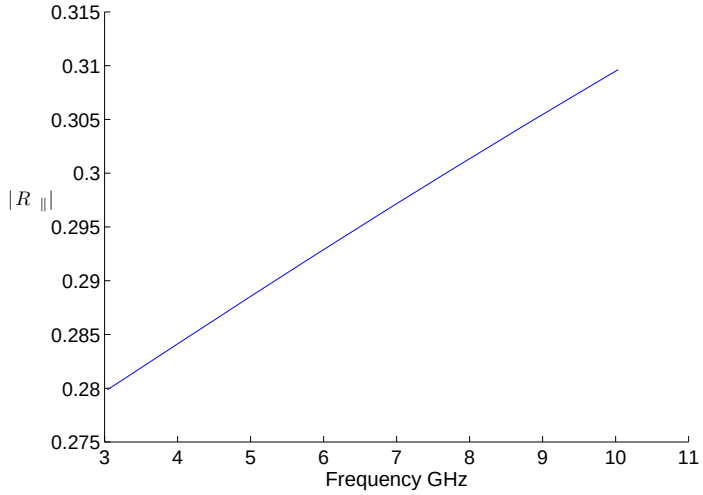

Figure 2.19: Variation of Parallel Reflection Coefficient $R_{\parallel}$ with Frequency at incident angle of 30^o

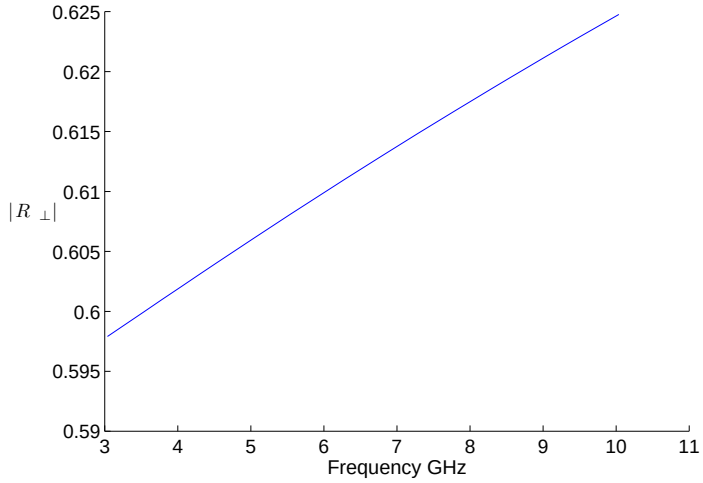

Figure 2.20: Variation of Perpendicular Reflection Coefficient $R_{\perp}$ with Frequency at incident angle of 63^o

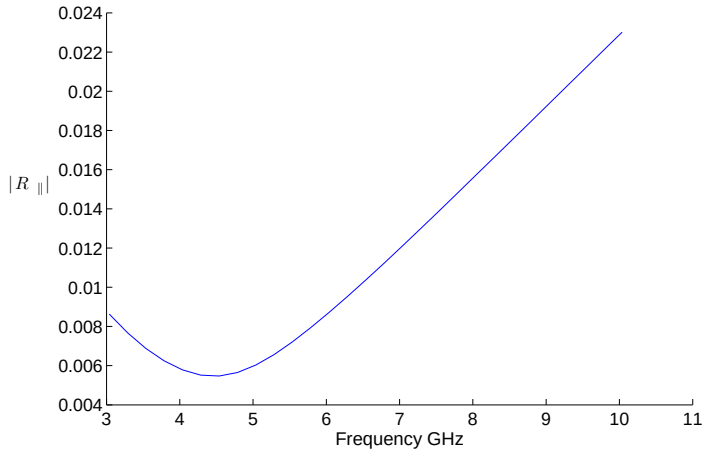

Figure 2.21: Variation of Parallel Reflection Coefficient $R_{\|}$ with Frequency at incident angle of 63^o

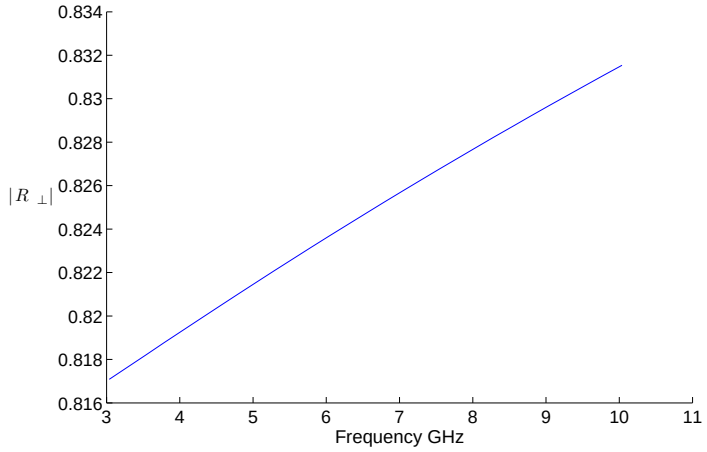

Figure 2.22: Variation of Perpendicular Reflection Coefficient $R_{\perp}$ with Frequency at incident angle of 80^o

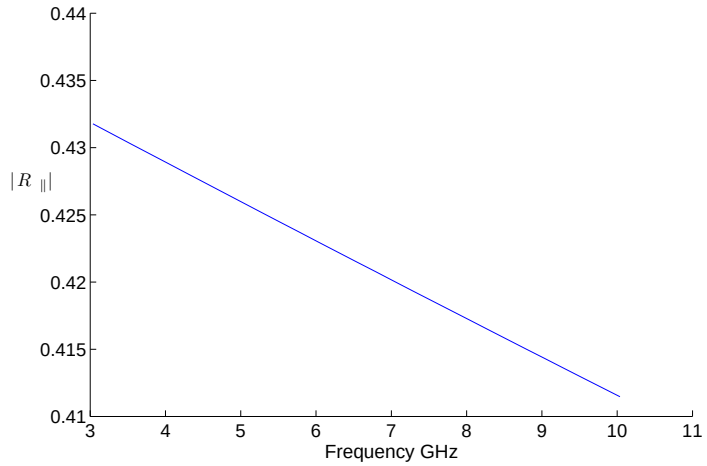

Figure 2.23: Variation of Parallel Reflection Coefficient $R_{\|}$ with Frequency at incident angle of 80^o

2.1.5.2 Frequency Dependent Transmissions

A ray re-emerging following transmission through a slab is expressed as,

$$\mathbf{E}^t(s_t) = \mathbf{E}^i(\rho_i) \cdot \overline{\mathbf{T}}^{\mathbf{12}} \cdot \overline{\mathbf{T}}^{\mathbf{21}} \frac{\rho_i}{\rho_i + s_t} e^{-k_2 s_t}. \tag{2.69}$$

where $\overline{\mathbf{T}}^{\mathbf{12}}$ and $\overline{\mathbf{T}}^{\mathbf{21}}$ are the transmission coefficients for the ray entering and leaving an object with a non free space effective permittivity $\varepsilon(\omega)$. These coefficients were originally introduced in Equations 2.34 and 2.37 of Section 2.1.2. Similar to the case of reflections, these transmission coefficients are dependent on an incident angle θ_i and the material permittivity $\varepsilon(\omega)$. The term $e^{-jk_2 s_t}$ in Equation 2.69 accounts for the effects of a ray propagating inside the slab material and consequently, its value will vary depending on $\varepsilon(\omega)$. A detailed expression of the propagation constant k_2 can be found in Equations 2.30-2.33 of Section 2.1.2. $\frac{\rho_i}{\rho_i + s_t}$ is a free space spatial attenuation term and as such does not have any dependency on material properties.

In order to examine transmission effects over UWB bandwidth a ray $\mathbf{E}^t(s_t)$ was simulated as propagating through a slab of $0.3m$ thickness. This slab shown in Figure 2.24 below is modelled as having the material properties of concrete in Figure 2.15.

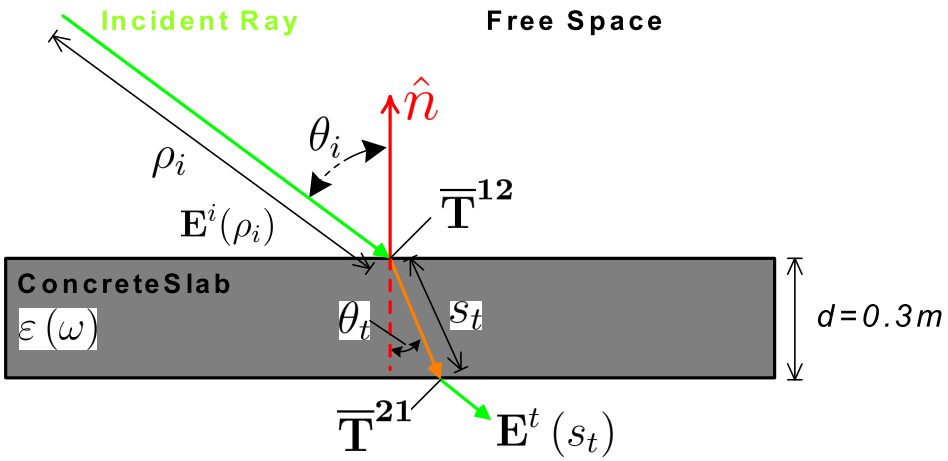

Figure 2.24: Ray Transmission through a Concrete Slab

Assuming an incident electric field $\mathbf{E}^i$ with a magnitude of 1 overs its entire bandwidth, the magnitude of the resultant electric field emerging from the slab, $|\mathbf{E}^t|$ was computed over a range of incident angles θ_i and is shown in

Figures 2.25-2.26. As in the case of the reflection coefficients these plots were created using spot frequencies separated by 1 GHz steps in the UWB range. Frequency domain representation of the variation of the field's magnitude are shown in Figures 2.27 and 2.28 for incident angles of 30^o, 60^o and 80^o respectively. From these plots a smooth variation that increases slightly at lower incident angles is observed. However, no inflection points, such as those of Figure 2.17 for the parallel reflection coefficient, are observed.

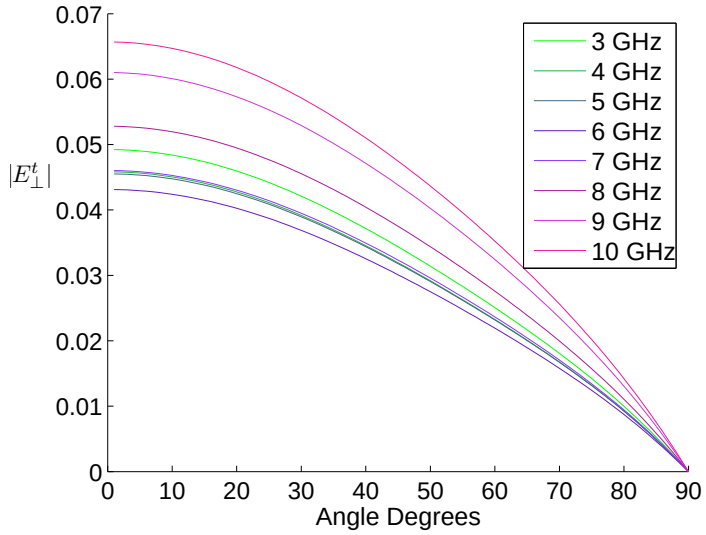

Figure 2.25: Variation of Perpendicular Component of Transmitted Field $|E^{\perp}|$ with incident angle from 3-10 GHz

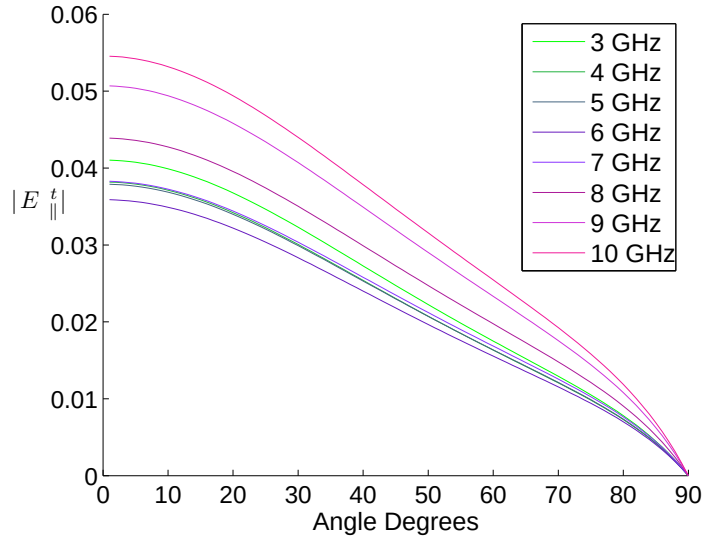

Figure 2.26: Variation of Parallel Component of Transmitted Field $|E^{\parallel}|$ with incident angle from 3-10 GHz

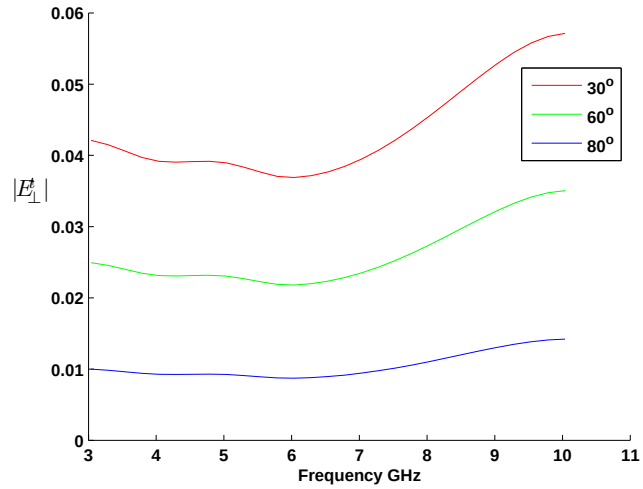

Figure 2.27: Variation of Perpendicular Component of Transmitted Field $|E_{\perp}^{t}|$ with Frequency at incident angles of 30^{o} 60^{o} and 80^{o}

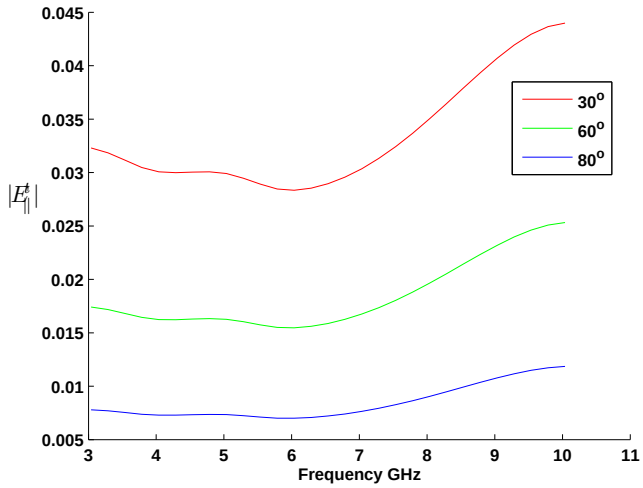

Figure 2.28: Variation of Parallel Component of Transmitted Field $|E_{\parallel}^{t}|$ with Frequency at incident angles of 30^{o} 60^{o} and 80^{o}

2.1.5.3 Frequency Dependent Diffractions

In order to examine the frequency domain characteristics of diffraction, diffraction coefficients from the concrete edge of Figure 2.29 were simulated over the UWB bandwidth. These coefficients were previously introduced in Section 2.1.3 and are composed of a hard D_h and soft D_s component of Equations 2.43-2.44.

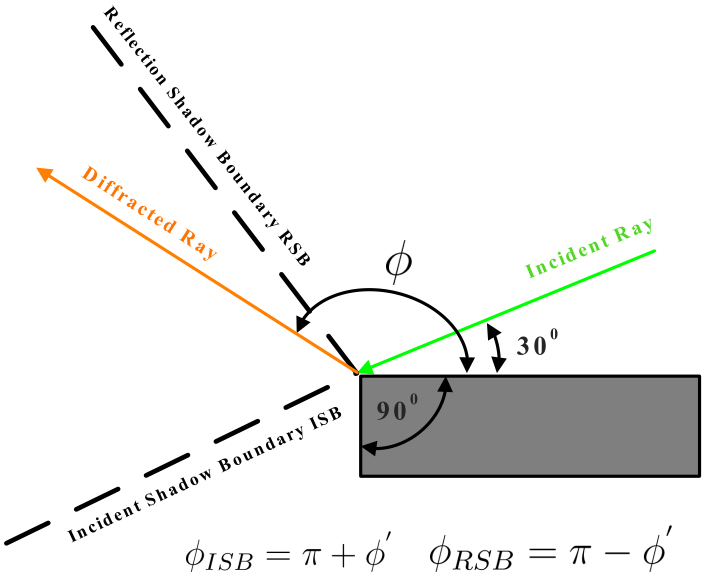

Figure 2.29: 90^O Diffraction edge

As in the previous examination of reflection and transmission, the material properties for concrete of Figure 2.15 were incorporated into the simulation. The incoming incident ray angle ϕ' was fixed at 30^o and it is assumed that the ray intersects perpendicularly with the edge. The diffraction coefficients were computed for the observation angle ϕ (shown in Figure 2.29) adjusted in a sweep between 1^o and 270^o. The resultant magnitudes of D_s and D_h are shown Figure 2.30-2.31 for spot frequencies from 3 GHz to 10 GHz. The maximum magnitude of the diffraction coefficients occurs where the observation angles ϕ is in the vicinity of a shadow boundary. In this simulation these shadow boundaries occur at 150^o and 210^o. Accordingly, it is at these angles that the greatest variation with frequency occurs. This can be seen in the frequency domain representation of the diffraction coefficient in Figures 2.32-2.33. In these

plots the coefficient demonstrates the greatest variation over the UWB bandwidth at angles of 153^o and 213^o, which border the shadow boundaries.

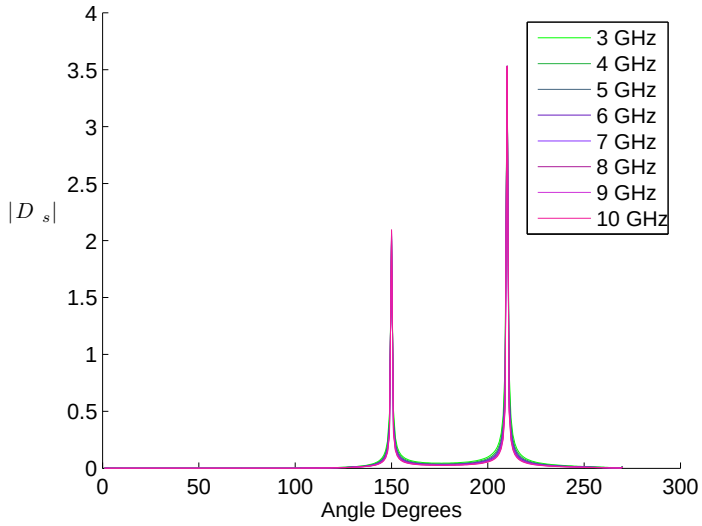

Figure 2.30: Variation of Soft Diffraction Coefficient D_s with incident angle from 3-10 GHz

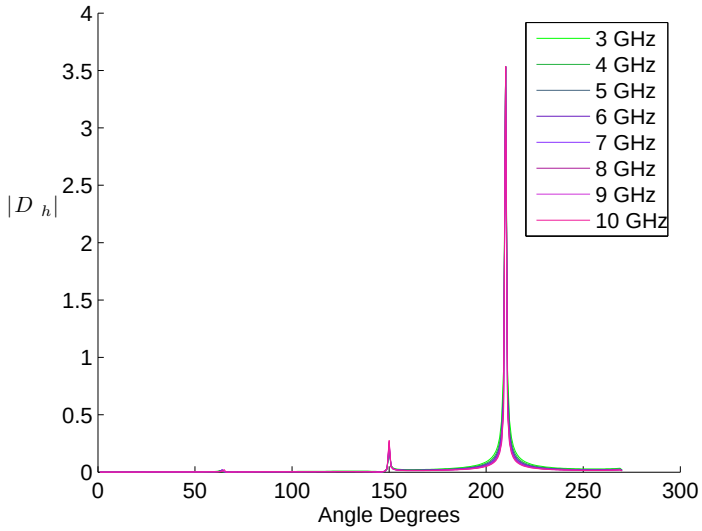

Figure 2.31: Variation of Hard Diffraction Coefficient D_h with incident angle from 3-10 GHz

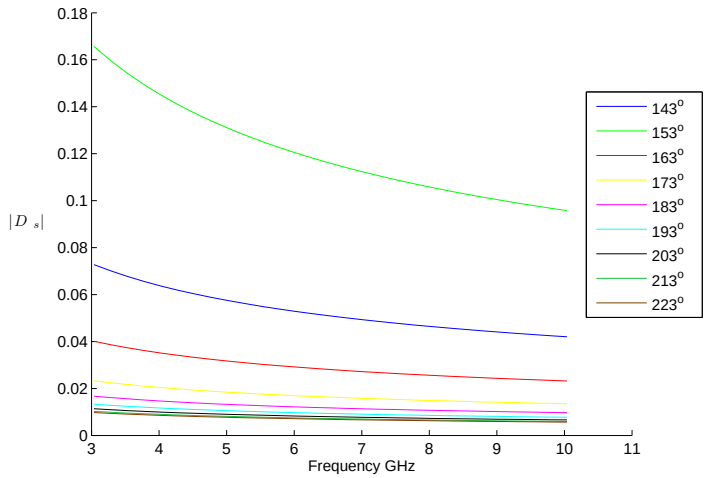

Figure 2.32: Variation of Soft Diffraction Coefficient D_s with Frequency at various incident angles

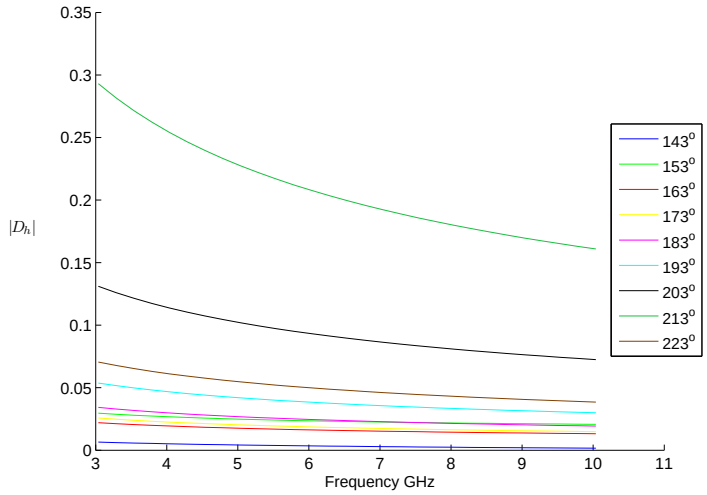

Figure 2.33: Variation of Hard Diffraction Coefficient D_h with Frequency at various incident angles

2.1.5.4 Frequency Domain Computations

This work of this thesis follows on from the development of a propagation simulator by Dr. Eamon Kenny of Trinity College Dublin [7]. This simulator employed ray tracing in order to model propagation for narrow band schemes in an indoor environment. Considering the amount of interest in the potential of UWB for use in location based algorithms [10], a wide-band modelling tool was deemed a necessity. The early stages of this project involved upgrading the original simulator created by Dr. Kenny such that it was capable of modelling UWB channels. This task entailed modifying computations in a simulation program so that scattering effects and free space propagation was computed at all frequencies in the UWB range. Specifically, diffraction, reflection and transmission coefficients of Sections 2.1.1-2.1.3 had to be computed for the vast number of discrete frequencies steps between 3 GHz and 10 GHz, instead of the single frequency point of a narrow band channel. Considering the frequency dependence of scattering coefficients as demonstrated in Sections 2.1.5.1-2.1.5.3, an accurate wide-band channel model necessitated the incorporation of frequency dependent permittivity variations into simulations. As a result, the ray tracing simulator was modified in order to incorporate the empirical permittivity measurements of Muqaibel [29, 38] as seen in Figure 2.15. Wide-band frequency domain ray tracing computations have been employed by previous authors. In [40, 41] wide-band channels were simulated but a constant permittivity is assumed by these authors at all frequencies. A series of sub-bands each spanning 500 MHz were combined for the purpose of computing a 4 GHz channel in [42]. Each sub-band used the permittivity values corresponding to the bands' centre frequency. In [37] the shoot and bounce (SBR) method, as discussed in Section 2.1.4, is combined with frequency domain computations that incorporate the permittivity variation of Muqaibel [29, 38]. Some authors have chosen the alternative of time domain ray tracing as an efficient means of modelling wide-band propagation without the need to compute a response over many frequencies or for multiple sub-bands [43, 44]. In these simulators time domain scattering coefficients are convolved with the transmitted pulse in order to attain a received time domain waveform. While this technique removes the need for the large frequency sweeps of computation of frequency domain ray tracing, the variations of relative permittivity $\varepsilon^{'}(\omega)$ and effective loss tangent $p_e(\omega)$ over frequency are not considered.

2.2 Ultra-Wideband

Ultra-Wideband (UWB) is a recently sanctioned wireless communications technique that aims to offer unprecedented high data capacity over short ranges. This is achieved by UWB channels occupying bandwidth of several Giga-Hertz (GHz) which allow for short time domain waveforms to be successfully transmitted. UWB has enjoyed growing publicity since the sanctioning of UWB for consumer device applications by the Federal Communication Commission (FCC) in 2002. Prior to this ruling most research in UWB systems was concerned with military applications, specifically in the area of airborne radar [45], with the term "Ultra-wideband" being initially coined by the United States Defense Department [9]. However, in recent years, UWB has been considered as a potential means of deploying high data rates over short range Personal Area Networks (PAN) for use in unlicensed domestic consumer products [8]. Applications include streaming video to display devices or as a wireless alternative to Universal Serial Bus (USB) cabling [46]. In addition the narrow time domain waveforms associated with UWB make it an ideal candidate for use in time based geo-location estimation algorithms where a high degree of accuracy is required [10]. In outdoor scenarios, UWB is being considered for use in vehicular radars as part of future collision avoidance systems [47].
The original bandwidth of UWB as sanctioned by the FCC spans from 3.1 GHz to 10.6 GHz. This bandwidth overlaps other existing wireless services and due to concerns of interference, the "mask" of permitted power level in Figure 2.34 was introduced. While the maximum power level is limited to -41.3 dBm, power levels at bandwidths in the vicinity of frequencies shared with existing services are limited further. Additionally, similar power restrictions are also present in European regulatory proposals [48]. Consequently, the realisable range for indoor channels is limited to below 15 meters. However, greater ranges are achievable at impaired data rates [8,49]. Generally, Ultra-Wideband is characterised by transmissions having a fractional bandwidth B_f greater than 0.2 or an absolute bandwidth greater than 500 MHz at all times. The fraction bandwidth B_f is given by

$$B_f = 2\frac{f_H - f_L}{f_H + f_L}, \tag{2.70}$$

where f_L and f_H are the lower and upper -10 dB emission cut off limits.

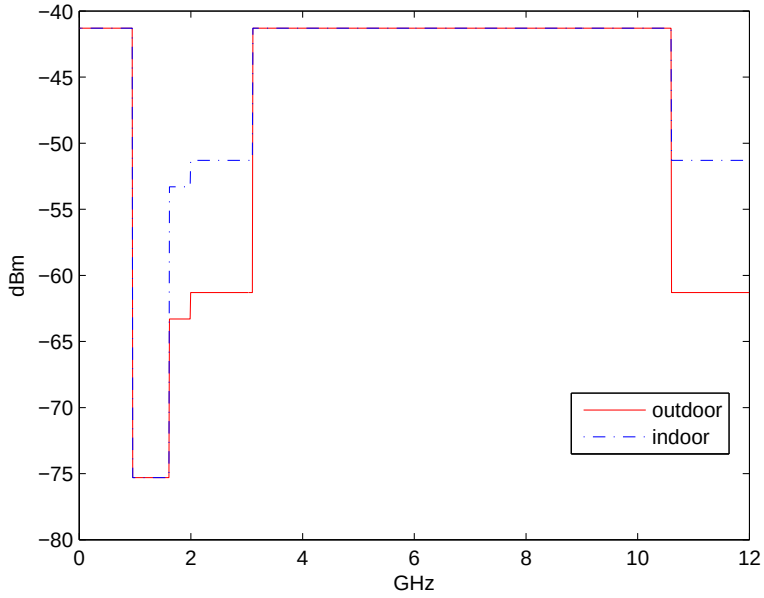

Figure 2.34: FCC UWB Mask

In order to utilize the enormous bandwidth available the transmitted waveform must have a narrow time domain pulsewidth T_p. The Gaussian monocycle is one such waveform and is expressed in the time domain as [50, 51],

$$s(t) = \left[1 - 4\pi\left(\frac{t}{t_n}\right)^2\right] \exp\left(-2\pi\left(\frac{t}{t_n}\right)^2\right), \tag{2.71}$$

where t_n is a scaling factor that determines the bandwidth of the pulse. A particularly useful characteristic of this pulse is that it does not contain any D.C. component making it ideal for wireless transmission. Shown below in Figures 2.35-2.36 are the time and frequency domain representation of a Gaussian monocycle for $t_n = 0.52$ nanoseconds. The ideal UWB pulse should allow for a discontinuous transmission in the time domain that occupies as much of the bandwidth allocated as possible. The technique of using such discontinuous transmissions to convey data over a wireless link is referred to as impulse radio (IR). In addition to Gaussian monocycles other waveforms such as Rayleigh, and higher order Gaussian pulse derivatives have been suggested for use in IR systems [52].

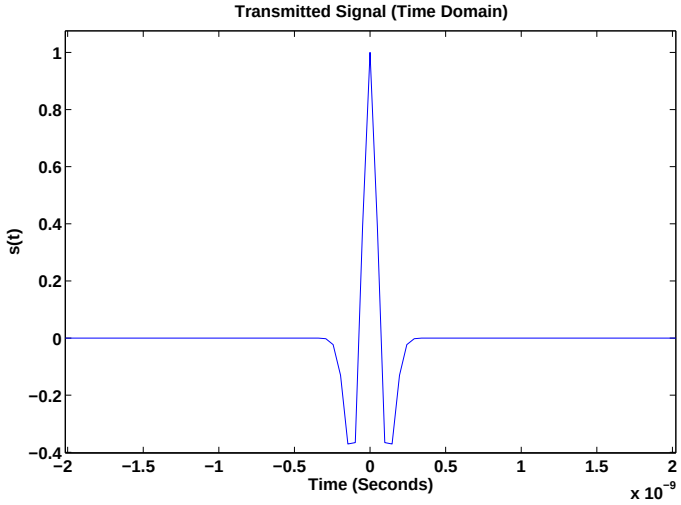

Figure 2.35: Gaussian Monocycle Pulse in Time Domain

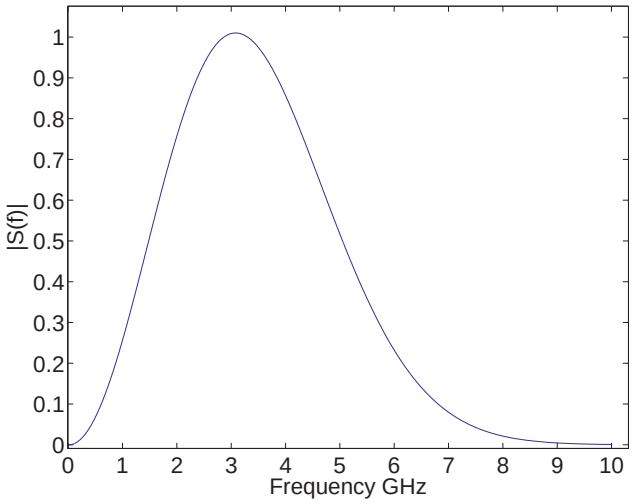

Figure 2.36: Gaussian Monocycle Pulse in Frequency Domain

2.2.0.5 Modulation

There are two principal techniques for transmitting data symbols using UWB; Pulse Amplitude Modulation (PAM) and Pulse Position Modulation (PPM). PAM represents transmitted bits as one of either two pulses that are antipodal with respect to each other. In this case, the transmitted signal $s(t)$ is given by

$$s(t) = m_j p(t), \tag{2.72}$$

where $p(t)$ is a pulse, such as the Gaussian monocycle of Figure 2.35, and m_j varies as,

$$m_j = \begin{cases} -1 & j = 0 \\ 1 & j = 1 \end{cases} \tag{2.73}$$

for a transmitted bit j. Also PAM can be modified to become On Off Keying (OOK) when,

$$m_j = \begin{cases} 0 & j = 0 \\ 1 & j = 1 \end{cases} \tag{2.74}$$

In the case of OOK changing the transmitted bit no longer results in variations between antipodal pulses but instead for the case of $j = 0$ no pulse is transmitted.

For Pulse Position Modulation (PPM) the transmitted signal $s(t)$ consists of a pulse $p(t)$ experiencing varied time shifts depending on the transmitted bit j where

$$s(t) = p(t - m_j \tau_p), \tag{2.75}$$

and

$$m_j = \begin{cases} 1 & j = 1 \\ 0 & j = 0 \end{cases} \tag{2.76}$$

In the above expression τ_p represents a predefined time shift. In addition to PAM and PPM some authors have explored using Pulse Shape Modulation whereby each bit is represented by differing pulse shapes [53]. An advantage of using transmitted pulses is that the received signal $s(t)$ can be directly converted to baseband by correlating $s(t)$ with all possible waveforms for either bit j. Consequently, this allows for simplified receiver designs that eliminate the need to down convert to intermediate frequencies when demodulating baseband data signals [54, 55].

2.3 Geo-Location

Since the emergence of modern wireless communications networks, there has been a growing interest in geo-location. In particular, the prospect of position location capabilities in indoor environments has lead to speculation on various possible future applications such as logistical tracking in warehouses, coordination of rescue services and medical patient tracking amongst others [11]. Early applications were concerned with providing outdoor geo-location over large areas. These include the Global Position System (GPS) [12] and the E-911 [13] emergency mobile phone location system. However this work focuses on short range indoor based schemes with a particular emphasis on UWB based systems [10, 14].

Initial indoor positioning schemes relied on infrared transmission between mobile and base nodes [56]. In [15] an RF based system for use in narrow band Wireless Local Area Networks (WLAN) was presented. This technique uses signal strength information in order to estimate a mobile client's location within a coverage region of several fixed base-stations. In recent times the advent of UWB, and in particular its use of narrow time domain pulses, encouraged research into precision time based location schemes [17, 19, 10].

Radio geo-location technology can be categorised into three distinct types; Signal Strength (SS), Angle of Arrival (AOA) and time based techniques (Time of Arrival TOA or Time Difference of Arrival TDOA). Also it is also possible to combine these technique in hybrid location schemes [57].

2.3.1 Signal Strength Geo-Location

Signal strength location relies on the principle of RF energy dissipating as it propagates from the transmitter in free-space. For an isotropic antenna pair this relationship between attenuation and free-space distance from the transmitter is expressed as,

$$A_{db} = 10 \log_{10} \left(\frac{\lambda}{4\pi d} \right)^2 \tag{2.77}$$

where A_{db} is the attenuation in Decibels, λ is the wavelength and d is the transmitter-receiver separation distance. Assuming a known transmitted power, the distance d from a base-station can be implied from the signal strength at the mobile station. Knowing the distances of a mobile client node from several base-stations allows for an estimate of position to be computed using trian-

gulation as in Figure 2.37. However, the attenuation due to the presence of obscuring objects in the propagation environment, such as people and walls, diminishes the achievable accuracy of signal strength based triangulation.

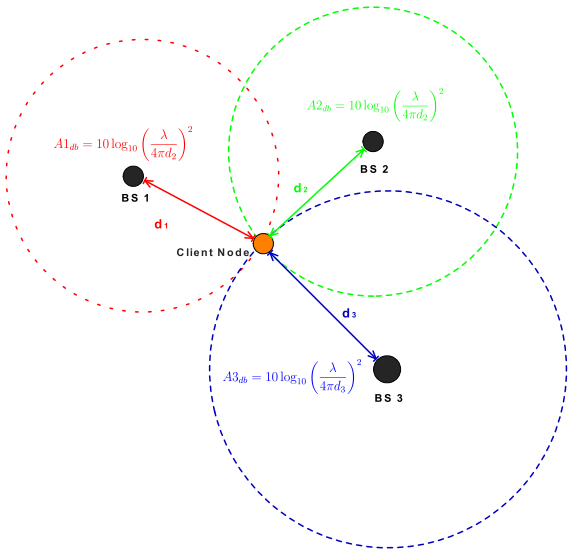

Figure 2.37: Signal Strength Triangulation

Alternatively, signal strength based "fingerprint" maps of an indoor location can be created such as in [15]. This method relies on a mobile client measuring received signal strength from multiple base-station nodes and subsequently comparing them to measurements for a grid of known locations. During an off-line phase signal strength between the mobile client and several base-stations are recorded in a database for each physical position in the environment. In the subsequent on-line phase, received signal strengths are compared with those of the prior constructed database and the location corresponding to the best match is returned.

2.3.2 Angle of Arrival (AOA) Geo-Location

Using an antenna array is it possible to measure the angle of incoming transmissions. By comparing the angles from two or more base-stations a client node's physical location can be estimated. The co-ordinates of this location corresponds to the intersection of straight lines originating at each base-station and having a slope equivalent to the measured angles of arrival as in Figure 2.38. A notable drawback of using an AOA based scheme is prohibitive additional infrastructure cost of an antenna array at each base-station. [10].

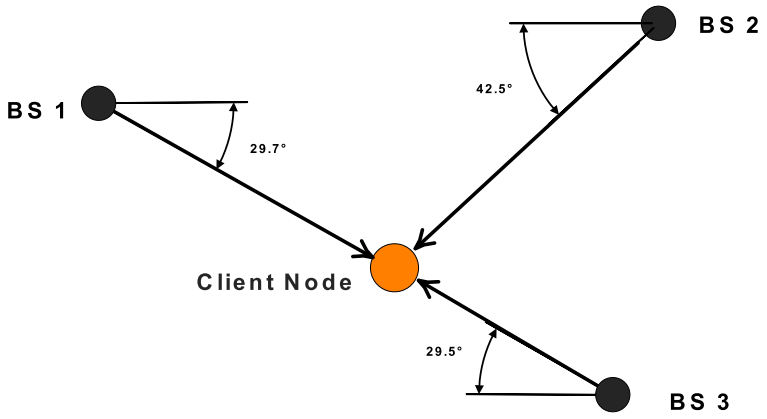

Figure 2.38: AOA Geo-location

2.3.3 Time Based Geo-Location

Time based schemes rely on the ability to measure the "time of flight" of wireless transmission between nodes in a network. Knowing that radio wave travel at a constant speed c in free-space, the distance travelled can be computed as the product

$$d = ct_{fl}, \tag{2.78}$$

where t_{fl} represents the aforementioned "time of flight". The narrow time domain pulses of UWB, as seen in Figure 2.35 of Section 2.2, allows for high levels of precision in location calculations. This is due to the fact that precise time of arrival can be obtained when using such narrow time domain waveforms. Consequently, much recent research has focused on using time based UWB schemes for precision location [16, 17, 18, 19] culminating in its adoption by the *IEEE* 802.15.4*a* standardization group [58]. This group was tasked with creating a physical standard that allows for precision location using unlicensed wireless spectrums. Time based geo-location technologies can be classified into one of two categories; Time of Arrival (TOA) or Time Difference of Arrival (TDOA) based schemes.

2.3.3.1 Time of Arrival (TOA)

A TOA system relies on measuring the time taken for a signal to travel from a base-station to a mobile client. This must be repeated for three or more base-stations in order to triangulate a client's position. Triangulation involves find-

ing a common intersection between the circles corresponding to the times of arrival t_1,t_2 and t_3 from each of the base-stations in Figure 2.39. The estimate of the mobile client node is located at this intersection. Since TOA is an absolute

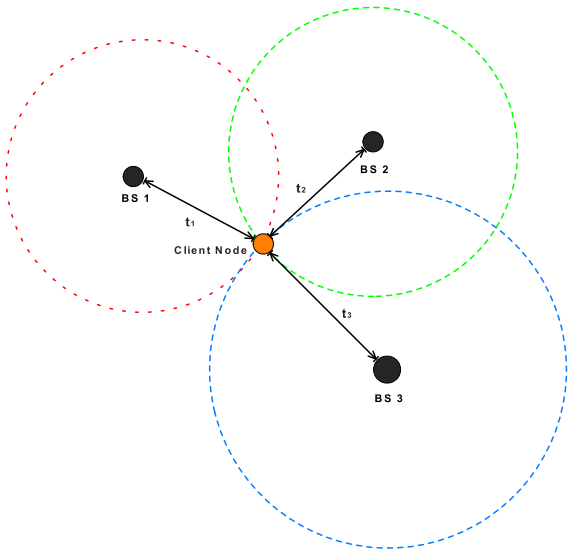

Figure 2.39: TOA Triangulation

time measurement, synchronization of the clocks between the base-stations and mobile client nodes is required. A potential drawback is that "jitters" or discrepancies between these clocks can limit the realizable accuracy. [59].

2.3.3.2 Time Difference of Arrival (TDOA)

TDOA differs from other time based schemes in that it doesn't require the ability to measure an absolute time of arrival. For conventional Time Difference of Arrival (TDOA) based geo-location systems the position of a client is estimated by using at least three fixed reference base stations [60, 61]. The client consists of a mobile transmitting station that broadcasts simultaneously to all base-stations. By obtaining the time difference between the arrival (TDOA) of a transmission at two fixed base-stations, a hyperbolic surface of possible locations of the mobile client is generated. However, in the case of a fixed client height, this can be reduced to a $2D$ hyperbolic curve (See Appendix B.1). Subsequently the client's exact location is computed as the intersection of two or more such hyperbolic curves as depicted in Figure 2.40. While this technique has the advantage of not requiring a shared timing reference between the mobile client and a base-station, synchronisation is still required between each

fixed base-station [13].

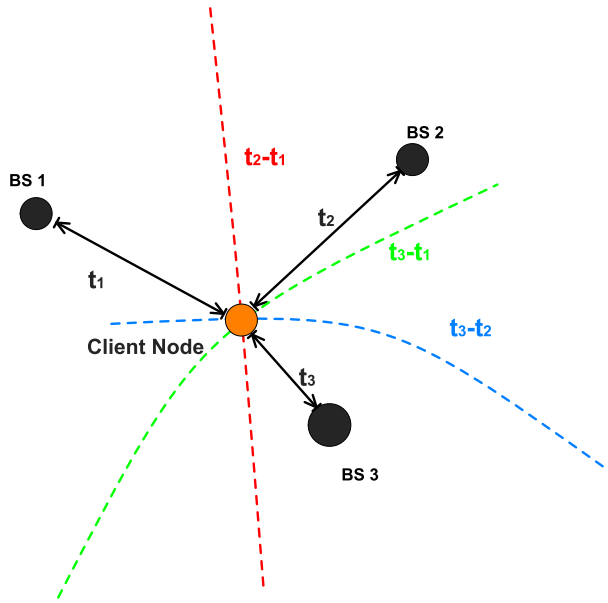

Figure 2.40: TDOA Geo-Location

Owing to the increased timing accuracy associated with using wide-band channels, in recent times there has been increased interest in UWB based indoor TDOA geo-location schemes [19, 16, 62]. In addition, there exists several commercial systems that employ UWB-TDOA : an example of such companies offering these solutions include Ubisense[2]and Zebra[3]. Further discussion of TDOA based techniques can be found later in Chapter 5.

2.3.3.3 Computational Efficiency in Time Based Techniques

While the narrow time domain signals of UWB allows for precise acquisition of a pulse arrival time, it also leads to an excessive computational overhead. This overhead can be attributed to each sampling bin of received time domain signal being searched in order to locate the position (or time) of a narrow pulse. The number of bins can be excessive in UWB systems as the sampling rate must be sufficient such that it can adequately sample a pulse that, in some cases, has a time domain width less than a nanosecond. For receivers listening over extended durations of time this leads to several thousand bins as candidates for the arrival time. The computational overhead is exacerbated further as in conventional UWB time based location systems searching for a pulse arrival

[2] http://www.ubisense.net
[3] http://zes.zebra.com/

involves cross correlation of the received signal with a copy of the expected pulse waveform [19]. As a consequence, a processing delay must be endured prior to obtaining a position estimate.
A potential solution to this problem is proposed in [17] for TOA based systems. A fast search for a pulse time of arrival is possible using a two step algorithm. The initial step computes a rough estimate of the pulse position by analyzing coarse regions in order to identify the one with largest received energy. Subsequently correlation is applied to the bins of this region yielding the precise arrival time of the pulse. Later in Chapter 5 of this thesis an algorithm for efficient TDOA acquisition is developed. This algorithm offers an novel means of determining the time difference between two pulses as an alternative to the computationally expensive cross correlation used in conventional TDOA implementations [19].

2.3.4 Hybrid Techniques

The techniques mentioned in the previous sections can also be combined in order to create a hybrid algorithm. By combining more than one method it is possible to obtain greater positioning accuracy [63]. Also hybrid techniques can reduce the infrastructure required for geo-location. In [57] a hybrid was developed that used both angle and time of arrival measurements in an outdoor mobile phone network. As a result only a single base-station is required in order to compute a client's handset location.

Chapter 3

Ray Tracing Visibility Algorithm

In this chapter a ray tracing image removal visibility algorithm is developed. The concept of employing image theory in order to compute reflected ray trajectories was previously introduced in Section 2.1.4 of Chapter 2. The technique presented within this chapter involves removing redundant reflecting surfaces at a pre processing stage thus reducing the computational burden of point to point ray tracing in environments that contain a large number of reflecting surfaces. The algorithm was specifically designed for use with simulations that allow multiple wall transmissions for each ray and can be applied to both wide-band and narrow-band simulations. This work has been previously presented at the 2006 European Conference on Antennas and Propagation in Nice, France [20].

3.1 Introduction

As the complexity and size of a building environment increases so too will the number of images that have to be processed and stored. A greater number of images leads to increased memory requirements and longer processing times. Consequently, the computational limits of conventional computing platforms cap the orders of reflection that can be calculated for complex environments. Similar concerns limit the number of transmissions that a ray can undergo. Some surfaces or facets will create redundant images due to this transmission limit; usually these will not be identified until ray tracing is carried out. This incurs simulation time penalties that can be avoided if such surfaces are identified at a pre-processing stage. In the proposed algorithm only surfaces that are visible to the transmitter, within the number of allowed transmissions, are considered during computation of first order images. Several methods exist where obscured surfaces and corresponding images are removed. In [64] and [65], surfaces that are completely obscured by others are removed during pre-processing by a sweep line algorithm. However these algorithms do not make provisions for a wall transmission limit and instead assume that ray transmission through objects do not occur. Other techniques employ visibility algorithms during run time that are concerned with eliminating facet surfaces from a particular ray path. These include multi-platen and angular Z-buffers [66,67]. In [68] a frustum ray tracing algorithm is used to speed up calculations of ray-object intersections. Line of sight and non line of sight regions are divided into different frustums[1] of a pyramid that has an apex corresponding to either the transmitter or an image point. Image trees of the transmitter and receiver point are created in [70]. Images that are not present in both trees are excluded from the ray trace. This algorithm is particulary suited for a parallel processing platform as both trees can be computed independently of each other.

The method proposed in this chapter removes redundant surfaces at a pre-processing stage for consideration during the calculations of first order images. Surfaces can be "shadowed" from direct paths to the transmitter by other facets in the propagation environment. Such a surface is deemed redundant when the number of obstructing facets exceeds a transmission limit set prior to a ray tracing simulation. This limit varies depending on the propagation characteristics the facets present within an environment and the maximum at-

[1] A Frustum is formed by two parallel planes cutting a solid [69]

tenuation threshold required for a particular simulation. Assuming a uniform dimension and material for each facet within an environment results in a fixed attenuation for each transmission thus allowing a transmission limit to be imposed. Surfaces contained within regions that exceed this limit will not be reached by an incident ray or yield for any first order reflections.
Assuming M valid reflecting surfaces without a transmission limit, the number of images created at each order of reflection is expressed as[2]

$$K = M\,(M-1)^{O-1}\,, \tag{3.1}$$

where O is the order of reflection. Figure 3.1 shows the cumulative number of images produced at successive orders of reflection. A single first order image results in K_a images at higher orders where,

$$K_a = \prod_{1}^{O_{max}-1} (M-1)\,, \tag{3.2}$$

and O_{max} is the highest order of reflection allowed for a ray tracing simulation. Consequently, for each redundant first order image removed by this algorithm there is an additional reduction of K_a images at higher orders.
Prior to removing redundant images facets that are shadowed from the transmitter must be identified. Initially a projection of the environment is made from the perspective of the transmitter on to several projection planes distributed within the environment. Subsequently a test is carried out on each plane to determine if it is entirely shadowed by a number of surfaces greater than the allowed number of transmissions. In what follows, it is assumed that the projected surfaces of the building environment are four sided polygons and as such only corner and intersection points need to be tested without discretising the entire area of the projection planes. If the prescribed number of layers covers a projection plane then facets completely shadowed by it can be removed for consideration in first order image calculations. However the algorithm incurs a preprocessing overhead and consequently, accelerated execution times are only obtained for simulations involving high orders of reflection in an environment with a large number of reflecting surfaces.

[2]In this example it is assumed that each reflecting surface creates images at every order of reflection. In a realistic implementation of ray tracing some surface may be positioned such that they do not face an image and as a result would be disregard during higher order image computations.

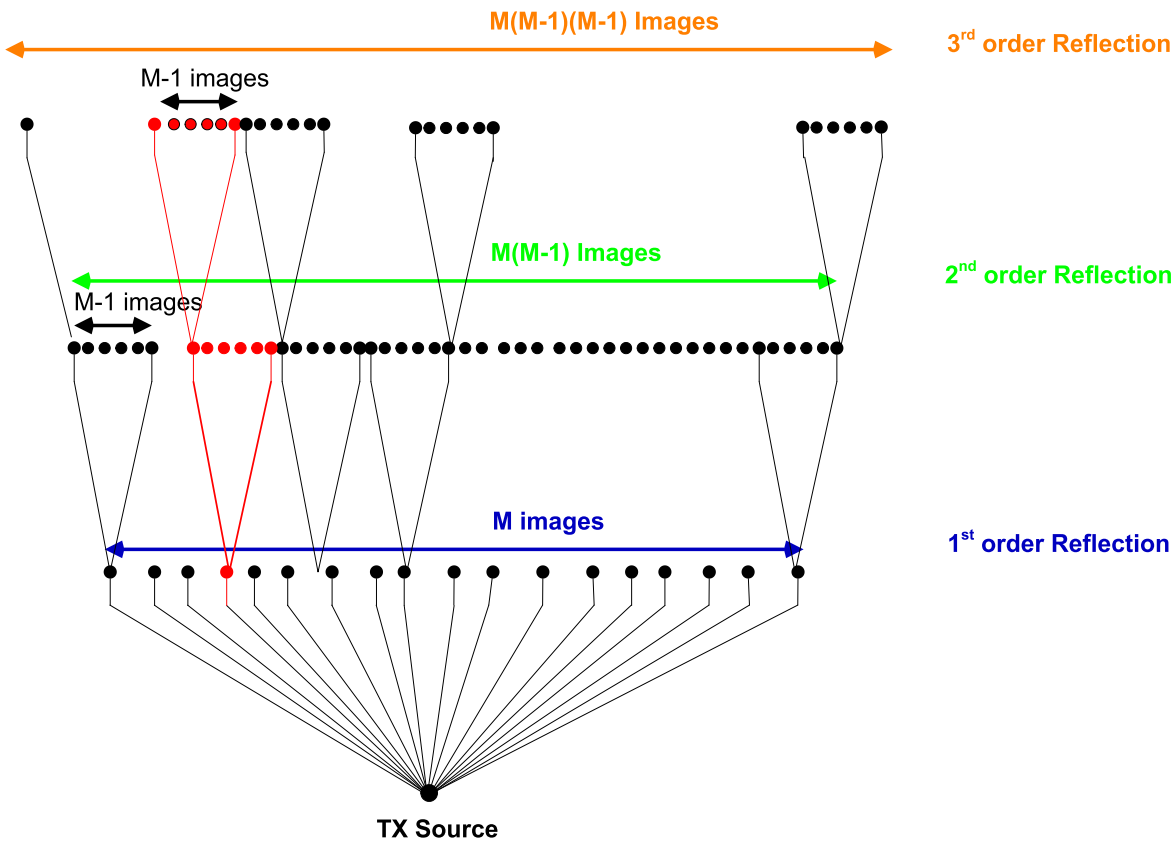

Figure 3.1: Image Growth for each order of Reflection

3.2 Description of Algorithm for a Single Projection Plane

Initially a projection of all the surfaces between the transmitter and a projection plane is created as shown in Figure 3.2. The transmitter location is used as the origin and the projection produces several overlapping polygons on the 2-D projection plane. This plane must be tested in order to check if a specified number of layers of polygons completely covers the plane area. While corner points of polygons are immediately identifiable on the projection plane, intersection points between polygon edges must be subsequently computed. Only the corner and intersection points need to be tested when trying to ascertain the number of polygons that shadow a particular projection plane. This eliminates any need to discretise the whole projection plane area in contrast to the multi-platen and angular Z-buffers techniques of [66, 67]. Once it is confirmed that the projection plane is completely covered by the required level of polygons, surfaces that are completely within its shadow, such as in Figure 3.3, can be disregarded as candidates for first order reflections.

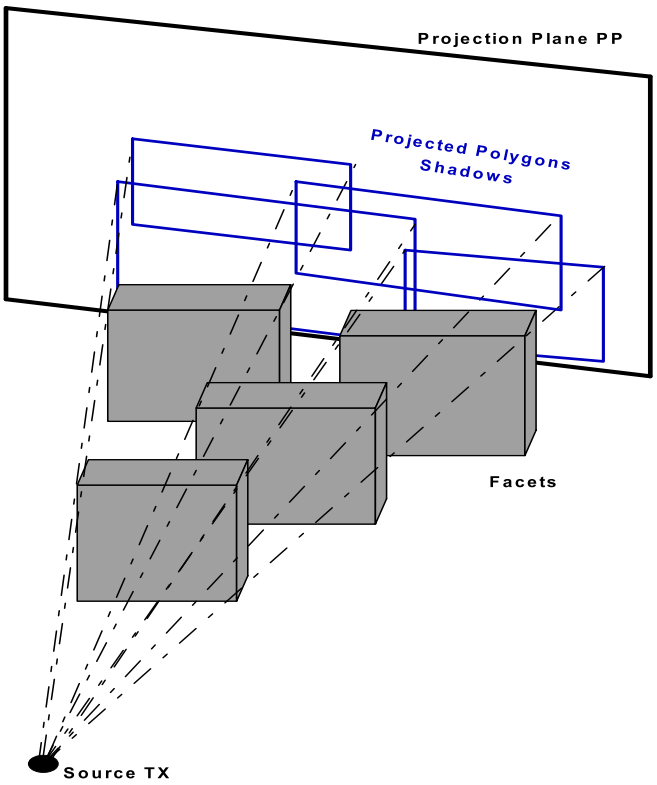

Figure 3.2: Plane Projection Polygon

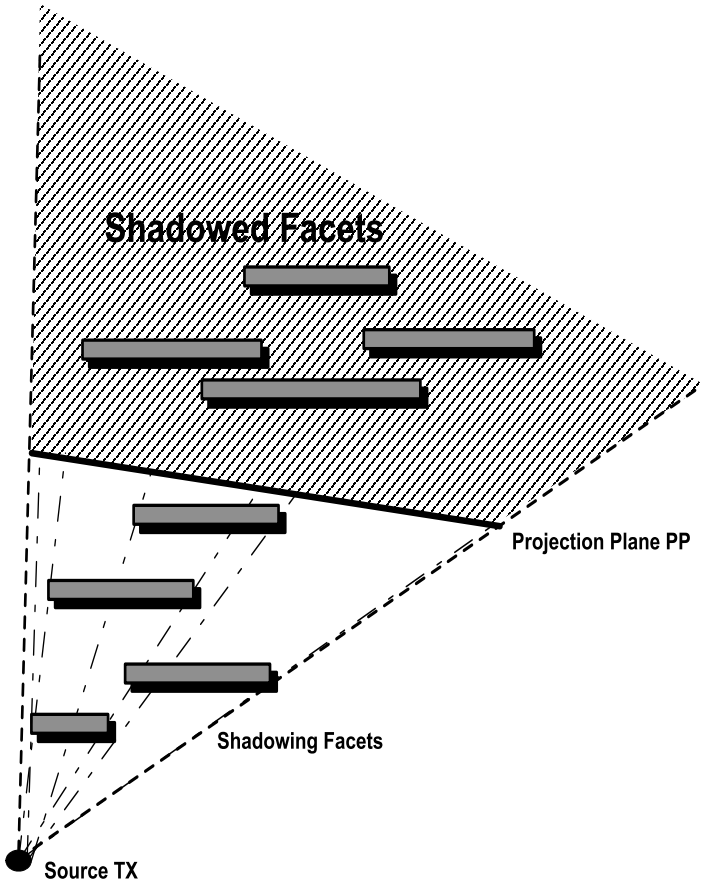

Figure 3.3: Projection Plane Projection shadowing Facets (Plan View)

3.2.1 Shadow Testing

This section outlines how projection planes are tested to determine if they are entirely covered by a specified number of layers of shadowing. Initially, for the purposes of clarity, a case where only one layer of shadowing is required on the projection plane is considered.

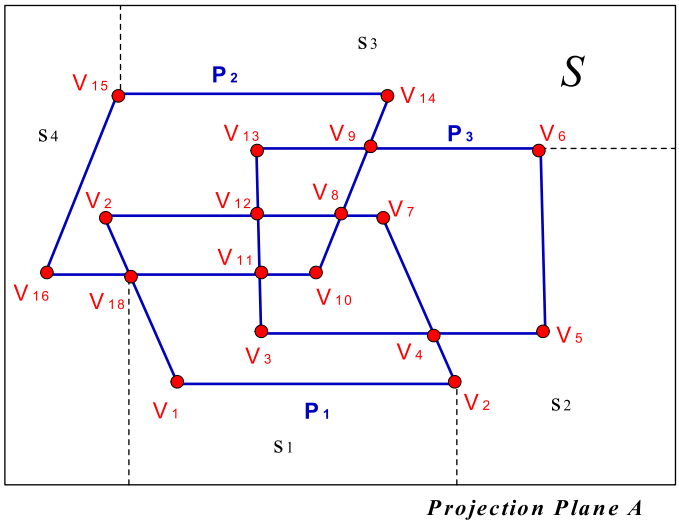

Figure 3.4: Projected polygon shadows P_i on projection plane A

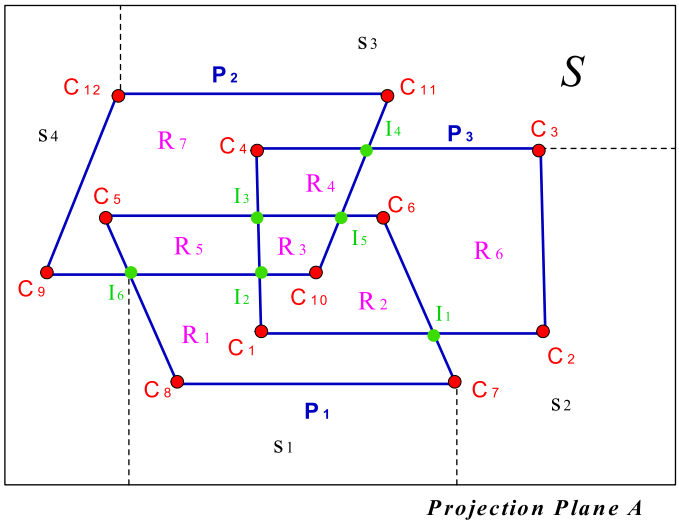

Figure 3.5: Shadowed regions R_i and unshadowed polygons S_i

Figure 3.4 shows projected polygons P_1, P_2 and P_3 on the projection plane A. These projected polygons are the resultant shadows from original facets in the building environment present between the transmitter and the projection plane. Projection plane A can be written as:

$$A = S \bigcup \{ \bigcup_{i=1}^{Q} P_i \}, \tag{3.3}$$

where A is the space enclosed in the projection plane, Q is the number of projected polygons P_i and S is the area of A that is not shadowed. The algorithm relies on the fact that A is entirely shadowed when S, the unshadowed region, has an area of zero.

The projected polygons $\bigcup_{i=1}^{Q} P_i$ intersect and can be decomposed into smaller non-overlapping shadowed regions R_i. For example, in Figure 3.4 the intersecting polygons P_1, P_2 and P_3 form the shadowed regions R_1 to R_7 in Figure 3.5, such that,

$$\bigcup_{i=1}^{Q} P_i = \bigcup_{i=1}^{M} R_i, \tag{3.4}$$

where M is the number of shadowed regions R_i created by Q projection polygons. The intersecting projection polygons $\bigcup_{i=1}^{Q} P_i$ will create the same or a greater number of R_i regions (ie: $M \geq Q$). Combining Equation 3.4 and Equation 3.3 gives Equation 3.5 as an expression for the entire plane A,

$$A = S \bigcup \{ \bigcup_{i=1}^{M} R_i \}. \tag{3.5}$$

A region R_i is uniquely described by its vertices V_i, of which it must have at least three.

$$R_i \longrightarrow \{V_1, V_2, V_3, ...\}. \tag{3.6}$$

These vertices V_i can be identified as corner points C_i of the original projected polygons P_i or intersection points I_i between the edges of these polygons. This is observed where the vertices V_2, V_4 and V_5 in Figure 3.4 are labelled C_7, I_1 and C_2 in Figure 3.5. The unshadowed area S can be conceived of as a union of smaller unshadowed regions s_i as in Equation 3.7.

$$S = \bigcup_{i=1}^{H} s_i, \tag{3.7}$$

where H is the number of unshadowed regions s_i that constitute S. For ex-

ample, in Figure 3.5, S is comprised of a union of unshadowed regions s_1, s_2, s_3 and s_4.

If an unshadowed region s_i exists it will invariably share some of the vertices V_i of the shadowed regions R_i. For example, in Figure 3.5, s_1 shares the vertices C_7, C_8 and I_5 with R_1. As stated earlier, the projection plane has to be tested to determine if an unshadowed region such as s_i is present. Each vertex V_i on the projection plane A is examined to ascertain if it is a vertex of an unshadowed region s_i. The existence of an unshadowed part of the projection plane is confirmed if any vertex V_i of shadowed region R_i is common to an unshadowed region s_i. For the purpose of testing a projection plane for shadowing, each vertex V_i is classified as either a corner point C_i, a shared corner point CS_i or intersection point I_i. The following sections describe these different types of points and their associated tests to determine if they are vertices of an unshadowed region s_i.

3.2.2 Corner Points

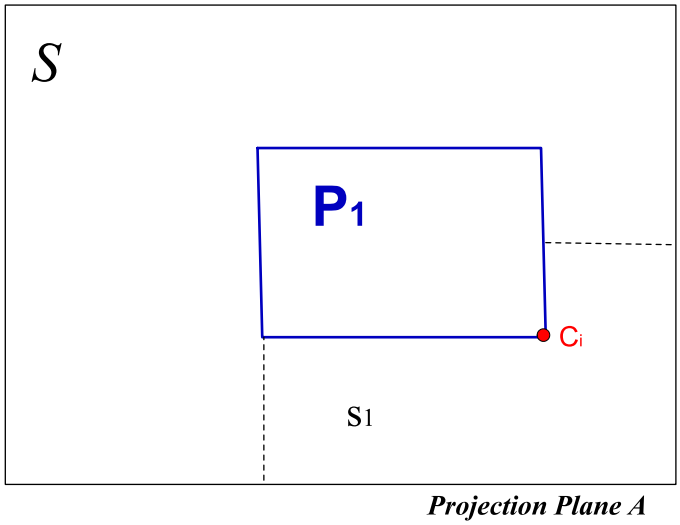

Figure 3.6: Projected Polygon P_1 and Corner Point C_i.

Figure 3.6 shows a corner point C_i as a vertex of a projected polygon P_1 and an unshadowed region s_1. In this example the entire projection plane A is not covered by a layer of shadowing, hence s_1 exists and has C_i as a vertex. In addition, it should be noted from Equation 3.7 that $s_1 \subset S$. Considering Figure 3.6, when the corner point C_i is a vertex of s_1 ,it is also present within at least one projected polygon, in this case P_1. As a result, in order to test whether C_i is a vertex of the unshadowed region s_1, it is sufficient to simply count the number of projected polygons P_i that C_i is present within. If C_i is found to be a vertex of s_1 then the projection plane A is not entirely covered by shadowed polygons P_i. Equation 3.8 forms the basis of such a test to determine whether a corner point C_i is also a vertex of some unshadowed region s_i.

$$N(C_i) = G(C_i) - 1, \tag{3.8}$$

where $G(C_i)$ is the number of projected polygons P_i that C_i is within. If $N(C_i)$ is zero then C_i is a vertex of s_i and the whole projection plane is not completely shadowed by projected polygons P_i. If $N(C_i)$ is greater than zero then this corner point is not touching an s_i unshadowed region and is contained within another projection polygon P_2 as in Figure 3.7. This indicates that C_i is not a vertex of any s_i.

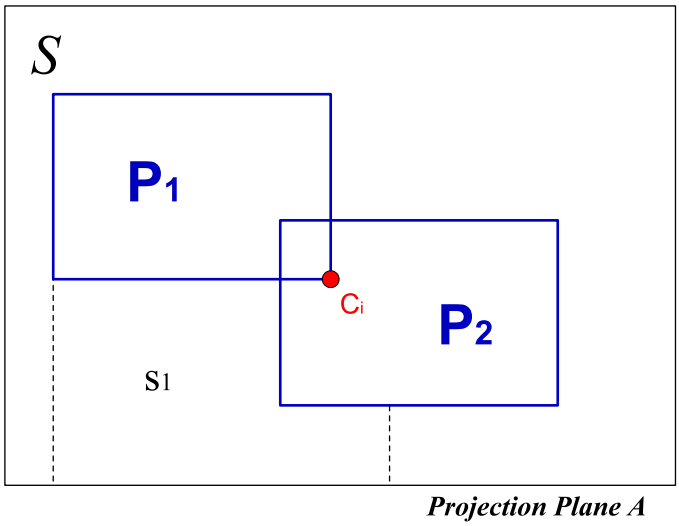

Figure 3.7: Projected Polygons P_1, P_2 and Corner Point C_i

3.2.3 Shared Corner Points

It may occur that a corner point is shared by several projected polygons as in Figure 3.8. If three or less polygons share a corner point CS_i as in Figure 3.8(a), it is possible for the corner point CS_i to be a vertex of an unshadowed region s_1. In this example a corner point CS_i is present within the three projected polygons P_1, P_2 and P_3. Equation 3.9 represents a test to check if CS_i is a vertex of an unshadowed region s_i (see Figure 3.8(a)).

$$N(CS_i) = G(CS_i) - NP(CS_i) \quad \{NP(CS_i) \leq 3\}, \tag{3.9}$$

where $G(CS_i)$ is the number of projected polygons that CS_i is present within and $NP(CS_i)$ is the number of projected polygons P_i that share the corner point CS_i. Being a shared corner point of several polygons contributes to the values of both $NP(CS_i)$ and $G(CS_i)$. Consequently, $NP(CS_i)$ is subtracted from $G(CS_i)$ in order to find the number of additional polygons that CS_i is contained with. If following this, $N(CS_i) = 0$, then an unshadowed region s_1 depicted by Figure 3.8(a) exists.

Due to the exclusive use of four sided regular rectangles for facets and rooms in the building layouts of this work, it is assumed that where four or more polygons share a corner point, CS_i is surrounded entirely by the projected polygons P_1,P_2,P_3 and P_4 as in 3.8(b). Incorporating this into Equation 3.9 results in Equation 3.10 as a means of obtaining the number of layers shadow-

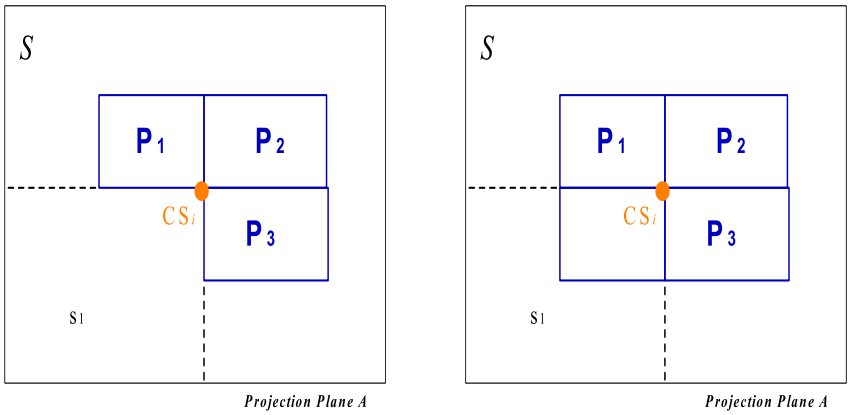

(a) 3 Polygons Sharing a Corner Point (b) 4 Polygons Sharing a Corner Point

Figure 3.8: Shared Corner Point

ing CS_i. As in the previous case of a single corner point, values of $N(CS_i) > 0$ for Equation 3.10 indicate that the point CS_i is not a vertex of an unshadowed region.

$$N(CS_i) = G(CS_i) - NP(CS_i) + 1 \quad \{NP(CS_i) \geq 4\}, \tag{3.10}$$

3.2.4 Intersection Points

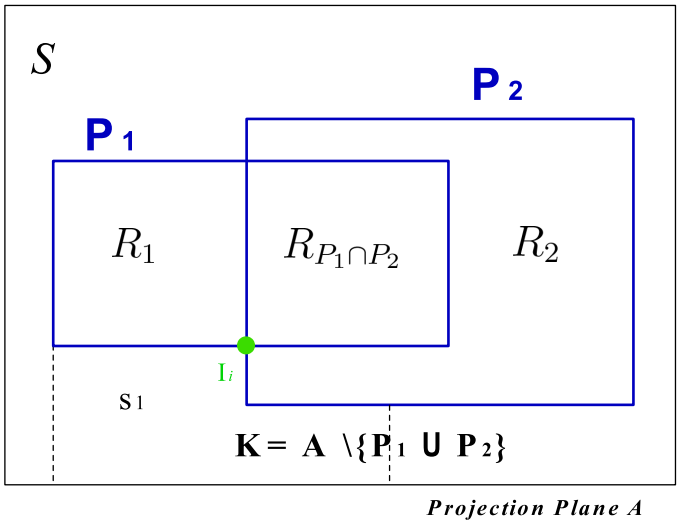

Figure 3.9: Intersection point I_i from $P_1 \bigcup P_2$

An intersection point I_i is formed when two edges of polygons intersect (see P_1 and P_2 in Figure 3.9). It can be seen that an intersection point I_i is a vertex bordering four regions and that the layer of shadowing L differs for each region. The intersection of P_1 and P_2 in Figure 3.9 can be decomposed in four regions R_1 ,R_2, $R_{P_1 \cap P_2}$, and K ($K = A \setminus \{P_1 \cup P_2\}$). The K region has the least number of shadowing layers[3]L it and could potentially be in a region in S without any layer of shadowing as in Figure 3.9.
Using Equation 3.11 it can be determined whether I_i is a vertex of an unshadowed region s_i.

$$N(I_i) = G(I_i) - 2, \tag{3.11}$$

where $G(I_i)$ is the number of projected polygons that the intersection point lies within. As in the case of the corner point, if $N(I_i)$ is zero then the projection plane A is not completely shadowed and I_i is a vertex of an unshadowed region s_i. It should be noted that an intersection point is considered to be within 2 polygons (P_1 and P_2) and that the region outside $P_1 \cup P_2$ ($A \setminus \{P_1 \cup P_2\}$), will

[3]"Shadowing Layers" or "Layers of Shadowing" refers to the number of facets that obscure a particular portion of the projection plane A from the transmitter. The effects of such facet's surfaces being projected on to the projection plane can be conceived as being analogous to classical shadowing associated with the visible portion of the electromagnetic spectrum. A region on the projection plane covered by L projected surfaces is considered to have L "layers of shadowing".

have a layer of shadowing L equivalent to $G(I_i) - 2$.

3.2.5 Variable Threshold of shadowing

In the previous sections, a technique was outlined for determining if a projection plane was entirely covered by at least one layer of shadowing. However, a ray-tracing simulation may allow for several consecutive transmissions per ray. This translates to a lower limit threshold of shadowing layers corresponding to the number of transmissions T permitted per ray. While the previous approaches outlined in Sections 3.2.2-3.2.4 are still applicable, the values of $N(C_i)$ $N(CS_i)$ and $N(I_i)$ from Eqs. 3.8, 3.9, 3.10, 3.11 must exceed this threshold $\geq T$ for a plane to be considered entirely shadowed by T layers.
In summary if Eqs. 3.12, 3.13, 3.14, hold true for all C_i, CS_i and I_i then a projection plane is completely shadowed by T layers,

$$N(C_i) \geq T, \tag{3.12}$$

$$N(CS_i) \geq T, \tag{3.13}$$

$$N(I_i) \geq T. \tag{3.14}$$

3.2.6 Plane Removal

If tests of the corner, intersection and shared corner points are all passed then the projection plane is considered to have the minimum level of shadowing T equivalent to the maximum permitted number of transmissions. A shadow zone is created using the transmitter location point as the origin of the zone and the projection plane as the source of the shadow (see Figure 3.10). Surfaces of facets contained in this shadow zone are ignored during the identification of first order images. Otherwise facets that are not contained in this zone are still considered when making first order images.

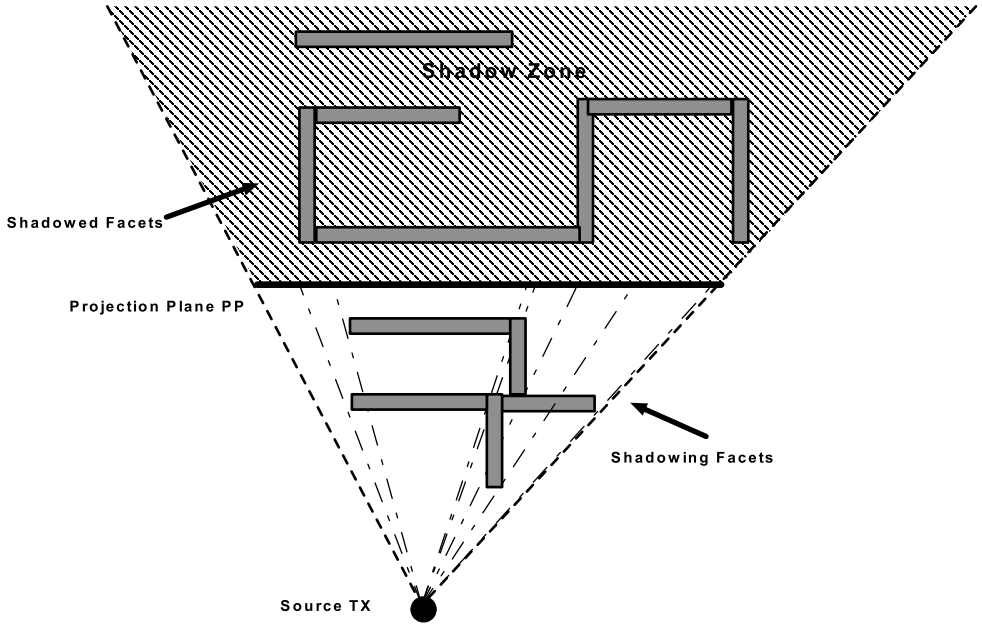

Figure 3.10: Projection Plane PP and Facets

3.3 Implementation of Image Removal Algorithm

The image removal algorithm is applied prior to running a ray tracing simulation. Surfaces found to be sufficiently shadowed are noted and subsequently disregarded when identifying first order images. The 3D co-ordinates of corner-points of the facets in the building environment are used to create 2D projections onto a series of projection planes. In the aforementioned ray-tracing simulator, twelve projection planes are located equidistant from the transmitter and at angles in increments of thirty degrees as in Figure 3.11. While a radius d of 60 meters was used for simulations in this chapter the configuration can be varied for different ray transmission limits and building layouts. Specifically, the choice of the transmission limit will depend on the attenuation of the walls in the environment. For this purpose it is assumed that each wall is of the same thickness and composed of identical materials. As a result an average attenuation can be attributed to each wall and a suitable transmission limit applied. Prior to simulation time the radius d can be specified such that there will be a number of walls equivalent or greater than the transmission limit present between the transmitter and at least one projection plane. In the case of this simulation the radius was chosen by visual inspection. While this process could be automated by recursively testing with ever increasing radii, this would entail a prohibitive computational cost.

The aforementioned projection planes have a height equal to that storey of the building. All facets that are located in the area between the transmitter and the projection plane are projected onto the plane. Projected polygons, even those that are on the plane but not within boundaries, are noted. However, only intersection points and corner points from within or on a projection plane boundaries are subject to coverage tests for that plane. Each projection plane in Figure 3.11 is tested in succession and in the case of an individual coverage test failing, the program immediately moves on to testing a subsequent plane. This is a time saving alternative to testing every point on a particular plane. Facets located behind a plane that meets the shadow threshold T are removed from the list of surfaces used to make first order images. As depicted in Figure 3.12 the corner points of the projection planes are the first tested for the minimum layer of coverage T. This is achieved by counting the number of projected polygons ($G(CS_i)$) that these points are present within. There are only four such points to be tested and failure results in the test for this plane being abandoned. Creating intersection points is computationally expensive as it involves checking each polygon side for an intersection with each other. To avoid

this time penalty the corner points of the projected polygons are checked for coverage before calculating intersection points. Intersection points are computed only when all corner points pass the coverage test. These points are tested before the shared corner points. When all twelve planes in Figure 3.11 are tested a reduced list of facets are used for creating first order images of the transmitter. This has an overall effect of reducing the amount of images that are created for all higher orders, resulting in less time for calculating ray paths.

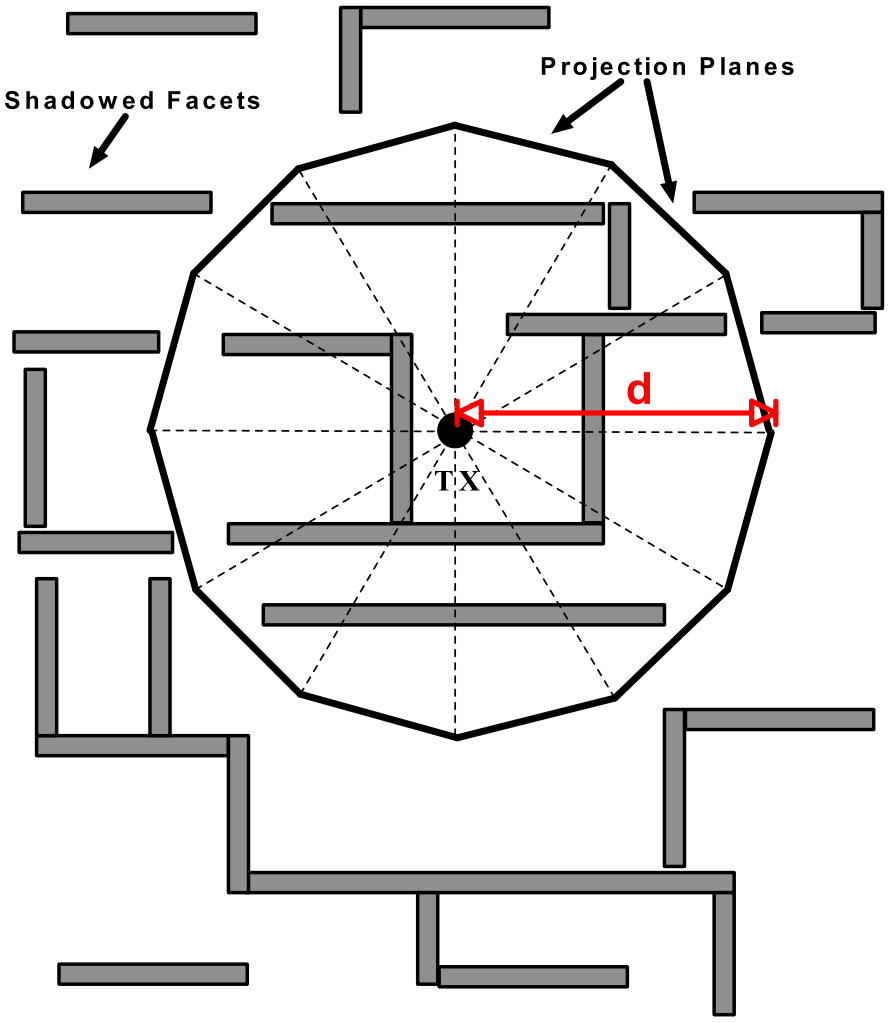

Figure 3.11: Planar view of 12 Projection Planes centred about a transmitted TX

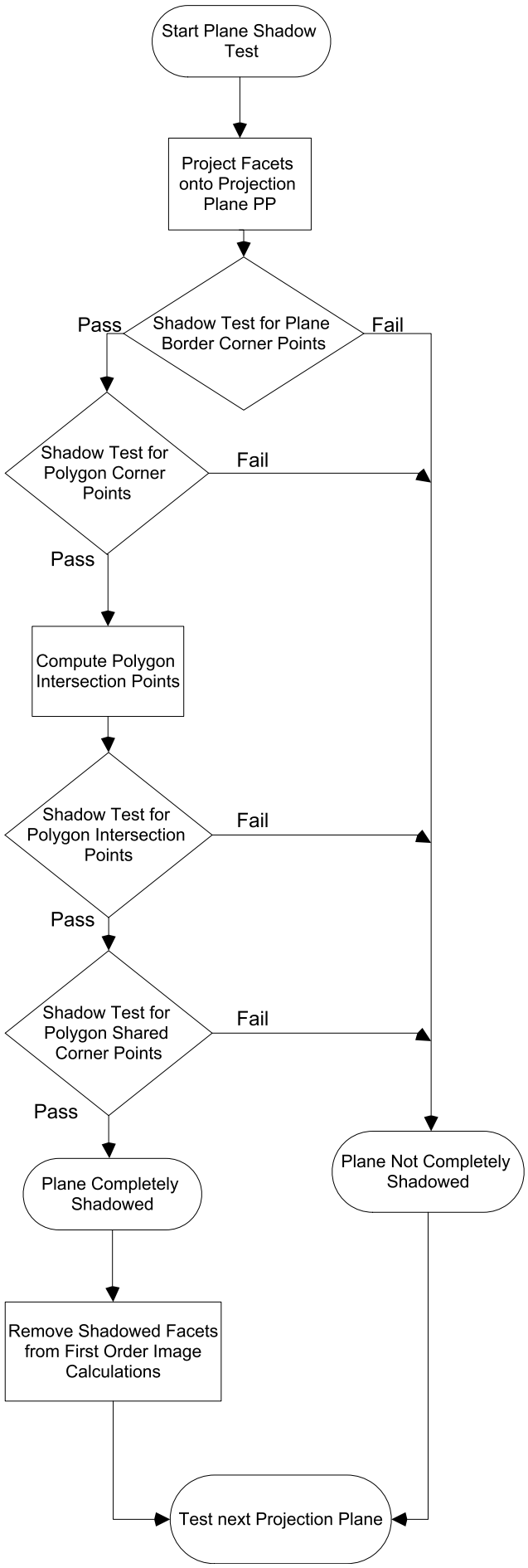

Figure 3.12: Implementation of Algorithm

3.4 Results

In order to evaluate the image removal algorithm, execution times were compared for both accelerated and un-accelerated simulations. For the purposes of testing this technique, the narrow-band ray-tracing simulator developed by Dr. Eamon Kenny [7] was employed. Figure 3.13 shows the percentage reduction in ray tracing execution time for each order of reflection as a result of applying the algorithm. The ray trace allowed a maximum of 8 transmissions per ray. Due to memory requirements of the computer used, 4^{th} order of reflection was the maximum that was possible. In this simulation the transmitter was located at (5, 5, 1.7) in the most south easterly room of the building (see Figure 3.16) . The building was populated by 64 receiver points. On application of the acceleration algorithm the number of facets considered for first order reflection calculations was reduced from 74 to 61. However, resultant higher order images are reduced as in Table 3.2 and Figure 3.14. There is a time saving associated with reducing the number of images but at lower orders of reflection this is outweighed by the pre-processing time resulting from applying the image removal algorithm. The average pre-processing time was 188.63 seconds[4]. From Table 3.1[5]it can be seen that for fourth order reflections the number of images removed is sufficient such that the time saving exceeds the pre-processing time. A net time saving of 18.09% was achieved by applying the algorithm which equates to an overall reduction of 3808 seconds (63.47 mins).

[4]Applying the algorithm results in an addition pre-processing computations prior to running an actual ray tracing simulation. As a result the total execution time is expressed as the sum of the preprocessing time overhead associated with applying the image removal algorithm and the ray tracing simulation time. This preprocessing time overhead is not included in time savings shown in Figure 3.13.

[5]"Ray Tracing Time" differs from "Total Execution Time" in that it does not include the time taken to load building data and create image lists.

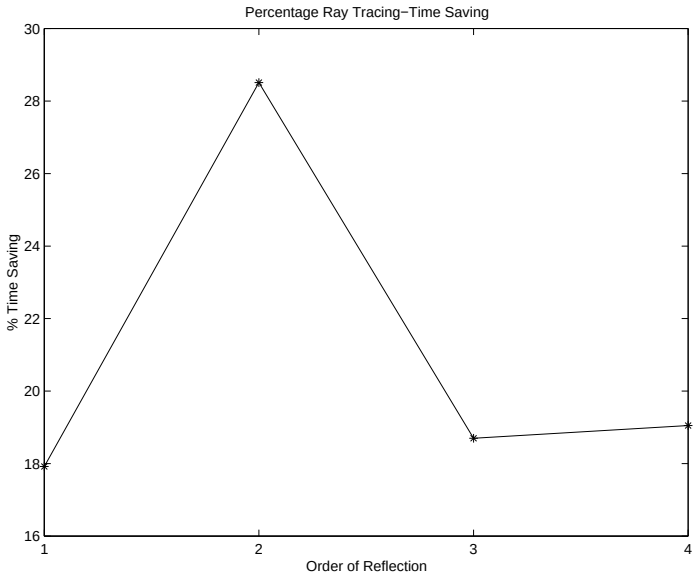

Figure 3.13: Percentage time saving per Reflection order for Ray-Tracing allowing 8 transmissions (Excluding Pre-Processing Times)

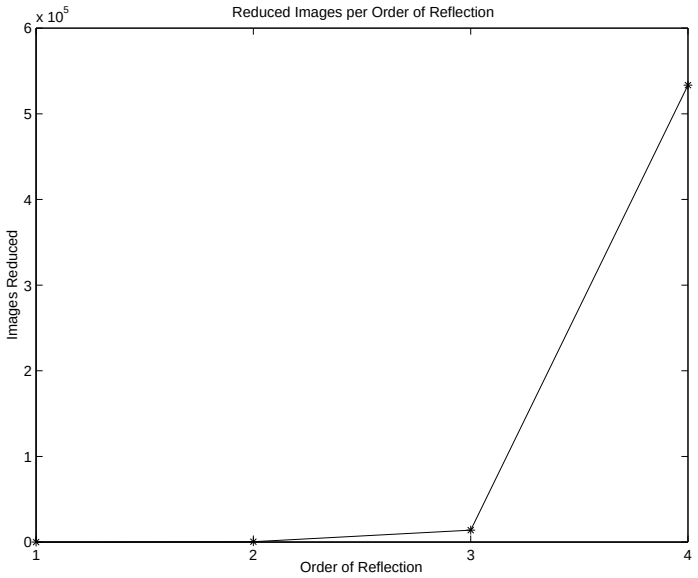

Figure 3.14: Number of Images Removed for Simulations allowing 8 Transmissions (TX @ 5,5,1.7)

Order of Reflection	**1st**	**2nd**	**3rd**	**4th**
Accelerated Times (Seconds)				
Ray Tracing Time	0.641	11.672	407	16977.8
Total Execution Time	264.266	274.453	668.593	17246
Non-Accelerated Time (Seconds)				
Ray Tracing Time	0.781	16.328	500.64	20972.4
Total Execution Time	77.031	89.766	573.046	21054.4
Time Savings (Seconds)				
Ray Tracing	0.14	4.656	93.64	3994.6
Total Execution	-187.235	-184.687	-95.547	3808.4
% Time Savings				
Ray Tracing Time	17.92	28.51	18.70	19.05
Total Execution Time	-243.06	-205.74	-16.67	18.09
Average Preprocessing Time (Seconds)	188.63			

Table 3.1: Time-savings for Ray Tracing allowing for 8 Transmissions

Order of Reflection	**Images Removed**	**Total Accelerated Images**	**Total Un-Accelerated Images**	**Total Images Removed**
1	9	35	44	9
2	352	1484	1845	361
3	13548	59110	73091	13909
4	519481	2306720	2840182	533390

Table 3.2: Images removed for Simulations allowing 8 Transmissions (TX @ 5 ,5 ,1.7).

An additional ray trace was carried out allowing for 4^{th} order transmission and reflections. This time the transmitter was located near the centre of the building at (75, 40, 1.7) (see Figure 3.16). There were 144 receiver points in the simulation and the number of facets considered during first order image calculations was reduced from 74 to 63. Figure 3.15 and Table 3.3 show the numbers of images reduced at each order of reflection. As in the case of the previous simulations, a net time saving was not realised until 4^{th} order reflections were used. However, at this order the accelerated simulator achieved a time saving in of 2404.5 seconds (40.07 mins) which corresponds to a 10.33% saving off the original ray tracing simulation execution time.

Order of Reflection	**Images Removed**	**Total Accelerated Images**	**Total Un-Accelerated Images**	**Total Images Removed**
1	5	34	39	5
2	180	1358	1543	185
3	6649	52317	59148	6831
4	248697	1999565	2255093	255528

Table 3.3: Images removed for Simulations allowing 4 Transmissions (TX @ 75, 40, 1.7)

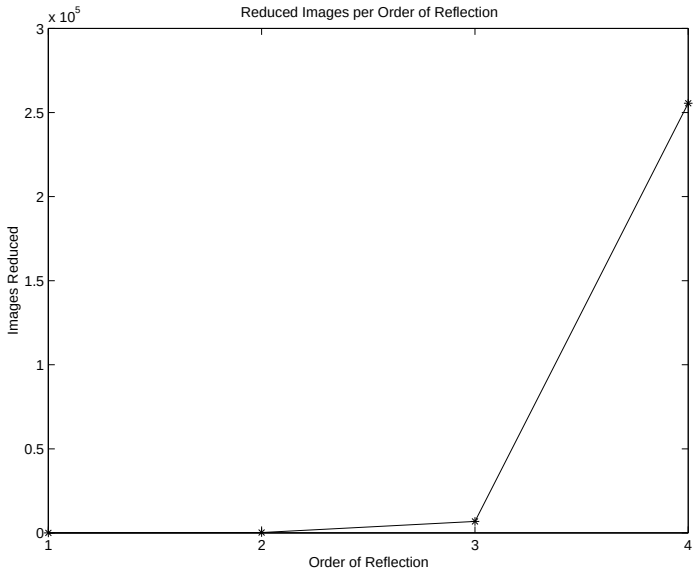

Figure 3.15: Number of Images Removed for Simulations Allowing 4 Transmissions (TX @ 75, 40, 1.7

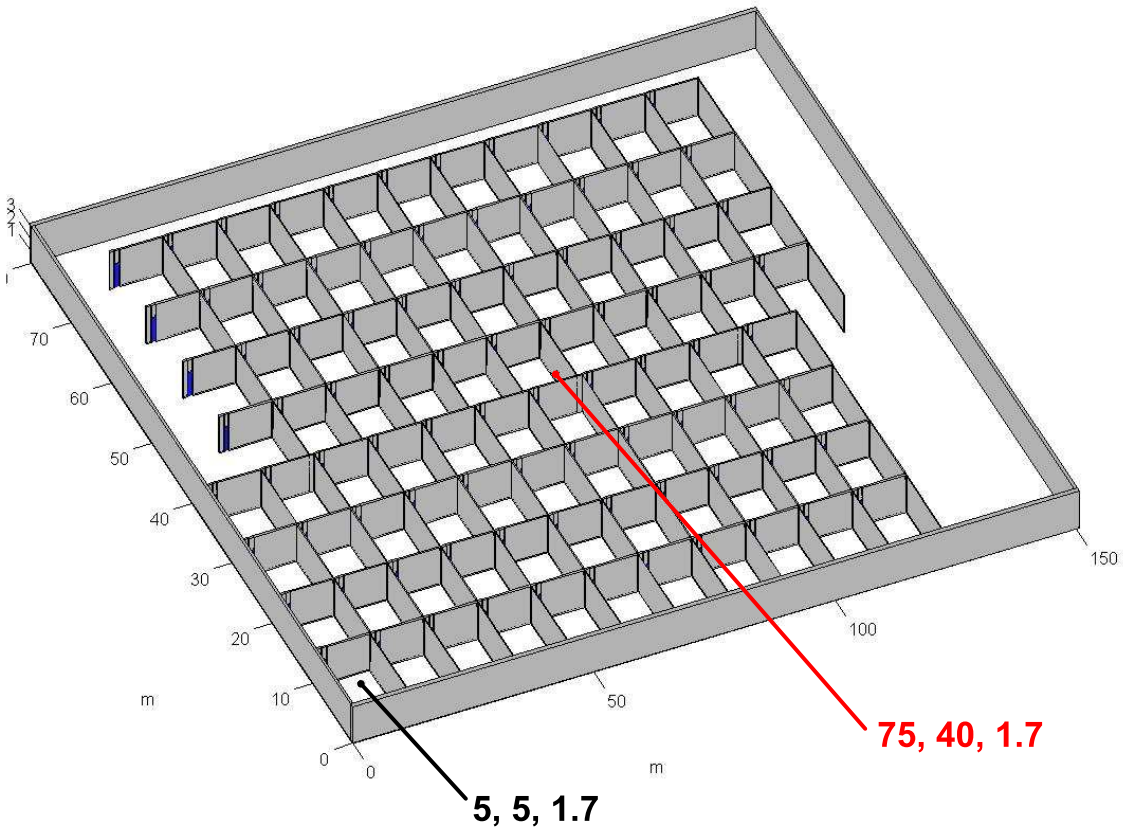

Figure 3.16: Ray Tracing Environment

3.5 Conclusion

In this chapter an image removal visibility algorithm was presented. The technique removes invalid images at a preprocessing stage thus resulting in a more efficient ray tracing simulation. Redundant first order images are identified by applying a projection plane based acceleration algorithm. The projection plane is tested in order to determine whether it is shadowed completely by at least T layer of facets, where T is the maximum number of transmissions permitted per ray. By analysing the vertices of overlapping facet projections the number of shadowing layers can be determined without the need to discretise the entire plane. Facets behind such a shadowed plane are not considered when computing first order ray tracing paths and subsequently this results in a reduced number of images.

The image removal algorithm was tested for an indoor building environment of Figure 3.16. A greater reduction in overall images and corresponding simulation times was noted as the order of reflections in a simulation increased. However such ray tracing simulation time savings must be considered against the preprocessing time taken to apply the algorithm. Consequently, a total net time saving is only realised for simulations permitting a maximum 4^{th} order reflections. Using this configuration a total execution saving in the order of 18% is achieved.

The algorithm presented in this chapter offers a distinct advantage of being suitable for use with ray tracing simulations where multiple transmission through objects are considered for each ray. In addition, it is applied without having to discretise entire propagation environments such as in the z-buffer techniques of [66, 67]. However, considering that the proposed algorithm in this work is applied during a preprocessing stage resulting in a pre-processing time overhead, a net reduction in execution times will not be achieved for all configuration. Specifically this algorithm works best with simulations that required a high order of reflection ($> 3^{rd}$ order) containing surfaces obscured by an amount of facets greater than the ray transmission limit T.

Chapter 4

Frequency Domain Acceleration Technique

Frequency domain based ray tracing computations were initially introduced in Section 2.1.5 of Chapter 2. In addition, the variation of ray scattering coefficients with frequency in these computations was demonstrated in Sections 2.1.5.1-2.1.5.3. A key advantage of employing frequency domain based simulations is that these variations can be rigorously calculated over a wide-bandwidth such as those used in Ultra-Wideband (UWB) systems. However, the large bandwidth of several Giga-Hertz can result in a challenging computational overhead. In this chapter an acceleration technique is introduced that aims to reduce this burden. The proposed algorithm allows full sweep UWB channels to be accurately approximated from a ray tracing simulation using only a reduced set of sample frequencies. Applying this technique to a conventional frequency domain simulator results in reduced simulation times while maintaining the capability of including frequency dependent scattering effects.

4.1 Frequency Domain Ray Tracing

Channel responses at specified receiver points are computed by means of a ray-tracing simulator. During such computations dominant paths by which energy propagates between the receiver and transmitter are identified. Subsequently these paths are calculated and summed to obtain the total channel response. At a point $\mathbf{r}$ this response can be written as,

$$\mathbf{H}(\mathbf{r}, \omega) = \sum_{i=1}^{N} \mathbf{R}_i(\mathbf{r}, \omega), \tag{4.1}$$

where N is the total number of rays and depends on the highest order of scattering events that is allowed. Each ray has an associated response $\mathbf{R}_i(\mathbf{r}, \omega)$ and is composed of a connected set of straight line segments between discrete scattering events, which can include reflections, transmission or diffractions. The variation of the response with frequency in Equation (4.1) is due to the frequency dependency of each ray, which in turn can be categorized into two separate propagation effects.

- A substantial contribution to frequency dependence is due to the propagation distance of a ray. Electric lengths of a ray will differ at each individual frequency. Although this results in a phase component that varies rapidly with frequency, the effect can be easily computed.
- Additional frequency dependent effects are attributable to interactions of the ray with objects in the propagation environment. Transmission and reflection coefficients of such objects' surfaces undergo variations due to the frequency dependence of the constituent materials' dielectric properties. Consequently, individual rays also exhibit frequency dependent variations. Such effects, while significant, vary slowly with frequency.

The proposed technique relies on separating these widely varying frequency dependencies for each ray. Fast variations are extracted and the remaining slowly varying effects are approximated using a low order polynomial. Using this method a channel response can be completely specified by analysing the ray at a reduced number of frequency sample points.

4.2 Efficient Frequency Sweep

In order to identify, and subsequently separate, rapidly and slowly varying frequency dependencies it is necessary to examine the constituents of a ray trace generated multi-path channel.
A channel response at a point $\mathbf{r}$ is given by,

$$H(\mathbf{r}, \omega) = \sum_{i=1}^{N} R_i(\mathbf{r}, \omega), \tag{4.2}$$

where $H(\mathbf{r}, \omega)$ is equivalent to the component of electric field at the point $\mathbf{r}$ in the direction of the receiver antenna polarisation and $\mathbf{R}_i(\mathbf{r}, \omega)$ is the associated electric field contribution from an individual ray at such a point. A

vertically polarised isotropic receiver antenna was assumed for simulations presented in this chapter. Typically a channel response must be computed for many frequency points ω_γ for $\gamma = 1 \ldots Q$, choosing Q large enough to ensure a satisfactory sampling rate. Hence a computational burden arises when the huge bandwidths of UWB channels are simulated. The proposed acceleration technique reduces the number of frequency samples that must be explicitly computed by separating the fast and slow varying components of each ray. For each point $\mathbf{r}$ Equation 4.2 is rewritten as (suppressing the $\mathbf{r}$ dependence for notational convenience),

$$H(\omega) = \sum_{i=1}^{N} A_i(\omega)\, e^{-\jmath\phi_i(\omega)}, \tag{4.3}$$

where the amplitude and phase frequency dependence of the ray contribution are made explicit. This is factorized as follows,

$$H(\omega) = \sum_{i=1}^{N} A_i(\omega)\, e^{-\jmath\tilde{\phi}_i(\omega)} e^{-\jmath\phi_i^d(\omega)}, \tag{4.4}$$

where ϕ_i^d is the phase behaviour associated with the free-space propagation of the ray and $\tilde{\phi}_i$ is the residual phase behaviour associated with object interactions.

The phase term ϕ_i^d has the form,

$$\phi_i^d(\omega) = \frac{d_i \omega}{c}, \tag{4.5}$$

where d_i is the distance ray i travels in free space and c is the speed of light in a vacuum. By dividing out this linear phase from a ray response, a slowly varying term $A_i(\omega)\, e^{-\jmath\tilde{\phi}_i(\omega)}$ remains. Consequently, this residual can be approximated by P_i, a polynomial of order m,

$$A_i(\omega)\, e^{-\jmath\tilde{\phi}_i(\omega)} \simeq P_i(\omega), \tag{4.6}$$

yielding,

$$H(\omega) \simeq \sum_{i=1}^{N} e^{-\jmath\phi_i^d(\omega)} P_i(\omega). \tag{4.7}$$

P_i can be completely specified for each ray by computing exactly the channel response at $m+1 \ll Q$ frequency points.

A received signal $r(t)$ can be obtained by multiplying the channel response by

$S(\omega)$, the Fourier transform of the transmitted signal $s(t)$, and subsequently computing an Inverse Fourier transform,

$$r(t) = \mathcal{F}^{-1}\left(S\left(\omega\right)H\left(\omega\right)\right). \tag{4.8}$$

However, an alternative analytical approach is also possible that eliminates the need to perform this inverse Fourier transform. A time domain ray contribution can be computed using the polynomial approximation P_i and the free space term $e^{-\jmath\phi_i^d(\omega)}$. This approach exploits the following identities of Fourier transforms,

$$\mathcal{F}^{-1}\{(\jmath\omega)^g\, S(\omega)\} = \frac{d_g}{dt^g}s(t) \tag{4.9}$$

$$s(t-a) = \mathcal{F}^{-1}\{S(\omega)e^{-\jmath a\omega}\}. \tag{4.10}$$

The received time domain signal $r(t)$ can be considered as a sum of individual ray contributions $r_i(t)$ where,

$$r_i\left(t\right) \simeq \mathcal{F}^{-1}\left(S\left(\omega\right)P_i e^{-\jmath\phi_i^d(\omega)}\right). \tag{4.11}$$

By utilizing the identities of Equations (4.9) and (4.5) this time domain ray can be expressed as,

$$\begin{aligned} r_i(t) \;\simeq\;& \alpha_{0i}s\left(t-\frac{d_i}{c}\right) - \beta_{0i}s_H(t-\frac{d_i}{c}) \\ &+ \sum_{g=1,3,5\ldots}^{m-1} \jmath^{g-1}\left(\alpha_{gi}\frac{d_g}{dt^g}s_H(t-\frac{d_i}{c}) + \beta_{gi}\frac{d_g}{dt^g}s\left(t-\frac{d_i}{c}\right)\right) \\ &+ \sum_{g=2,4,6\ldots}^{m} \jmath^{g}\left(\alpha_{gi}\frac{d_g}{dt^g}s\left(t-\frac{d_i}{c}\right) - \beta_{gi}\frac{d_g}{dt^g}s_H(t-\frac{d_i}{c})\right), \end{aligned} \tag{4.12}$$

where

$$s_H(t) = \mathcal{F}^{-1}\{\mathcal{H}\{S(t)\}\}. \tag{4.13}$$

In this expression $\mathcal{H}$ represents the Hilbert transform while c is the speed of light in a vacuum and d_i is the propagation length of the ray. α_{gi} and β_{gi} are the respective real and imaginary parts of the g^{th} order coefficient of the poly-

nomial P_i of Equation (4.11) such that,

$$P_i(\omega) = \sum_{g=0}^{M} \left(\alpha_{gi} - \jmath\beta_{gi}\right) \omega^g, \tag{4.14}$$

where M is the highest order coefficient present within $P_i(\omega)$. Assuming a known set of waveforms for the transmitted signal $s(t)$, successive derivatives of both $s(t)$ and $S_H(t)$ can be computed prior to simulations. This leaves only the polynomial coefficients α_{gi} and β_{gi} and the ray path delays $\frac{d_i}{c}$ to be computed during runtime. Subsequently, the time domain received signal can be computed from ray contributions without the need to employ interpolation in the frequency domain. Also the inverse Fourier transform of Equation 4.9 is no longer necessary and this leaves only the polynomial coefficients α_{gi} and β_{gi} and the ray path delays $\frac{d_i}{c}$ to be computed during runtime[1]. Assuming a prior known set of transmitted waveforms for $s(t)$, this results in an efficient means of computing the time domain received signal $r(t)$ without the need to evaluate the polynomial $P_i(\omega)$ at each frequency or perform an inverse Fourier transform.

[1] A more detailed discussion of the use of the Hilbert transform in Equation 4.12 can be found in Appendix A.1

4.2.1 Frequency Dependency of Residual Term

In the previous section a slowly varying residual component $A_i(\omega)e^{-j\tilde{\Phi}_i(\omega)}$ was introduced. This component contains the frequency dependent effects that a propagated ray experiences due to its interactions with objects in the propagation environment. Specifically these events entail either reflection, transmission or diffraction. Recalling the discussion of wide-band scattering effects in Section 2.1.5 of Chapter 2, the frequency dependance of scattering coefficients can be attributed to frequency variations of the scattering object material properties, specifically the effective complex permittivity $\varepsilon(\omega)$. This permittivity is given by,

$$\varepsilon(\omega) = \varepsilon^{'}(\omega) - \jmath\varepsilon^{'}(\omega)\, p_e(\omega), \tag{4.15}$$

where

$$\varepsilon^{'}(\omega) = \varepsilon_r(\omega)\,\varepsilon_0. \tag{4.16}$$

In the above expressions, the free-space permittivity, dielectric constant and effective loss tangent are given by ε_0, $\varepsilon_r(\omega)$ and $p_e(\omega)$ respectively. Both the dielectric constant and loss tangent vary with frequency and differ for each material. In [38] a study of these variations was carried out using measurements of common indoor materials. The results of this study for concrete are incorporated into the UWB simulation presented in this chapter. This has resulted in more realistic values for the reflection, transmission and diffraction coefficients. Furthermore, this ensures that the frequency variation of these scattering coefficients are rigorously accounted for.

4.2.2 Implementation of Algorithm

The proposed algorithm is applied to each frequency domain ray individually. For the purposes of demonstrating the operation of this method, the electric field R_i associated with the i^{th} ray shown in Figure 4.1 will now be examined. This complex valued field can be divided into a magnitude and phase response that varies with frequency as in Figures 4.1(a)-4.1(b).

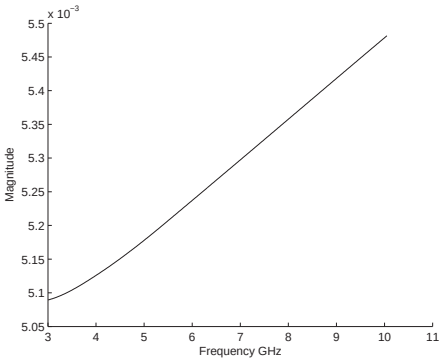

(a) Magnitude Frequency Response

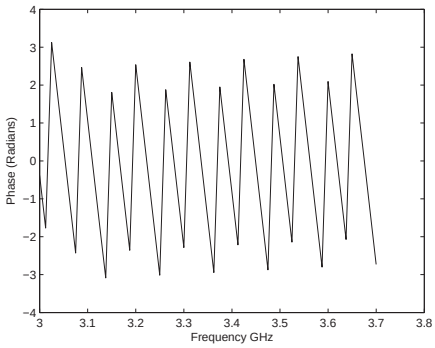

(b) Phase Frequency Response (700 MHz Section)

Figure 4.1: Frequency Response of a Ray

Considering Figure (4.1(b)) it is observed that the ray's phase varies extremely rapidly with frequency. At this stage it would be impossible to approximate this ray's frequency response with a low order polynomial. However, by dividing out the phase associated with the free-space propagation of the ray, ϕ_i^d, the residual component of Figure 4.2 remains. This phase of this component in Figure 4.2(b) varies much more slowly with frequency.

Consequently, this residual can be approximated accurately by a low order polynomial that requires only a reduced number of sample points to make the approximation for the complete bandwidth. Once the residual approximation has been obtained the phase effects from the propagation path length can be reintroduced by simply multiplying the approximated residual ray by $e^{-\jmath\phi_i^d(\omega)}$. This produces a satisfactory approximation to the original ray frequency response with minimal errors as illustrated by Figure 4.3 [2]. Furthermore, a time domain received signal can be generated using the analytic technique of Equation 4.12. Prior knowledge of the transmitted pulse $s(t)$ is prerequisite for this approach. Nevertheless, it offers a convenient means of computing the received signal without the need to evaluate the response of a residual at each

frequency domain sample.

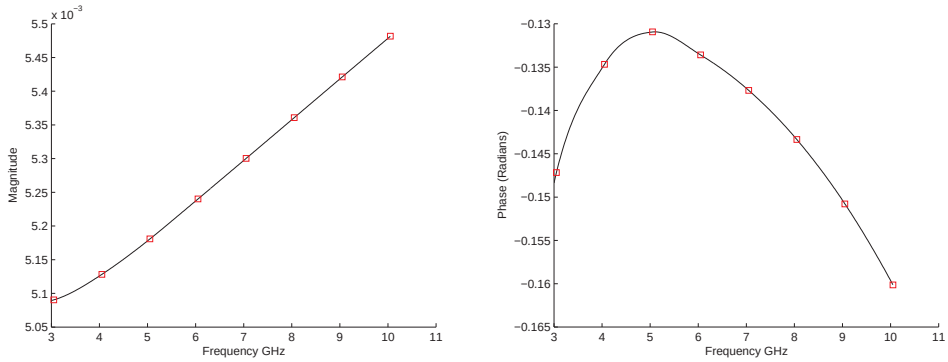

(a) Magnitude Frequency Response (b) Phase Frequency Response

Figure 4.2: Residual Ray Frequency Response

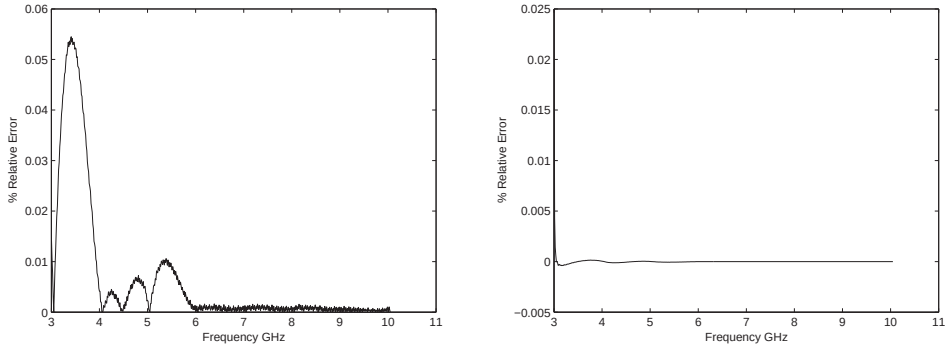

(a) Magnitude Error (Absolute) (b) Phase Error (Absolute)

Figure 4.3: Approximation Error

[2]The error is computed as $R_i(\omega) - R_i^{acc}(\omega)$ where $R_i(\omega)$ is the frequency domain ray response computed using the full frequency sweep simulation and $R_i^{acc}(\omega)$ is obtained using the acceleration technique.

A summary of the steps involved in applying the acceleration technique to a ray are shown in Figure 4.4. It is assumed that the ray lengths are available from the ray tracing simulator in order to compute the phase $e^{-J\phi_i^d}$ due to free space propagation. Also, the ray tracing simulator is configured such that individual ray responses are available. The simulator computes a field associated with this ray for a reduced set of frequency points. Following the removal of the free space component from the reduced ray response, a polynomial is fitted to the resultant residual. The polynomial $P_i(\omega)$ is of an order never greater than m where the reduced ray is specified at $m+1$ frequency sample points. However, from observing simulation results, in practice it is not necessary for the polynomial $P_i(\omega)$ to contain higher than 10^{th} order coefficients. Using the known transmitted signal $s(t)$ and it corresponding Hilbert transform $\mathcal{H}\{s(t)\}$ the time domain ray contribution $r_i(t)$ is computed from the coefficients of the polynomial $P_i(\omega)$. Finally, in order to obtain the complete multi-path received signal $r(t)$, each of the time domain ray contributions $r_i(t)$ are summed.

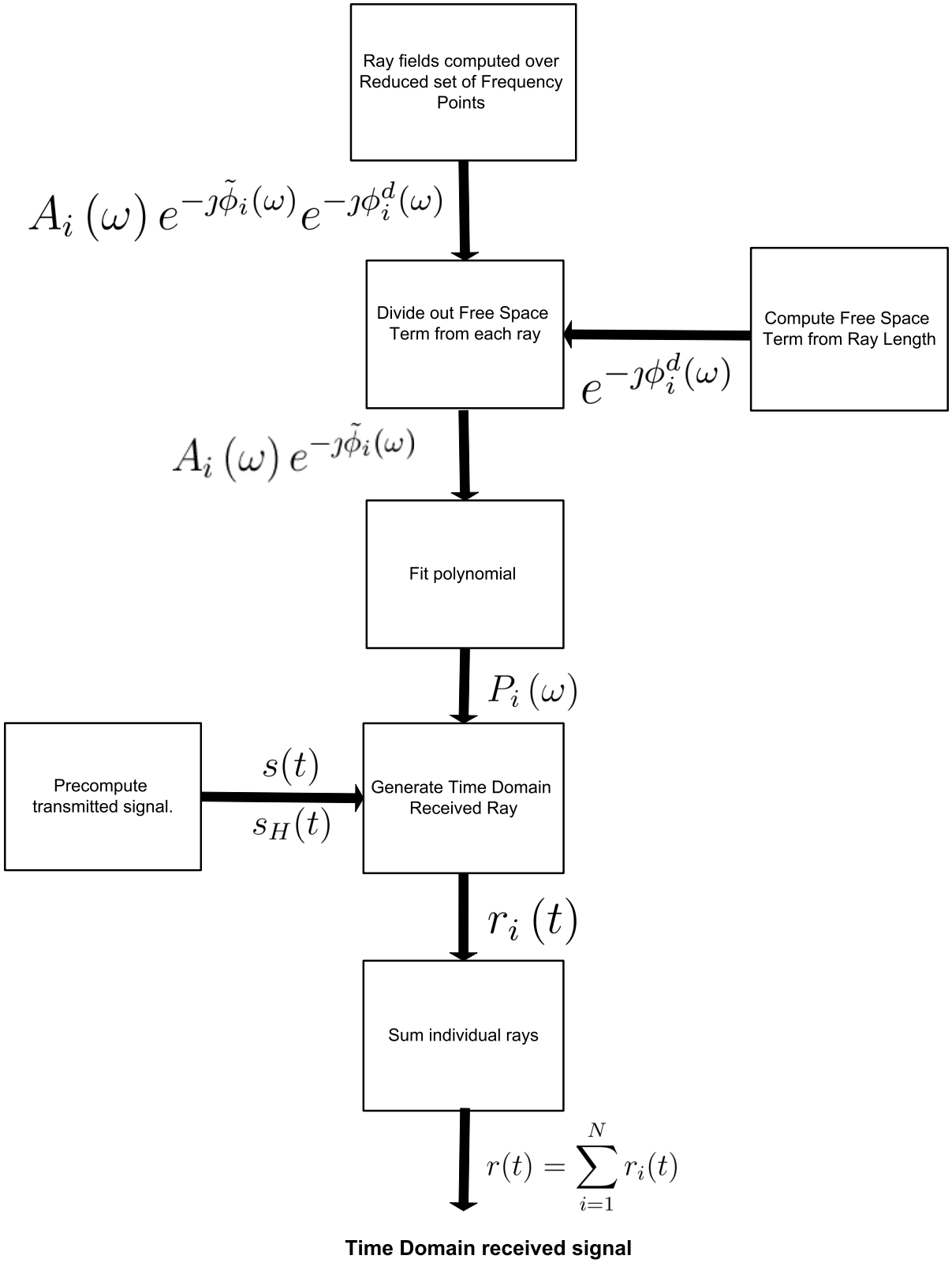

Figure 4.4: Summary of Frequency Acceleration Algorithm

4.3 Results

For the purposes of evaluating the accuracy and efficiency of the algorithm a ray tracing simulation was computed for the building environments of Figures 4.8 and 4.17. The facets of these building were modelled using the material properties of concrete shown in Figure 4.6 as obtained through the experimental measurements of Muqaibel in [38]. The transmitted signal consisted of a Gaussian mono-cycle pulse, shown in Figures 4.5(a) and 4.5(b) which is expressed in the time domain as,

$$s(t) = \left[1 - 4\pi\left(\frac{t}{t_n}\right)^2\right] \exp\left(-2\pi\left(\frac{t}{t_n}\right)^2\right), \tag{4.17}$$

where t_n is a scaling factor that determines the bandwidth of the pulse and in this simulation $t_n = 0.520$ nanoseconds.

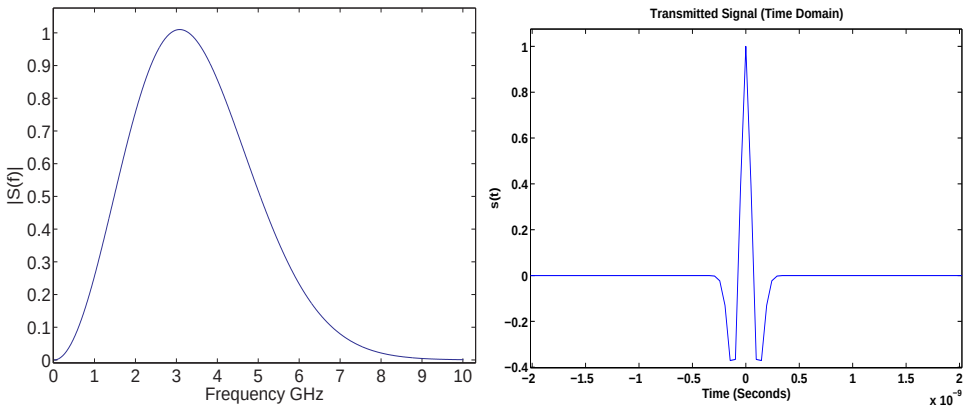

(a) Frequency Response of Gaussian Doublet Pulse

(b) Gaussian Doublet Pulse in time domain

Figure 4.5: Gaussian Doublet UWB Pulse

A series of accelerated ray tracing simulations were carried out using differing numbers of reduced frequency samples for each propagation environment. These accelerated simulation were compared with an un-accelerated simulation consisting of 801 frequency points each separated by 12.5 MHz spanning from 0 to 10 GHz. Each ray was constrained to include no higher than 1^{st} order reflection effects (See Section 2.1.4 Chapter 2 for explanation of reflection orders). Using the un-accelerated simulation as a reference the time saving and percentage error incurred when computing the time domain received signals will be presented later in Sections 4.3.1 and 4.3.2.

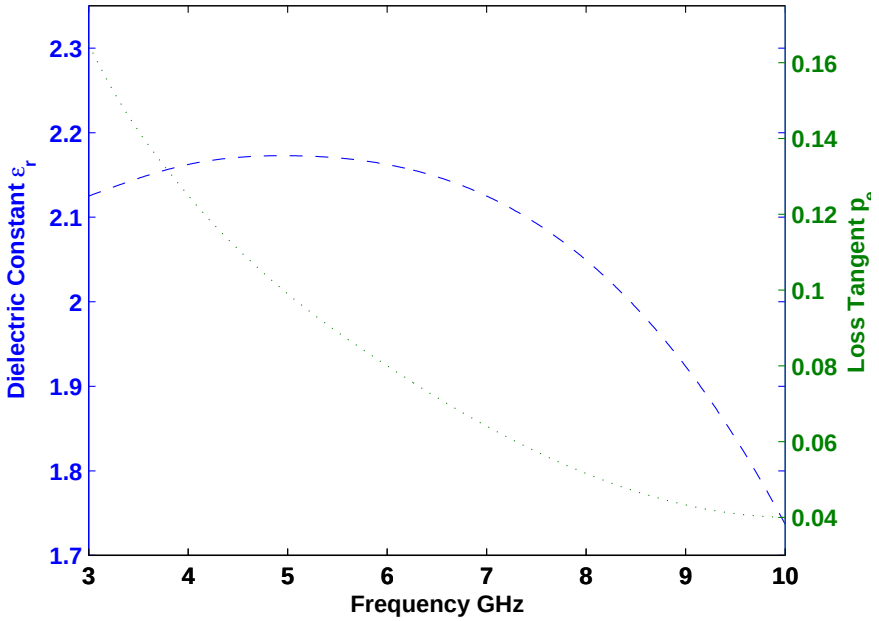

Figure 4.6: Variation of Permittivity of concrete Dashed Line: Dielectric Constant Dotted Line Loss Tangent

4.3.1 Simulation containing Reflections and Diffractions

The initial simulation entailed propagation in an environment containing only reflection and diffraction effects. In this scenario the transmitter and receiver have a direct unobscured line of sight (LOS) path between them. This path along with the reflected and diffracted multi-paths are shown in the propagation environments of Figures 4.7-4.8.

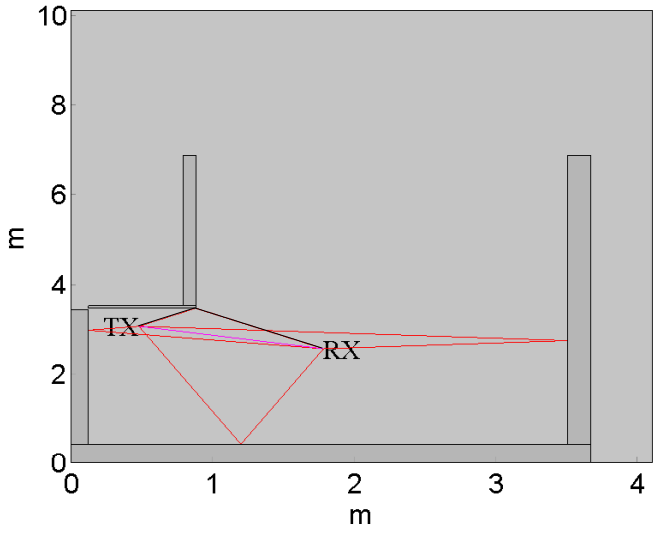

Figure 4.7: Plan View of Building Environment containing Diffraction Edge

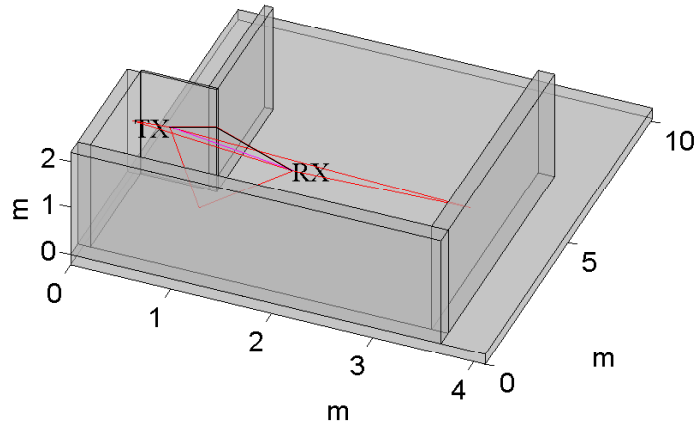

Figure 4.8: 3*D* View of Building Environment containing Diffraction Edge

In Figure 4.9 the time domain received time domain signals computed by the respective un-accelerated and accelerated simulations are shown. Using 11 frequency samples for the accelerated simulation a good agreement is observed between the received signals from the accelerated and un-accelerated simulations. However, in Figure 4.10, reducing the number of frequency samples to 3 leads to greater discrepancies between the received waveforms. Figures 4.11-4.15 show these discrepancies in the form of a relative error[3]for each configuration of the acceleration technique using differing number of reduced frequency domain samples. It should be noted that error values corresponding to where the received signal is less than 1% of maximum are disregarded as such amplitudes could not be expected in a "real-world" scenario to exceed the noise floor. Assuming a regulatory transmission limit of -41.3 dBm [48] and a receiver noise figure in the region of 6 dB [71], 1% of the maximum received signal will not exceed a noise floor of -87.4 dBm [16]. These errors percentages along with the corresponding reduction in simulation times are tabulated in Table 4.3.1. While, as expected, reducing the number of frequency samples lead to shorter simulation times, the accuracy was also adversely affected by such reductions. This problem can be observed in Table 4.3.1 where less than 6 samples resulted in maximum errors exceeding 16%. Fortunately more tolerable errors of below 3.5% were achieved when the number of frequency points was increased to 41, 21 and 11 samples. Employing the accelerated algorithm with such configurations resulted in simulation time savings in the order of 25%.

[3]This error is computed as $e_r(t) = 100\left(\frac{|r_a(t)-r_u(t)|}{|r_u(t)|}\right)$ where $r_u(t)$ and $r_a(t)$ are the received time domain signals computed using the respective un-accelerated and accelerated simulations

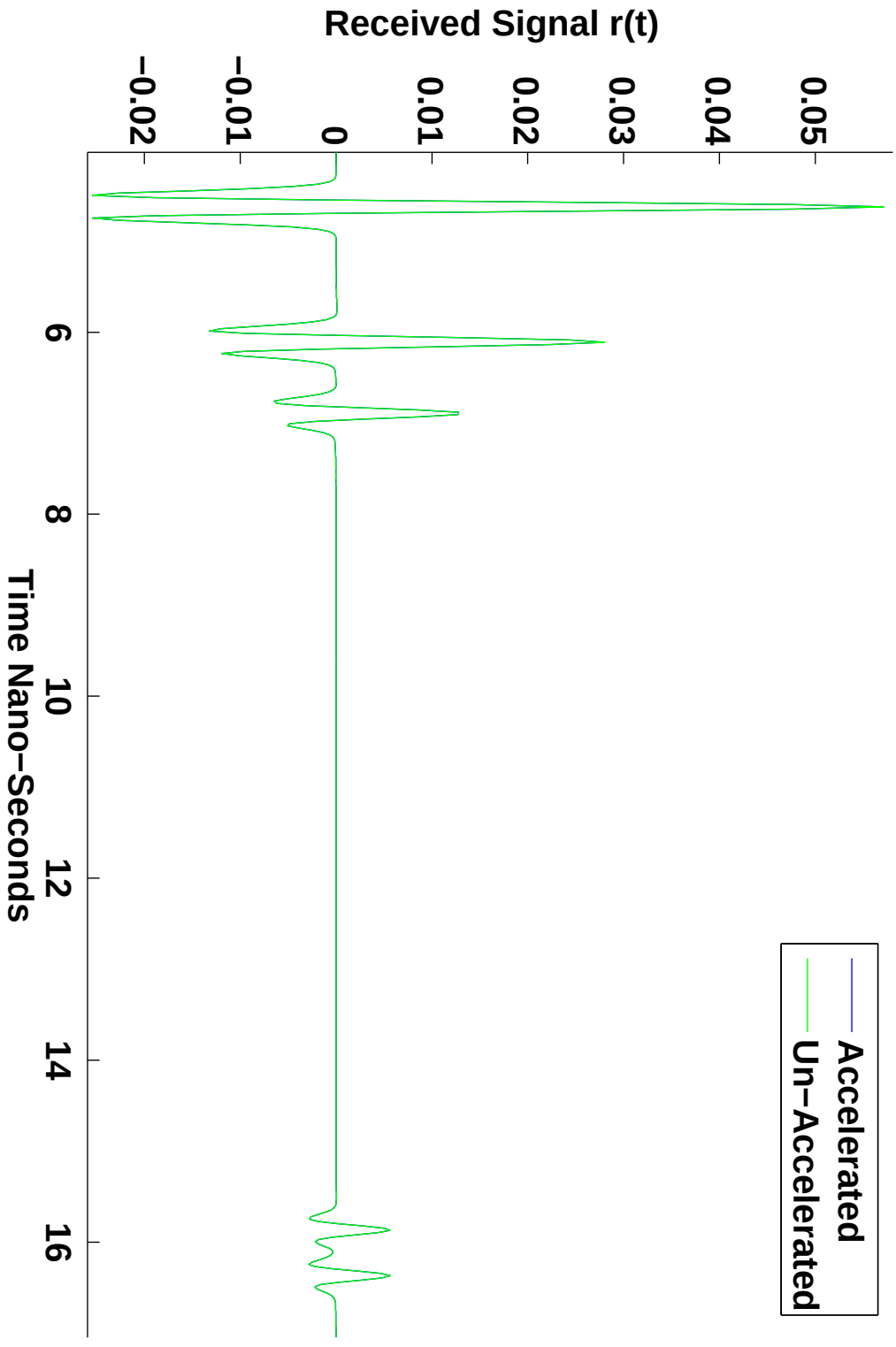

Figure 4.9: Received Signal Un-Accelerated and Accelerated using 11 Frequency Samples

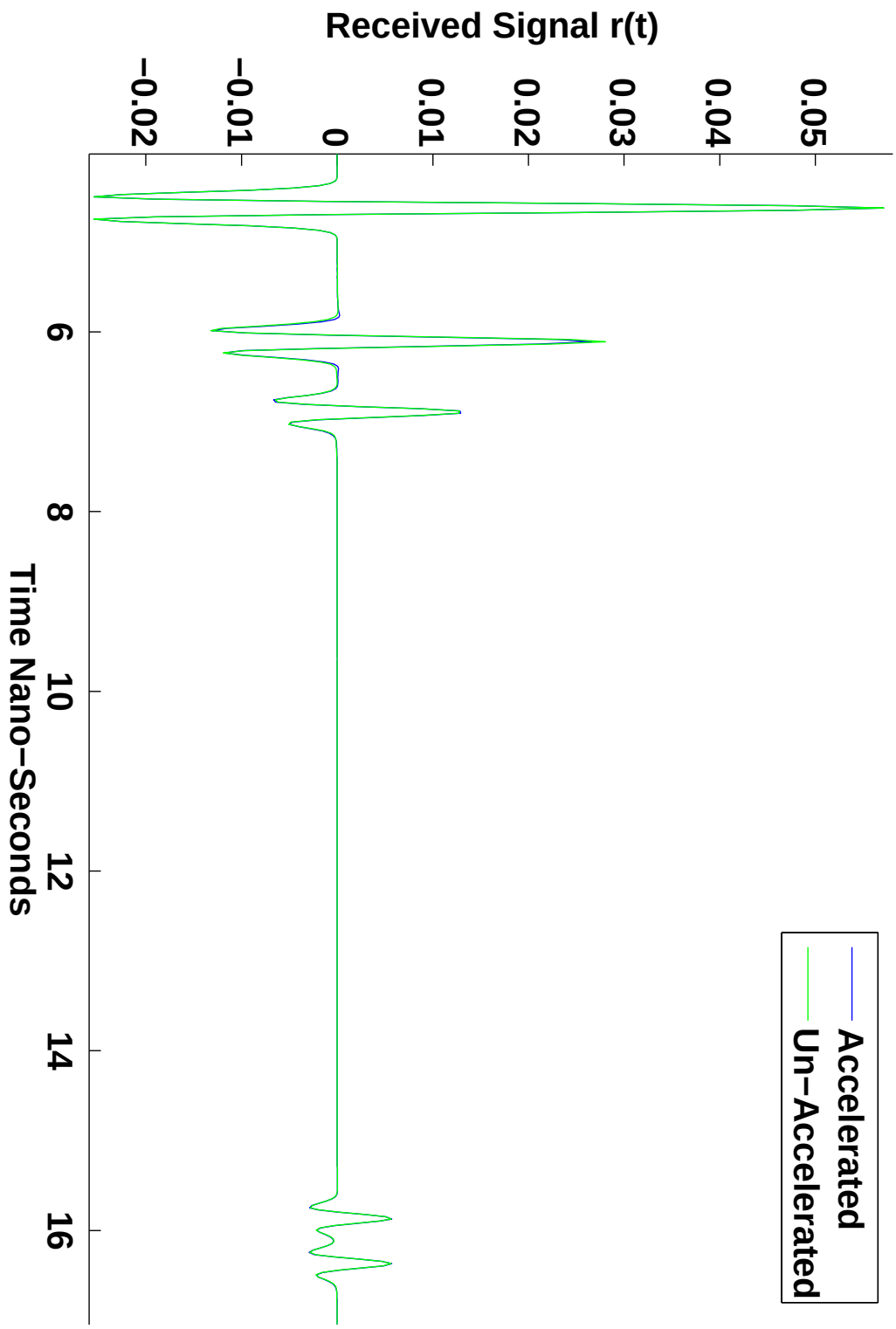

Figure 4.10: Received Signal Un-Accelerated and Accelerated using 3 Frequency Samples

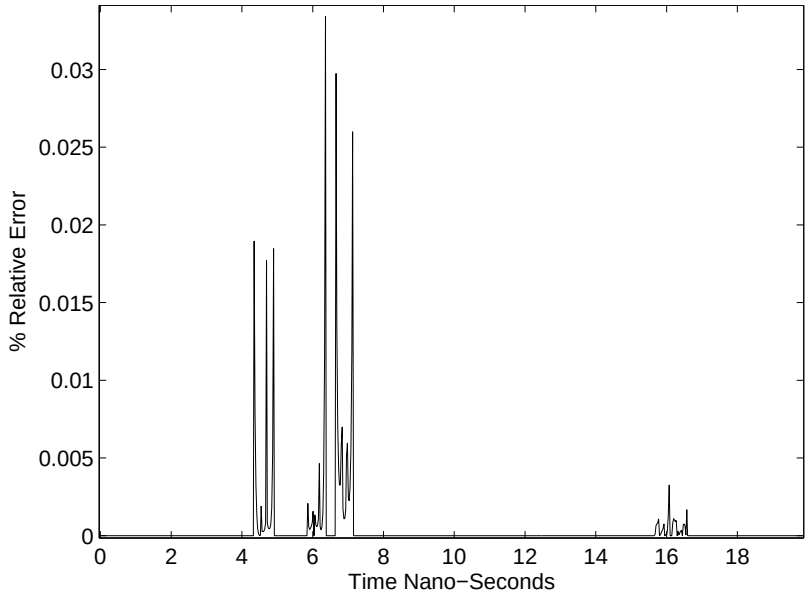

Figure 4.11: Time Domain Error using 41 Frequency Samples

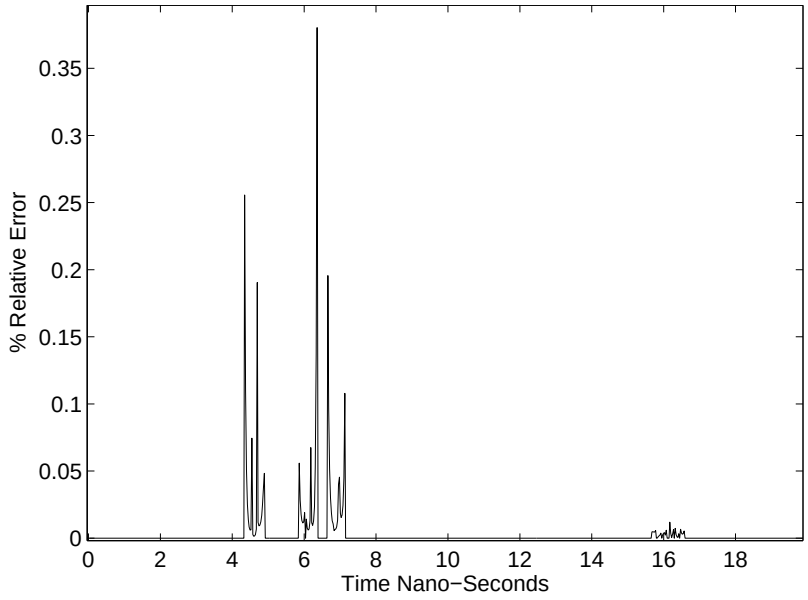

Figure 4.12: Time Domain Error using 21 Frequency Samples

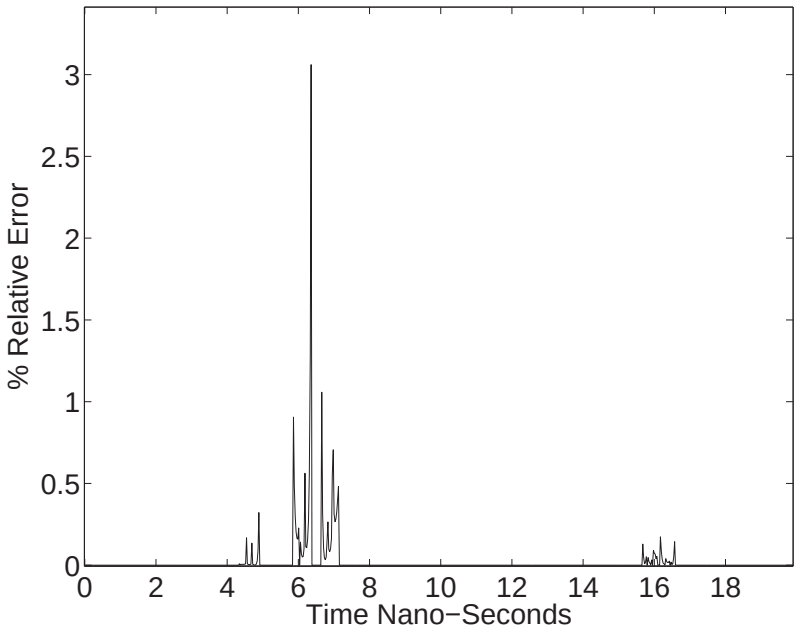

Figure 4.13: Time Domain Error using 11 Frequency Samples

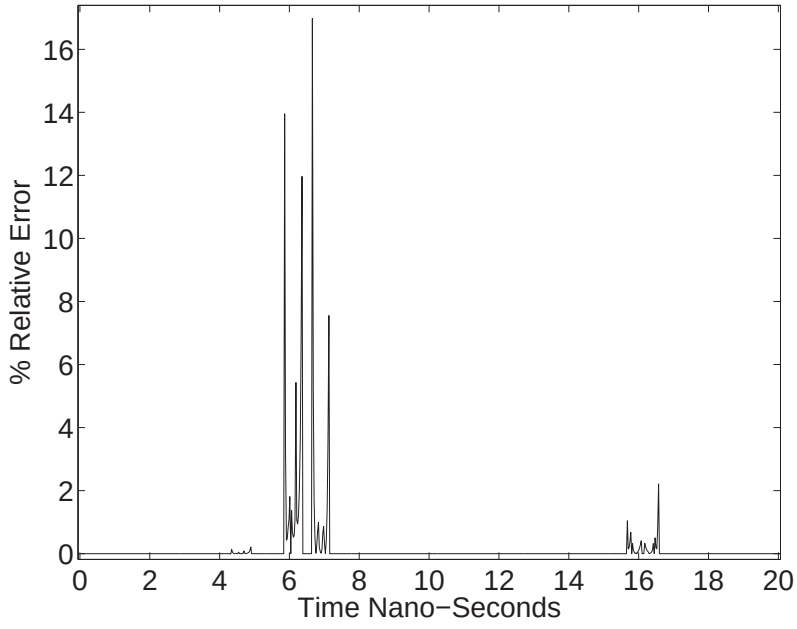

Figure 4.14: Time Domain Error using 6 Frequency Samples

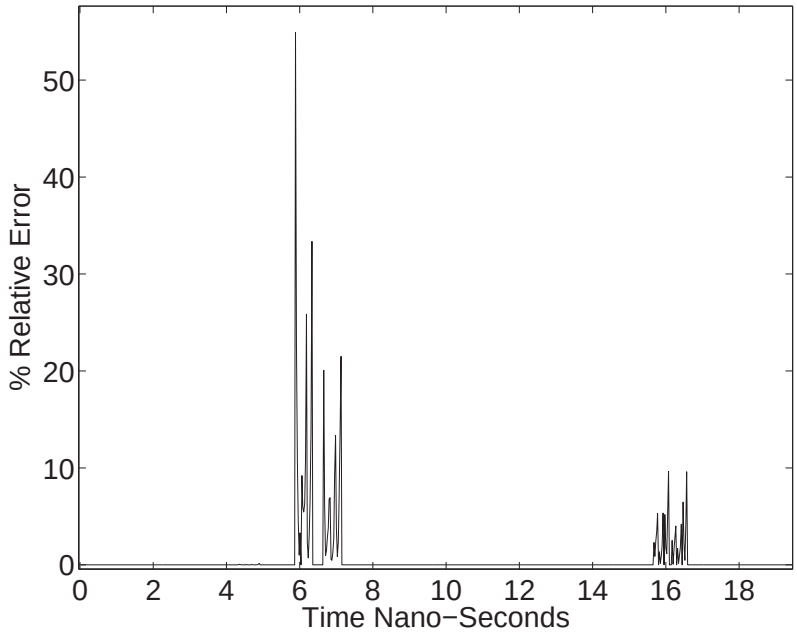

Figure 4.15: Time Domain Error using 3 Frequency Samples

Step Size	Number of Samples	Max % Error	Execution Time	Time Saving (Secs)	% Time Saving (Secs)
20	41	0.03	1.534	0.512	25.02
40	21	0.38	1.503	0.543	26.54
80	11	3.07	1.471	0.575	28.10
100	9	3.33	1.471	0.575	28.10
160	6	16.98	1.456	0.590	28.84
400	3	54.01	1.44	0.606	29.62

Table 4.1: Percentage Time Saving and Relative error using Accelerated Ray Tracing (Reflections and Diffractions only)

4.3.2 Simulations containing Transmissions

In order to evaluate the acceleration algorithm for rays that undergo transmission through walls, a simulation was carried out using the environment of Figures 4.16-4.17. A prominent characteristic of this structure is that a wall separates the transmitter and receiver locations resulting in every ray experiencing transmission effects. As in the previous simulation the acceleration algorithm was applied using different numbers of frequency samples. Figure 4.18 shows the computed received signal for both the un-accelerated and an accelerated simulation applied with 11 frequency samples. The poor performance of an alternative simulation configuration using only 6 samples can be seen in Figure 4.19 where a larger discrepancy occurs between accelerated and un-accelerated computations. The relative time domain errors associated with using a different number of samples are plotted in Figures 4.20-4.24. These errors are calculated as the relative percentage difference between the un-accelerated computed received waveform (using 801 frequency samples) and the results of accelerated simulations using 41, 21, 11, 9, 6 and 3 samples respectively. Observing Table 4.3.2 time savings in the order of 30% were achieved using 21 frequency samples while enduring a relative error of only 4.28%. Additionally, increasing the number of samples to 41 resulted in a lower maximum error of 0.38%. However, reductions to 11 samples resulted in excessive errors that exceed 30%. Consequently, the use of 21 samples with the acceleration algorithm can be considered as an ideal compromise between time savings and accuracy.

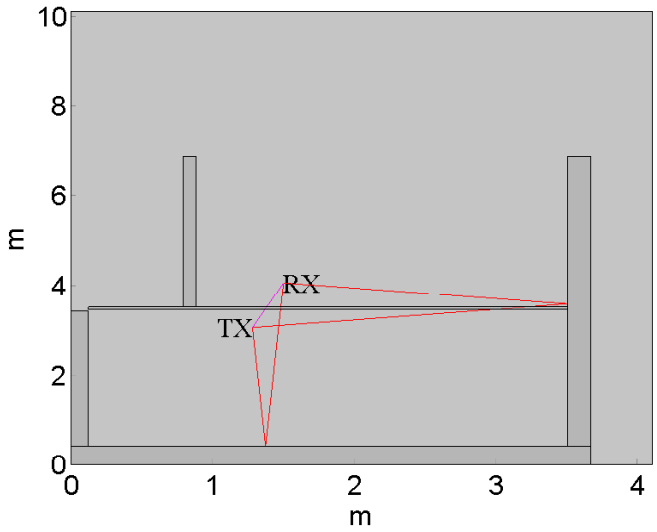

Figure 4.16: Plan View of Building Environment containing Centre Wall

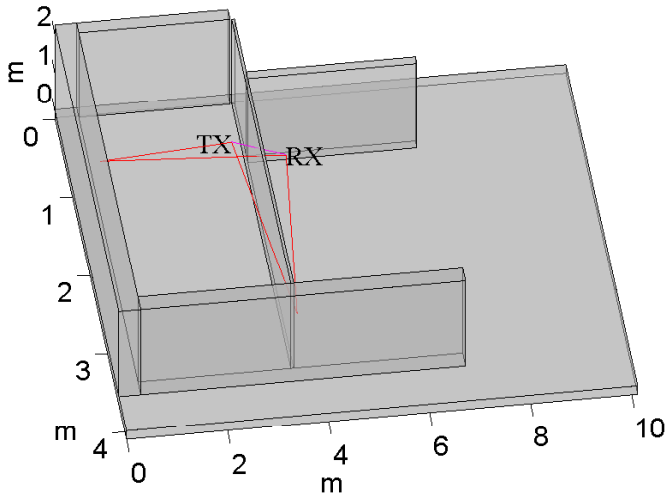

Figure 4.17: 3*D* View of Building Environment containing Centre Wall

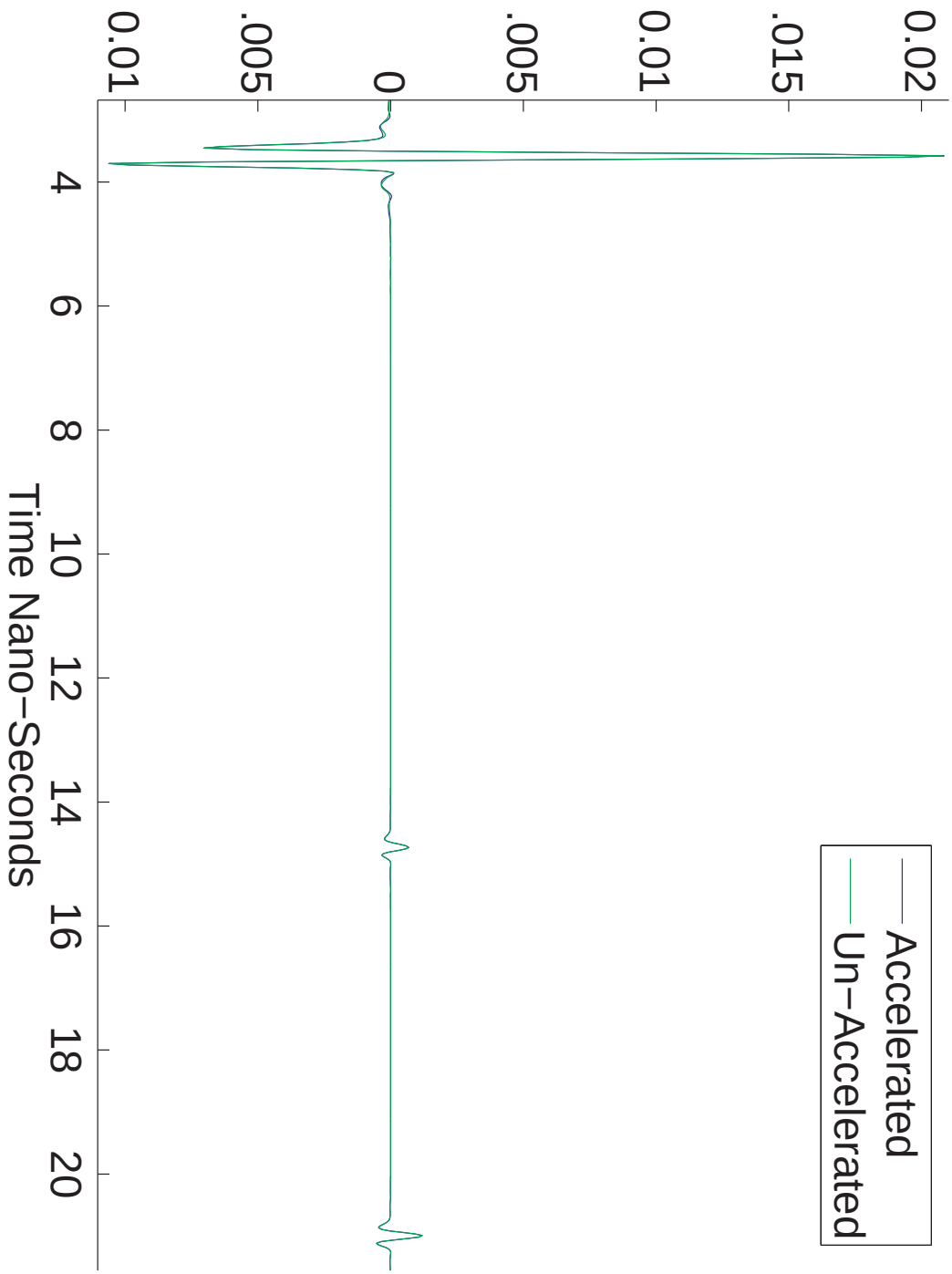

Figure 4.18: Received Signal Un-Accelerated and Accelerated using 11 Frequency Samples

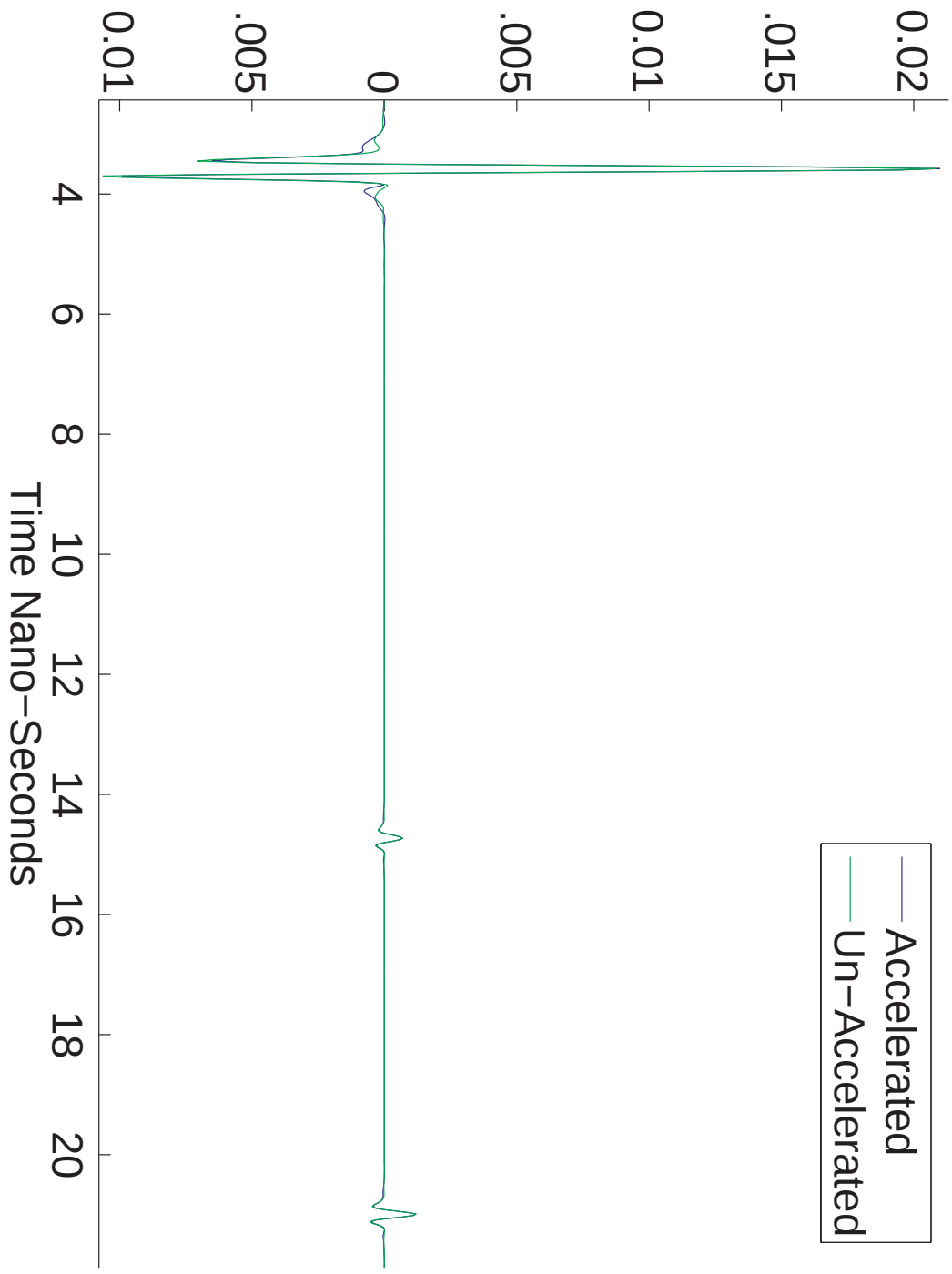

Figure 4.19: Received Signal Un-Accelerated and Accelerated using 6 Frequency Samples

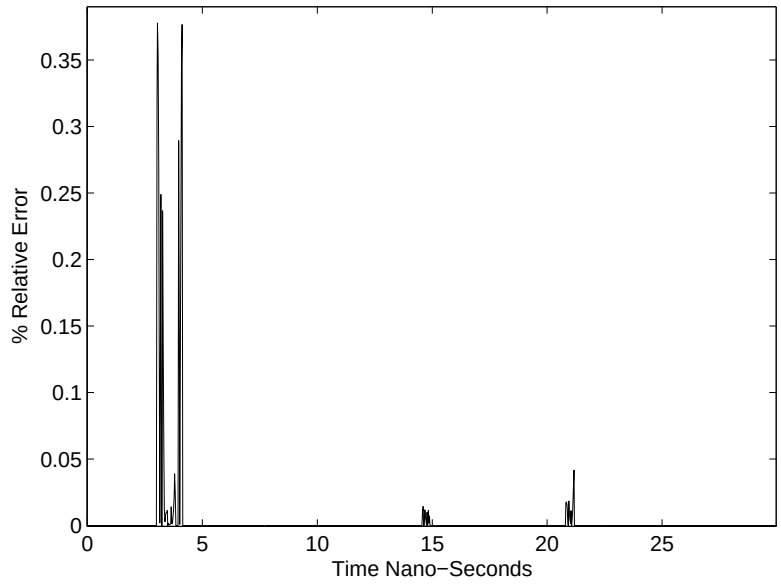

Figure 4.20: Time Domain Error using 41 Frequency Samples

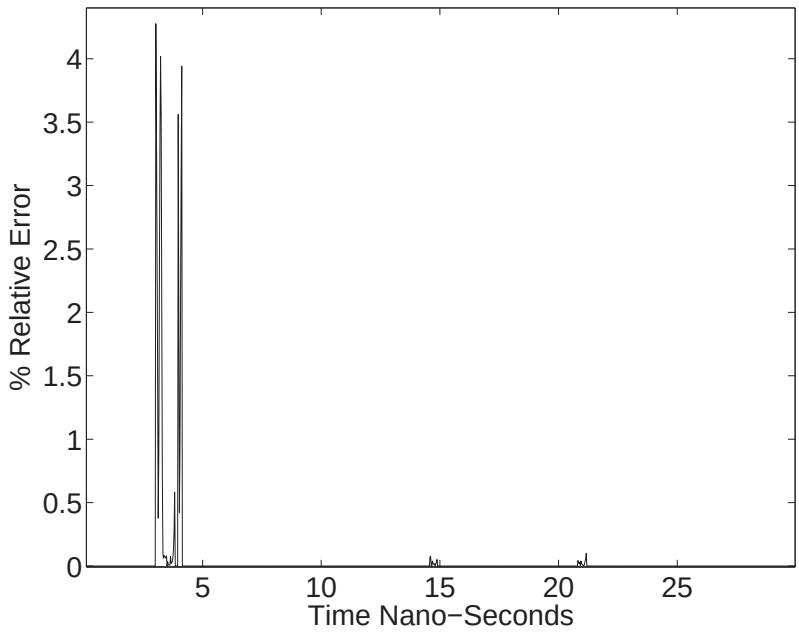

Figure 4.21: Time Domain Error using 21 Frequency Samples

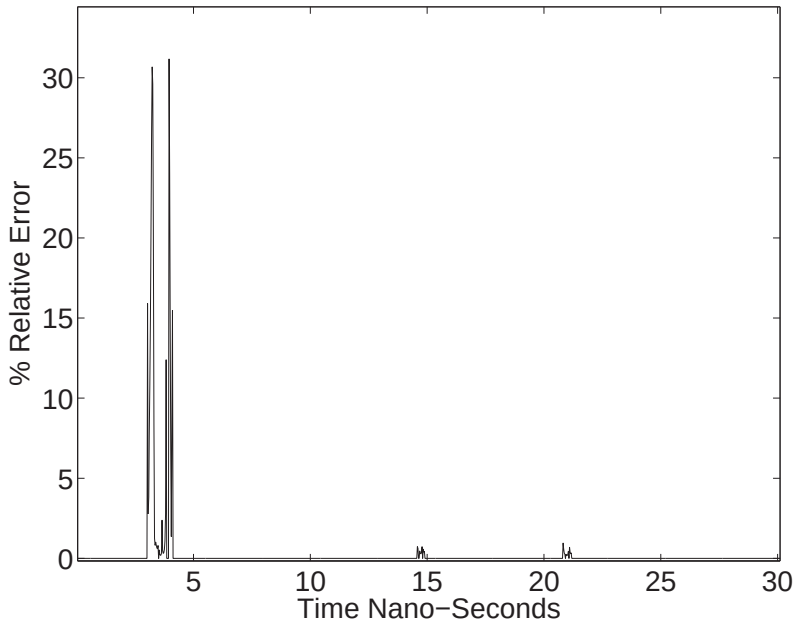

Figure 4.22: Time Domain Error using 11 Frequency Samples

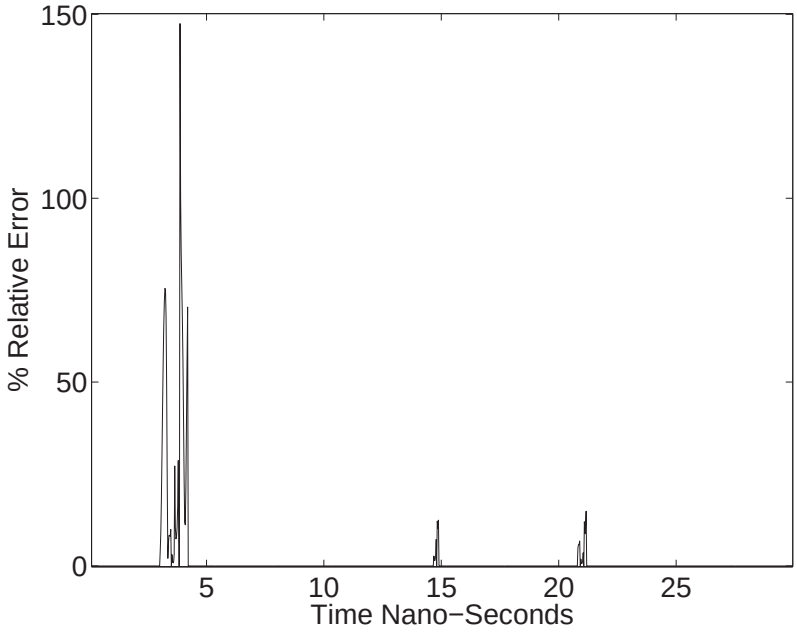

Figure 4.23: Time Domain Error using 6 Frequency Samples

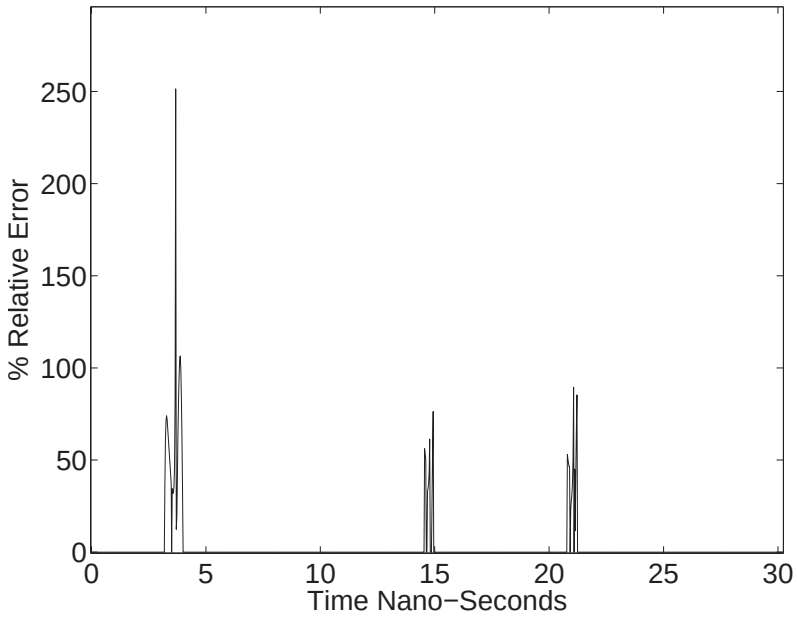

Figure 4.24: Time Domain Error using 3 Frequency Samples

Step Size	Number of Samples	Max % Error	Execution Time	Time Saving (Secs)	% Time Saving (Secs)
1	801	NA	2.188	NA	NA
20	41	0.38	1.550	0.638	29.16
40	21	4.28	1.518	0.670	30.62
80	11	31.17	1.503	0.685	31.31
100	9	74.78	1.487	0.701	32.04
160	6	147.00	1.471	0.717	32.77
400	3	250.00	1.456	0.732	33.46

Table 4.2: Percentage Time Saving and Relative error using Accelerated Ray Tracing (Including Transmissions)

By comparing Table 4.3.2 above with the results of simulation containing only diffractions and reflections in Table 4.3.1, it is noted that the presence of transmissions results in errors that grow more rapidly as the number of frequency samples are reduced. As an example 11 samples yielded an error of 3.07% in Table 4.3.1 when diffraction and reflection were modelled in simulation while the same configuration resulted in errors exceeding 30% when modelling transmissions in Table 4.3.2. This is a result of transmissions scattering experiencing more fluctuations with frequency (as seen previously in Sections 2.1.5.1-2.1.5.2 of Chapter 2) and as a consequence requiring a greater number of frequency samples for an accurate application of the acceleration technique.

4.4 Conclusion

In this chapter a novel frequency domain ray tracing acceleration algorithm was presented. This technique reduced the computational expense associated with simulating wide-band channels while preserving the ability to account for frequency dependent effects. Also an alternative means of obtaining the time domain received signal was introduced that eliminates the need for interpolation of frequency domain samples and a subsequent inverse Fourier transform to the time domain. The performance of the acceleration algorithm was appraised using simulations which incorporated empirical material properties that vary with frequency. Applying the frequency sweep acceleration technique to such simulations resulted in a reduction of simulation times in the order of 30% while errors of less than 4.5% in the time domain were achieved. This reduction in frequency samples should be considered in the context of the un-accelerated ray tracing simulations using 801 samples. Furthermore, for simulation where transmissions were not present, a greater reduction in frequency samples point was observed. In such scenarios the accelerated simulation used 9 samples while achieving an error of less than 3.5%. However, for the case of a practical implementation of the acceleration algorithm in a propagation simulator, transmissions must be considered as likely scattering events.

Chapter 5

Client Geographical Position Estimation

Since the emergence of modern wireless communications networks, there has been a growing interest in geo-location. In particular, the prospect of position location capabilities in indoor environment has lead to speculation of various possible future applications such as logistical tracking in warehouses, coordination of rescue services and medical patient tracking amongst others [11]. This work focusses on a short range indoor based geo-location solution that relies on Ultra Wide-Band(UWB) signal propagation. Specifically, in what follows, refinements to Time Difference of Arrival (TDOA) based techniques are presented which deliver reduced infrastructure and computational requirements when deploying geo-location in indoor environments.

In this chapter two novel approaches to time difference of arrival (TDOA) based geo-positioning using Ultra-Wideband (UWB) signal propagation are developed. Accordingly, the discussion herein is composed of two separate but complementary topics:

- Initially in Section 5.2, a geo-location scheme which incorporates information from reflections is outlined. This approach allows for a receiver's position to be obtained using fewer fixed reference base-stations than existing TDOA schemes [10, 19, 18]. This technique involves measuring the time difference between an initial direct line of sight and a scattered pulse received at a mobile client station. By employing image theory, which was introduced earlier in Section 2.1.4 of Chapter 2, reflections from permanent scattering objects can be considered as predictable propagation phenomena. By using such reflections as additional geo-location references, fewer base-stations are required when predicting the physical position of a mobile station.

- In addition to developing a geo-location scheme that operates using reduced infrastructure, this work is also concerned with alleviating the computational cost associated with such techniques. Reflection based TDOA geo-location relies on the ability to compute the time difference of arrival between two consecutive received pulses. To date the most efficient means of carrying out such an operation has been to use auto-correlation based on Fast Fourier Transforms (FFT) [23]. However, in Section 5.4 an alternative approach is developed, which reduces the overall computational cost of obtaining TDOA measurements.

Finally, in Section 5.6 the reflection based TDOA scheme is integrated with the accelerated auto-correlation technique and their combined operation demonstrated using ray-tracing simulations of an indoor propagation environment. Subsequent results demonstrating the accuracy of employing these novel approaches in combination are presented.

5.1 Conventional TDOA Geo-Positioning

For conventional UWB Time Difference of Arrival (TDOA) based geo-location systems the position of a client is estimated by using at least three fixed reference base stations [10, 19, 18]. The client consists of a mobile transmitting station that broadcasts simultaneously to all base-stations. In the case of ultra-wideband systems this transmission consists of a narrow time domain pulse which allows for high resolution position estimation in time based systems. By obtaining the time difference between the arrival (TDOA) of such a pulse at two fixed base-stations, a hyperbola of possible location points on which the mobile client's physical position lies is generated. The client's exact location corresponds to the intersection of several hyperbolic curves[1]generated from different base-station pairs such as in Figure 5.1.

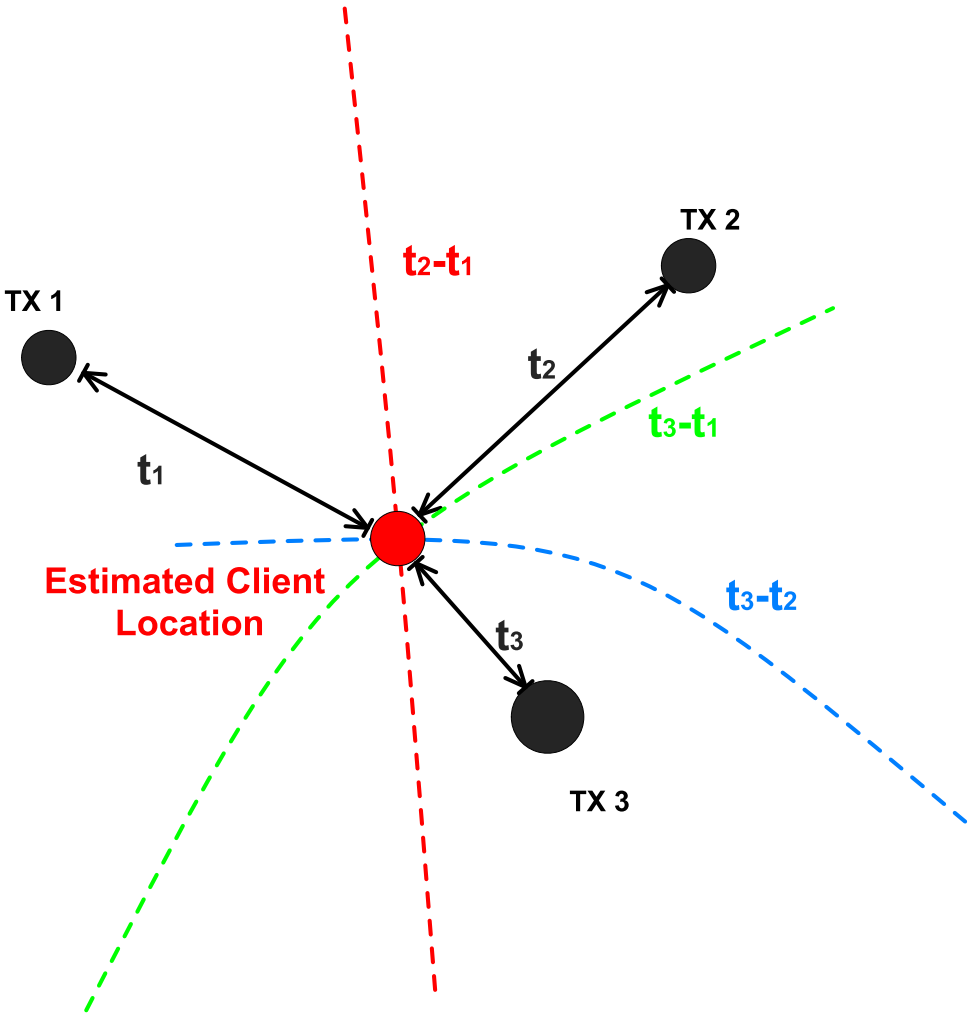

Figure 5.1: Classical TDOA based positioning using 3 Fixed Base Stations

In order to generate the two or more hyperbolae necessary to compute this intersection a minimum of three fixed base stations are required. For the purpose of measuring the time difference of arrival, synchronisation is required between base-station pairs and this usually entails wired communications between fixed base-stations as in Figure 5.2.

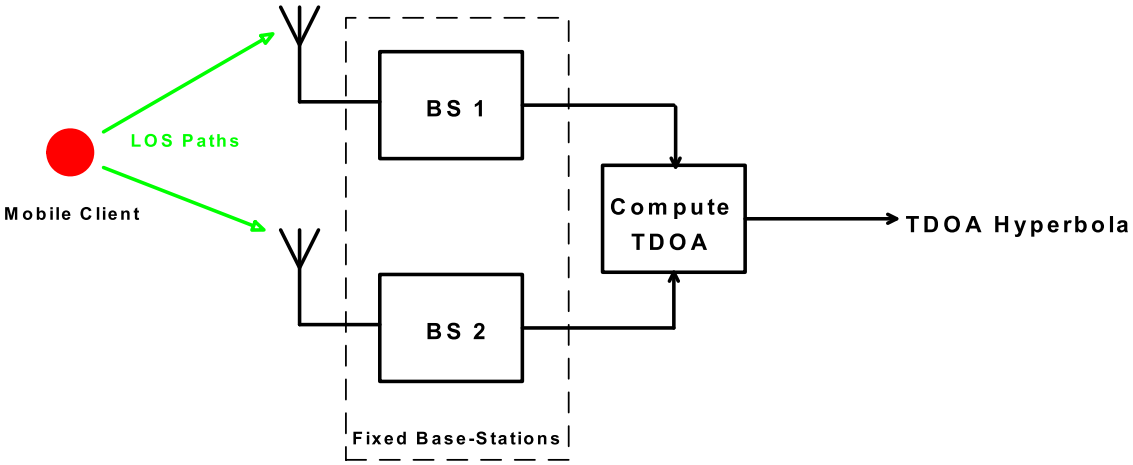

Figure 5.2: TDOA using Fixed Base-station

[1]In this work it is assumed that mobile stations are located at a uniform fixed height. Resultant geo-location solutions corresponds to the intersection of $2D$ hyperbolic curves (See Appendix B.1). In scenarios where height is variable a mobile client's location is computed as the intersection between several $3D$ hyperbolic surfaces.

5.2 Reflection Based TDOA

The aforementioned conventional TDOA techniques rely solely on direct line of sight (LOS) propagation paths between the mobile client and each fixed base station. However, in the case of indoor wireless channels, several additional multi-paths between a transmitter and receiver exist due to scattering effects from objects in the environment. Some of these scattering effects are attributable to reflections of RF energy from fixed objects, such as walls. Owing to the permanence of such objects resultant reflections are predictable. Previously in Section 2.1.4 of Chapter 2, image theory was introduced as a means of predicting the reflected ray trajectories from a flat surface. In what follows, for the purpose of explanation the mobile client is designated the role of a receiver while the base-stations are considered to be transmitting units. It should be noted that this configuration is the reverse of that for conventional TDOA as presented previously in Figure 5.2. By creating an image of a transmitter's location, a reflection path and corresponding reflection point can be computed. In addition, the total propagation length of a reflected multi-path is calculable as being equivalent to the distance between the image point and receiver/mobile client as shown in Figure 5.3.

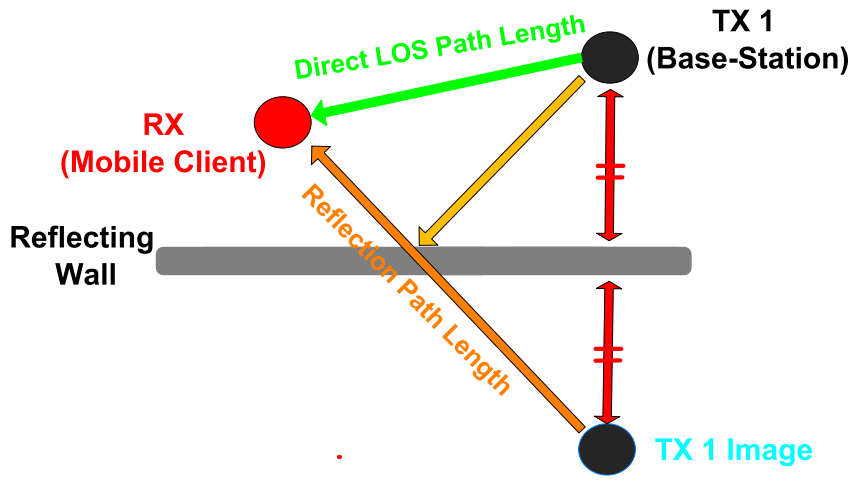

Figure 5.3: Calculating Reflections using Images

In the case of reflections from a flat surface, the image of the transmitter can be considered as an additional virtual transmitter source. For a fixed surface in a propagation environment this virtual transmitter point is constantly present at a fixed physical position. Consequently, such image points can be used in conjunction with an original transmitter source for the purpose of computing a hyperbolic curve of possible client locations. In the proposed scheme the time difference of arrival of a direct LOS path and reflected path between a fixed base-station and mobile client is measured. This approach has the advantage of requiring only a single fixed base-station in order to generate a hyperbola corresponding to possible client locations as shown in Figure 5.4.
Employing a second base-station in a room enables an additional hyperbola of possible client locations to be generated using this technique. Assuming a fixed constant height, the mobile client's exact location can then be found as the intersection of two such hyperbolae as in Figure 5.5.

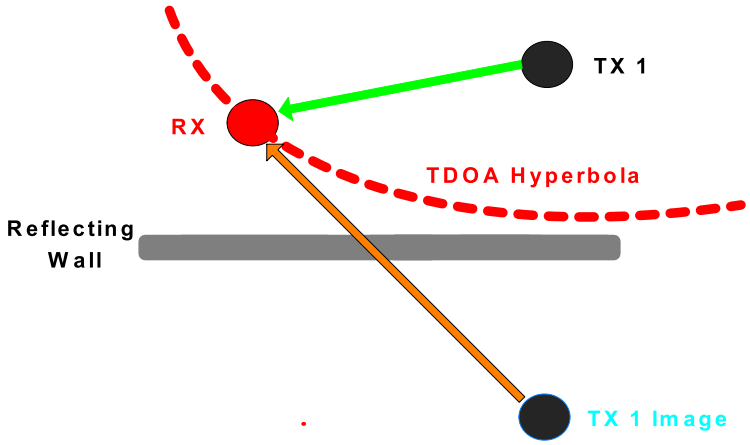

Figure 5.4: Using Images as Additional Virtual Transmitters/Base-stations

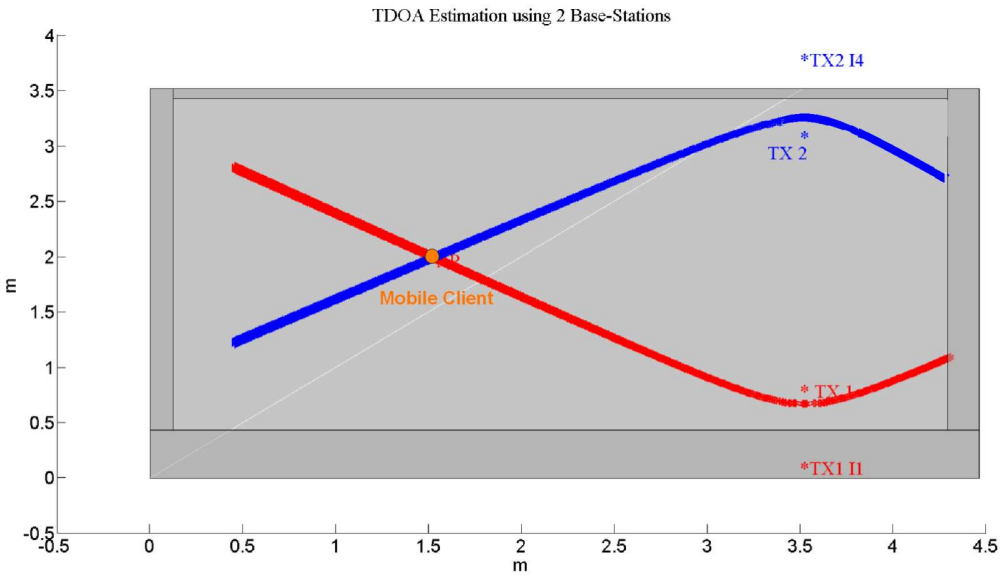

Figure 5.5: Location using Reflection TDOA

5.2.1 Configuration and Limitations of Reflection based TDOA

For the purposes of demonstrating the proposed reflection based TDOA position algorithm, a ray tracing simulated propagation environment (Figures 5.7-5.8) was created which represents a typical rectangular shaped room. This room consists of four vertical walls and a floor all having the material properties of concrete previously discussed in Section 2.1.5 of Chapter 2. It should be noted that a ceiling facet was omitted in these simulations. Two base-stations $TX1$ and $TX2$ are present within the structure and in turn individually transmit an UWB pulse that is received by the mobile client as depicted in Figure 5.15. The UWB pulse transmitted from a base-station results in a multi-path signal being received at the client which is comprised of a LOS component and several multi-path components as shown in Figure 5.6. In the simulations used for this work the transmitted pulse consisted of a Gaussian mono-cycle waveform whose time and frequency domain characteristics are shown in Figures 5.9-5.10.

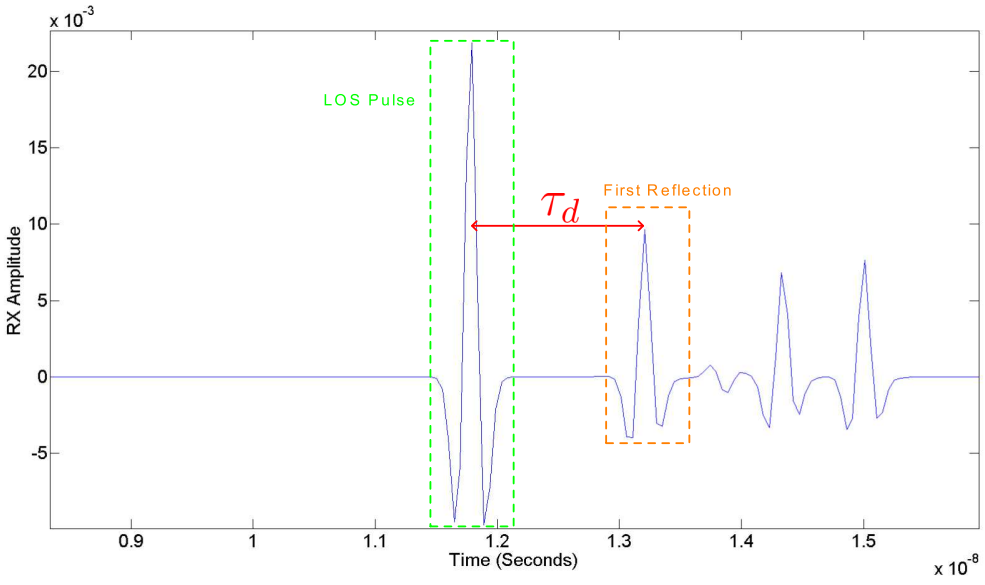

Figure 5.6: TDOA between Direct and Reflected Received Pulses

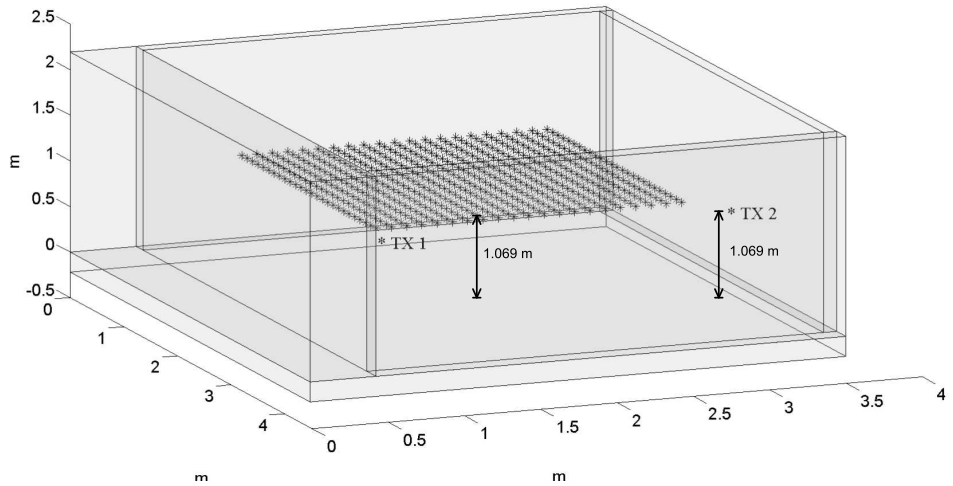

Figure 5.7: 3*D* View of Propagation Environment

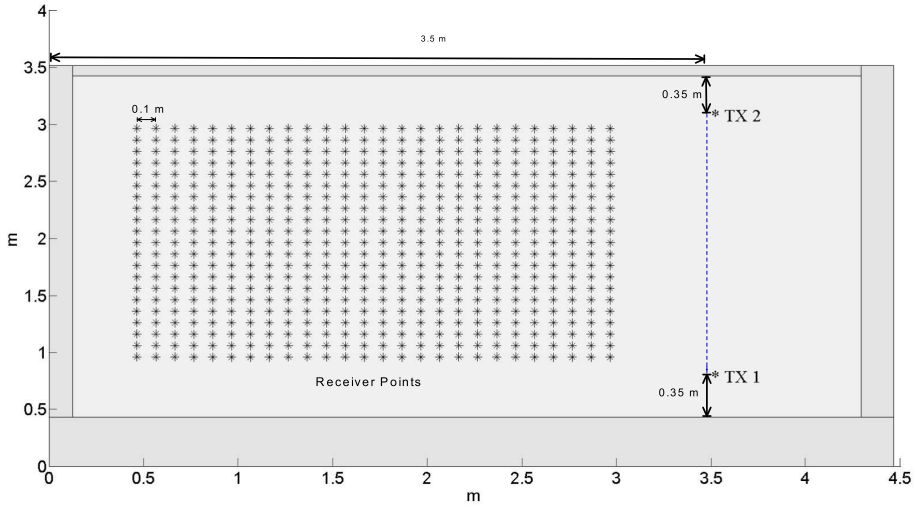

Figure 5.8: Plan View of Propagation Environment

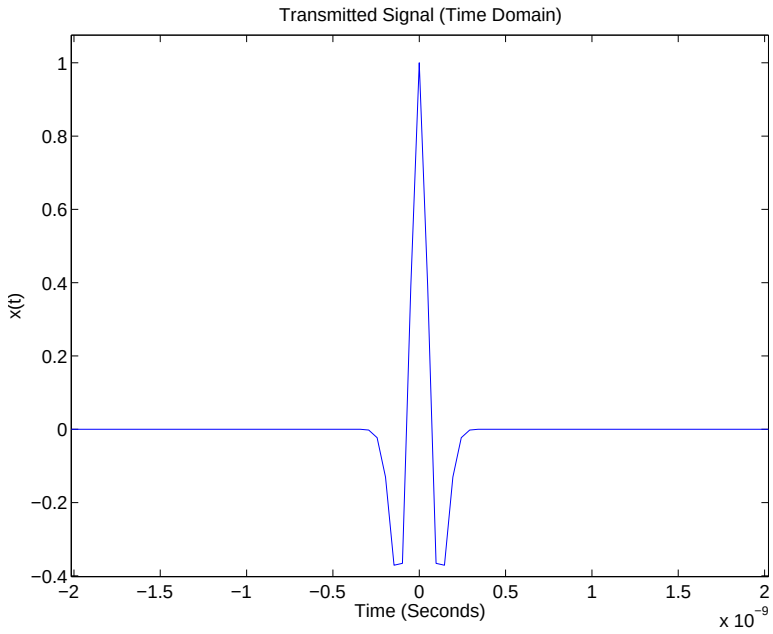

Figure 5.9: Transmitted Pulse in Time Domain

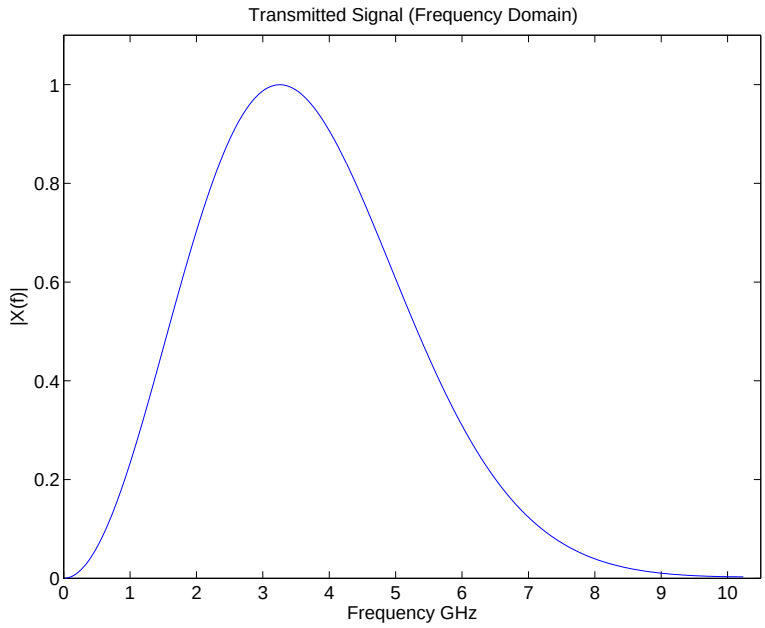

Figure 5.10: Transmitted Pulse in Frequency Domain

Placing a base-station close to a single wall ensures that, for a majority of locations in the room, the second arriving pulse will correspond to reflections from that wall. This is seen in Figures 5.7-5.8 where the base-stations are placed at a distance of 0.35m from a reflecting wall. However, due to reflections from additional walls, the room is subdivided into 4 separate regions as in Figures 5.11-5.12. Each region corresponds to the surface from which the first arriving reflection originates. Also, each region can be considered as being associated with its nearest image point. For example, the region labeled as 1 in Figure 5.11 contains the receiver points that are located nearest to the image $I1$. This entails that for this region, $I1$ can be considered as the virtual source responsible for the earliest arriving (or 1^{st}) reflected pulse. The time difference between pulses arriving from the fixed base-station $TX1$ and virtual source/image $I1$ corresponds to the TDOA value τ_d. This in turn allows for a hyperbola of possible receiver locations to be computed. While region 1 covers the majority of the potential client locations in the room of Figures 5.11, other reflecting walls in the environment result in additional regions 2,3 and 4. This effectively limits the zones in which a reflection based TDOA can operate as in order to obtain a unique hyperbola only reflections from the nearest wall to the base-station $TX1$ are considered. A similar effect is observed for the case of the second base-station $TX2$ in Figure 5.12 where $I4$ is considered as the virtual

image source for first arriving reflection for most receiver locations. Considering these effects for both $TX1$ and $TX2$, the locations in which the proposed algorithm can operate while using one reflecting surface for each base-station is limited to the zone of operation shown in both Figures 5.13 and 5.14. For locations outside this zone, the first arriving reflection (or second received pulse) originate from walls other than that nearest to the base-station.

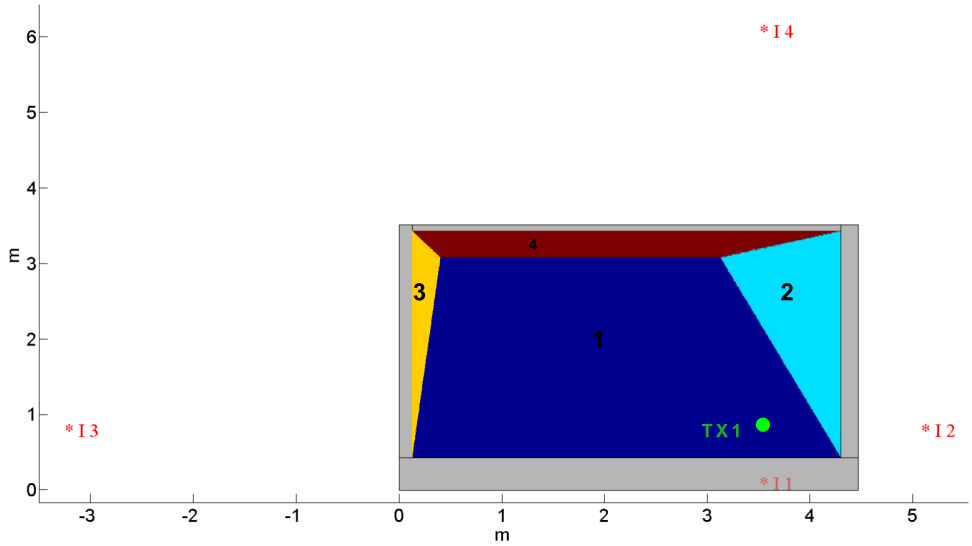

Figure 5.11: TDOA zones for $TX1$

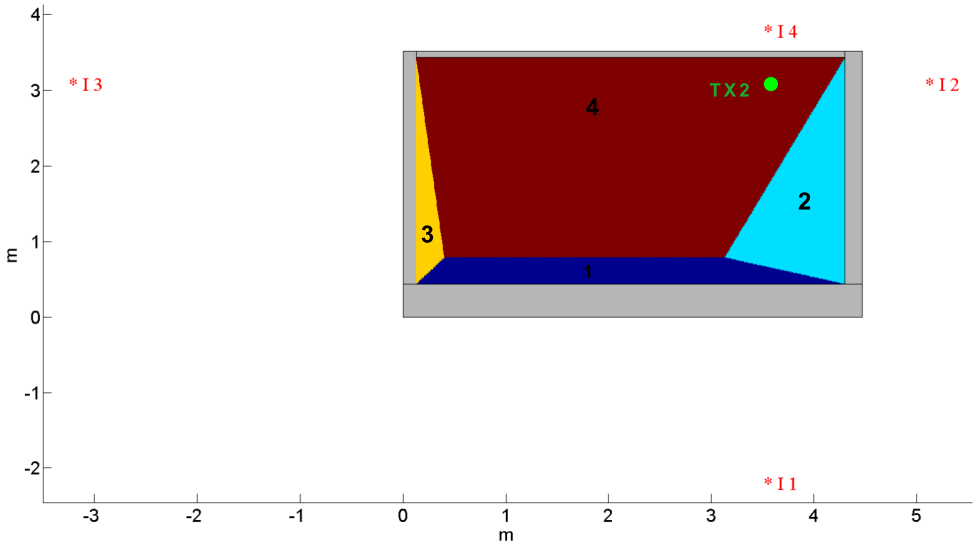

Figure 5.12: TDOA zones for $TX2$

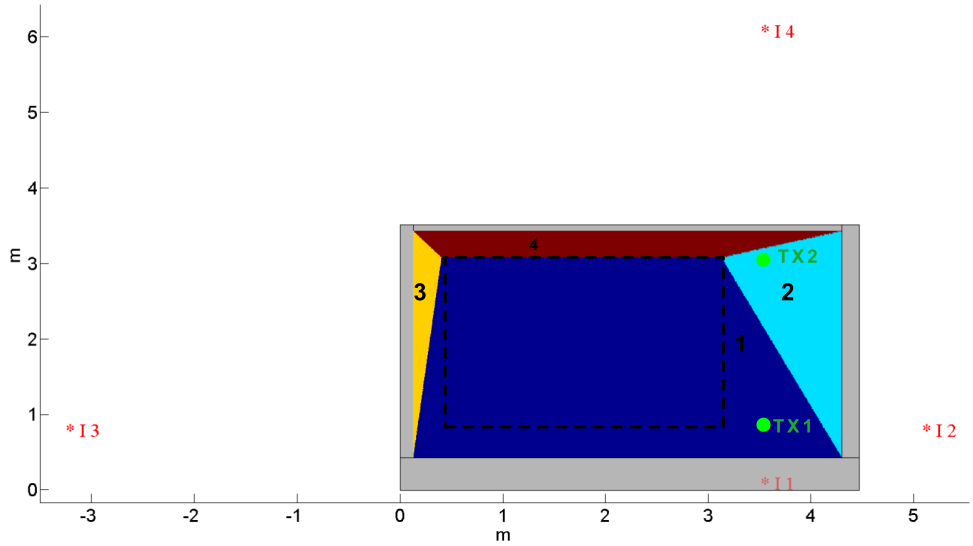

Figure 5.13: Limited Zone of Operation for Transmissions from $TX1$

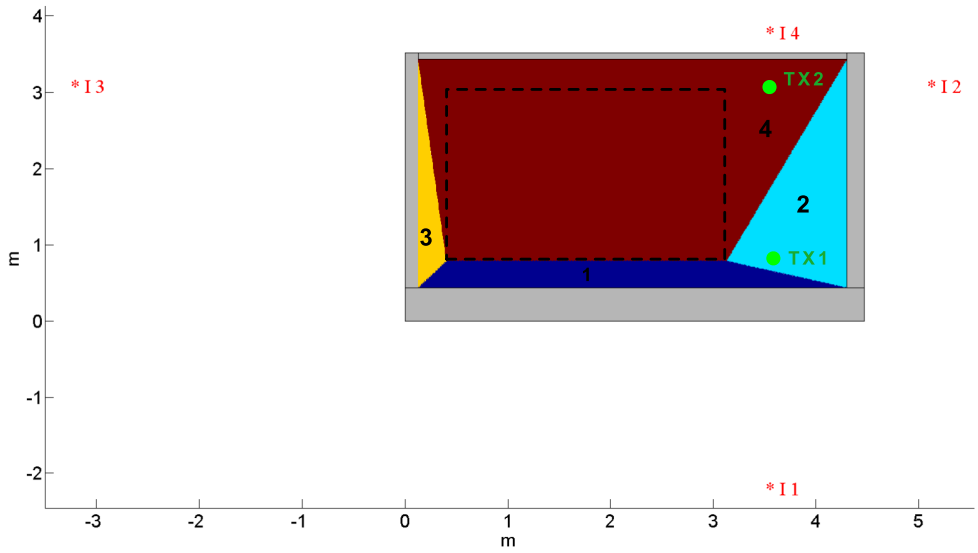

Figure 5.14: Limited Zone of Operation for Transmissions from $TX2$

The time difference between the LOS and first arriving multi-path pulse is measured as the TDOA value between the received pulse from the base-station and the corresponding virtual image. This is observable in Figure 5.16 where a LOS pulse is received followed by a reflected pulse arriving τ_d seconds later. Alternatively, it is possible that the scheme can be configured so that the mobile client station transmits to the fixed base-stations that subsequently measures TDOA and computes resultant hyperbolic curves. Such an arrangement, as employed by existing TDOA techniques, was described earlier in Figures 5.1 and 5.2. However, for the purposes of explanation of this novel technique, it is assumed that the time difference computation between direct and reflected pulses is performed at the mobile client as in Figure 5.15.

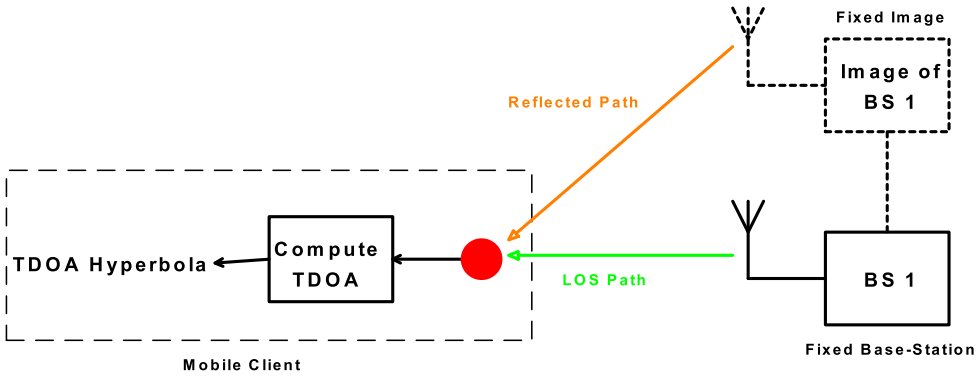

Figure 5.15: TDOA using Reflections at Client

In order to ascertain τ_d the process of autocorrelation is employed which will be the subject of further discussion later in Section 5.3. However, at this juncture is it regarded as merely a method of obtaining the time separation between the first arriving LOS and first arriving reflected received pulses as shown in Figure 5.16.

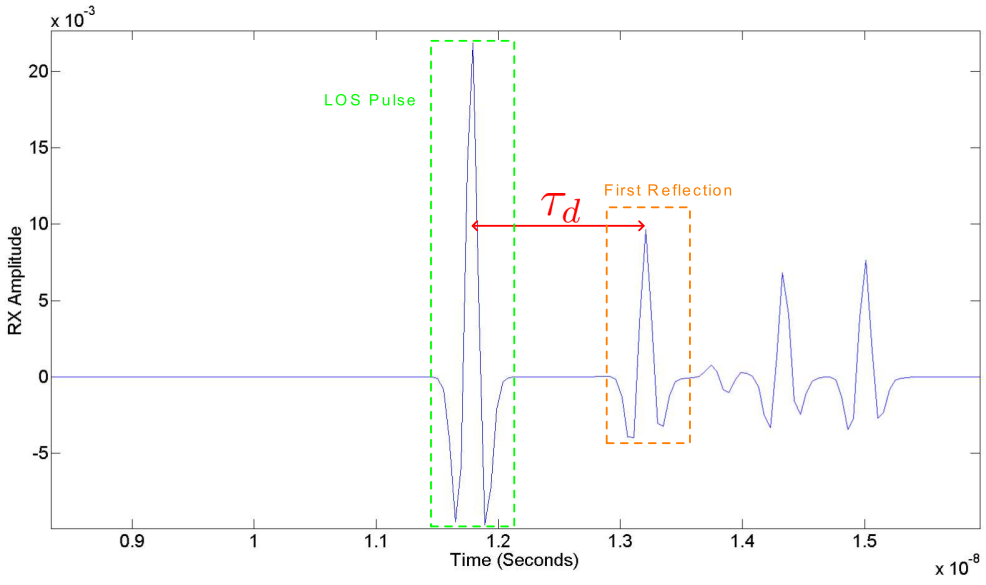

Figure 5.16: TDOA between Direct and Reflected Received Pulses

5.2.2 Simulation Results using Reflection based TDOA

In order to demonstrate the proposed reflection based technique, a ray tracing simulation was carried out for the receiver points shown in Figure 5.8. Each point corresponds to a possible physical location of the client station and are arranged such that they are contained within a zone of operation where the reflection algorithm can be successful applied as shown in Figures 5.13-5.14. The received signal at each of the 546 receiver points was computed separately for base-stations $TX1$ and $TX2$. Using these results 2 hyperbolic curves were calculated for each point and the corresponding intersections of these curves were served as an estimate of the client's physical position (See Figure 5.5). Figure 5.17 shows the positioning error incurred when employing the algorithm for each receiver physical receiver/client location. While initial results were obtained for a noise-free simulated received signal $y(t)$, noise effects were added to subsequent simulations in order to reflect more realistic propagation conditions. This resulted in the overall noisy received time domain waveform of,

$$y_{tot}(t) = y(t) + n(t), \tag{5.1}$$

where $n(t)$ is an additive white Gaussian noise signal whose magnitude is limited, depending on the simulation, to either 4%, 6% or 8% of the maximum amplitude of the received signal $y(t)$. The overall effect of this addition of noise to $y(t)$ can be seen in Figure 5.22. In addition, the accuracy of reflection based geo-location when using such noisy channels for the environment of Figure 5.8 is depicted in Figures 5.18-5.20.

A comparison of these noise-free and noisy simulation results is shown in Figure 5.21. In this Figure the location errors of Figures 5.17-5.20 are sorted by magnitude. In both the noise-free and 4% noise scenarios a location error of less than 0.06m is incurred for the initial 477 sorted receiver points. However, thereafter a sharp increase in this error is observed at remaining points, culminating in maximum errors of the order of 0.14m for both scenarios. While the addition of 4% noise results in a similar maximum error, a sharper increase in this error is observable from Figure 5.21. Further increasing the maximum noise amplitude to 6% and 8% results in maximum errors of 0.176m and 0.1942m respectively. While a reasonable level of accuracy of 0.06m is achieved for 474 receiver locations in Figure 5.21, the remaining errors incurred for the 6% and 8% scenarios diminish the usefulness of the algorithm in such noisy conditions.

Previously the limitations of the reflection based geo-location scheme in a rectangular room was discussed in Section 5.2.1. The zones associated with each reflecting surface were shown in Figures 5.13 and 5.14. Recalling these zones and the errors at each physical location in Figures 5.17-5.20, it is observed that the largest errors occur at the corners nearest to the base-station $TX1$ and $TX2$. These locations also correspond to regions bordering zone 2 in Figures 5.13 and 5.14 and such errors are attributable to the reflections from image $I2$ being incorrectly incorporated into time difference of arrival computations. The addition of noise can also exacerbate this problem further by slightly skewing the position and amplitude of these interfering reflected pulses closer to those of the first arriving reflection. Alternatively, for some receiver points in Figure 5.21 the addition of noise appears to improve accuracy. This is due to the additive noise changing the amplitude of multi-paths such that first arriving reflection appears at a greater amplitude than a close subsequent pulse. At lower noise levels, the second arriving pulse may have a similar or greater peak amplitude which results in the incorrect time delay being computed by auto-correlation. An example of such an effect is seen in Figure 5.21 where for RX points number 531 to 533 improved positioning accuracy is achieved when errors associated with 8% and 4% noise levels are contrasted.
However, it should be considered that in these simulations the algorithm has demonstrated an ability to perform geo-location using only two bases-stations, albeit while incurring such errors. This is in contrast to the infrastructure used by existing TDOA schemes that require at least three base-stations in order to obtain a unique position estimate.

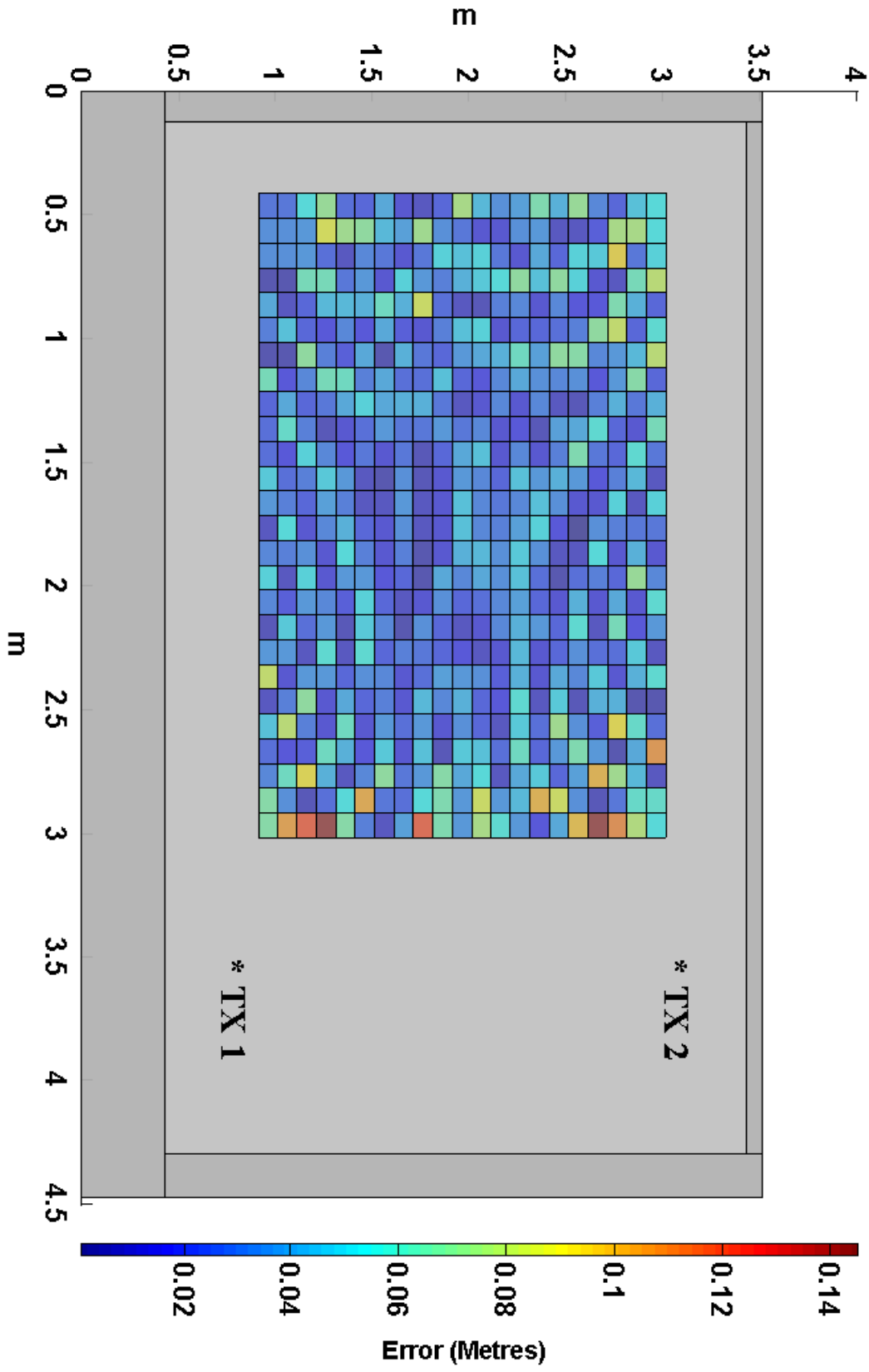

Figure 5.17: Location Error in Room using reflection based TDOA

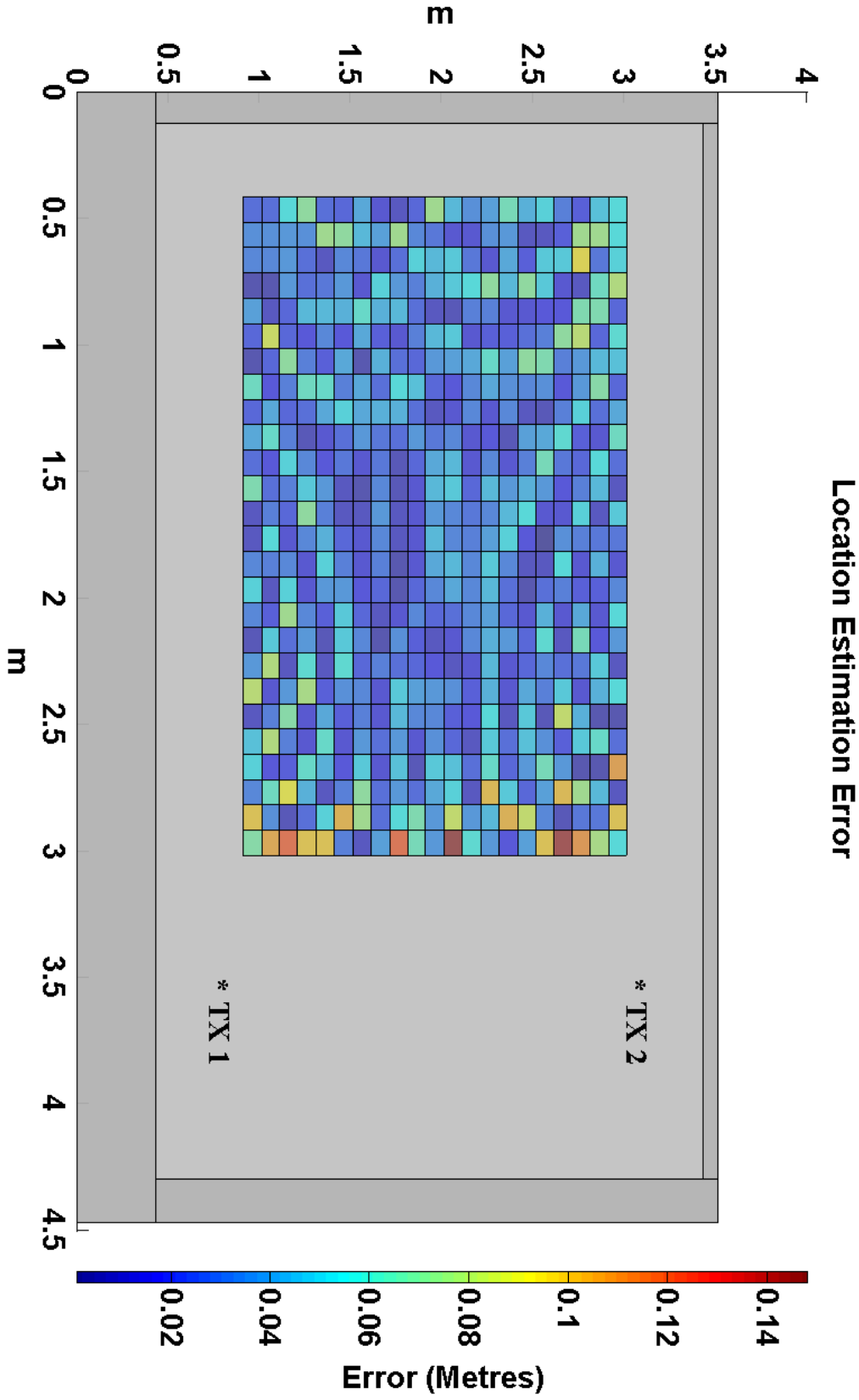

Figure 5.18: Location Error in Room using reflection based TDOA with 4% added noise

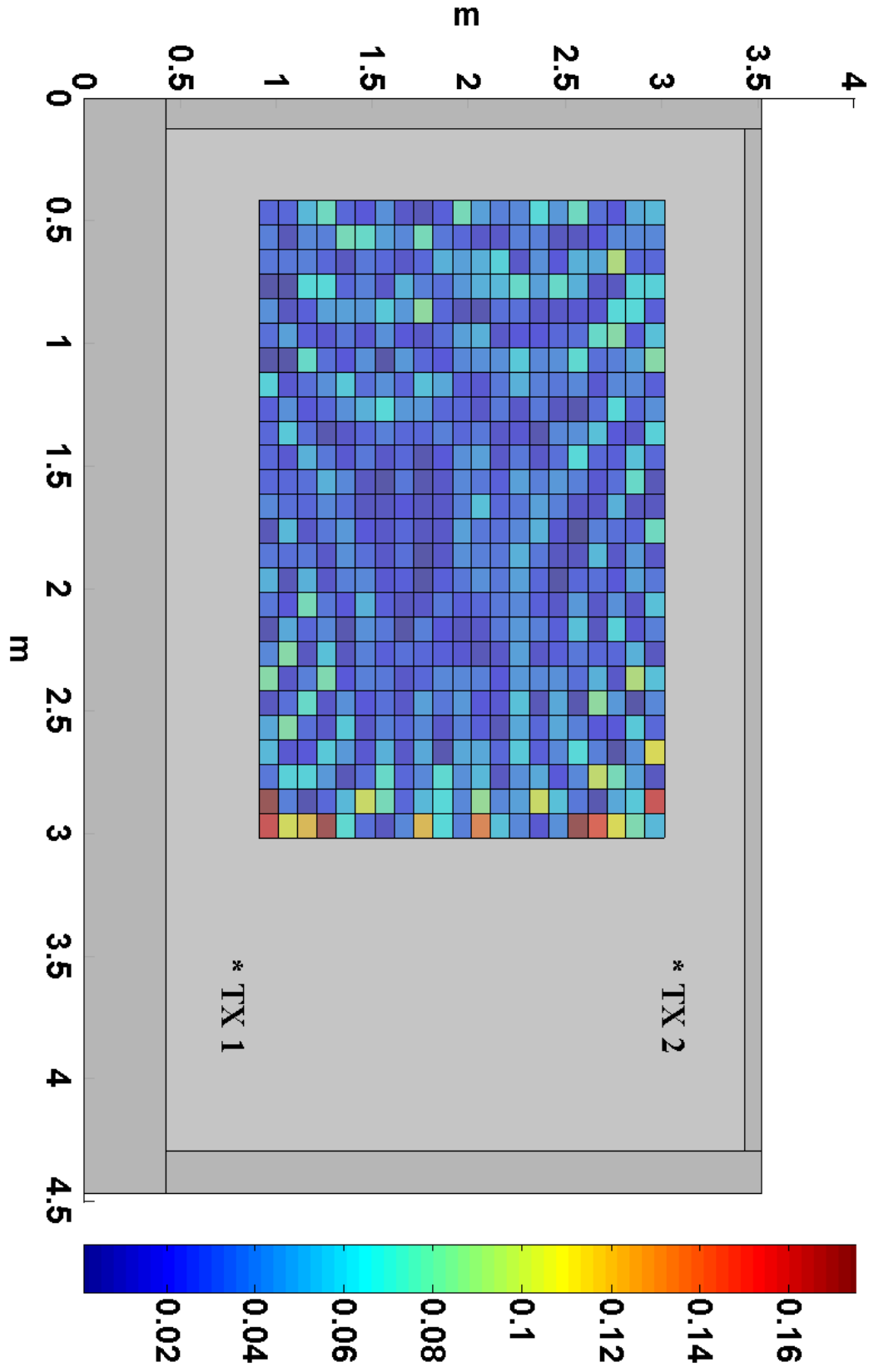

Figure 5.19: Location Error in Room using reflection based TDOA with 6% added noise

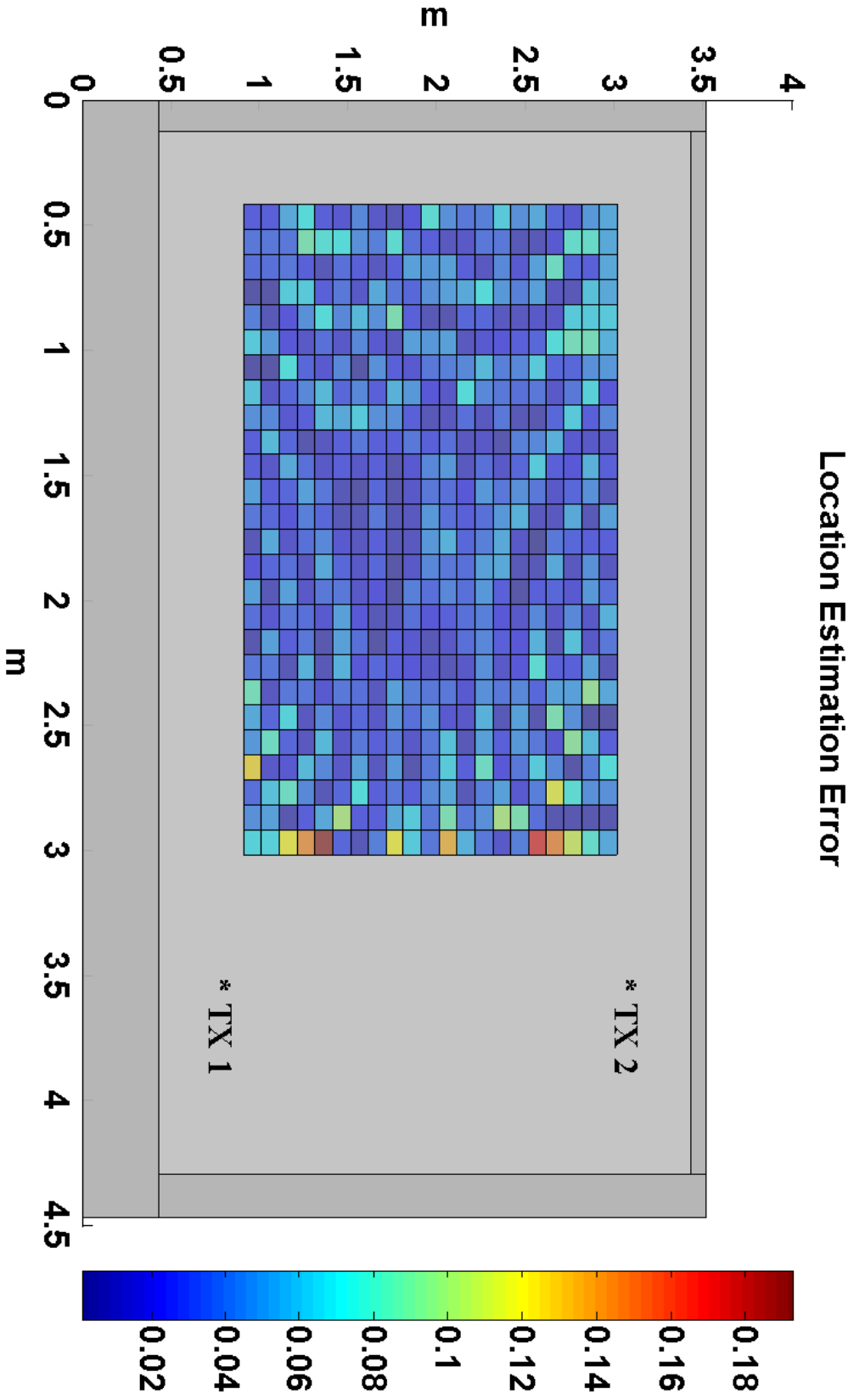

Figure 5.20: Location Error in Room using reflection based TDOA with 8% added noise

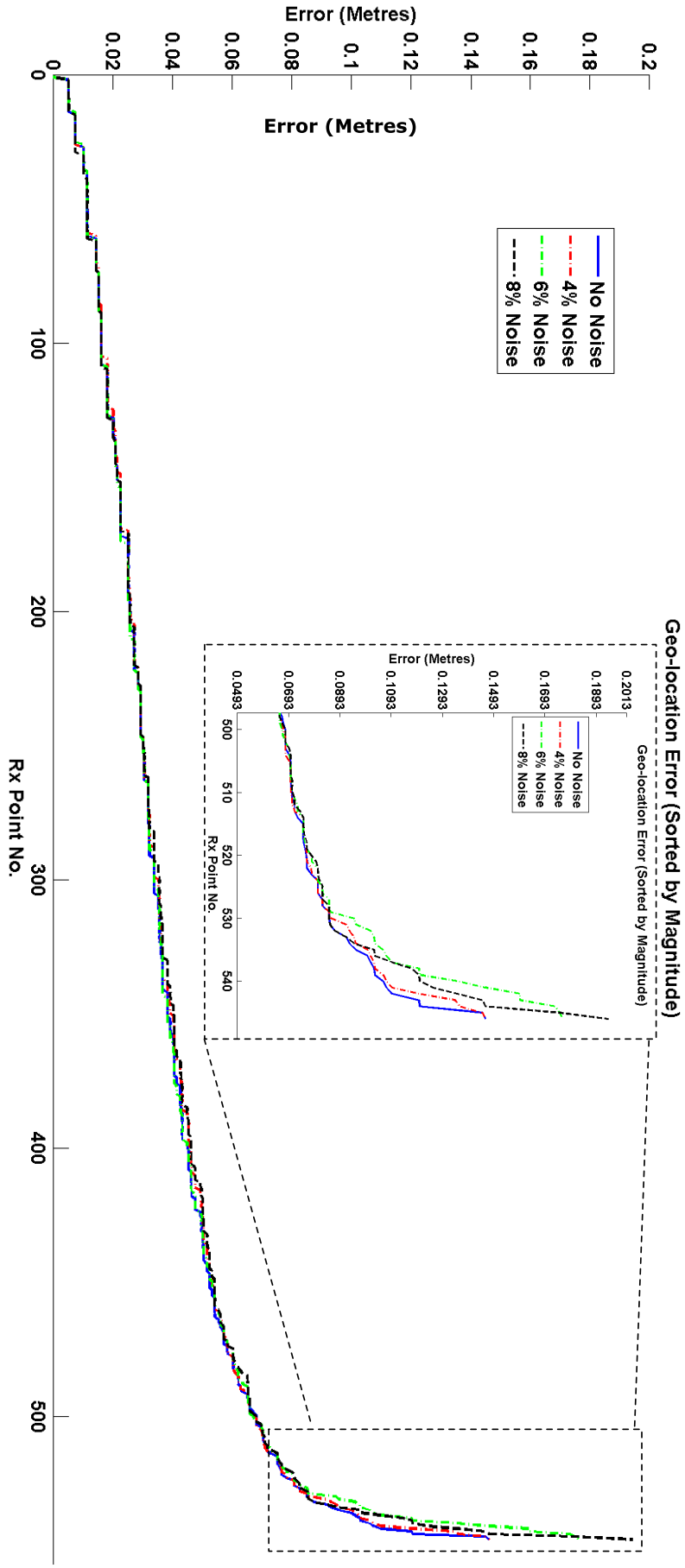

Figure 5.21: Geo-location Errors sorted by magnitude

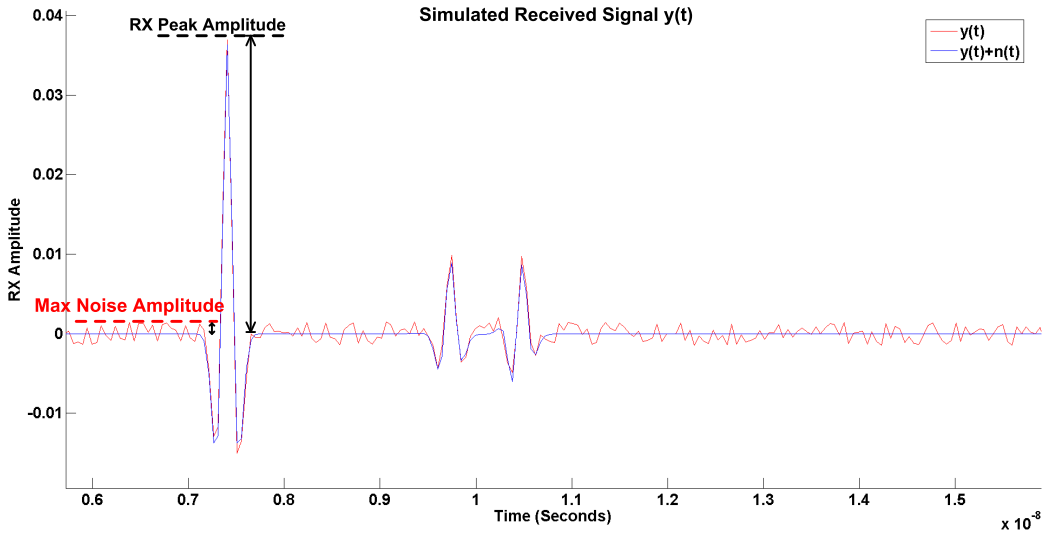

Figure 5.22: Simulated Time Domain Received Signal $y(t)$ with noise $n(t)$

5.3 Autocorrelation

Previously in Section 5.2 a novel approach of geo-positioning was introduced that utilizes time difference of arrival (TDOA) between direct and reflected paths. A prerequisite for applying this technique is the ability to obtain the TDOA τ_d between a direct and reflected pulse in a multi-path received signal $y(t)$ such as that of Figure 5.23.

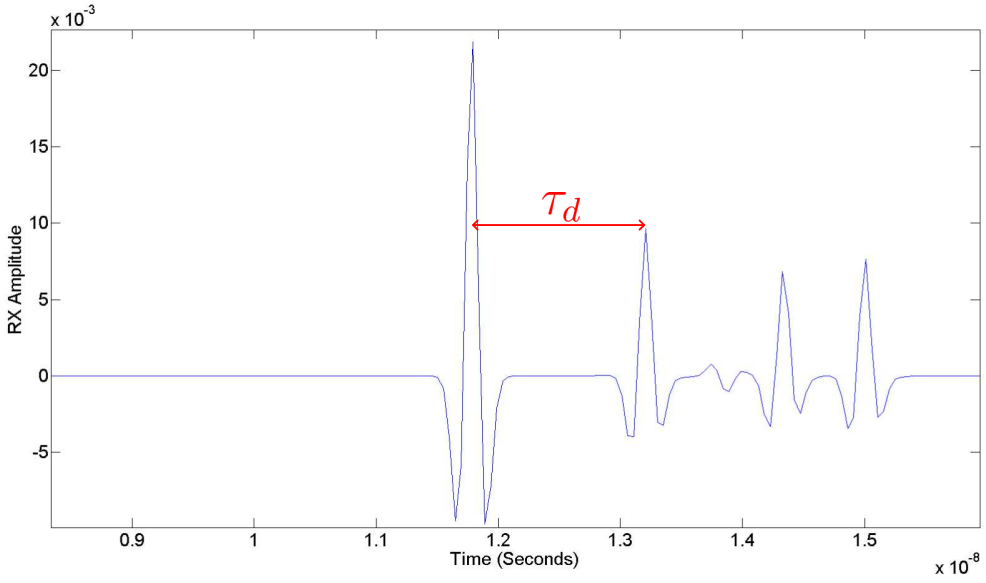

Figure 5.23: TDOA between Direct and Reflected Received Pulse (Zoomed View)

This is achieved using autocorrelation, which entails computing a correlation function $R_{yy}(\tau)$ where,

$$R_{yy}(\tau) = \int_{-\infty}^{\infty} y(t)y(t+\tau)dt. \tag{5.2}$$

In this expression $y(t)$ denotes the received time domain waveform of Figure 5.23 while $R_{yy}(\tau)$ is computed for a range of time delays τ. Observing a typical correlation function $R_{yy}(\tau)$ in Figure 5.24, a peak occurs at the value of τ corresponding to the TDOA value τ_d (ie: where $\tau = \tau_d$). Hence τ_d can be found by applying a peak detection algorithm to $R_{yy}(\tau)$.

Implementing autocorrelation in terms of practical computation involves processing a discrete time domain input $y(n)$, which is in effect a sampled version of the continuous input $y(t)$ of Equation 5.2. Assuming an input of M samples for the sequence $y(n)$, the discrete correlation function $R_{yy}(\tau)$ can be

computed as,

$$R_{yy}(\tau) = \sum_{\tau=1}^{M} y(n)y(n+\tau), \tag{5.3}$$

which in terms of computational operations consists of M^2 additions and multiplications.

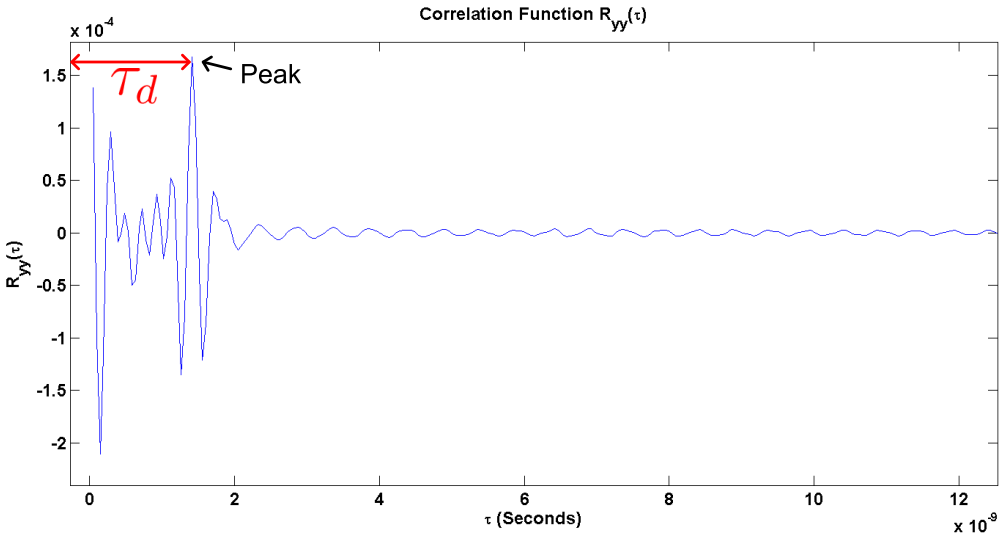

Figure 5.24: Peak Detection of Correlation Function $R_{yy}(\tau)$ (Zoomed View)

Alternatively, autocorrelation can be carried out more efficiently using a Fast Fourier Transform (FFT). Such a technique, described in Section 13.2 of [23], employs frequency domain computations in order to compute a correlation function $R_{yy}(\tau)$ using the correlation theorem whereby,

$$R_{yy}(\tau) = \int_{-\infty}^{\infty} Y(f)Y^*(f)e^{j2\pi f\tau}d\tau. \tag{5.4}$$

In Equation 5.4, $Y(f)$ represents the Fourier Transform of a continuous time domain received signal $y(t)$. Additionally the corresponding complex conjugate of $Y(f)$ is denoted by $Y^*(f)$. Essentially Equation 5.4 involves multiplication of the frequency domain representation of the received signal $Y(f)$ by its complex conjugate $Y^*(f)$ and subsequently employing an Inverse Fourier Transform in order to obtain the correlation function $R_{yy}(\tau)$. For discrete sampled inputs, such as the received UWB sampled waveform $y(n)$, Equation 5.4 is implemented using both a Fast Fourier Transform (FTT) and inverse Fast Fourier Transform $IFFT$ as depicted in Figure 5.25.

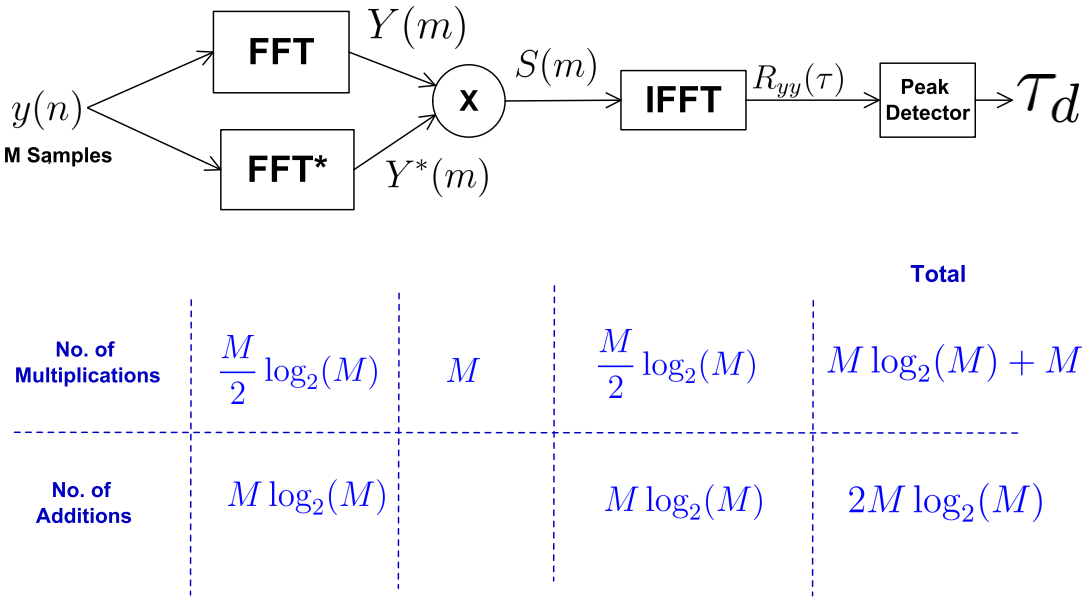

Figure 5.25: Using an FFT to compute autocorrelation of a sequence $y(n)$

Assuming $\frac{M}{2}\log_2 M$ multiply and $M\log_2 M$ addition operations (where M is the length of the input sequence $y(n)$) for each FFT and $IFFT$ [72, 73], frequency domain based autocorrelation can be achieved using a total of $M\log_2 M + M$ multiply and $2M\log_2 M$ addition operations. This represents a considerable saving when compared to the M^2 additions and multiplies required by the time domain technique seen earlier in Equation 5.3.

This saving is especially significant when considering UWB based systems. As a result of the narrow time domain pulse width associated with transmitted UWB pulses (Figure 5.9), a high sampling rate is required when detecting such waveforms at a receiver. This is exacerbated further when a receiver station must listen over an extended period of time for a transmitted pulse. Consequently, this results in a large number of sample bins (M) in which a pulse may be present. Considering such a scenario where M is several thousand samples, the computational savings of employing FFT based auto-correlation are dramatic.

Computational efficiency is also a concern in classical TDOA systems. In [19] an UWB localization algorithm is presented that employs a frequency domain based correlation technique based on generalized cross-correlation [74] in or-

der to obtain a TDOA value between two waveforms transmitted from separate base-stations. This technique, depicted in Figure 5.26, utilizes frequency domain computations in a similar fashion to the auto-correlation approach of Figure 5.25. However, in contrast to the single input of auto-correlation, this cross-correlation technique must find the time difference of arrival between direct LOS pulses in two separate sampled time domain received signals $y_1(n)$ and $y_2(n)$. Furthermore, in scenarios where the line of sight (LOS) propagation path is obscured or where there are many scattering objects in the environment, the accuracy of TDOA calculations obtained using regular cross-correlation can be diminished. In response to this, weighting functions were employed in [19] as a means of mitigating against such effects. Such functions include the Smoothed Coherence Transform (SCOT) or Phase Transform (PHAT) [74] and their application to measured channels in [19] has been reported as improving the accuracy of TDOA measurements. In contrast, the reflection based TDOA algorithm of this work (presented earlier in Section 5.2) employs these previously problematic multi-path reflections in order to aid geo-location.

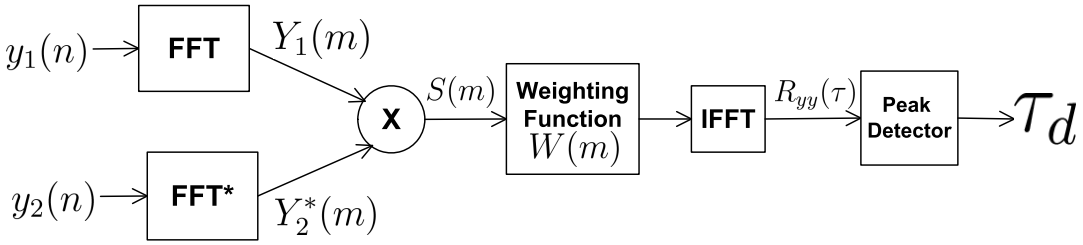

Figure 5.26: Generalized Cross Correlation

The computational challenges associated with UWB pulse arrival time acquisition in Time of Arrival (TOA) schemes have been previously identified in [71]. This can lead to a delay in acquiring geo-location estimates and in response to this problem, Molisch at al. [17] developed a two step TOA acceleration algorithm. This approach offers an efficient means of finding a Line of Sight (LOS) pulse arrival time. Initially a coarse technique based on analyzing the cumulative received energy in blocks of consecutive samples is applied. After calculating a coarse estimate of the pulse location based on received signal energy, a candidate block of samples is then subjected to a rigorous auto-correlation algorithm in order to find the exact pulse position. Ultimately this method results in shorter delays when trying to acquire TOA measurements.
Noting the processing overheads associated with UWB time based schemes,

the remaining sections of this chapter are concerned with improving the computational efficiency of the proposed reflection based TDOA technique. A modification of the existing frequency domain based autocorrelation algorithm of Figure 5.25 will be presented. The purpose of this technique is to reduce the overall computation required when trying to obtain the time difference of arrival between a line of sight and reflected pulse contained within a UWB received waveform. This accelerated technique will be integrated with the reflection based TDOA scheme, presented earlier in Section 5.2. Ultimately this will yield a computationally efficient alternative to conventional UWB line of sight based TDOA [19], that is also capable of providing geo-location estimates using fewer fixed base-stations.

5.4 Accelerated TDOA Technique

Previously in Section 5.3 the computational challenges associated with time based geo-location algorithms were discussed. Specifically, these computational overheads stem from such techniques having to process received time domain UWB sequences containing possibly thousands of sample bins. Recalling the frequency domain FFT based auto-correlation approach of Figure 5.25, this technique consists of $M\log_2(M) + M$ multiply and $2M\log_2(M)$ addition operations when applying auto-correlation to a M sample input. An input of length $M = 1024$ samples will result in a computational cost of 11264 multiplies and 20480 additions, which can prolong the processing time required when attempting to obtain TDOA values. In order to address this, an accelerated auto-correlation scheme is proposed that reduces the computational overhead associated with calculating the TDOA τ_d between a LOS and reflected pulse in a received time domain signal $y(t)$. While this technique employs frequency domain calculations, it offers the advantage of using less computational operations than the existing FFT based auto-correlation discussed in Section 5.3. For the purposes of analysis consider a received multi-path continuous time domain signal $y(t)$ of Figure 5.27, which consists of a Direct Line of Sight (LOS) and a single reflected pulse. This waveform can be conceived as a single UWB pulse $x(t)$ followed by a delayed and attenuated copy $Ax(t-\tau_d)$ such that,

$$y(t) = x(t) + Ax(t-\tau_d), \tag{5.5}$$

where τ_d is the time difference between the pulses and A is a scalar attenuation coefficient with a real value within the range $0 < A < 1$.

When computing auto-correlation using the frequency domain computation method, as previously outlined in Figure 5.25, the input signal is initially converted to its frequency domain representation $Y(f)$ and corresponding complex conjugate[2] $Y^*(f)$. Subsequently, the spectral density function $S(f)$ is computed as

$$S(f) = Y(f)Y^*(f). \tag{5.6}$$

Observing $S(f)$ in Figure 5.28 a distinctive period F_d is noticeable in its variation with frequency. This period is a result of two similar shaped pulse being present in $y(t)$ specifically $x(t)$ and $Ax(t-\tau_d)$ of Equation 5.5. Furthermore, the period F_d is dependent on the time difference τ_d between these pulses.

[2] f denotes frequency in Hertz (Hz)

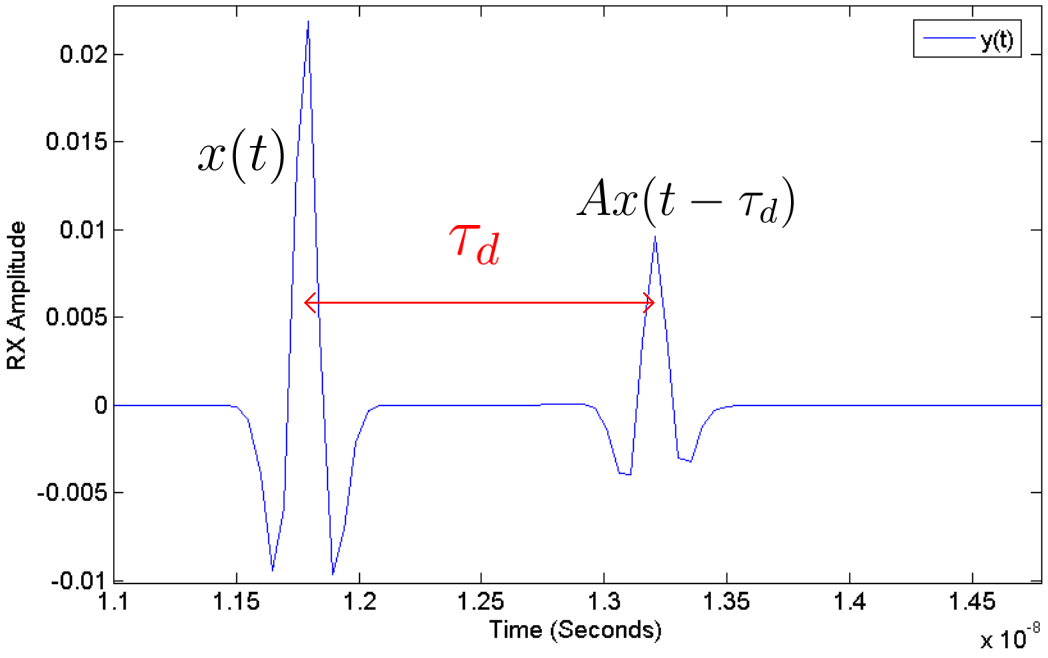

Figure 5.27: Received LOS and Reflected Pulse

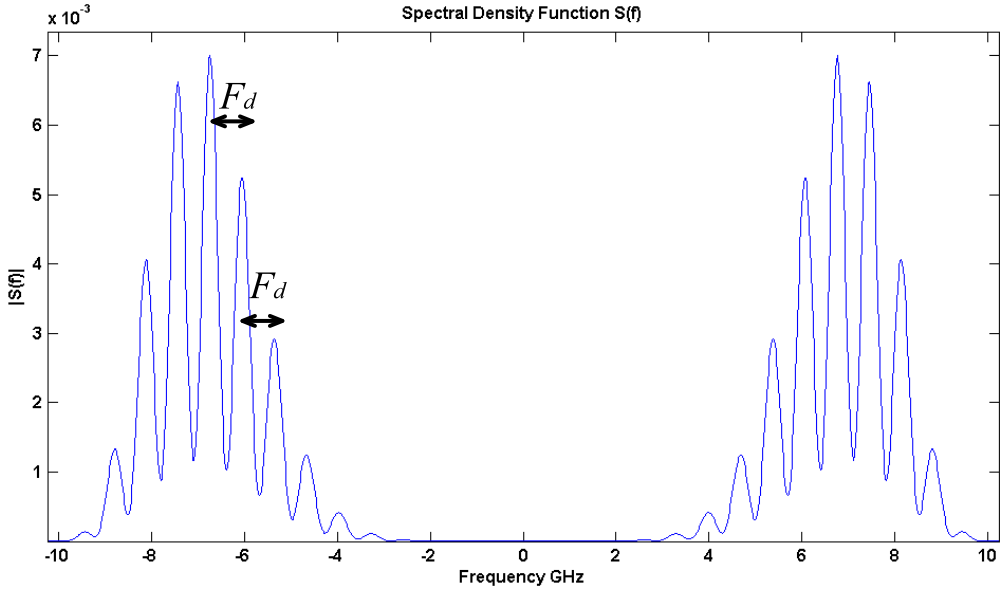

Figure 5.28: Spectral Density $S(f)$

At this point the relationship between the period F_d observed in the spectral density function $S(f)$ of Figure 5.28 and the time delay τ_d between the pulses of Figure 5.27 will be examined. Recalling Equation 5.6 where $S(f)$ is expressed as,

$$S(f) = Y(f)Y^*(f). \tag{5.7}$$

$Y(f)$ is the frequency domain representation of the received time domain signal $y(t)$ which is expressed in Equation 5.5 as,

$$y(t) = x(t) + Ax(t - \tau_d). \tag{5.8}$$

Noting this representation of the received signal, the spectral density function $S(f)$ of Equation 5.7 can be written as,

$$S(f) = Y(f)\,Y^*(f) = \mathcal{F}\{x(t) + Ax(t - \tau_d)\}\mathcal{F}^*\{x(t) + Ax(t - \tau_d)\}, \tag{5.9}$$

where $\mathcal{F}$ denotes a Fourier Transform. Noting the following identity of Fourier Transforms,

$$\mathcal{F}\{x(t - \tau_d)\} = X(f)\,e^{-\jmath 2\pi f \tau_d}, \tag{5.10}$$

allows Equation 5.9 to be written as,

$$S(f) = \left[X(f) + AX(f)\,e^{-\jmath 2\pi f \tau_d}\right]\left[X(f) + AX(f)\,e^{-\jmath 2\pi f \tau_d}\right]^*, \tag{5.11}$$

where $X(f)$ is the frequency domain representation of $x(t)$. Expressing the exponential terms in Equation 5.11 using Euler's formula yields,

$$\begin{aligned} S(f) &= X(f)\,X^*(f)\left[1 + A\left(\cos 2\pi f\tau_d - \jmath \sin 2\pi f\tau_d\right)\right] \\ &\quad \left[1 + A\left(\cos 2\pi f\tau_d - \jmath \sin 2\pi f\tau_d\right)\right]^*, \end{aligned} \tag{5.12}$$

Rearranging yields the following expression for the spectral density function,

$$S(f) = X(f)\,X^*(f)\left[1 + 2A\cos 2\pi f\tau_d + A^2\left(\cos^2 2\pi f\tau_d + \sin^2 2\pi f\tau_d\right)\right]. \tag{5.13}$$

Subsequently employing the trigonometric identity,

$$\sin^2 2\pi f\tau_d + \cos^2 2\pi f\tau_d = 1, \tag{5.14}$$

allows $S(f)$ to be written as[3],

$$S(f) = X(f) X^*(f) \left[A^2 + 1 + 2A\cos 2\pi f \tau_d\right]. \tag{5.15}$$

Noting that,

$$X(f) X^*(f) = |X(f)|^2 \tag{5.16}$$

Equation 5.15 now becomes

$$S(f) = |X(f)|^2 \left[A^2 + 1 + 2A\cos 2\pi f \tau_d\right] \tag{5.17}$$

$S(f)$ can be thought of as the product of the magnitude response of the transmitted pulse squared $|X(f)|^2$ and the term $\left[A^2 + 1 + 2A\cos 2\pi f \tau_d\right]$ term. Recalling that A is a real valued scalar attenuation factor and constant at all frequencies, this latter term contains only one frequency varying component, namely $\cos 2\pi f \tau_d$. Consequently, this sinusoid is responsible for the observable period F_d within $S(f)$ of Figure 5.28. Recognizing that the period of the cosine component in the frequency domain (f) is determined by τ_d, essentially F_d can now be calculated as

$$F_d = \frac{1}{\tau_d}, \tag{5.18}$$

where τ_d, the time difference between the received pulses of $y(t)$ in Figure 5.27. Conversely τ_d may also be calculated from F_d whereby,

$$\tau_d = \frac{1}{F_d}. \tag{5.19}$$

Using this relationship it is now possible to calculate the TDOA value τ_d from knowledge of the period F_d present in the spectral density function $S(f)$.
The variation of F_d and τ_d over the respective bandwidth of $S(f)$ and time duration of $y(t)$, is shown in Figure 5.29. A notable feature is the sharp decrease in F_d as τ_d begins to grow. This relationship of Equation 5.19 has a useful property whereby values of τ_d above a specified threshold leads to F_d being limited to a determinable maximum. For example in Figure 5.29, when the minimum of τ_d is limited to 0.390625 nanoseconds, the maximum value of F_d will be limited to 2.56 GHz. Recalling that F_d is a period within the spectral density function $S(f)$, this limited F_d can be observed over a narrower bandwidth. Furthermore, by assigning a predefined minimum TDOA between LOS and reflected received pulses in $y(t)$, the value of τ_d can be computed from a

[3]For a more comprehensive derivation please see Appendix B.2

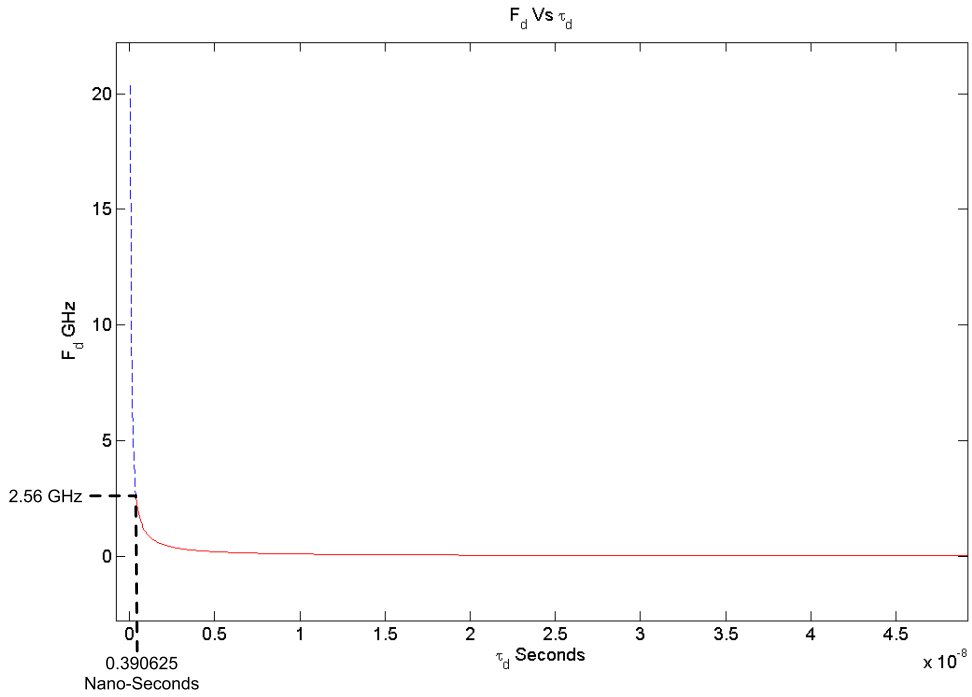

Figure 5.29: F_d Vs τ_d showing results of limited F_d

sub-band of $S(f)$. However, it should be noted that the band-width of this sub-band must be sufficient such that the period F_d is observable within it. In the subsequent Section 5.5, an algorithm will be presented that exploits this characteristic in order to offer a more efficient auto-correlation technique for computing the time difference of arrival τ_d between multi-path pulses within a discrete sample received signal $y(n)$.

5.5 Implementation of Accelerated Correlation

Previously in Section 5.3 autocorrelation employing Fast Fourier Transforms (FFT) was discussed. In the discussion of Section 5.4, the relationship between pulse separation τ_d and a corresponding period F_d in the spectral density $S(f)$ was established. From Figure 5.29 it was concluded that the maximum value of F_d can be limited by specifying a minimum time delay τ_d between LOS and reflected pulses. Consequently, this limited period F_d is observable within a smaller bandwidth of $S(f)$. In this section an algorithm that exploits this property, in order to efficiently compute the time difference of arrival (TDOA) τ_d, will be outlined.

5.5.1 Reduced Bandwidth Auto-Correlation

For the purpose of examining an accelerated TDOA scheme consider the discrete time domain input $y(n)$ of Figure 5.30. Noting that continuous signals were employed in prior discussions, $y(n)$ can be considered as the sampled equivalent of the continuous received signal $y(t)$ previously seen in Figure 5.23. $y(n)$ as depicted in Figure 5.30 below consists of $M = 1024$ discrete values sampled using a time step of 0.04882812 nano-seconds.

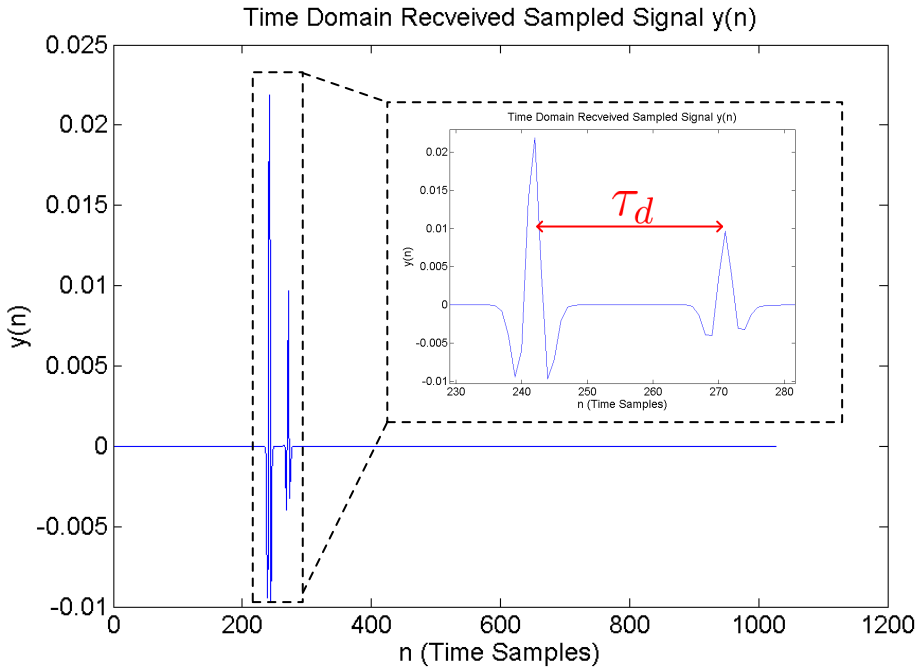

Figure 5.30: Discrete time domain RX signal $y(n)$

The purpose of the proposed technique is to find the time difference τ_d between two pulses present in $y(n)$ in a less computationally intensive operation than the existing FFT based autocorrelation technique of Figure 5.25 in Section 5.3. In order to demonstrate the accelerated correlation method, a sub-band of length $M_R = 128$ was selected which, for a frequency step size of $20MHz$, corresponds to a bandwidth of 2.56 GHz. While the reasoning behind the selection of $M_R = 128$ samples will be discussed later in Section 5.5.2, the sample step size of 20 MHz is an arbitrary choice for the purpose of simulation. In a practical deployment this value depends on how long a station must listen for a transmitted pulse. Application specific characteristics such as the data transmission rates/scheme used would determine this duration and ultimately the frequency step size. For a time domain signal containing M samples, the same number of samples is present in the frequency domain representation of this waveform. Assuming that the bandwidth of the received waveform remains constant, increasing the listening time directly results in a reduced frequency domain step size.

The consequences of the reduced bandwidth is observable from Figure 5.31 where using only $M_R = 128$ samples (out of a total of $M = 1024$) limits the minimum value of the time difference of arrival τ_d to 8 samples or 0.390625 nano-seconds. Figure 5.31 can be considered a sampled counterpart of Figure 5.29 in Section 5.4 which demonstrated the relationship between τ_d and F_d for a continuous time scale.

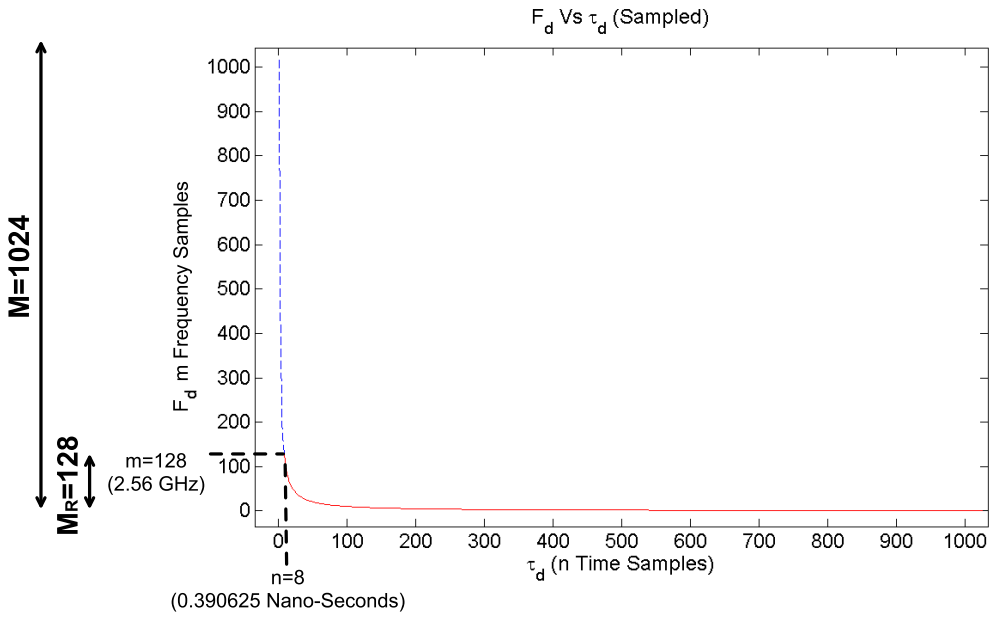

Figure 5.31: F_d Vs τ_d (For Sampled Input)

Furthermore, for the range of receiver locations of a propagation environment some TDOA values will fall below this threshold of 0.390625 nano-seconds. Consequently, this will result in inaccurate values for τ_d being returned for such locations when utilizing the proposed accelerated technique. In Figure 5.32, the TDOA values between a LOS and reflected path is shown for a sample room. The TDOA value τ_d reduces to below the minimum threshold of 0.390625 nano-seconds in a triangular region adjacent to the reflecting surface (denoted by the dark blue segment). It can be concluded from this Figure that, an acceleration technique with a configuration using $M_R = 128$ frequency domain samples will fail to yield an accurate TDOA value in this region. However, the algorithm can be applied to receivers located in the remaining portions of the environment, which constitutes the majority of the room shown in Figure 5.32.

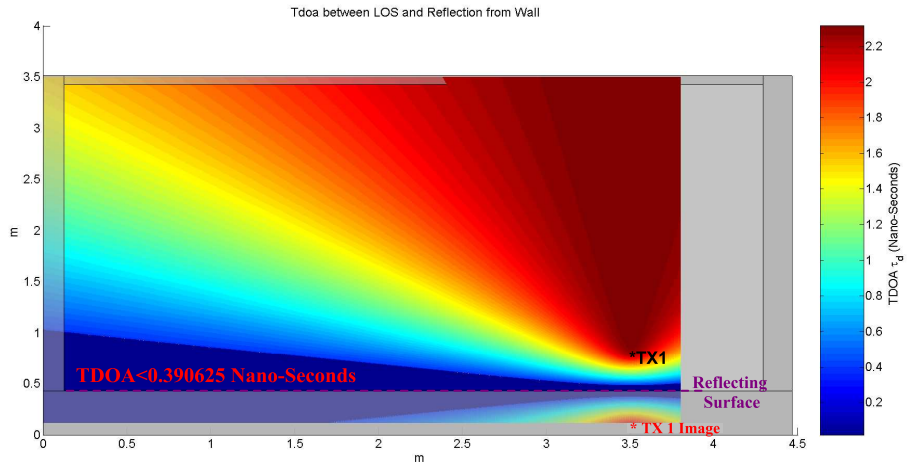

Figure 5.32: Time Difference of Arrival (TDOA) between LOS and reflection multi-paths

A summary of the steps involved in applying auto-correlation using exisiting FFT frequency domain based computations when computing TDOA is given in Figure 5.33. In addition the stages of the proposed accelerated technique is presented on the bottom half of this Figure. The initial input to both techniques is the same time domain received sequence $y(n)$. However, in the accelerated scheme the next step involves a modified FFT that computes the frequency domain signal $Y_R(m)$, where m represents a discrete frequency index. $Y_R(m)$ can be considered to be equal to the original $Y(m)$ within the subbandwidth specified by M_R samples but zero valued at all other remaining frequency samples. As a consequence of $Y_R(m)$ only containing M_R non-zero values the modified FFT can be arranged to use less computation than a regu-

lar FFT. This will be discussed in further detail in Sections 5.5.2 and 5.5.3. An additional computational saving is realized when trying to multiply $Y_R(m)$ and its corresponding complex conjugate $Y_R^*(m)$ for the purposes of obtaining the spectral density function $S_R(m)$. The original legacy FFT based autocorrelation method of Figure 5.33 requires M multiplications when computing the product of $Y(m)$ and $Y^*(m)$. In contrast when using the accelerated technique only M_R multiplications are necessary when finding the product of $Y_R(m)$ and $Y_R^*(m)$ as only M_R entries in each sequence contain non-zero values. A further computation saving is attributed to the use of a modified Inverse Fast Fourier Transform $IFFT$ when computing the correlation function $R_{yy}(n)$ from $S_R(m)$. In the case of the accelerated technique the input to this $IFFT$ consists of $S_R(m)$ containing only zero valued samples outside of a sub-band of M_R samples. The computations within the modified FFT and $IFFT$ seen in Figure 5.33 will be explored in the subsequent Sections 5.5.2-5.5.3.

5.5.2 Modified FFT

As an alternative to the FFT used in conventional frequency domain based auto-correlation, the proposed accelerated technique of Figure 5.33 employs a modified FFT which offers a reduction in the computation required when calculating the spectral density function $S_R(m)$. The butterfly diagram of Figure 5.34 shows the arrangement of an 8 input ($M = 8$) decimation in frequency FFT. Using such a butterfly diagram allows the FFT to be decomposed into the individual multiply and addition operations of Figure 5.35. Also it should be noted that the appearance of W_P^k in Figures 5.34-5.35 denotes multiplication by the complex coefficient $e^{-j\frac{2k\pi}{P}}$, where $P = \frac{M}{2}$ and k varies between 0 and $\frac{M}{2}$. The specific arrangement of Figure 5.34 is referred to as a decimation in frequency FFT and is of particular interest due to the large number of complex multiplications applied immediately prior to obtaining the output $Y(m)$. This characteristic lends itself for the purposes of computational reduction in a scenario where only a subsection of the output $S(m)$ is required. A comprehensive description of the decimation in frequency FFT can be found in Chapter 9 of [72]. However, for the purposes of creating an accelerated auto-correlation algorithm, this discussion is purely concerned with the overall computations structure of the FFT and possible reductions within it. The implementation of such a reduction is shown for a $M = 1024$ input FFT in Figure 5.36. Recalling from Figure 5.33 that the output of the modified FFT, $Y_R(m)$, contains only M_R non-zero values out of a total of M samples, this result in $M - M_R$ zero valued outputs. Knowing that such samples will be set to zero, the corresponding outputs are hence redundant. Consequently, the multiplication and addition operations exclusively associated with such outputs are no longer necessary and can be disregarded. In the case where $M = 1024$ and $M_R = 128$, such as that of Figure 5.36, the outputs and associated computations shown in red can be removed from the overall FFT, thus yielding the modified FFT seen previously in Figure 5.33 . However, the remaining computations of the latter stage of the FFT shown in black are still necessary in order to produce the M_R non-zero valued outputs of $Y_R(m)$. It should be noted that the overall computational savings achieved by the modified FFT, seen in Table 5.1, is dependent on the position of M_R within the M length sequence of $Y_R(m)$. In the scenario presented in Figure 5.36, the $M_R = 128$ non zeros samples are located between sample bins 99 to 227. These samples are all located within the first 256 (or $\frac{1}{4}$ of $M = 1024$), which are chosen to correspond to the largest magnitudes of the frequency domain signal $Y(m)$. Ulti-

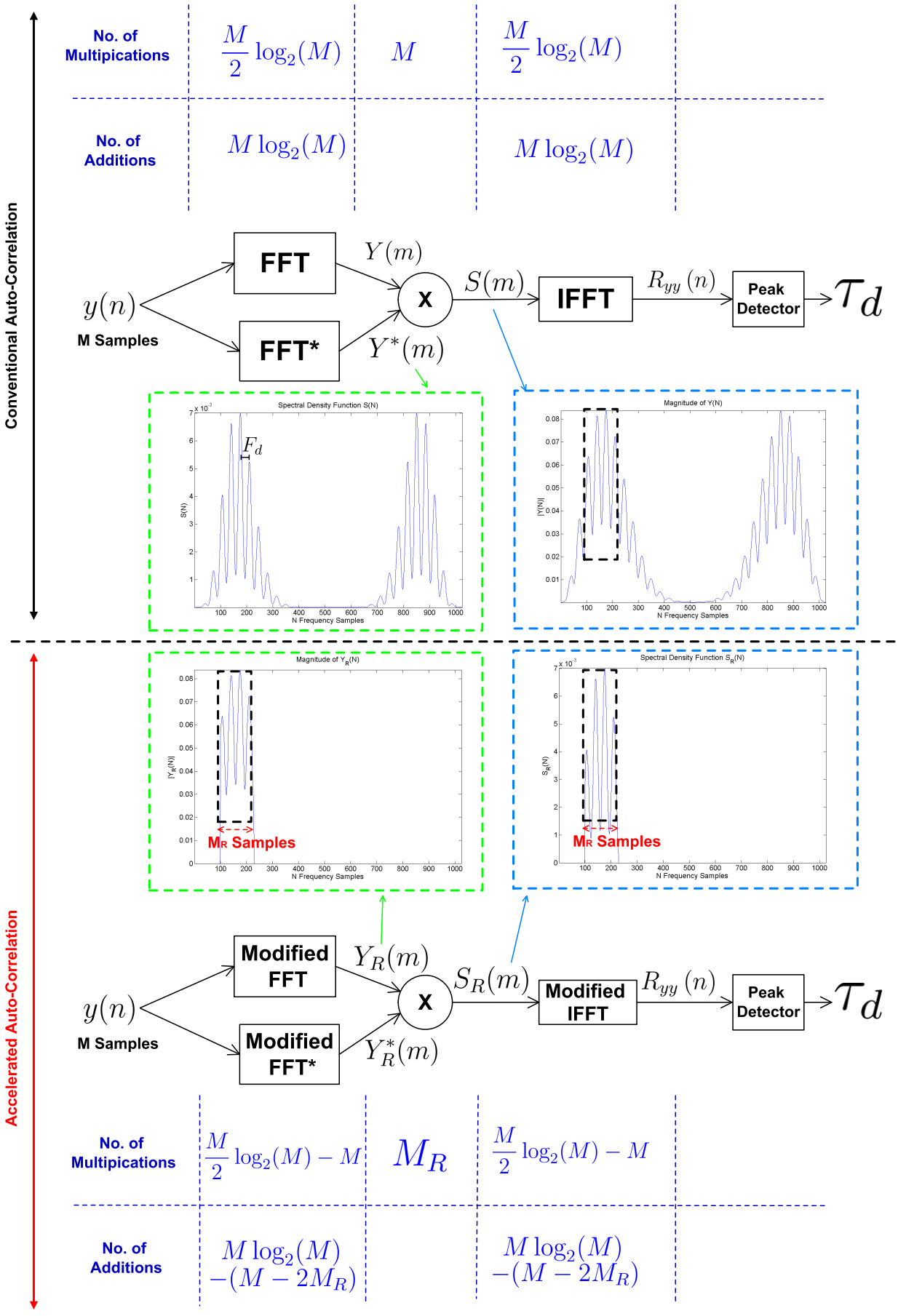

Figure 5.33: Existing Frequency Domain Auto-Correlation along side Accelerated Technique

mately the location of this sub-band determines how many operations may be disregarded. For M_R located elsewhere within the $M = 1024$ bins, specifically outside the first 265 samples, this would alter the computation saving possible when employing the modified FFT.

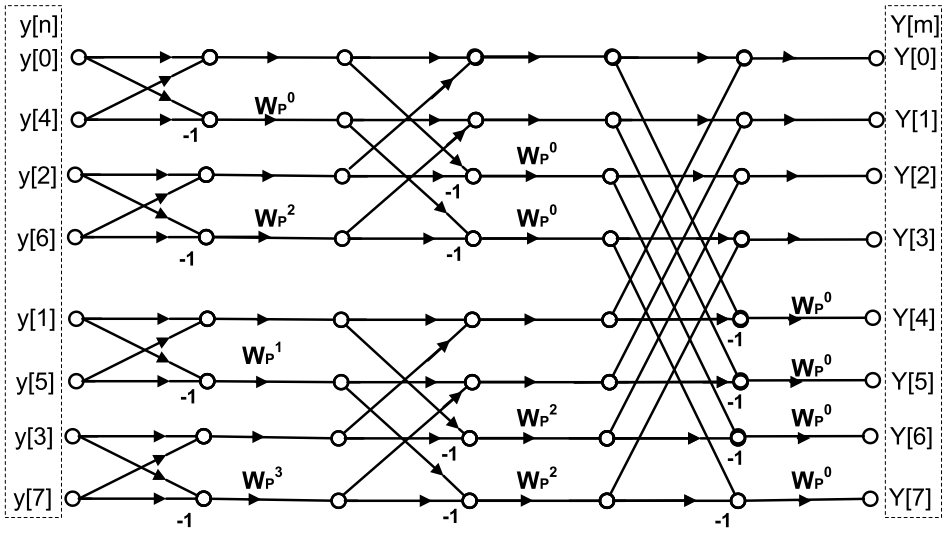

Figure 5.34: 8 point Decimation in Frequency *FFT* Butterfly Diagram

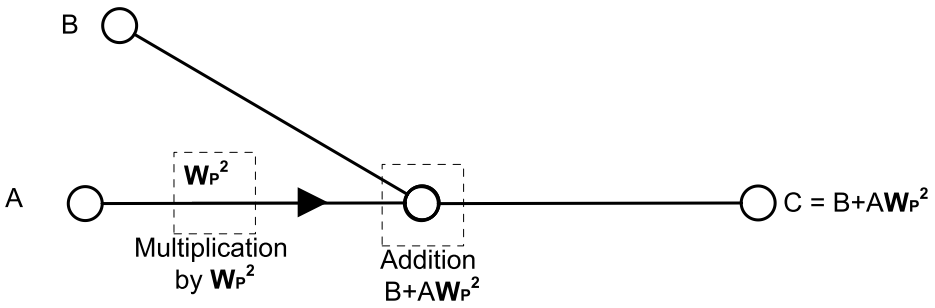

Figure 5.35: Multiply and Summation Butterfly Diagram Operations

	Original FFT	Modified FFT	Saving
No. of Multiplication	$\frac{M}{2}\log_2(M)$	$\frac{M}{2}\log_2(M) - M$	M
No. of Additions	$M\log_2(M)$	$M\log_2(M) - (M - 2M_R)$	$M - 2M_R$

Table 5.1: Computation Operation for FFT of Figure 5.36

Figure 5.36: 1024 Input Modified FFT

5.5.3 Modified IFFT

In the later stages of the proposed accelerated autocorrelation technique of Figure 5.33 a modified $IFFT$ is introduced in order to compute the correlation function $R_{yy}(n)$ from the spectral density function $S_R(m)$. This replaces the existing $IFFT$ of the legacy frequency domain autocorrelation with a more computationally efficient alternative. In Figure 5.37 the butterfly diagram for a decimation in time $IFFT$ with $M = 8$ inputs is shown (Chapter 9 [72]). This depicts the operations required in order to transform a frequency domain signal $S(m)$ into the time domain sequence $R_{yy}(n)$. In total this requires $\frac{M}{2}\log_2(M)$ multiplication and $M\log_2(M)$ addition operations. Observing the arrangement, it can be noted that multiplication operations are immediately applied to $\frac{M}{2}$ inputs from $S(4)$-$S(7)$. Considering a scenario whereby some of the inputs to an $IFFT$ are known to be zero values, such as in the case of $S_R(m)$ of the accelerated technique, multiplication operations applied to these zero valued input bins can be disregarded. Indeed this particular characteristic of the decimation in time $IFFT$ is what is exploited in the modified $IFFT$ of Figure 5.38. As can be seen in this Figure, only a M_R long subsection of the M spectral density function input $S_R(m)$ contains non-zero values. The remaining zero valued samples correspond to the inputs shown in red. Furthermore, the computations exclusively associated with these zero valued inputs, also denoted by red, can be disregarded from the computation of the discrete correlation function $R_{yy}(n)$ (Figure 5.40). The overall computation saving of employing this arrangement compared to a regular $IFFT$ amounts to M multiplication and $M - 2M_R$ addition operations (Table 5.2).

	Original $IFFT$	Modified $IFFT$	Saving
No. of Multiplication	$\frac{M}{2}\log_2(M)$	$\frac{M}{2}\log_2(M) - M$	M
No. of Additions	$M\log_2(M)$	$M\log_2(M) - (M - 2M_R)$	$M - 2M_R$

Table 5.2: Computation Operation for $IFFT$ of Figure 5.38

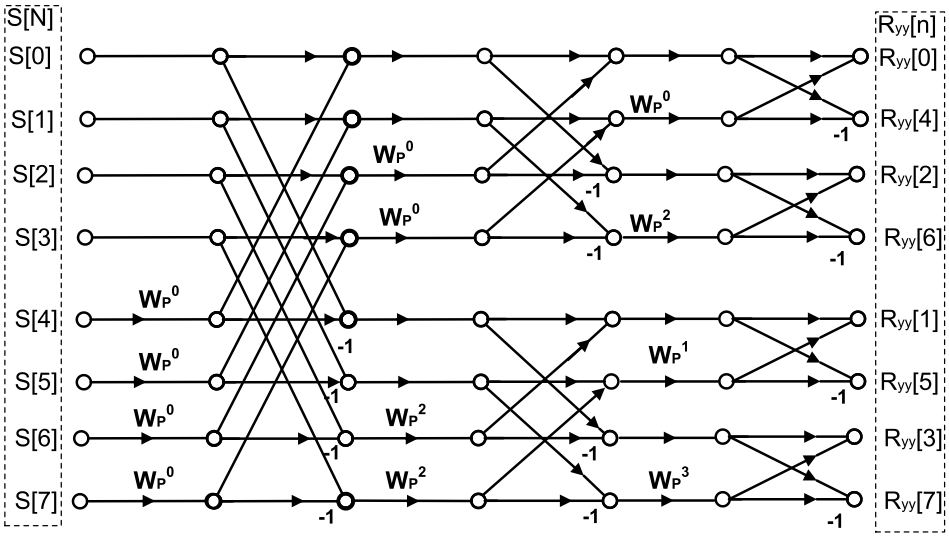

Figure 5.37: 8 point Decimation in Time $IFFT$ Butterfly Diagram

Figure 5.38: 1024 bit modified *IFFT*

5.5.4 Overview of Acceleration algorithm

A summary of the accelerated auto-correlation technique is shown in Figure 5.39. This arrangement incorporates the modified FFT and $IFFT$ of Figures 5.36 and 5.38. The initial stages of this algorithm involve obtaining the frequency domain signals $Y_R(m)$ and $Y_R^*(m)$ from the received time domain sampled input $y(n)$ using the modified FFT of Section 5.5.2. Knowing that this input is purely real valued, the complex conjugate $Y_R^*(m)$ is computed by simply reversing the sequence of $Y_R(m)$. Consequently, obtaining both $Y_R(m)$ and $Y_R^*(m)$ requires just $\frac{M}{2}\log_2(M) - M$ multiplies and $M\log_2(M) - M + 2M_R$ additions in total. Recalling that $Y_R(m)$ contains M_R non- zero valued samples, the subsequent multiplication of $Y_R(m)$ and $Y_R^*(m)$, can be reduced to just M_R individual bit multiply operations. Finally, the discrete correlation function $R_{yy}(n)$ is found using the modified $IFFT$ (described in Section 5.5.3), which also consists of $\frac{M}{2}\log_2(M) - M$ multiplies and $M\log_2(M) - M + 2M_R$ additions. Applying a peak detection algorithm to $R_{yy}(n)$ of Figure 5.40 reveals the TDOA value τ_d as being equivalent to the position of the maximum value in $R_{yy}(n)$. This value for τ_d corresponds to the number of samples that separate the Line of Sight (LOS) and the first arriving reflected pulse in the received time domain sequence $y(n)$.

A comparison of the computation cost of using the accelerated and legacy frequency domain auto-correlation technique is presented in Tables 5.3-5.6. Assuming a configuration using $M = 1024$ and $M_R = 128$, an overall reduction of 2944 multiplies and 1536 additions is achieved. This represents a respective saving of 26.1% and 7.5% for each type of operation when compared to the existing approach of computing autocorrelation using regular FFT and $IFFT$ structures.

	Original Cross Correlation	**Accelerated Cross Correlation**	**Saving**
FFT	$\frac{M}{2}\log_2(M)$	$\frac{M}{2}\log_2(M) - M$	M
Multiply $(\mathbf{S_R}(\mathbf{m}) = \mathbf{Y_R}(\mathbf{m})\mathbf{Y_R^*}(\mathbf{m}))$	M	M_R	$M - M_R$
IFFT	$\frac{M}{2}\log_2(M)$	$\frac{M}{2}\log_2(M) - M$	M
Total	$M\log_2(M) + M$	$M\log_2(M) - 2M + M_R$	$\mathbf{3M - M_R}$

Table 5.3: Reduction in Multiplication Operations using Accelerated Cross Correlation

M = 1024 **M_R = 128**	**Original Cross Correlation**	**Accelerated Cross Correlation**	**Saving**
FFT	5120	4096	1024
Multiply $(\mathbf{S_R}(\mathbf{m}) = \mathbf{Y_R}(\mathbf{m})\mathbf{Y_R^*}(\mathbf{m}))$	1024	128	896
IFFT	5120	4096	1024
Total	**11264**	**8320**	**2944**

Table 5.4: Reduction in Multiplication Operations using Accelerated Cross Correlation

	Original Cross Correlation	**Accelerated Cross Correlation**	**Saving**
FFT	$M\log_2(M)$	$M\log_2(M) - (M - 2M_R)$	$M - 2M_R$
IFFT	$M\log_2(M)$	$M\log_2(M) - (M - 2M_R)$	$M - 2M_R$
Total	$2M\log_2(M)$	$2M\log_2(M) - (2M - 4M_R)$	$\mathbf{2M - 4M_R}$

Table 5.5: Reduction in Addition Operations using Accelerated Cross Correlation

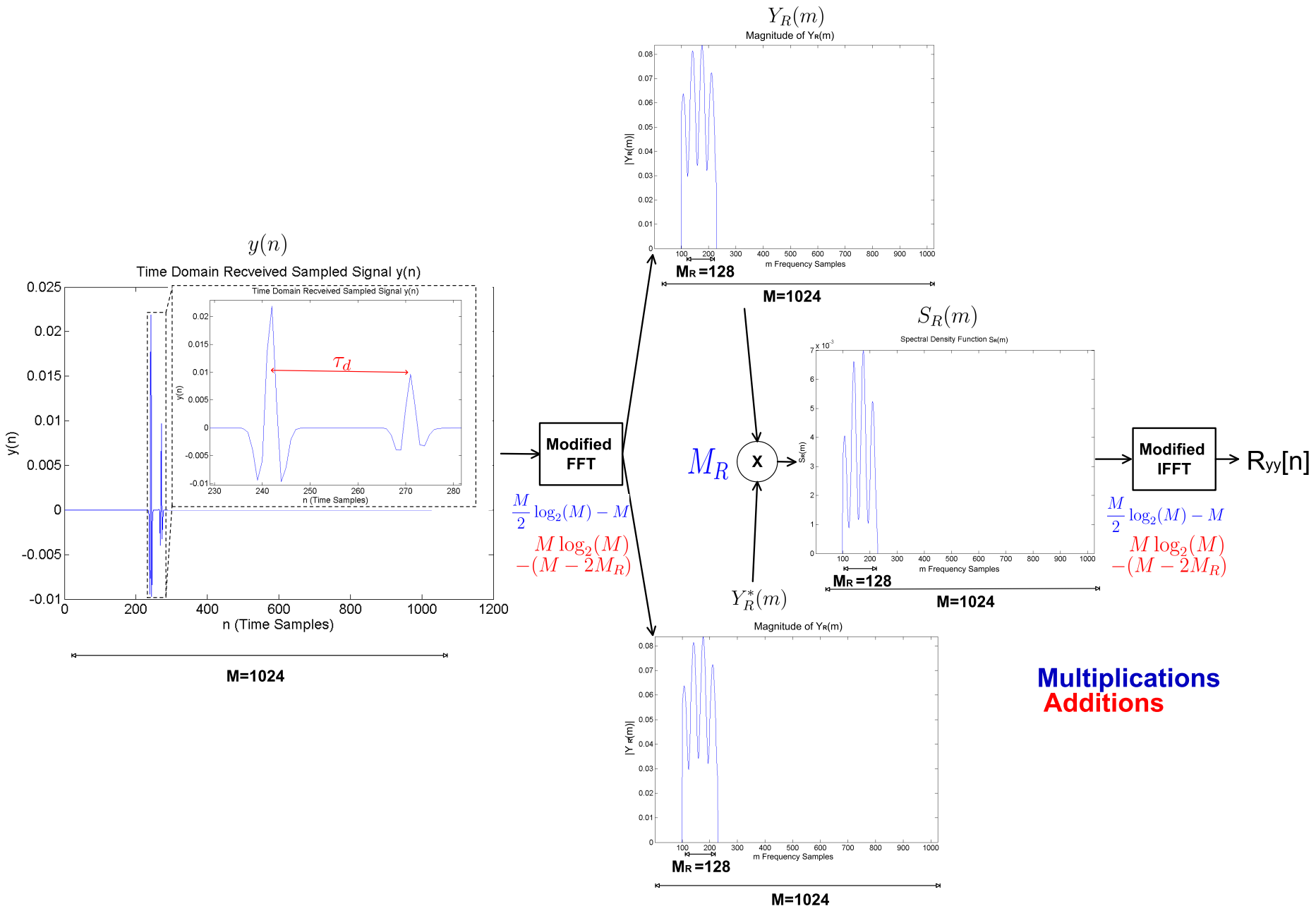

Figure 5.39: Stages of Accelerated Algorithm for input of 1024 samples

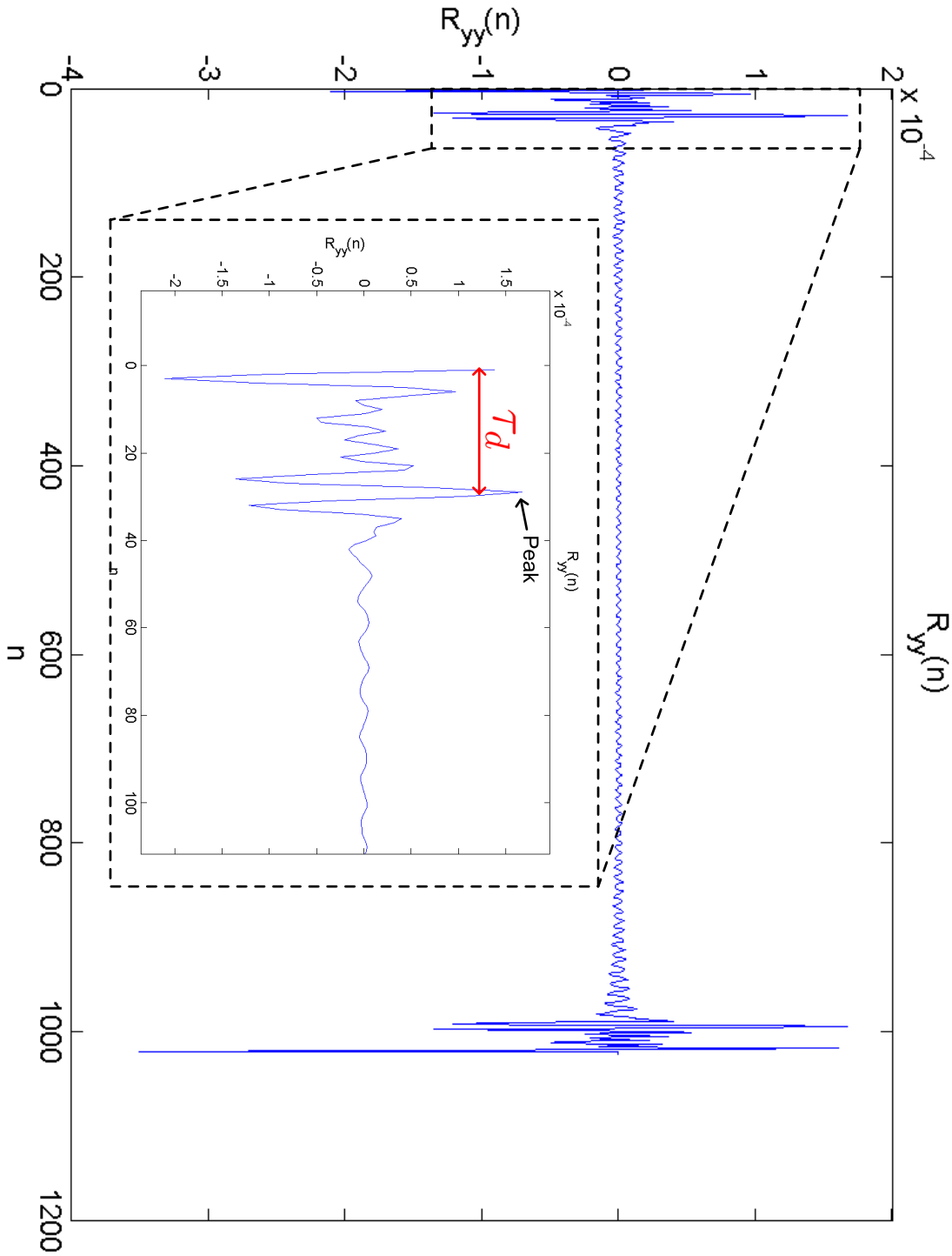

Figure 5.40: $R_{yy}(n)$

$\mathbf{M = 1024}$ $\mathbf{M_R = 128}$	**Original Cross Correlation**	**Accelerated Cross Correlation**	**Saving**
FFT	10240	9472	768
IFFT	10240	9472	768
Total	**20480**	**18944**	**1536**

Table 5.6: Reduction in Addition Operations using Accelerated Cross Correlation

5.6 Simulation of Acceleration Algorithm combined with Reflection based TDOA

The performance of the proposed accelerated auto-correlation technique was examined by employing ray tracing propagation modelling. Such simulations were computed for the indoor environment of Figure 5.42 , which contains 5 concrete facets. As with the earlier simulations of Section 5.2.2, 2 fixed base-station transmitters are placed within the room while the transmitted waveform from these base-stations consist of the Gaussian monocycle pulse of Figures 5.9-5.10. The physical position of the mobile receiver varies over each of the 546 locations represented in Figure 5.43.

Initial simulations involved the use of a noise-free received signal $y(t)$ generated by ray tracing computations. The results from employing such an approach are presented in the color coded propagation environment map of Figure 5.44, which show the location error for each of the 546 physical receiver locations. Subsequent simulations incorporated a pseudo random noise signal $n(t)$ added to a noise-free simulated received signal $y(t)$. An example of such a received signal is depicted in Figure 5.41 where the noise is limited to a peak amplitude proportional to the maximum received signal. Figure 5.45 show the geo-location errors incurred when employing a maximum noise amplitude corresponding to 4% of the maximum received amplitude. Additional simulations incorporated noise signals limited to 6% and 8% of this peak amplitude. The errors incurred for these differing noise levels are plotted alongside each-other in Figure 5.48 where error values are sorted in terms of ascending magnitude. Observing this Figure it can be seen that both the noise-free and 4% noise simulations result in errors below 0.1m (or 10cm) for most receiver locations with the exception of 5 positions (RX Point No. 541-546). However, even at the worst performing locations the position accuracy does not deteriorate beyond 0.146m. An average error over the 546 points of 0.037m and 0.038m was incurred for the noise-free and 4% noise respective channels. Using the accelerated technique this average error has only marginally increased compared to the full auto-correlation simulation of Section 5.2.2. In that un-accelerated configuration of the reflection based TDOA technique, average errors of 0.035m and 0.036 were observed using the same channel noise characteristics.

Noting Figure 5.48 it can be seen that incorporating 6% and 8% maximum noise amplitudes result in very poor performance. Such noise characteristics yield maximum errors exceeding 0.6m and 0.7m for 6% and 8% noise amp-

litudes respectively. In contrast more acceptable accuracy is achieved for the receiver point numbered $1 - 539$ where the error remains below 0.15m. However, beyond these points the error grows rapidly thus rendering the accelerated reflection based TDOA scheme unreliable when the received signal contains noise levels in excess of 6%. It seems that the addition of such noise level have a substantial detrimental effect when using the accelerated algorithm. This should be considered in contrast to the effect of noise on the un-accelerated geo-location algorithm of Section 5.2.2 where 6% and 8% resulted in maximum errors of 0.176m and 0.1942m respectively. As in the case of the un-accelerated simulations, increasing the noise levels can improve accuracy at certain locations. Specifically, for RX point numbers 541 to 543 in Figure 5.48 the addition of 4% noise results in lower errors compared to the noise free simulation. Recalling Section 5.2.2, this is due to the additive noise modifying peak amplitudes of received pulses. In scenarios where accuracy is improved with increasing noise levels, the first arriving reflected pulse peak amplitude is increased above the amplitudes of close consecutively arriving pulses. In such cases, autocorrelation correctly identifies the time difference between the line of sight and first arriving reflected pulses.

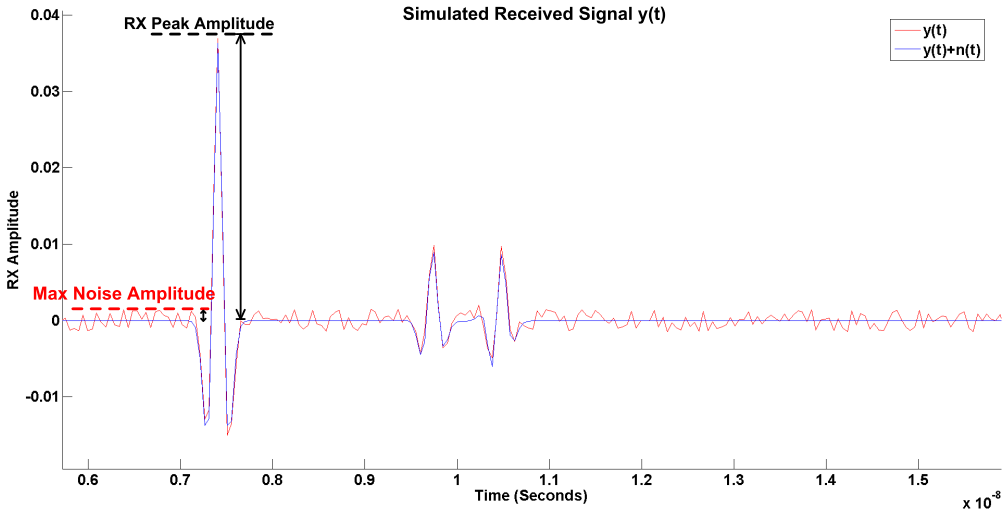

Figure 5.41: Received signal with added noise

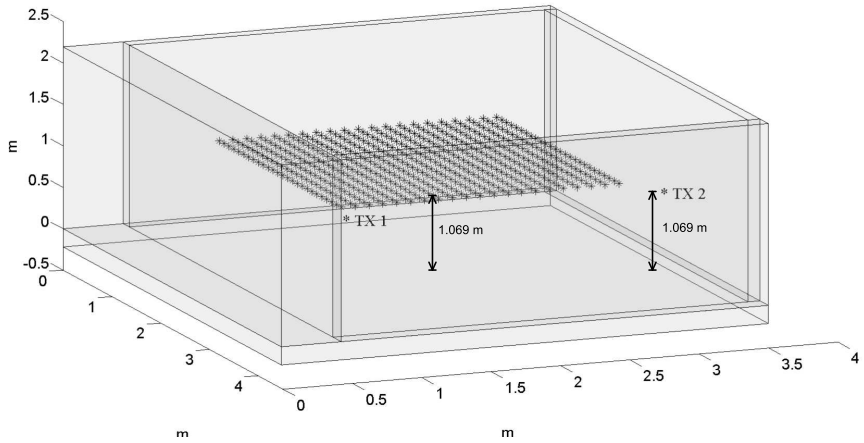

Figure 5.42: 3*D* View of Propagation Environment

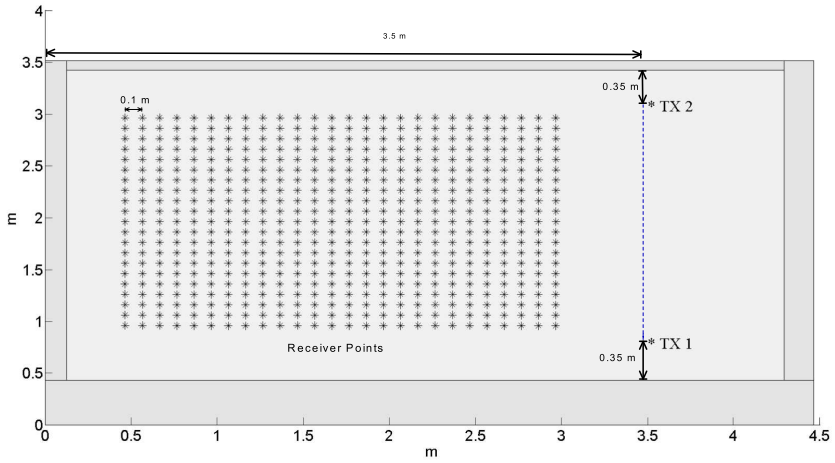

Figure 5.43: Plan View of Propagation Environment

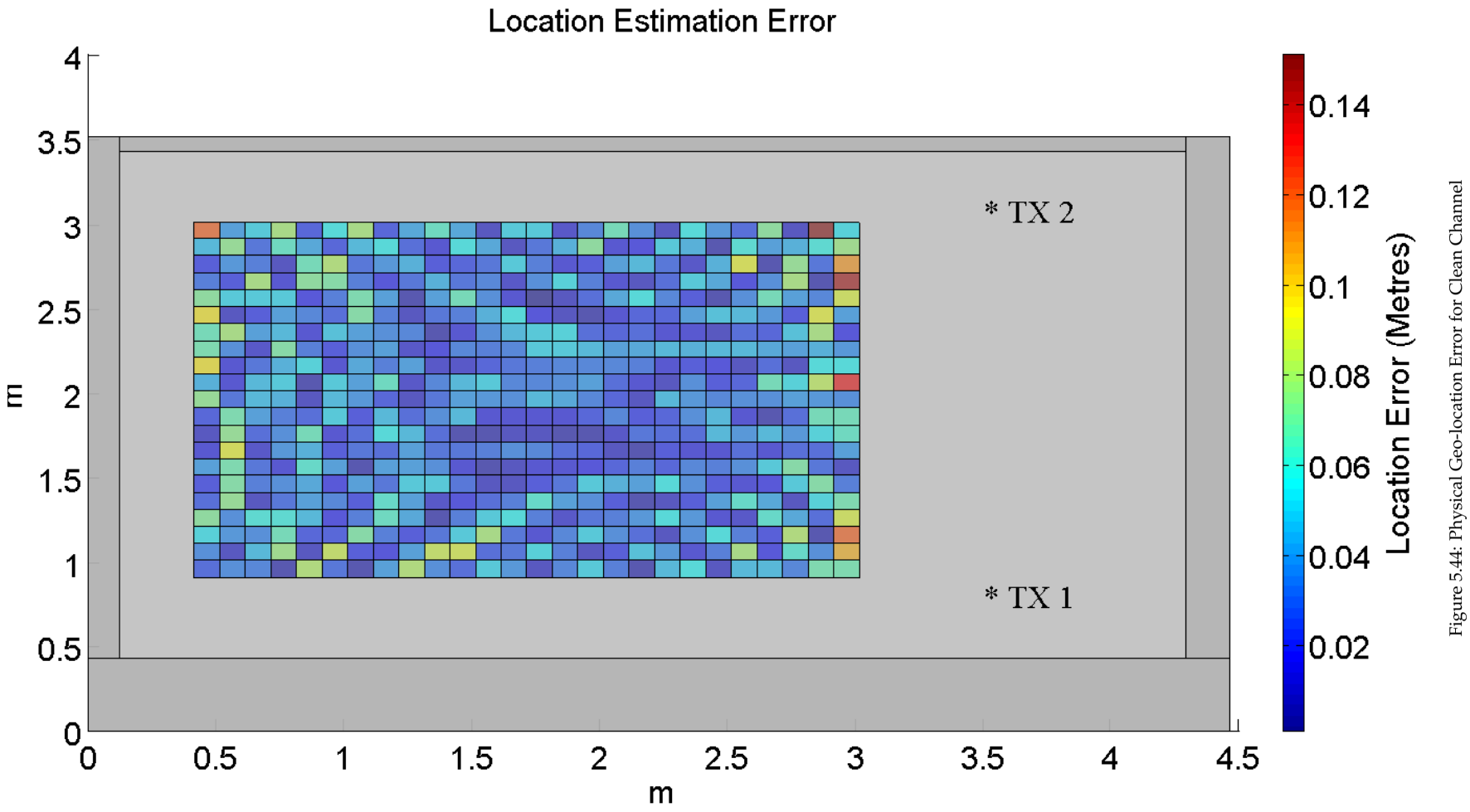

Figure 5.44: Physical Geo-location Error for Clean Channel

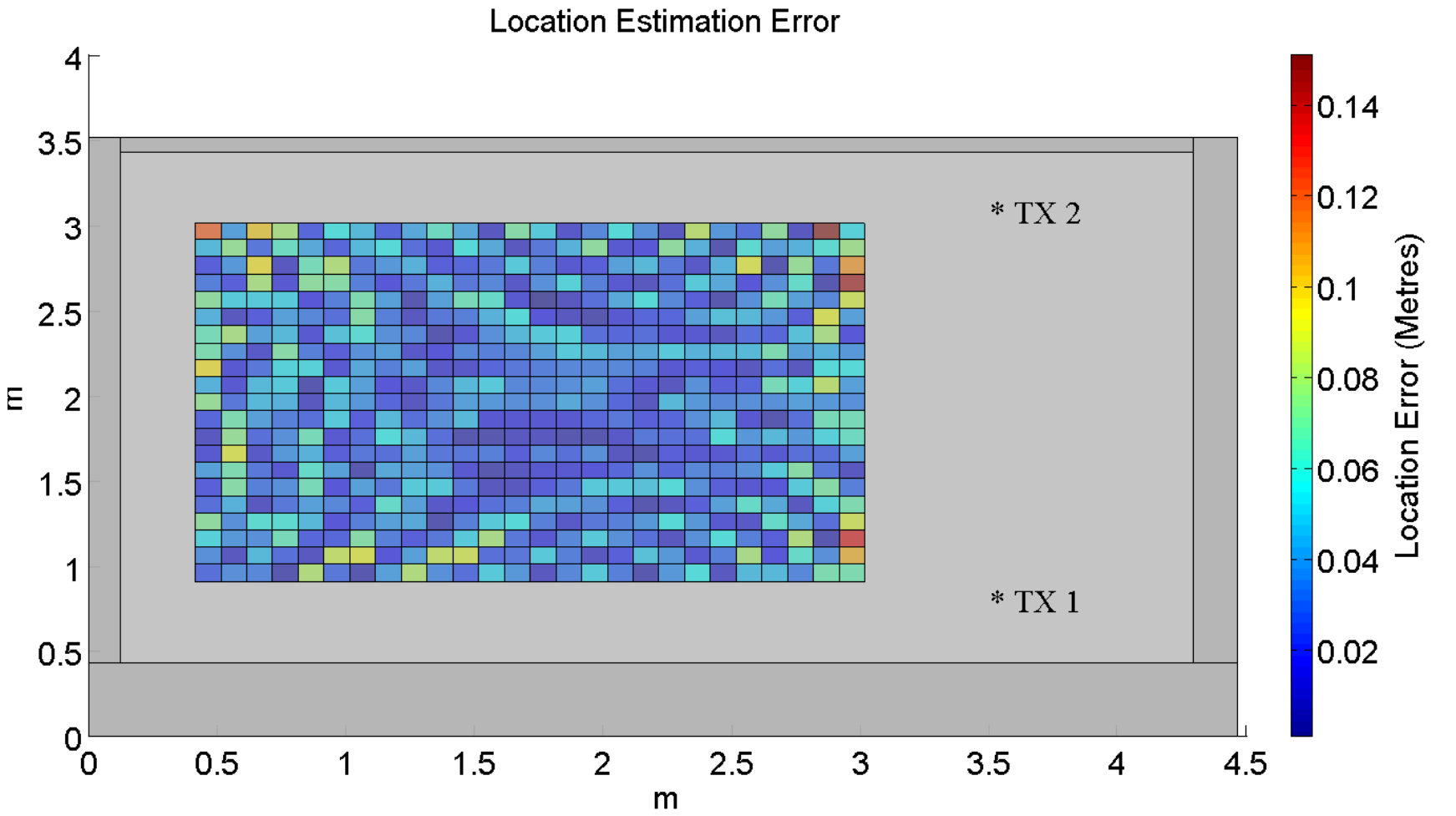

Figure 5.45: Physical Geo-location Error for 4% Noise in Channel

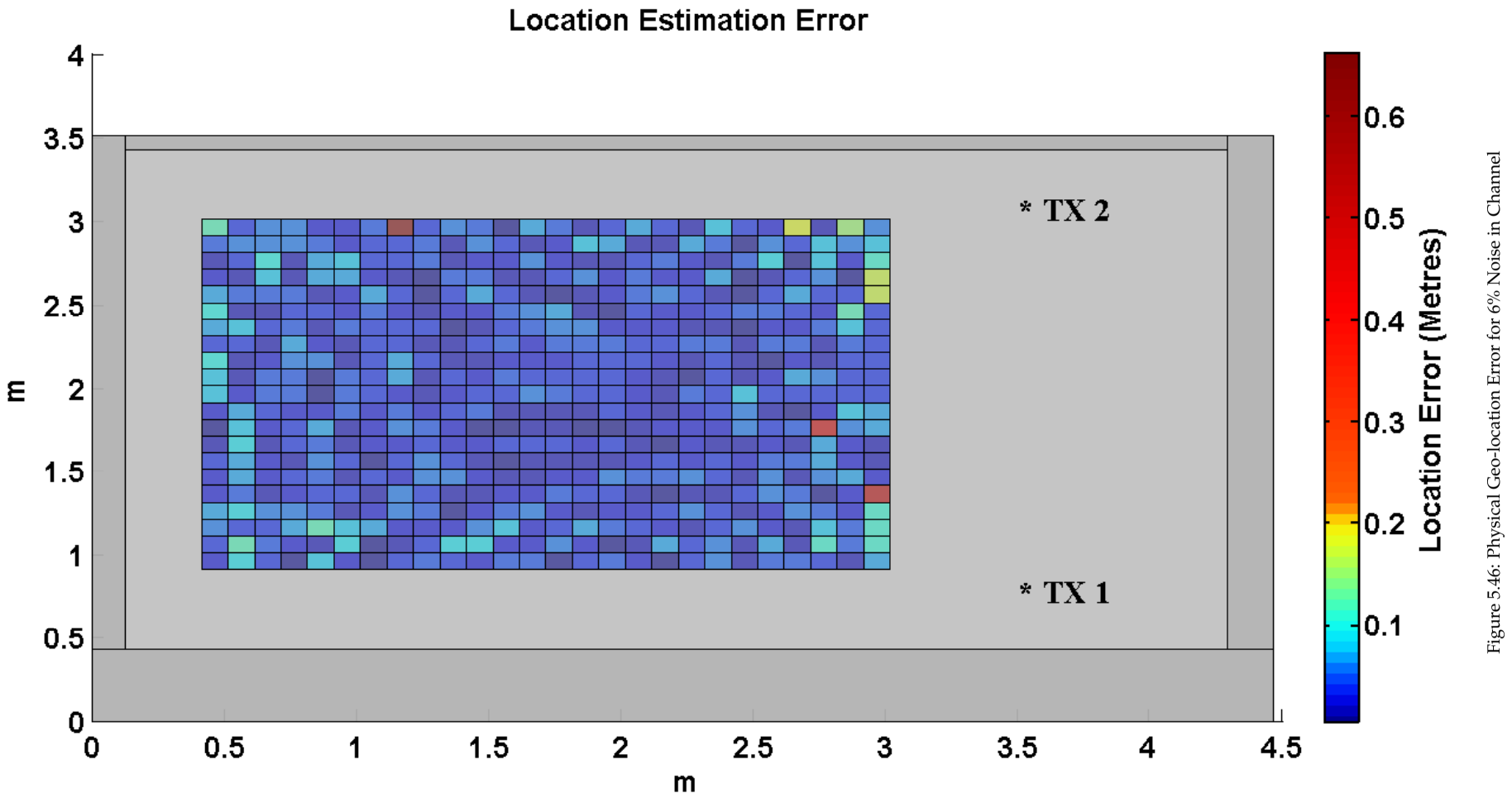

Figure 5.46: Physical Geo-location Error for 6% Noise in Channel

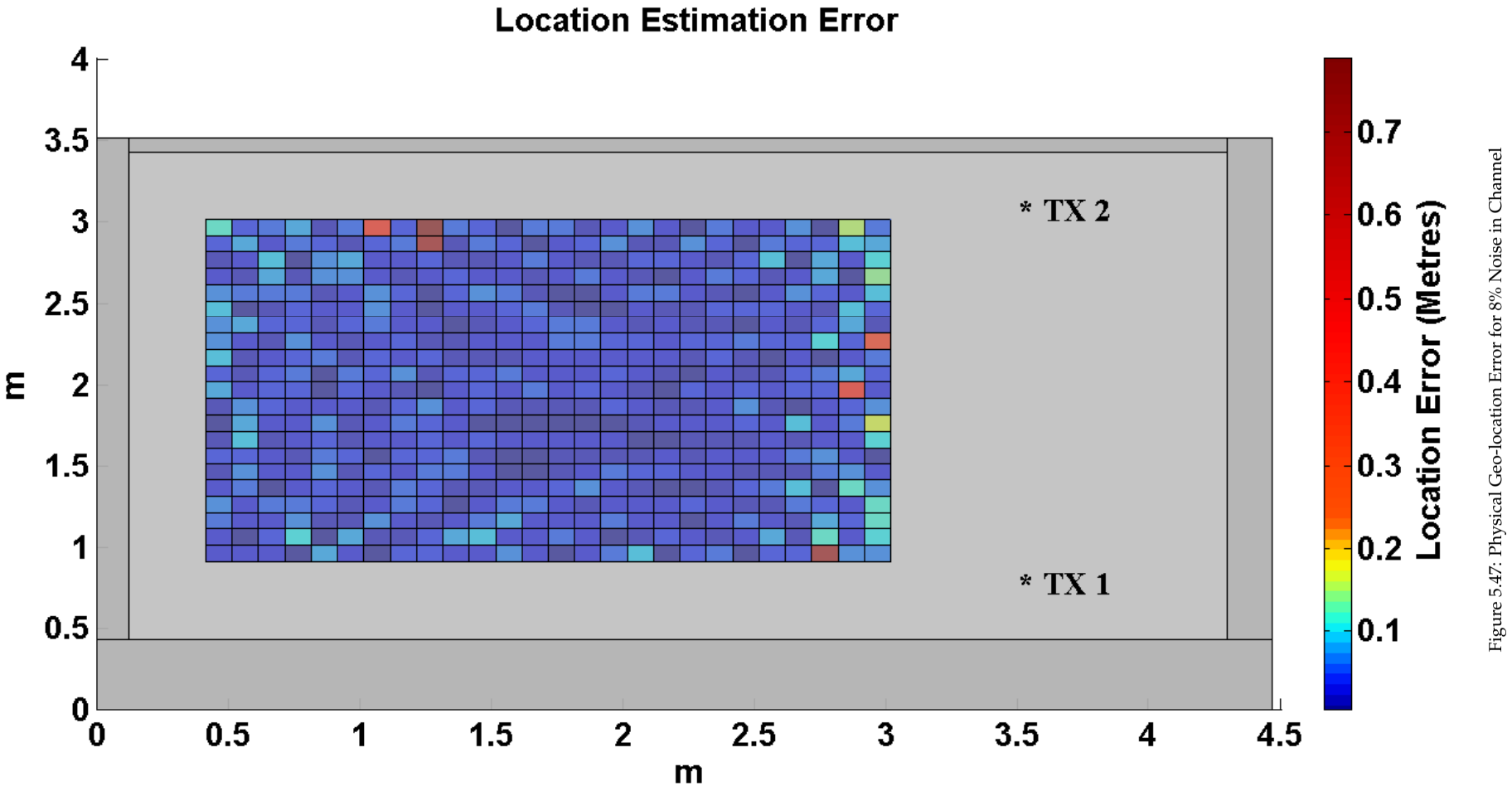

Figure 5.47: Physical Geo-location Error for 8% Noise in Channel

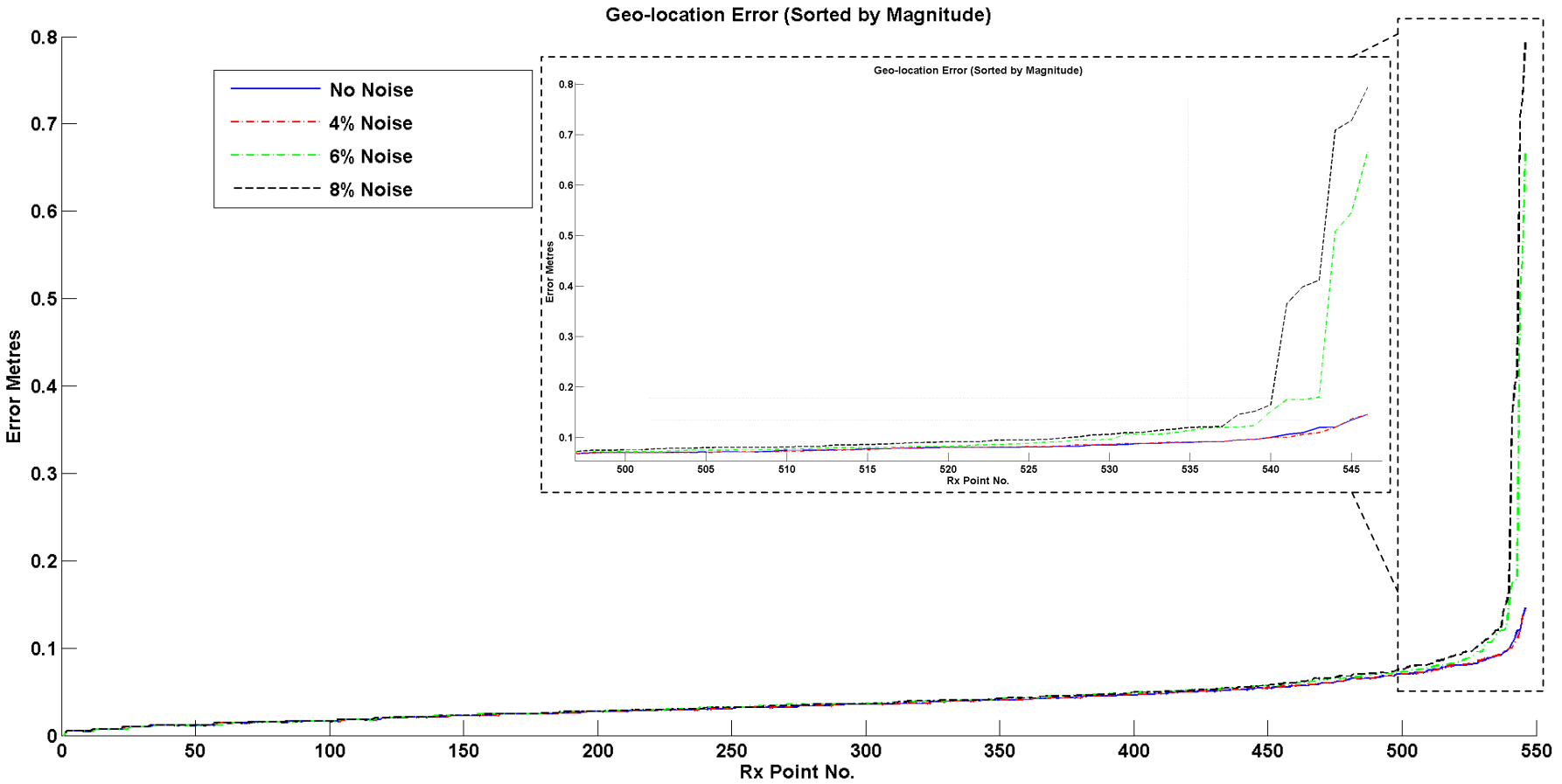

Figure 5.48: Geo-location Errors sorted by magnitude

5.7 Conclusion

Previously in Section 5.2, a reflection based TDOA positioning algorithm for UWB systems was introduced. This technique allows for a time based geo-location scheme using only 2 fixed base-stations to be deployed in the simulated environment of Section 5.2.2. While this approach achieves reasonable accuracy, incurring position errors on the order of 0.1m, the area in which the algorithm can be successfully applied is restricted. Recalling Section 5.2.1 this is attributable to the fact that different regions in the rectangular room of Figure 5.7 receive the first arriving reflected multi-path from a variety of scattering surfaces, as demonstrated earlier in Figure 5.11. As a consequence, the reflection based TDOA geo-location algorithm in its present form cannot be deployed to the entire propagation environment. Further work could eliminate this limitation by employing an initial mapping database created off-line whereby the regions of Figure 5.11-5.12 associated with each reflecting surface are cross referenced with TDOA measurements. However, most of the propagation environment is contained within a region where the first arriving multi-path component from each fixed base-station is attributable to a single reflecting facet, as shown in Figures 5.13-5.14. As a result, the algorithm in its current form can operate within most of the floor area of Figure 5.8. Ray-tracing propagation simulations of this scheme within this area of operation demonstrated minimum levels of accuracy in the order of 0.15m (15cm) with an average error of 0.036m (3.6cm) when pseudo random noise levels of 4% were incorporated into computed channels. However, increasing this noise level to 6% and 8% levels lead to maximum errors in excess of 0.17m (17cm).
A further addition to TDOA reflection based location was introduced in Section 5.4. This technique involved modifying the existing auto-correlation technique previously employed when determining the time difference of arrival between received UWB pulses. While applying correlation methods to heavily sampled UWB time domain signals can result in a significant processing overhead, the proposed accelerated auto-correlation technique reduces the amount of such computations required when computing TDOA values for reflection based geo-location. When employing a time domain received signal containing 1024 samples, the application of this acceleration algorithm reduces the amount of required additions and multiplication operation by 7.5% and 26.1% respectively. This enables TDOA measurements to be acquired faster than when using conventional frequency domain auto-correlation. Similar computational overhead associated with UWB time based schemes have previously

been identified [71, 17] when obtaining physical positions. However, combining reflection based TDOA, introduced in Section 5.2, with the proposed accelerated auto-correlation offers an approach for UWB time based geo-location that requires both less fixed base-stations and subsequent computation resources than conventional UWB based approaches [19]. Furthermore, simulations of this novel position technique yield an average error of $0.038m$ (3.8cm) with a maximum error in the order of 0.15m (15cm) for channels incorporating 4% additional noise. In contrast to the un-accelerated algorithm, quite large errors in excess of 0.6m are incurred when employing noise levels exceeding 6%. This deterioration of accuracy results in the application of the accelerated algorithm in such noise conditions to be deemed impractical.

In this chapter, the reflection-based reflection algorithm and subsequent acceleration technique were appraised using ray tracing simulations. However, a more realistic test of both could be obtained using empirical measurements from a typical indoor propagation environment. I recommend that any future work in pursuance of this topic would employ such measurement with an aim to appraising the performance and resilience of the algorithms presented here. In-particular such work should focus on studying the effects on accuracy of channel noise and time dependent fading due to the presence of moving objects in the environment.

Chapter 6

Conclusion and Future Directions

This research project has been concerned with the refinement of indoor radio frequency propagation techniques and the development of a novel reflection based geo-location scheme. Initial efforts of this work pertained to improvements of ray-tracing based modelling techniques. Specifically this involved the development of the acceleration algorithms presented in Chapters 3 and 4. These algorithms sought to improve the computational efficiency of ray tracing based propagation modelling thus resulting in faster simulation times and reduced computational requirements. Subsequent to these efforts, a novel UWB reflection based geo-location scheme was presented in Chapter 5. This scheme allows for geo-location to be carried out in a indoor room using reduced base-station infrastructure. It should be noted that the development and evaluation of this scheme was aided by the use of ray tracing propagation simulations. Furthermore, an alternative to traditional auto-correlation based time difference acquisition was also presented. This technique speeds up the processing associated with obtaining time difference of arrival (TDOA) measurements required by the aforementioned reflection based geo-location scheme.

6.1 Contribution

Initial efforts of this project resulted in the image removal visibility algorithm of Chapter 3. This technique removes invalid images at a preprocessing stage thus resulting in more efficient ray tracing simulations. Redundant first order images are identified by applying a projection plane based acceleration algorithm. A projection plane is tested in order to determine whether it is shadowed completely by at least T layers of facets, where T is the maximum transmissions permitted per ray. Facets behind such a shadowed plane are not considered when computing first order ray tracing paths and subsequently this results in a reduced number of images. Reductions in simulation times of up to 18.09% were achieved for large building environments. However, the performance of this algorithm in terms of computational savings is determined by the number of shadowed surfaces present. Furthermore, this in turn depends on the combination of the building environment's structure and the maximum permitted number of ray transmission in a simulation. This algorithm offers the distinct advantage of being suitable for use with ray tracing simulations where multiple transmissions through objects are considered for each ray. In addition it is applied without having to discretise entire propagation environments as was the case with previous techniques [66, 67].

In recognizing the importance of UWB wireless propagation as a means of precise indoor geo-location, it was imperative to incorporate the capability of modelling such channels in a ray tracing simulator. By employing frequency domain based simulations, propagation effects, such as those described in Sections 2.1.5.1-2.1.5.3 of Chapter 2, can be rigorously calculated over the wide-bandwidths of Ultra-Wideband (UWB) systems. However, such bandwidths of several Giga-Hertz can result in an enormous computational overhead. In Chapter 4 an acceleration technique was introduced that alleviates this burden. This approach reduces the computational expense associated with simulating wide-band channels while preserving the ability to rigorously account for frequency-dependent effects. An alternative means of obtaining the time domain received signal was also introduced that eliminates the need for interpolation of frequency domain samples and subsequent inverse Fourier transform operations. The performance of the acceleration algorithm was appraised using simulations which incorporated frequency-dependent empirical material properties. Applying the frequency sweep acceleration technique to such simulations resulted in a reduction of computation times on the order of 30% while incurring errors in the time domain of less than 4.5%.

Subsequent to these improvements of ray tracing modelling techniques, a reflection based TDOA positioning algorithm for UWB systems was introduced in Section 5.2 of Chapter 5. This technique enables time based geo-location using only 2 fixed base-stations to be deployed over an operational zone contained within a typical rectangular shaped room. Ray-tracing propagation simulations of this scheme demonstrated minimum levels of accuracy of 0.15m (15cm) with an average error of 0.036m (3.6cm) for simulated channels incorporating a noise level of 4%.

A further addition to TDOA reflection based location was introduced in Section 5.4. This algorithm involved modifying the existing auto-correlation technique previously employed when determining the time difference of arrival between received UWB pulses. While applying correlation methods to heavily sampled UWB time domain signals can result in a significant processing overhead, the proposed accelerated auto-correlation technique reduces the number of these computations needed. Applying this algorithm to a time domain signal containing 1024 samples resulted in addition and multiplication operations being reduced by 7.5% and 26.1% respectively. Essentially, this technique enables TDOA measurements between consecutively received pulses (In this case the LOS and first arriving reflected pulse) to be acquired faster than using conventional frequency domain based auto-correlation.

6.2 Future Directions

6.2.1 Ray-tracing Based Propagation Modelling

In the course of this work there has been an emphasis on improving the efficiency of ray tracing based propagation modelling. However, the developments presented in this thesis have been based on the assumption that simulations were executed using computer architectures comprising of single or even possibly dual core CPU technologies. A notable trend of modern multimedia based computing has been the introduction of Graphical Processing Units (GPU) [75]. Originally this processor was developed for multi-media graphical applications as a dedicated hardware component for the purposes of executing graphic-based computations. Previously such operations were carried out by the CPU but with the advent of more demanding graphical applications, such as those found in modern computer games, a specialized processing unit was required [76].

A particular characteristic of GPU units is the large number of processing cores available. In some cases, such as that of the NVIDIA GTX 260 this can be as many as 240 separate cores [77]. Consequently such architecture lends itself to be used in computational applications requiring parallel processing [78]. Ray tracing based propagation simulation is a potential application that would benefit from such a computational resource: For example, reduced simulations times may be possible when modelling wide-band propagation effects, such as those discussed in Section 2.1.5 and Chapter 4. This could be achieved by apportioning certain bandwidths of discrete frequencies to individual processing cores. An additional possible use of multiple processing cores could be the simultaneous simulation of multiple channels responses at varying physical transmitter-receiver locations. This would be of particular use in the generation of coverage maps where propagation predictions for a large number of receiver points are required.

While in the past programming graphics based processors may have been a cumbersome task, recently developed Application Programming Interfaces (API), such as NVIDIA's Compute Unified Device Architecture (CUDA) [79], have introduced C Programming type syntax to GPU based instructions [80]. Accordingly this allows non-specialist programmers to access the powerful resource of the GPU while maintaining the familiarities of classical C-based programming. In acknowledging this and continuing developments in GPU based computation , I recommend consideration of this technique in any fu-

ture possible developments of ray-tracing based propagation modelling.

6.2.2 UWB Geo-location

In chapter 5 a novel reflection-based geo-location algorithm was presented. In addition to this, a complementary computational acceleration technique was developed. While ray-tracing based simulations incorporating pseudo random noise were employed to demonstrate the operation of these approaches, a more comprehensive test would include empirical UWB channel data containing real-world noise and fading effects. Consequently, I recommend that any further work should include such physical measurements obtained from an indoor environment. Of particular interest would be the performance of the acceleration algorithm in practical noise conditions. Previously in Section 5.6 detrimental effects in the accuracy of this algorithm have been observed with levels of pseudo random noise in excess of 6% of the maximum received amplitude.

A computationally efficient alternative to auto-correlation was developed in Chapter 5. Central to this technique was the use of modified fast Fourier transforms (FFTs) that were optimised to produce sub-bands of full frequency domain outputs. A possible substitute to such operations might be a technique known as the Goertzel Algorithm [81]. This algorithm is already employed in applications where a Discrete Fourier Transform (DFT) is only required at several arbitrary chosen frequencies [82]. This is in contrast to an FFT which computes the DFT over the complete spectrum of frequencies. However, the Goertzel Algorithm is only more efficient than an FFT when it is required to compute a DFT for less than $\log_2 M$ frequency points out of a total spectrum of M (Chapter 9 of [72]). In the case of the acceleration algorithm of Section 5.4, the sub-band of 128 out of 1024 exceeds this ratio. However, with the use of parallel processing this limitation could be overcome. In [83] an implementation of the Goertzel on Field Programmable Gate Arrays (FPGA) hardware for the purpose of electronic device testing is described. Furthermore, such FPGA architecture, as used in modern electronic component design, include parallel processing capabilities making them ideal platforms for such implementations [84]. Consequently, any further development of the time difference acceleration algorithm present in Chapter 5 should consider the possibility of employing such an approach in place of FFT computations.

Appendix A

Frequency Domain Acceleration Technique

A.1 Freqeuncy Domain Polynomial

Previously in Chapter 4 a UWB ray tracing acceleration technique was presented. Central to this technique was the use of a polynomial to approximate a frequency domain ray response thus reducing the number of frequency samples required when modelling an UWB channel. This section provides a more comprehensive description of how the coefficients associated with such polynomials are employed in an analytical expression of the time domain received signal $r(t)$ seen in Equation 4.12 of Chapter 4.
In Section 4.2 of Chapter 4 an ultra-wideband channel was approximated as,

$$H(\omega) \simeq \sum_{i=1}^{N} e^{-\jmath\phi_i^d(\omega)} P_i(\omega). \tag{A.1}$$

where $P_i(\omega)$ is a m^{th} order polynomial and ϕ_i^d is the phase behaviour associated with the free-space propagation and is given by,

$$\phi_i^d(\omega) = \frac{d_i\omega}{c}, \tag{A.2}$$

where d_i is the distance ray i travels in free space and c is the speed of light in a vacuum.
Assuming a channel consisting of a single ray, Equation A.1 becomes,

$$H(\omega) \simeq e^{-\jmath\phi_1^d(\omega)} P_1(\omega). \tag{A.3}$$

The received time domain signal from transmitting a waveform $S(\omega)$ over

such a channel is computed as

$$r(t) = \mathcal{F}^{-1}\left(S\left(\omega\right)H\left(\omega\right)\right). \tag{A.4}$$

In essence this expression consists of an inverse Fourier transform of the product of the transmitted signal $S\left(\omega\right)$ and the frequency domain channel response $H\left(\omega\right)$. However when employing the approximation of Equation A.1, this received signal is given by,

$$r(t) \simeq \mathcal{F}^{-1}\left(S\left(\omega\right)P_1\left(\omega\right)e^{-\jmath\phi_1^d(\omega)}\right). \tag{A.5}$$

Since $r(t)$ is a real valued time domain signal, its frequency domain representation $R\left(\omega\right)$ must demonstrate complex conjugate symmetry such that $R^*\left(\omega\right) = R\left(-\omega\right)$. Accordingly the term $S\left(\omega\right)e^{-\jmath\phi_1^d}\left(\omega\right)P_1\left(\omega\right)$ in Equation A.5 must also adhere to complex conjugate symmetry.

The polynomial P_1 of Equation A.5 is expressed as

$$P_1(\omega) = \sum_{g=0}^{M}\left(\alpha_g + \jmath\beta_g\right)\omega^g, \tag{A.6}$$

where α_g and β_g are the respective real and imaginary parts of the g^{th} order coefficient and M is the highest order coefficient present in the polynomial. It should be noted that this polynomial is an approximation of the channel response for positive frequencies only and as a result does not demonstrate complex conjugate symmetry. This is seen for the 0^{th} order ($g = 0$) polynomial terms in Equation A.7 where,

$$\left(\alpha_0 + \jmath\beta_0\right)\omega^0 = \begin{cases} \alpha_0 + \jmath\beta_0 & \omega > 0 \\ \alpha_0 + \jmath\beta_0 & \omega < 0 \end{cases}. \tag{A.7}$$

Recalling from Equation A.5 that the polynomial $P_1(\omega)$ is eventually multiplied by $S(\omega)$, for a 0^{th} order terms this product is given by[1].

$$S(\omega)\left(\alpha_0 + \jmath\beta_0\right) = \begin{cases} S(\omega)\alpha_0 + \jmath S(\omega)\beta_0 & \omega > 0 \\ S(\omega)\alpha_0 + \jmath S(\omega)\beta_0 & \omega < 0 \end{cases}. \tag{A.8}$$

Clearly this expression does not demonstrate complex conjugate symmetry and in order to compensate for this a Hilbert transform is introduced. Such a

[1]The phase term $e^{-\jmath\phi_1^d}\left(\omega\right)$ is suppressed here for the purposes of clarity but is re-introduced later as a delay in the time domain

Hilbert transform of the time domain transmitted waveform $s(t)$ is given by,

$$\mathcal{H}\{s(t)\} = \begin{cases} -\jmath S(\omega) & \omega > 0 \\ \jmath S(\omega) & \omega < 0 \end{cases} . \tag{A.9}$$

where $S(\omega)$ is the frequency domain representation of the transmitted signal (ie. $S(\omega) = \mathcal{F}\{s(t)\}$).

This relationship between the Fourier and Hilbert transforms can be used to compensate for the non conjugate symmetry of a frequency domain expression. By substituting the term $\jmath\mathcal{H}\{s(t)\}$ in the place of $S(\omega)$ for the imaginary components of Equation A.8 the product of the 0^{th} order term of P_1 and the transmitted signal $S(\omega)$ now satisfy complex conjugate symmetry where,

$$(S(\omega)\alpha_0 - \mathcal{H}\{s(t)\}\beta_0) = \begin{cases} S(\omega)\alpha_0 + \jmath S(\omega)\beta_0 & \omega > 0 \\ S(\omega)\alpha_0 - \jmath S(\omega)\beta_0 & \omega < 0. \end{cases} . \tag{A.10}$$

This last step may seem controversial as $S(\omega)$ remains present in the real part of the coefficient $S(\omega)\alpha_0$. However this is permissable if the real and imaginary parts of the polynomial coefficient are herein treated separately. Reintroducing the phase term $e^{-\jmath\phi_1^d}(\omega)$ gives an expression for the contribution to the received signal for a 0^{th} order coefficient of the polynomial $P_1(\omega)$ as,

$$C_0(\omega) = S(\omega)\alpha_0 e^{-\jmath\phi_1^d} - \mathcal{H}\{S(t)\}\beta_0 e^{-\jmath\phi_1^d} \tag{A.11}$$

Noting the following identity of Fourier transforms,

$$s(t-a) = \mathcal{F}^{-1}\{S(\omega)e^{-\jmath a\omega}\}. \tag{A.12}$$

the time domain contribution $c_0(t)$ of the 0^{th} order polynomial coefficient is given by,

$$c_0(t) = \alpha_0 s(t - \frac{d_1}{c}) - \beta_0 s_H(t - \frac{d_1}{c}) \tag{A.13}$$

where

$$s(t - \frac{d_1}{c}) = \mathcal{F}^{-1}\{S(\omega)e^{-\jmath\phi_1^d}\}, \tag{A.14}$$

and

$$s_H(t) = \mathcal{F}^{-1}\{\mathcal{H}\{s(t)\}\}. \tag{A.15}$$

As a result of employing the Hilbert transform $\mathcal{H}\{S(t)\}$ seen previously in Equation A.11 the time domain contribution of Equation A.13 now yields a real valued received signal $r(t)$. While obtaining $s_H(t) = \mathcal{F}^{-1}\{\mathcal{H}\{S(t)\}\}$ may

seem like a cumbersome step, for a known transmitted waveform $s(t)$ this computation can be obtained prior to ray tracing simulation. In addition both $s(t)$ and $s_H(t)$ can be re-used for different channel simulations where the transmitted signal remains constant. This leaves only the polynomial coefficients (α_0, β_0) and the time delay $\frac{d_1}{c}$ to be obtained from ray tracing simulations.

The Hilbert transform is also employed for higher order polynomial coefficient. As in the case of the 0^{th} order coefficient, the product of the 1^{st} ($g = 1$) order polynomial coefficient and $S(\omega)$ does not exhibit complex conjugate symmetry. Suppressing the free-space propagation phase term $e^{-\jmath\phi_1^d}$, the frequency domain contribution of this product is given by

$$S(\omega)\left(\alpha_1 + \jmath\beta_1\right)(\omega) = \begin{cases} S(\omega)\alpha_1 \mid \omega \mid +\jmath S(\omega)\beta_1 \mid \omega \mid & \omega > 0 \\ -S(\omega)\alpha_1 \mid \omega \mid -\jmath S(\omega)\beta_1 \mid \omega \mid & \omega < 0 \end{cases}. \quad \text{(A.16)}$$

Substituting $j\mathcal{H}\{s(t)\}$ for $S(\omega)$ of the real part yields,

$$\left(\jmath\mathcal{H}\{s(t)\}\alpha_1 + \jmath S(\omega)\beta_1\right)(\omega) = \begin{cases} S(\omega)\alpha_1 \mid \omega \mid +\jmath S(\omega)\beta_1 \mid \omega \mid & \omega > 0 \\ S(\omega)\alpha_1 \mid \omega \mid -\jmath S(\omega)\beta_1 \mid \omega \mid & \omega < 0 \end{cases}. \quad \text{(A.17)}$$

Re-introducing the phase $e^{-\jmath\phi_1^d}$ associated with free space propagation, the contribution from the 1^{st} order polynomial coefficient is given by,

$$C_1(\omega) = \jmath\mathcal{H}\{s(t)\}\alpha_1\omega e^{-\jmath\phi_1^d(\omega)} + S(\omega)\jmath\beta_1\omega e^{-\jmath\phi_1^d(\omega)} \quad \text{(A.18)}$$

where

$$\phi_1^d(\omega) = \frac{d_1\omega}{c}. \quad \text{(A.19)}$$

Noting the Fourier transform identity,

$$\mathcal{F}^{-1}\{(\jmath\omega)^g S(\omega)\} = \frac{d_g}{dt^g}s(t), \quad \text{(A.20)}$$

the overall time domain contribution $c_1(t)$ from the 1^{st} order polynomial coefficients is expressed as,

$$c_1(t) = \alpha_1\frac{d_g}{dt^g}s_H\left(t - \frac{d_1}{c}\right) + \beta_1\frac{d_g}{dt^g}s\left(t - \frac{d_1}{c}\right), \quad \text{(A.21)}$$

where c is the speed of light in a vacuum and d_1 is the propagation length of the ray.

Extending a similar treatment to higher order polynomial coefficients, gives

an approximation for the overall contribution from a single ray $r(t)$,

$$\begin{aligned} r(t) &\simeq \alpha_0 s\left(t-\frac{d_1}{c}\right) - \beta_0 s_H\left(t-\frac{d_1}{c}\right) \\ &+ \sum_{g=1,3,5\ldots}^{m-1} j^{g-1}\left(\alpha_g \frac{d_g}{dt^g} s_H\left(t-\frac{d_1}{c}\right) + \beta_g \frac{d_g}{dt^g} s\left(t-\frac{d_1}{c}\right)\right) \\ &+ \sum_{g=2,4,6\ldots}^{m} j^{g}\left(\alpha_g \frac{d_g}{dt^g} s\left(t-\frac{d_1}{c}\right) - \beta_g \frac{d_g}{dt^g} s_H\left(t-\frac{d_1}{c}\right)\right), \end{aligned} \tag{A.22}$$

where m is the highest order of the polynomial approximation.
An example of a typical waveform employed as the transmitted signal $s(t)$ in Equation A.22 is shown in Figure A.1. This signal consists of a Gaussian mono-cycle pulse expressed in the time domain as,

$$s\left(t\right) = \left[1 - 4\pi\left(\frac{t}{t_n}\right)^2\right] \exp\left(-2\pi\left(\frac{t}{t_n}\right)^2\right), \tag{A.23}$$

where t_n is a scaling factor that determines the bandwidth of the pulse. For this particular case $t_n = 0.520$ nanoseconds. In addition the waveform $s_H(t)$, which is calculable as $s_H(t) = \mathcal{F}^{-1}\{\mathcal{H}\{S(t)\}\}$ is also shown along side $s(t)$. For a pre-known transmitted pulse both these waveform ($s(t)$ and $S_H(t)$) can be computed prior to ray tracing simulation.
Equation A.22 offers an alternative to the existing approach of computing a received time domain signal $r(t)$ where,

$$r(t) = \mathcal{F}^{-1}\left(S\left(\omega\right) H\left(\omega\right)\right). \tag{A.24}$$

Furthermore the novel technique of Equation A.22 avoids having to interpolate the channel response $H\left(\omega\right)$ for all frequencies ω present within $S\left(\omega\right)$. Assuming knowledge of the transmitted time domain waveform $s(t)$, $s_H(t)$ can be pre-computed prior to ray tracing simulation computations. Employing the expression in Equation A.22, $r(t)$ is calculated using a combination of the coefficients of the polynomial P_1 and the path delays $\frac{d_1}{c}$ of a ray, both of which are obtained from the ray tracing simulation.

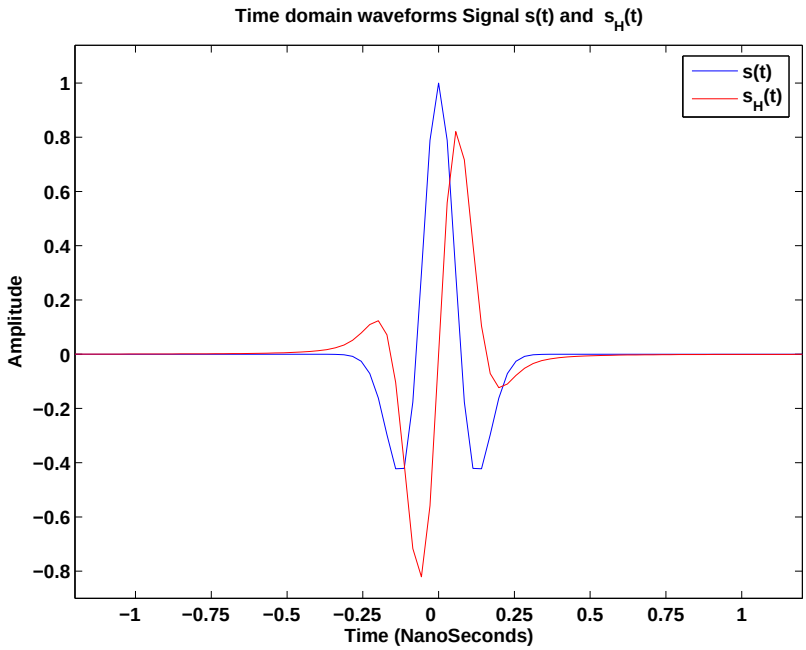

Figure A.1: Pre-computed waveforms $s(t)$ and $s_H(t)$

Appendix B

Geo-location

B.1 2D TDOA Hyperbola

The following is a brief outline of the method of computing a hyperbola of possible client locations using TDOA measurements in a scenario where a constant client station height z is assumed. For a recorded time difference of arrival value τ_d between 2 fixed base-stations ($TX1$, $TX2$), a client station's geographical position will lie on a hyperbolic curve similar to that shown in Figure B.1.

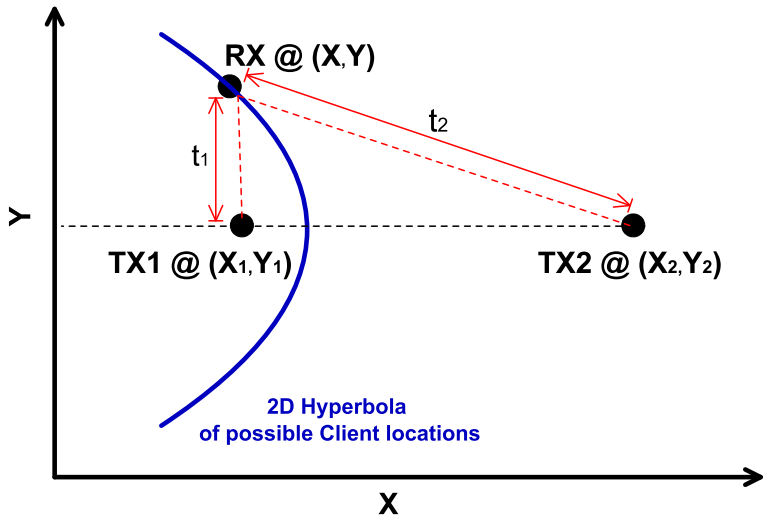

Figure B.1: 2D TDOA Hyperbola for Fixed Height z

The time difference of arrival τ_d is given by,

$$\tau_d = t_2 - t_1, \tag{B.1}$$

where t_1 and t_2 are the respective times of flight from base-stations $TX1$ and $TX2$ to a mobile client. The duration t_1 is expressed as,

$$t_1 = \frac{\sqrt{(x_1 - x)^2 + (y_1 - y)^2}}{c}, \tag{B.2}$$

where c is the speed of electromagnetic wave propagation, (x, y) is a physical position on the curve of Figure B.1 and (x_1, y_1) corresponds to the location of the base-station $TX1$. Rearranging Equation B.2 allows t_1 to be expressed as,

$$c^2 t_1^2 = x_1^2 - 2x_1 x + x^2 + y_1^2 - 2y_1 y + y^2. \tag{B.3}$$

Applying a similar treatment to the time of flight t_2 from the base-station $TX2$ gives,

$$c^2 t_2^2 = x_2^2 - 2x_2 x + x^2 + y_2^2 - 2y_2 y + y^2, \tag{B.4}$$

where (x_2, y_2) represents the location of the base-station $TX2$. Noting Equation B.1, the time difference of arrival $\tau_d = t_2 - t_1$ becomes,

$$c^2 \tau_d^2 = x_2^2 - x_1^2 + y_2^2 - y_1^2 + 2x\,(x_1 - x_2) + 2y\,(y_1 - y_2)\,. \tag{B.5}$$

This equation describes the hyperbola of possible client station locations seen previously in Figure B.1. In conventional TDOA schemes the client's position is obtained by finding an intersection point between 2 of more such hyperbolic curves. The additional hyperbola is obtained using an extra base-station in conjunction with $TX1$ or $TX2$.

B.2 Derivation of relationship between period F_d and time delay τ_d

In Chapter 5 the relationship between a frequency domain period F_d and a time domain delay τ_d was explored. The following is a more detailed derivation of the expression for spectral density function $S(f)$ with respect to the TDOA delay τ_d seen previously in Section 5.4[1].

$$S(f) = Y(f)Y^*(f). \tag{B.6}$$

$Y(f)$ is the frequency domain representation of the received time domain signal $y(t)$ which is expressed in Equation 5.5 as,

$$y(t) = x(t) + Ax(t - \tau_d). \tag{B.7}$$

Noting this representation of the received signal, the spectral density function $S(f)$ of Equation B.6 can be written as,

$$S\left(f\right) = Y\left(f\right)Y^*\left(f\right) = \mathcal{F}\{x(t) + Ax(t - \tau_d)\}\mathcal{F}^*\{x(t) + Ax(t - \tau_d)\}, \tag{B.8}$$

where $\mathcal{F}$ denotes a Fourier transform. Noting the following identity of Fourier transforms,

$$\mathcal{F}\{x(t - \tau_d)\} = X\left(f\right)e^{-\jmath 2\pi f\tau_d}, \tag{B.9}$$

allows Equation B.8 to be written as,

$$S\left(f\right) = \left[X\left(f\right) + AX\left(f\right)e^{-\jmath 2\pi f\tau_d}\right]\left[X\left(f\right) + AX\left(f\right)e^{-\jmath 2\pi f\tau_d}\right]^*, \tag{B.10}$$

where $X\left(f\right)$ is the frequency domain representation of $x\left(t\right)$. Expressing the exponential term in Equation B.10 using Euler's formula yields,

$$\begin{aligned} S\left(f\right) &= X\left(f\right)X^*\left(f\right)\left[1 + A\left(\cos 2\pi f\tau_d - \jmath \sin 2\pi f\tau_d\right)\right] \\ &\quad \left[1 + A\left(\cos 2\pi f\tau_d - \jmath \sin 2\pi f\tau_d\right)\right]^*, \end{aligned} \tag{B.11}$$

Accounting for the complex conjugate, denoted by $*$ in Equation B.11 becomes,

$$\begin{aligned} S\left(f\right) &= X\left(f\right)X^*\left(f\right)\left[1 + A\left(\cos 2\pi f\tau_d - \jmath \sin 2\pi f\tau_d\right)\right] \\ &\quad \left[1 + A\left(\cos 2\pi f\tau_d + \jmath \sin 2\pi f\tau_d\right)\right]. \end{aligned} \tag{B.12}$$

[1] f denotes frequency in Hertz (Hz)

Expanding the expression of Equation B.12,

$$\begin{aligned} S(f) &= X(f)\,X^*(f) \\ &\quad [1 + A(\cos 2\pi f\tau_d - \jmath \sin 2\pi f\tau_d) + A(\cos 2\pi f\tau_d + \jmath \sin 2\pi f\tau_d) \\ &\quad + A^2(\cos 2\pi f\tau_d - \jmath \sin 2\pi f\tau_d)(\cos 2\pi f\tau_d + \jmath \sin 2\pi f\tau_d)], \end{aligned} \quad \text{(B.13)}$$

which reduces to,

$$S(f) = X(f)\,X^*(f)\left[1 + 2A\cos 2\pi f\tau_d + A^2\left(\cos^2 2\pi f\tau_d + \sin^2 2\pi f\tau_d\right)\right]. \quad \text{(B.14)}$$

Subsequently employing the trigonometric identity,

$$\sin^2 2\pi f\tau_d + \cos^2 2\pi f\tau_d = 1, \quad \text{(B.15)}$$

allows $S(f)$ to be written as,

$$S(f) = X(f)\,X^*(f)\left[1 + A^2 + 2A\cos 2\pi f\tau_d\right] \quad \text{(B.16)}$$

or alternatively,

$$S(f) = X(f)\,X^*(f)\left[1 + A^2 + 2A\cos 2\pi f\tau_d\right]. \quad \text{(B.17)}$$

Noting that,

$$X(f)\,X^*(f) = |X(f)|^2 \quad \text{(B.18)}$$

Equation B.17 now becomes

$$S(f) = |X(f)|^2\left[A^2 + 1 + 2A\cos 2\pi f\tau_d\right] \quad \text{(B.19)}$$

This equation serves as an expression of $S(f)$ in terms of the TDOA delay τ_d. This delay value τ_d, which is present within the term $2A\cos 2\pi f\tau_d$ of Equation B.17, is ultimately responsible for the period observed in $S(f)$.

Appendix C

Acronyms and Abbreviations

AOA	Angle of Arrival
API	Application Programming Interface
CPU	Central Processing Unit
DFT	Discrete Fourier Transforms
f	frequency
FFT	Fast Fourier Transforms
FCC	Federal Communication Commission
FEM	Finite Element Method
FDTD	Finite Difference Time Domain
GCC	Generalized Cross Correlation
GO	Geometric Optics
GHz	Giga-Hertz
GPS	Global Positioning System
GPU	Graphical Processing Unit
GTD	Geometrical Theory of Diffraction
Hz	Hertz
IDFT	Inverse Discrete Fourier Transforms
IEEE	Institute of Electrical and Electronics Engineers
IFFT	Inverse Fast Fourier Transforms
LAN	Local Area Network
LOS	Line of Sight
m	metre
MHz	Mega-Hertz
NLOS	Non Line of Sight
PAM	Pulse Amplitude Modulation
PPM	Pulse Position Modulation

UWB	Ultra Wideband
UTD	Unform Theory of Diffraction
WLAN	Wireless Local Area Network
RX	Receiver
RF	Radio Frequency
SBR	Shoot and Bounce Ray-Tracing
SS	Signal Strength
t	time
TDOA	Time Difference of Arrival
TOA	Time of Arrival
TX	Transmitter
2D	Two Dimensional
3D	Three Dimensional

Bibliography

[1] H. Hashemi and D. Tholl. Statistical modeling and simulation of the rms delay spread of indoor radio propagation channels. *IEEE Transactions on Vehicular Technology*, 43(1):110–120, Feb. 1994.

[2] A. Saleh and R. Valenzuela. A statistical model for indoor multipath propagation. *IEEE Journal on Selected Areas in Communications*, 5(2):128–137, Feb. 1987.

[3] A.J. Motley and J.M.P. Keenan. Personal communication radio coverage in buildings at 900 mhz and 1700 mhz. *IET Electronics Letters*, 24(12):763–764, June 1988.

[4] S. C. Kim, Jr. Guarino, B. J., III Willis, T. M., V. Erceg, S. J. Fortune, R. A. Valenzuela, L. W. Thomas, J. Ling, and J. D. Moore. Radio propagation measurements and prediction using three-dimensional ray tracing in urban environments at 908 mhz and 1.9 ghz. *IEEE Transactions on Vehicular Technology*, 48(3):931–946, May 1999.

[5] J.L. Volakis and L.C. Kempel. Electromagnetics: computational methods and considerations. *IEEE Computational Science and Engineering*, 2(1):42–57, Spring 1995.

[6] A. Taflove. Review of the formulation and applications of the finite-difference time-domain method for numerical modeling of electromagnetic wave interactions with arbitrary structures. *Wave Motion*, 10(6):547–582, Dec. 1988.

[7] Eamon M. Kenny. *An Indoor Resourse Optimisation for TDMA Incorporating a Convex Space Building Configuration and Accurate Ray-Tracing*. PhD thesis, Department of Electronic Engineering, University of Dublin, Trinity College, Oct. 2003.

[8] D. Porcino and W. Hirt. Ultra-wideband radio technology: potential and challenges ahead. *IEEE Communications Magazine*, 41(7):66–74, July 2003.

[9] Liuqing Yang and G.B. Giannakis. Ultra-wideband communications: an idea whose time has come. *IEEE Signal Processing Magazine*, 21(6):26–54, Nov. 2004.

[10] S. Gezici, Z. Tian, G. B. Giannakis, H. Kobayashi, A. F. Molisch, H. V. Poor, and Z. Sahinoglu. Localization via ultra-wideband radios: a look at positioning aspects for future sensor networks. *IEEE Signal Processing Magazine*, 22(4):70–84, July 2005.

[11] K. Pahlavan, Xinrong Li, and J.P. Makela. Indoor geolocation science and technology. *IEEE Communications Magazine*, 40(2):112–118, Feb. 2002.

[12] M.S. Braasch and A.J. van Dierendonck. Gps receiver architectures and measurements. *Proceedings of the IEEE*, 87(1):48–64, Jan. 1999.

[13] Jr. Caffery, J. and G.L. Stuber. Subscriber location in cdma cellular networks. *IEEE Transactions on Vehicular Technology*, 47(2):406–416, May 1998.

[14] M. Porretta, P. Nepa, G. Manara, and F. Giannetti. Location, location, location. *IEEE Vehicular Technology Magazine*, 3(2):20–29, June 2008.

[15] P. Bahl and V.N. Padmanabhan. Radar: an in-building rf-based user location and tracking system. In *Proceedings of the 19th Annual Joint Conference of the IEEE Computer and Communications Societies*, volume 2, pages 775–784 vol.2, 2000.

[16] R.J. Fontana, E. Richley, and J. Barney. Commercialization of an ultra wideband precision asset location system. In *Proceedins of the IEEE Conference on Ultra Wideband Systems and Technologies*, pages 369–373, Nov. 2003.

[17] A. Molisch, H. Kobayashi, V. Poor, S. Gezici, and Z Sahinoglu. A two-step time of arrival estimation algorithm for impulse radio ultra wideband systems. In *Proceedings of the 13th European Signal Processing Conference*, pages 4–8, 2005.

[18] J. Xu, M. Ma, and C.L. Law. Position estimation using uwb tdoa measurements. pages 605–610, Sept. 2006.

[19] D. P. Young, C. M. Keller, D. W. Bliss, and K. W. Forsythe. Ultra-wideband (uwb) transmitter location using time difference of arrival (tdoa) techniques. In *Record of the 37th Asilomar Conference on Signals, Systems and Computers*, volume 2, pages 1225–1229, Nov. 2003.

[20] J. Diskin and C. Brennan. An efficient ray-tracing image removal algorithm for indoor 3d radiowave propagation modelling. In *Proceedings of the European Conference on Antennas and Propagation*, number ESA SP-626, page 743, Nice, France, Nov. 2006.

[21] J. Diskin and C. Brennan. Accelerated ray-tracing for indoor ultra-wideband propagation modelling. In *Proceedings of the 65th IEEE Vehicular Technology Conference*, pages 418 –422, Dublin, Ireland, April 2007.

[22] J. Diskin, A. Alomainy, and C. Brennan. An accelerated frequency domain ray-tracing simulator for ultra-wideband communications. In *Proceedings of the Progress in Elecromagnetics Research Symposium*, volume 5, pages 266–230, Beijing, China., March 2009. Progress in Electromagnetics Research Symposium (PIERS).

[23] William H. Press, Saul A. Teukolsky, William T. Vetterling, and Brian P. Flannery. *Numerical recipes in C: the art of scientific computing*. Cambridge University Press, New York, USA, 2nd edition, 1992.

[24] R. G. Kouyoumjian and P. H. Pathak. A uniform geometrical theory of diffraction for an edge in a perfectly conducting surface. *Proceedings of the IEEE*, 62(11):1448–1461, 1974.

[25] G. Liang and H.L. Bertoni. A new approach to 3-d ray tracing for propagation prediction in cities. *IEEE Transactions on Antennas and Propagation*, 46(6):853–863, June 1998.

[26] R.K. Luneburg and M. Herzberger. *Mathematical theory of optics*. University of California Press, 1964.

[27] M. Kline. An asymptotic solution of maxwell's equations. *Communications on Pure and Applied Mathematics*, 4(2-3):225–263, 1951.

[28] D. A. McNamara and C. W. I. Pistorius. *Introduction to the Uniform Geometrical Theory of Diffraction*. Artech House, 46 Gillingham Street, London SW1V 1AH, UK, 1990.

[29] Ali Hussein Muqaibel. *Characterization of Ultra Wideband Communication Channels*. PhD thesis, The Bradley Department of Electrical and Computer Engineering, Virginia Polytechnic Institute and State University, 2003.

[30] David M. Pozar. *Microwave Engineering*. Wiley, New York, NY, USA, 2nd edition, 1998.

[31] Constantine A Balanis. *Advanced Engineering Elecromagnetics*. John Wiley & Sons, Inc., 1989.

[32] US Inan and AS Inan. *Engineering Electromagnetics*. Addison-Wesley Inc, California, 1999.

[33] J. B. Keller. Geometrical theory of diffraction. *Journal of the Optical Society of America*, 52:116–130, Feb. 1962.

[34] M. C. Lawton and J. P. McGeehan. The application of gtd and ray launching techniques to channel modelling for cordless radio systems. In *Proceedings of the 42nd IEEE Vehicular Technology Conference*, pages 125–130, May 1992.

[35] M.C. Lawton and J.P. McGeehan. The application of a deterministic ray launching algorithm for the prediction of radio channel characteristics in small-cell environments. *IEEE Transactions on Vehicular Technology*, 43(4):955–969, Nov. 1994.

[36] S.Y. Seidel and T.S. Rappaport. Site-specific propagation prediction for wireless in-building personal communication system design. *IEEE Transactions on Vehicular Technology*, 43(4):879–891, Nov. 1994.

[37] A. M. Attiya and A. Safaai-Jazi. Simulation of ultra-wideband indoor propagation. *Microwave and Optical Technology Letters*, 42:103–108, 2004.

[38] A. Muqaibel, A. Safaai-Jazi, A. Bayram, A. M. Attiya, and S. M. Riad. Ultrawideband through-the-wall propagation. *IEE Proceedings Microwaves, Antennas and Propagation*, 152(6):581–588, Dec. 2005.

[39] A. Hirose and S. Masuyama. Uwb measurement, complex-amplitude texture, and walled-ltsa array in plastic landmine visualization. In *IEEE International Conference on Ultra-Wideband, 2007. ICUWB 2007.*, pages 46 –49, Sept. 2007.

[40] C.P. Lim, R.J. Burkholder, J.L. Volakis, and R.J. Marhefka. Propagation modeling of indoor wireless communications at 60 ghz. In *Proceedings of IEEE Antennas and Propagation Society International Symposium*, pages 2149–2152, July 2006.

[41] G. Tiberi, S. Bertini, W.Q. Malik, A. Monorchio, D.J. Edwards, and G. Manara. Modeling of uwb channels by using an efficient ray tracing procedure. In *Proceedings of the IEEE Antennas and Propagation Society International Symposium*, pages 349–352, June 2007.

[42] J. Jemai, P. Peggers, G.F. Pedersen, and T. Kurner. On the applicability of deterministic modelling to indoor uwb channels. In *Proceedings of the 3rd workshop on Positioning, Navigation and Communication*, pages 139–148, Hanover, Germany, 2006.

[43] Y. Yao. A time-domain ray model for predicting indoor wideband radio channel propagation characteristics. In *Proceedings of 6th IEEE International Conference on Universal Personal Communications*, volume 2, pages 848–852, Oct. 1997.

[44] Richard Yao, Wenwu Zhu, and Zhenq Chen. An efficient time-domain ray model for uwb indoor multipath propagation channel. In *Proceedings of the 58th IEEE Vehicular Technology Conference*, volume 2, pages 1293–1297, Oct. 2003.

[45] T.W. Barrett. History of ultrawideband (uwb) radar & communications: pioneers and innovators. In *Proceedings of Progress in Electromagnetics Research Symposium*. Progress in Electromagnetics Research Symposium (PIERS), 2000.

[46] T.S.P. See and Zhi Ning Chen. A small uwb antenna for wireless usb. In *Proceedings of the IEEE International Conference on Ultra-Wideband*, pages 198–203, Sept. 2007.

[47] I. Gresham, A. Jenkins, R. Egri, C. Eswarappa, N. Kinayman, N. Jain, R. Anderson, F. Kolak, R. Wohlert, S.P. Bawell, J. Bennett, and J.P. Lanteri. Ultra-wideband radar sensors for short-range vehicular applications. *IEEE Transactions on Microwave Theory and Techniques*, 52(9):2105–2122, Sept. 2004.

[48] European Conference of Postal and Telecommunications Administrations (CEPT). Final report from cept in response to ec mandates on the harmonised introduction of radio applications based on ultra-wideband (uwb) technology. Technical Report RSCOM07-23 Final, European Commission, March 2007.

[49] S. Roy, J.R. Foerster, V.S. Somayazulu, and D.G. Leeper. Ultrawideband radio design: the promise of high-speed, short-range wireless connectivity. *Proceedings of the IEEE*, 92(2):295–311, Feb. 2004.

[50] M. Di Benedetto, T. Kaiser, A. F. Molisch, I. Oppermann, C. Politano, and D. Porcino. *UWB Communication Systems. A comprehensive over-*

view. EURASIP Book Series on Signal Processing and Communications. Hindawi Publishing Corporation, New York, NY 10022, USA, 2006.

[51] M. Ghavami, L. B. Michael, and R. Kohno. *Ultra-wideband signals and systems in communication engineering*. John Wiley & Sons, Inc., 2004.

[52] J.T. Conroy, J.L. LoCicero, and D.R. Ucci. Communication techniques using monopulse waveforms. In *Proceedings of the IEEE Military Communications Conference*, volume 2, pages 1181–1185, Nov. 1999.

[53] Kefeng Fan, Subing Zhang, and Xiufen Liu. A uwb pulse shapes modulation scheme based on modified hermite polynomials. In *Proceedins of the 4th International Conference on Wireless Communications, Networking and Mobile Computing*, pages 1–4, Oct. 2008.

[54] R. Blazquez, P.P. Newaskar, F.S. Lee, and A.P. Chandrakasan. A baseband processor for pulsed ultra-wideband signals. In *Proceedings of the IEEE Custom Integrated Circuits Conference*, pages 587–590, Oct. 2004.

[55] F. S. Lee, D. D. Wentzloff, and A. P. Chandrakasan. An ultra-wideband baseband front-end. In *Digest of Papers from IEEE Radio Frequency Integrated Circuits Symposium*, pages 493–496, June 2004.

[56] A. Harter and A. Hopper. A distributed location system for the active office. *IEEE Network*, 8(1):62–70, Jan/Feb 1994.

[57] M. Porretta, P. Nepa, G. Manara, F. Giannetti, M. Dohler, B. Allen, and A.H. Aghvami. A novel single base station location technique for microcellular wireless networks: description and validation by a deterministic propagation model. *IEEE Transactions on Vehicular Technology*, 53(5):1502–1514, Sept. 2004.

[58] L. De Nardis and M.-G. Di Benedetto. Overview of the ieee 802.15.4/4a standards for low data rate wireless personal data networks. In *Proceedins of 4th Workshop on Positioning, Navigation and Communication*, pages 285–289, March 2007.

[59] Y. Shimizu and Y. Sanada. Accuracy of relative distance measurement with ultra wideband system. In *Procedings of the IEEE Confernce on Ultra Wideband Systems and Technologies*, pages 374–378, Nov. 2003.

[60] M. Porretta, P. Nepa, G. Manara, F. Giannetti, M. Dohler, B. Allen, and A.H. Aghvami. A novel single base station location technique for microcellular wireless networks: description and validation by a deterministic

propagation model. *IEEE Transactions on Vehicular Technology*, 53(5):1502–1514, Sept. 2004.

[61] P. Goud, A. Sesay, and M. Fattouche. A spread spectrum radiolocation technique and its application to cellular radio. In *Proceedings of the IEEE Pacific Rim Conference on Communications, Computers and Signal Processing*, volume 2, pages 661–664, July 1991.

[62] Hui Liu, H. Darabi, P. Banerjee, and Jing Liu. Survey of wireless indoor positioning techniques and systems. *IEEE Transactions on Systems, Man, and Cybernetics*, 37(6):1067 –1080, Nov. 2007.

[63] Z. Sahinoglu and A. Catovic. A hybrid location estimation scheme (h-les) for partially synchronized wireless sensor networks. In *Proceedings of the IEEE International Conference on Communications*, volume 7, pages 3797–3801, June 2004.

[64] J. Maurer, O. Drumm, D. Didascalou, and W. Wiesbeck. A novel approach in the determination of visible surfaces in 3d vector geometries for ray-optical wave propagation modelling. In *Proceedings of the 51st IEEE Vehicular Technology Conference*, volume 3, pages 1651–1655, Tokyo, Japan, 2000.

[65] F. Aguado Agelet, A. Formella, J.M. Hernando Rabanos, F. Isasi de Vicente, and F. Perez Fontan. Efficient ray-tracing acceleration techniques for radio propagation modeling. *IEEE Transactions on Vehicular Technology*, 49(6):2089–2104, Nov. 2000.

[66] Y. Zhou and H. Ling. On the multiplaten z-buffer algorithm for ray tracing in high-frequency electromagnetic scattering computations. *Microwave and Optical Technology Letters*, 43:298–301, 2004.

[67] F. Saez de Adana, O. Gutierrez Blanco, I. Gonzalez Diego, J. Perez Arriaga, and M.F. Catedra. Propagation model based on ray tracing for the design of personal communication systems in indoor environments. *IEEE Transactions on Vehicular Technology*, 49(6):2105–2112, Nov. 2000.

[68] H. Suzuki and A.S. Mohan. Measurement and prediction of high spatial resolution indoor radio channel characteristic map. *IEEE Transactions on Vehicular Technology*, 49(4):1321–1333, July 2000.

[69] E.J. Borowski and J.M. Borwein. *The HarperCollins Dictionary of Mathematics*. HarperCollins, 1991.

[70] D.N. Schettino and F.J.S. Moreira. A ray-tracing algorithm based on a double-tree image theory. In *Proceedings of the 2001 SBMO/IEEE MTT-S International Microwave and Optoelectronics Conference*, volume 1, pages 199–202, 2001.

[71] V.S. Somayazulu, J.R. Foerster, and S. Roy. Design challenges for very high data rate uwb systems. In *Conference Record of the 36th Asilomar Conference on Signals, Systems and Computers*, volume 1, pages 717–721, Nov. 2002.

[72] Alan V. Oppenheim and Ronald W. Schafer. *Discrete-time signal processing*. Prentice-Hall, Inc., Upper Saddle River, NJ, USA, 1st edition, 1989.

[73] Simon Haykin and Barry Van Veen. *Signals and Systems*. John Wiley & Sons, Inc., New York, NY, USA, 2002.

[74] C. Knapp and G. Carter. The generalized correlation method for estimation of time delay. *IEEE Transactions on Acoustics, Speech and Signal Processing*, 24(4):320–327, 1976.

[75] J.D. Owens, M. Houston, D. Luebke, S. Green, J.E. Stone, and J.C. Phillips. Gpu computing. *Proceedings of the IEEE*, 96(5):879 –899, May 2008.

[76] D. Manocha. General-purpose computations using graphics processors. *IEEE Computer*, 38(8):85 – 88, Aug. 2005.

[77] Rui Jiang, Feng Zeng, Wangshu Zhang, Xuebing Wu, and Zhihong Yu. Accelerating genome-wide association studies using cuda compatible graphics processing units. In *Proceedings of 2009 International Joint Conference on Bioinformatics, Systems Biology and Intelligent Computing*, pages 70 –76, Aug. 2009.

[78] Xiaowen Chu, Kaiyong Zhao, and Mea Wang. Massively parallel network coding on gpus. In *Proceedings of IEEE International Performance, Computing and Communications Conference*, pages 144 –151, Dec. 2008.

[79] Nvidia cuda programming guide web resourses. `http://developer.download.nvidia.com/compute/cuda/2_0/docs/NVIDIA_CUDA_Programming_Guide_2.0.pdf`.

[80] A.F. Abdelrazek, M. Kaschub, C. Blankenhorn, and M.C. Necker. A novel architecture using nvidia cuda to speed up simulation of multi-path fast fading channels. In *Proceedings of IEEE 69th Vehicular Technology Conference*, pages 1 –5, April 2009.

[81] R. Beck, A.G. Dempster, and I. Kale. Finite-precision goertzel filters used for signal tone detection. *IEEE Transactions on Circuits and Systems II: Analog and Digital Signal Processing,*, 48(7):691 –700, July 2001.

[82] D. Schwingshackl, T. Mayerdorfer, and D. Straussnigg. Universal tone detection based on the goertzel algorithm. In *Proceedings of the 49th IEEE International Midwest Symposium on Circuits and Systems, 2006. MWSCAS '06.*, volume 1, pages 410 –413, 6-9 2006.

[83] A. Tchegho, H. Mattes, and S. Sattler. Optimal high-resolution spectral analyzer. In *Proceedings of Conference on Design, Automation and Test in Europe, 2008.*, pages 62 –67, March 2008.

[84] Min-Chuan Lin, Guo-Ruey Tsai, Yung-Chin Tu, Tai-Hsiung Chang, and Ching-Hui Lin. Fpga-based spectrum analyzer with high area efficiency by goertzel algorithm. In *Proceedings of Congress on Image and Signal Processing, 2008. CISP '08.*, volume 1, pages 157–159, 27-30 2008.

Publications

J. Diskin and C. Brennan, "A 3D ray tracing tool for indoor UWB signal propagation modelling", IEE Irish Signals and Systems Conference, Dublin, Ireland, 2005.

J. Diskin and C. Brennan, "An Efficient Ray-Tracing Image Removal Algorithm for Indoor 3D Radiowave Propagation Modelling", European Conference on Antennas and Propagation, Nice, France, 2006.

J. Diskin and C. Brennan, "Accelerated Ray-Tracing for Indoor Ultra-wideband Propagation Modelling", The 65th IEEE Vehicular Technology Conference, Dublin, Ireland, 2007.

J. Diskin, C. Brennan and A. Alomainy, "An Accelerated Frequency Domain Ray-tracing Simulator for Ultra-Wideband Communications", Progress in Electromagnetics Research Symposium, Beijing, China, 2009.

Acknowledgments

This work has only possible due to the financial support from the Irish Research Council for Science Engineering and Technology. I have always greatly appreciated this support during this project. In addition, this author graciously acknowledges Dr. Eamonn Kenny and Trinity College Dublin for the contribution of the original narrow-band ray tracing simulator. I would like to take this opportunity to thank all those who have helped me during this research project. I wish to acknowledge the continuing and enthusiastic support of my supervisor Dr. Conor Brennan. I thank my colleagues for their enduring friendship during my time in DCU, in particular Diana Bogushevski, Patrick Bradley, Bijilash Babu, Sean Begley, Emira Dautbegovic, Aubrey Dunne, Andrew Errity, Barry Kirkpatrick, Patricia Moore and Marie Mullen. This project was greatly helped by the support and counsel from my good friend Robert Burmiston. Furthermore, I would like to thank Hazel Weigl for her understanding and inspiring friendship over the last few months. Most of all, I am perpetually indebted to my parents for their unwavering support over the years.

John Diskin
Dublin
January 17, 2011